國立臺灣大學電機資訊學院電信工程學研究所

博士論文

Graduate Institute of Communication Engineering

College of Electrical Engineering and Computer Science

National Taiwan University

Doctoral Dissertation

部分元素等效電路法輻射阻抗、時域模擬、及穩定性之研究

On the Radiation Resistance, Transient Simulation, and Stability of the Partial Element Equivalent Circuit Method

周求致

Chiu-Chih Chou

指導教授：吳宗霖 博士

Advisor: Tzong-Lin Wu, Ph.D.

中華民國 108 年 6 月

June 2019

doi: 10.6342/NTU201902629

國立臺灣大學博士學位論文
口試委員會審定書

部分元素等效電路法輻射阻抗、時域模擬、及穩定性之研究

On the Radiation Resistance, Transient Simulation, and Stability of the Partial Element Equivalent Circuit Method

本論文係周求致君（F00942009）在國立臺灣大學電信工程學研究所完成之博士學位論文，於民國 108 年 6 月 27 日承下列考試委員審查通過及口試及格，特此證明

口試委員：

吳宗霖（簽名）

（指導教授）

吳瑞北

江衍偉　　曹恆偉

鄭士康　　莊晴光

所　　長　蘇炫榮（簽名）

誌謝

衷心感謝指導教授吳宗霖老師對我的支持與激勵，在研究所前幾年，不斷的在換題目，老師總是完全支持，鼓勵我勇於嘗試。在專業上老師多方指導，在尋找研究題目上種種啟發，各種國際交流鼓勵我們參加，使我的學業能不斷的前進；在生活上老師對學生也十分照顧關心，非常感謝老師這幾年的辛勞與費心。

在台大有幸受到許多老師課堂上的啟迪，感謝物理系的林清凉教授、朱國瑞教授、賀培銘教授，建立我電磁學的物理觀念；數學系的張志中教授與陳宏教授，不斷的強調要自己念書，修正我以往重上課而不重讀書的習慣；電信所張宏鈞教授與鐘嘉德教授，上課都是「逢放假必補課，上不完必加課」，認真敬業的態度令學生景仰；口試委員老師們，對本論文多所指正，點出我所忽略的問題；以及吳瑞北老師的電源完整度、莊晴光老師的微波工程、林怡成老師的電磁理論、傅立成老師的非線性系統、薛克民老師的數值線代等，還有許多老師的課程、大學部導師李建模教授、以及中學時期的老師們，從上課中求致都獲益良多。

剛進實驗室時，感謝皓翔學長的帶領；學長畢業後，泓銓、逸民、偉強、志穎、齊軒、英誠、揚智、祺凱、培森、兆凱等學長，都對求致多有照顧，或者討論研究，或者教導軟體使用，或者指點實驗操作，感謝學長們付出的時間與精神。實驗室的學弟妹們也都非常優秀，求致時常從你們得到啟發，本論文第四章的部分內容，就是在跟培洋的討論中得到靈感，在此一併致謝。

我的祖父母曾在艱困的環境中，憑藉著堅忍的毅力與勤奮的態度走過來。我的父母將這份美德教導予我，使我今天能夠在台大拿到博士學位，並繼續向前邁進。感謝我的父母與祖先。

周求致

108.08.08

doi: 10.6342/NTU201902629

THIS PAGE INTENTIONALLY LEFT BLANK.

摘要

本論文針對部分元素等效電路法(partial element equivalent circuit，以下簡稱 PEEC)的三個面向進行探討。第一個面向為全波(full-wave) PEEC 所具有的複數電感與複數電位係數之物理意義。經由理論推導，本論文嚴格的證明了此複數電感電位所引生的功率損耗，完全對應到該結構的總輻射功率；若該結構本身沒有電源，而是受入射波的激發，則此功率損耗對應該結構的總散射功率。因此，此複數電感電位，其虛部具有該結構之輻射電阻(radiation resistance)的物理意義。

第二個面向為全波 PEEC 之時域模擬方法。由於全波模型中，互感與互容的耦合皆帶有時間延遲(time delay)，而一般的電路模擬軟體並不支援帶時延之互感，故傳統上必須自行撰寫程式來解全波模型之時延微分方程，因而限縮了全波 PEEC 與其他電路之整合性。本論文提出一種方法，利用電路模擬軟體中受控電源(controlled source)之時延功能，將全波 PEEC 模型實現成電路模擬軟體支援的形式，進而可用一般商用軟體來模擬時域響應。此法使得全波 PEEC 之模擬困難度大幅降低。又，透過此方法，我們得以模擬許多不同的模型，從中觀察到全波 PEEC 在時域上經常會出現不穩定的響應，因而啟發了本論文第三部分的研究。

第三個面向即為全波 PEEC 之穩定性(stability)分析。此穩定性問題又可分為三個部分：一、如何判斷一個模型穩定與否。二、若不穩定，是何原因導致其不穩定。三、如何改善其穩定性。對於第一個問題，本論文提出一套演算法，能將電路模型一部分的自然頻率(natural frequency)找出來，作為判斷穩定性的必要條件。第二個問題，本論文從被動性(passivity)的角度來分析，證明了標準的 PEEC 模型，其電感與電位矩陣，不具備被動性；相反的，其可產生大量的能量，以供應電路的發散響應。第三個問題，本論文先將文獻中的各種阻尼電路彙整，並做系統性的分析，再利用前述自然頻率的檢測，提出一個系統性的阻尼設計方法。最後，本論文再探討如何從被動性的角度來進行阻尼的設計。

關鍵字：部分元素等效電路、數值方法、穩定性、被動性。

doi: 10.6342/NTU201902629

ABSTRACT

This dissertation studies three aspects of the partial element equivalent circuit (PEEC) method. The first one is the physical meaning of the complex inductance and potential coefficient occurred in full-wave (FW) PEEC model. Through rigorous derivation, we prove that the total power consumed in these complex coupling networks corresponds to the total radiated power of the circuit. If the circuit is not excited internally, but illuminated by an incident wave, then this power consumption corresponds to the total scattered power. Consequently, the imaginary parts of these complex couplings have the physical meaning of radiation resistance of the structure.

The second part deals with the time domain simulation method of FW PEEC. Due to the presence of time delay, the inductive and potential couplings are not supported by typical circuit simulators such as SPICE. Traditionally, researchers had to write their own differential equation solver in order to conduct transient simulation. In this dissertation, we exploit the time delay function of the controlled sources in typical SPICE and propose a method to cast the FW PEEC model into a fully SPICE-compatible form, which greatly eases the effort of conducting time domain simulation as well as the co-simulation with external linear or nonlinear lumped circuit. Also, from several simulation results, we observe that the time domain response of FW PEEC often suffers from unstable resonance. This then motivates the study of the third part.

doi: 10.6342/NTU201902629

The third part of the dissertation focuses on the stability properties of FW PEEC. The stability problem can be further divided into three subparts: (a) how do we test if a given model is stable or not; (b) if it is unstable, what is the reason for its instability; and (c) what are the methods that we can apply to improve the stability. In part (a), we propose an algorithm that can efficiently obtain some of the natural frequencies of the circuit. Such information serves as a necessary-condition test for stability. In part (b), we show that the inductive and potential coupling matrices of general FW PEEC models are far from being passive. They are thus the energy sources that support the unstable resonances of the circuit. In part (c), we first summarize existing damping method in the literature. And then we present systematic analysis of various damping structures, and propose two design approaches based on stability and passivity.

Index terms – partial element equivalent circuit, numerical method, stability, passivity.

CONTENTS

doi: 10.6342/NTU201902629

doi: 10.6342/NTU201902629

LIST OF FIGURES

doi: 10.6342/NTU201902629

LIST OF TABLES

doi: 10.6342/NTU201902629

GLOSSARY

General
FD: Frequency domain
TD: Time domain
RHS: Right hand side
LHS: Left hand side
RHP: Right half plane
LHP: Left half plane

System and Stability
BIBO: Bounded-input bounded-output
LTI: Linear time-invariant
ADE: Associated difference equation
FDE: Functional differential equation
NFDE: Neutral FDE
RFDE: Retarded FDE
LMI: Linear matrix inequality

Electromagnetic
EM: Electromagnetic
ESD: Electrostatic discharge
FDTD: Finite difference time domain
FEM: Finite element method
FW: Full-wave
MoM: Method of moment
MPIE: Mixed potential integral equation
PEEC: Partial element equivalent circuit
PEC: Perfect electric conductor
QS: Quasi-static
RWG: Rao-Wilton-Glisson

Circuit
DC: Direct current
LPF: Lowpass filter
KCL: Kirchhoff current law
MNA: Modified nodal analysis
VCVS: Voltage-controlled voltage source
VCCS: Voltage-controlled current source
CCVS: Current-controlled voltage source
CCCS: Current-controlled current source

Damping Structures
GRP: Garrett-Ruehli-Paul (Fig. 4.22)
EAR: Ekman-Antonini-Ruehli (Fig. 4.25)
MKW: Modified-Kochetov-Wollenberg (Fig. 4.23)
KW: Kochetov-Wollenberg (Fig. 4.26)

Software
ADS: Advanced Design System (a circuit simulator of Keysight)
HFSS: High Frequency Structure Simulator (an EM simulator of ANSYS)
HSPICE (a circuit simulator of SYNOPSYS)
MATLAB (a matrix computation software of MathWorks)
SPICE: Simulation Program with Integrated Circuit Emphasis

doi: 10.6342/NTU201902629

Chapter 1 Introduction

1.1 General Introduction

The partial element equivalent circuit (PEEC) [1] is a computational electromagnetic (EM) method featuring circuit-oriented solutions for full-wave EM problems. Classic EM methods such as finite element method (FEM) [2], method of moment (MoM) [3], and finite difference time domain (FDTD) [4] usually solve an EM problem algebraically, by a dedicated solver program. PEEC, on the other hand, features the capability of transforming an arbitrary three dimensional structure consisting of conductors and dielectric/magnetic materials into an equivalent circuit made of resistors, capacitors, inductors, and controlled sources. Accordingly, the original EM problem can be solved by a SPICE-like simulator. An immediate advantage of PEEC is its ease of co-simulation with other lumped circuits, linear or nonlinear, connected to the EM structure.

As a historical note, the PEEC method was first proposed by Dr. Ruehli in 1974 [1]. The foundation of PEEC is the important concept of partial inductance, which was also proposed by Ruehli in 1972 [5], two years earlier than PEEC. Since PEEC transforms an EM problem into an equivalent circuit, we thus need an efficient method to solve a circuit problem. In 1975, Ho, Ruehli, and Brennan published the first paper on the modified nodal analysis (MNA) [6], whose importance was far-reaching. The MNA quickly became one of the major algorithms in most circuit simulators [7], while PEEC, an EM algorithm, was not widely recognized until the 1990s. Since then, various extension of the PEEC method were published, such as the inclusion of dielectric material [8], the nonorthogonal discretization [9], and the modeling of skin effect [10].

In this dissertation, we focus on three distinct but related subjects of PEEC. The first one is the meaning of complex inductance and potential coefficients. The second one is the methods to conduct time domain simulation of PEEC models. The third one is the stability and passivity properties of PEEC. The motivation of these studies and corresponding literature reviews will be given in due course.

doi: 10.6342/NTU201902629

1.2 Introduction to the PEEC Method

Maxwell’s equations in phasor domain are given by

$$\varepsilon_0 \nabla \cdot \mathbf{E} = \rho \tag{1.1}$$

$$\nabla \cdot \mathbf{B} = 0 \tag{1.2}$$

$$\nabla \times \mathbf{B} = \mu_0 \mathbf{J} + j\omega \mu_0 \varepsilon_0 \mathbf{E} \tag{1.3}$$

$$\nabla \times \mathbf{E} = -j\omega \mathbf{B} \tag{1.4}$$

We will use boldface letters to denote vectors and matrices except for unit vectors which have a hat above them, whereas lightface letters for scalars. The equation of charge conservation, or continuity equation, is given by

$$\nabla \cdot \mathbf{J} + j\omega \rho = 0 \tag{1.5}$$

Mathematically, the divergence of the curl of any function is identically zero, i.e.,

$$\nabla \cdot (\nabla \times \mathbf{A}) = 0$$

for any function **A**. Then, from Gauss’ law for magnetism (1.2), we can define a vector potential **A** to be any function that satisfies

$$\mathbf{B} = \nabla \times \mathbf{A} \tag{1.6}$$

Such definition for **A**, however, will render the vector potential undetermined up to the addition of the gradient of any scalar function, ψ. That is to say,

$$\mathbf{A}' = \mathbf{A} + \nabla \psi$$

will still be a valid vector potential that satisfies (1.6), because the curl of the gradient of any function is identically zero, i.e., $\nabla \times \nabla \psi = 0, \forall \psi$. Nevertheless, the ambiguity of $\mathbf{A}$ will be settled down as we enforce Lorenz's gauge and causality.

Substituting (1.6) into Faraday's law (1.4), we obtain

$$\nabla \times (\mathbf{E} + j\omega \mathbf{A}) = 0$$

From this equation we can define the scalar potential Φ to be any function that satisfies

$$\mathbf{E} + j\omega \mathbf{A} = -\nabla \Phi$$

The minus sign is just a convention. Again, this definition for Φ renders it undetermined up to the addition of any constant: $\Phi' = \Phi$ + constant. Similarly, this ambiguity will be removed as we fix the gauge and require causality.

We can rewrite the above expression for **E** as

$$\mathbf{E} = -j\omega \mathbf{A} - \nabla \Phi \tag{1.7}$$

Substituting (1.6) and (1.7) into Ampere-Maxwell's equation (1.3), we obtain

$$\nabla \times \nabla \times \mathbf{A} = \mu_0 \mathbf{J} + j\omega \mu_0 \varepsilon_0 (-j\omega \mathbf{A} - \nabla \Phi)$$

With the vector identity

$$\nabla \times \nabla \times \mathbf{A} = \nabla(\nabla \cdot \mathbf{A}) - \nabla^2 \mathbf{A}$$

we have,

$$(\nabla^2 + \omega^2 \mu_0 \varepsilon_0)\mathbf{A} = -\mu_0 \mathbf{J} + \nabla(\nabla \cdot \mathbf{A} + j\omega \mu_0 \varepsilon_0 \Phi)$$

At this stage, we may apply the Lorenz gauge [11]

$$\nabla \cdot \mathbf{A} + j\omega \mu_0 \varepsilon_0 \Phi = 0$$

doi: 10.6342/NTU201902629

to obtain

$$(\nabla^2 + k^2)\mathbf{A} = -\mu_0 \mathbf{J} \tag{1.8}$$

where $k = \omega\sqrt{\mu_0 \varepsilon_0} = \frac{\omega}{c}$ is the wavenumber. This is recognized to be the Helmholtz equation, or wave equation, for **A**, the source of which being the current **J**.

Substituting (1.7) into Gauss' law for electricity (1.1), and again using the Lorenz gauge, we have

$$(\nabla^2 + k^2)\Phi = -\frac{\rho}{\varepsilon_0} \tag{1.9}$$

At this moment, we have successfully transformed the original Maxwell's equations in terms of **E** and **B** into two equations in terms of **A** and Φ. The sources of the fields are **J** and ρ. Through (1.8) and (1.9) we can solve for **A** and Φ, and through (1.6) and (1.7) we obtain the physical quantities **E** and **B**. It is remarkable that, under Lorenz gauge, both **A** and Φ satisfy the same wave equation with propagation velocity equal to the speed of light, *c*. We also point out that the Lorenz gauge is not complete, in the sense that any vector (scalar) function that satisfies the homogeneous wave equation can be added to **A** (Φ) without nulling any equalities. This remaining gauge freedom can be removed if proper boundary conditions are enforced. For example, if the sources **J** and ρ are in free space but are localized, then from the physical requirement of causality, there can be no any homogeneous solutions to (1.8) and (1.9).

In free space, it is known [12] that the particular solution to (1.8) is given by

doi: 10.6342/NTU201902629

$$\mathbf{A}(\mathbf{r}) = \mu_0 \int_V G(\mathbf{r},\mathbf{r}')\mathbf{J}(\mathbf{r}')\mathrm{d}^3x' = \frac{\mu_0}{4\pi}\int_V \frac{e^{-jkR}}{R}\mathbf{J}(\mathbf{r}')\mathrm{d}^3x' \tag{1.10}$$

where the volume of integration, *V*, includes all current sources $\mathbf{J}$. The Green's function for three-dimensional wave equation is given by

$$G(\mathbf{r},\mathbf{r}') = \frac{e^{-jkR}}{4\pi R} = \frac{e^{-jk|\mathbf{r}-\mathbf{r}'|}}{4\pi|\mathbf{r}-\mathbf{r}'|} \tag{1.11}$$

Similarly, the particular solution to (1.9) is given by

$$\Phi(\mathbf{r}) = \frac{1}{4\pi\varepsilon_0}\int_V \frac{e^{-jkR}}{R}\rho(\mathbf{r}')\mathrm{d}^3x' \tag{1.12}$$

The term "free space" deserves some clarification. The Green's function (1.11) inherently assumes that the problem domain is unbounded in all directions, and that there is no any "obstacles" including conductors and dielectric materials. However, practically currents flow on conductors. How can there be currents but with no conductors? The key point here is that all conductors are treated nothing more than media that support current and charge. When the fields generated by these current and charge are properly accounted for, the "conductors" are no longer an "object" in the problem domain, in some sense penetrable. The effects of the conductors are completely reflected by the current and charge on them. These current and charge on one hand generate fields as if they were in free space, and on the other hand they satisfy certain boundary conditions especially the Ohm's law. In other words, to use the Green's function (1.11) as in (1.10) and (1.12), we must include the current and charge on all conductors in the volume of integration *V*, with the complement of *V* being a truly "free space", free of objects in any form. The

doi: 10.6342/NTU201902629

polarization current on dielectric materials should also be included in the integration. However, in this dissertation, we will only consider conductors in free space, with no dielectric materials present.

The Ohm's law for a linear conductor is given by

$$\mathbf{J} = \sigma\mathbf{E}_{\mathrm{total}} = \sigma(\mathbf{E}_{\mathrm{inc}} + \mathbf{E}) \tag{1.13}$$

where σ is the conductivity, $\mathbf{E}_{\mathrm{inc}}$ is the incident electric field, and **E** is the electric field generated by local current and charge. This is the boundary condition that must be satisfied by currents on the conductors.

Now, we are ready to formulate an integral equation in terms of **J** and ρ. By putting (1.7), (1.10), and (1.12) together into (1.13), we arrive at the mixed-potential integral equation (MPIE):

$$\frac{\mathbf{J}(\mathbf{r})}{\sigma} + j\omega\mu_0 \int_V G(\mathbf{r},\mathbf{r}')\mathbf{J}(\mathbf{r}')\mathrm{d}^3r' = \mathbf{E}_{\mathrm{inc}} - \frac{1}{\varepsilon_0}\nabla \int_{\mathrm{V}} G(\mathbf{r},\mathbf{r}')\rho(\mathbf{r}')\mathrm{d}^3r' \tag{1.14}$$

where the point of observation, **r**, is located on conductors. The classic MoM [3] further simplify this equation by expressing the charge density ρ in terms of current density **J** using the continuity equation (1.5). The obvious advantage is that the number of unknowns is reduced to that of current density only. The drawback, however, is that because ρ is proportional to $1/\omega$, at extremely low frequencies this formulation is prone to serious numerical error, a phenomenon called low-frequency breakdown. In PEEC, instead, both **J** and ρ are kept as unknowns. The continuity equation is enforced by the

doi: 10.6342/NTU201902629

Kirchhoff’s Current Law (KCL) in the circuit domain. Consequently, for high frequency problems, the efficiency of PEEC will be lower than MoM due to the extra unknowns. However, PEEC permits a dc-to-daylight solution of the EM problem, both in frequency domain (FD) and time domain (TD). This differentiates PEEC form MoM.

The next step in PEEC formulation is to adopt a discretization scheme for both **J** and ρ. The original basis used by Ruehli [1] is the rectangular pulse basis function:

$$f_j(\mathbf{r}) = \begin{cases} 1 \ldots \mathbf{r} \in j^{\text{th}} \text{ current mesh} \\ 0 \ldots \text{otherwise} \end{cases}$$

$$\mathbf{J}(\mathbf{r}) = \sum_{j=1}^{n} \frac{I_j}{a_j} \hat{t}_j f_j(\mathbf{r}) \tag{1.15}$$

where I_j, a_j and $\hat{t}_j$ are the current, cross sectional area, and unit vector of the *j*-th current mesh, respectively, and *n* is the total number of current meshes. The charge density ρ is also discretized using pulse basis. However, to facilitate the enforcement of charge conservation, the charge meshes and current meshes do not coincide with each other. Instead, the charge meshes are partitioned in a manner such that the two endpoints of a current mesh correspond to the center points of two charge meshes, except for the current meshes located at the edges of conductors. That is to say, the charge basis is shifted with respect to the current basis by a half cell, as illustrated in Fig. 1.1. With this *interlaced* meshing, the continuity equation (1.5) becomes exactly the KCL at each node in the circuit domain.

doi: 10.6342/NTU201902629

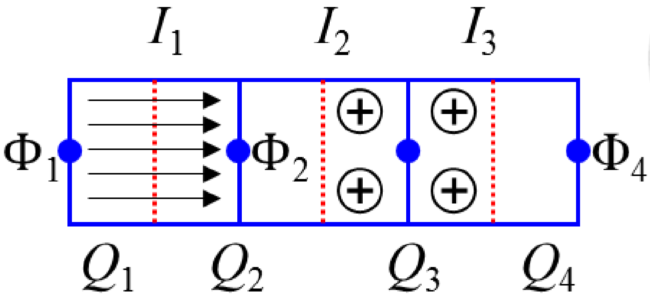

Fig. 1.1. Example of PEEC mesh of a thin strip conductor with four capacitive cells (nodes) partitioned by red dashed lines, and three inductive cells (branches) partitioned by blue solid lines.

In addition, since charge will reside only on the surfaces of conductors and any charge inside a conductor fades out exponentially [13], we only need to partition the surfaces of conductors for charge meshes. Then, we can write

$$\rho(\mathbf{r}) = \sum_{j=1}^{m} \frac{Q_j}{S_j} g_j(\mathbf{r}) \tag{1.16}$$

where Q_j and S_j are the charge and surface area of the j-th charge mesh, respectively, and m is the total number of charge meshes. The pulse basis g_j is similar to (1.15), but is understood to have a Dirac delta function in the direction perpendicular to the j-th surface mesh, so that the volume integral in (1.14) reduces to a surface integral.

Before moving on, we point out that although there are more sophisticated meshing methods for PEEC in the literature, such as nonorthogonal basis [9] and Rao-Wilton-Glisson (RWG) basis [14], in this dissertation we will only consider the standard rectangular basis. Since all the topics of the ensuing chapters are not tightly bonded to any particular meshing, it can be expected the methods and results of this dissertation are applicable to other PEEC discretization schemes.

The next step is to substitute (1.15) and (1.16) into (1.14). For simplicity, only the *z* component is written out. Equation (1.14) becomes

$$\frac{J_{\mathrm{z}}(\mathbf{r})}{\sigma} + j\omega\mu_0 \sum_{j=1}^{n_{\mathrm{z}}} \left(\hat{z}\cdot\hat{t}_j\right)\left[\int_{V_j} G(\mathbf{r},\mathbf{r}')\mathrm{d}^3r'\right]\frac{I_{\mathrm{z}j}}{a_j} = \mathbf{E}_{\mathrm{inc}} - \frac{1}{\varepsilon_0}\frac{\partial}{\partial z}\sum_{j=1}^{m}\left[\int_{S_j} G(\mathbf{r},\mathbf{r}')\mathrm{d}^2r'\right]\frac{Q_j}{S_j} \tag{1.17}$$

Similar to conventional MoM, the Galerkin's method is adopted in PEEC, which means that we use the same pulse basis as the testing function, and take the inner product with (1.17). Specifically, we multiply $f_i\,(\mathbf{r})/a_i$ to (1.17), where the *i*-th current mesh is in z direction, i.e., $\hat{t}_i = \hat{z}$, and integrate over V_i, the support of the *i*-th mesh, which results in

$$\begin{aligned}\frac{I_i}{\sigma a_i^2}\int_{V_i}\mathrm{d}^3r' + j\omega\mu_0\sum_{j=1}^{n_{\mathrm{z}}}\left(\hat{z}\cdot\hat{t}_j\right)&\left[\int_{V_i}\int_{V_j}G(\mathbf{r},\mathbf{r}')\mathrm{d}^3r'\mathrm{d}^3r\right]\frac{I_{\mathrm{z}j}}{a_i a_j}\\ &= \frac{1}{a_i}\int_{V_i}\hat{z}\cdot\mathbf{E}_{\mathrm{inc}}\mathrm{d}^3r' - \frac{1}{\varepsilon_0}\sum_{j=1}^{m}\left[\frac{1}{a_i}\int_{V_i}\frac{\partial}{\partial z}\int_{S_j}G(\mathbf{r},\mathbf{r}')\mathrm{d}^2r'\mathrm{d}^3r\right]\frac{Q_j}{S_j}\end{aligned} \tag{1.18}$$

Carry out the differentiation and integration of the *z* component of the right hand side (RHS) of (1.18), we have

$$\begin{aligned}&\frac{1}{a_i}\int_{V_i}\frac{\partial}{\partial z}\int_{S_j}G(\mathbf{r},\mathbf{r}')\mathrm{d}^2r'\mathrm{d}^3r\\ &\qquad = \frac{1}{a_i}\int_{a_i}\left[\int_{S_j}G\left(x,y,z_i+\frac{l_i}{2},\mathbf{r}'\right) - G\left(x,y,z_i-\frac{l_i}{2},\mathbf{r}'\right)\mathrm{d}^2r'\right]\mathrm{d}^2r\end{aligned} \tag{1.19}$$

where l_i is the length of the *i*-th current mesh along the direction of current flow, here, $\hat{z}$.

The points (z_i ± l_i)/2 are at the two endpoints of the i-th mesh. According to our discretization rule for charge basis, they coincide with the center points of the two charge meshes connected to this i-th current mesh. The integrals can be further simplified as

$$\frac{1}{a_i}\int_{a_i}\int_{S_j} G\left(x, y, z_i \pm \frac{l_i}{2}, \mathbf{r}'\right) \mathrm{d}^2r'\,\mathrm{d}^2r \cong \frac{1}{w_i}\int_{w_i}\int_{S_j} G\left(x, y, z_i \pm \frac{l_i}{2}, \mathbf{r}'\right) \mathrm{d}^2r'\,\mathrm{d}r$$

$$\cong \frac{1}{S_{i\pm}}\int_{S_{i\pm}}\int_{S_j} G\left(x, y, z_i \pm \frac{l_i}{2}, \mathbf{r}'\right) \mathrm{d}^2r'\,\mathrm{d}^2r$$

where w_i is the width of the i-th current mesh. The first approximation is valid as long as the thickness of the current mesh is much smaller than its width and length. Hence, in the examples of the following chapters we only consider very thin metal strips. Treatment for conductors with non-negligible thickness can be found in [15]. We should be careful about the second approximation. The integration domain $S_{i\pm}$ is the surface area of the *charge* mesh located at the sink/source of the i-th current mesh. Integration over $S_{i\pm}$ and then divided by $S_{i\pm}$ means to average the potential generated by the charges on S_j over the charge cell of observation [15, Ch 4]. It also makes the potential matrix symmetric as we will see immediately. Putting these results into (1.19) yields

$$R_i I_i + j\omega \sum_{j=1}^{n} \Lambda_{ij} I_j = V_{\mathrm{s}i} - \sum_{j=1}^{m} \left(\Pi_{i^+j} - \Pi_{i^-j}\right) Q_j \tag{1.20}$$

where we define

$$R_i = \frac{1}{\sigma a_i^2}\int_{V_i} \mathrm{d}^3r'$$

$$V_{\mathrm{s}i} = \frac{1}{a_i}\int_{V_i} \hat{t}_i \cdot \mathbf{E}_{\mathrm{inc}} \mathrm{d}^3r'$$

$$\begin{aligned}\Pi_{i\pm j} &= \frac{1}{\varepsilon_0 S_{i\pm} S_j}\int_{S_{i\pm}}\int_{S_j} G(\mathbf{r},\mathbf{r}')\,\mathrm{d}^2r\,\mathrm{d}^2r' \\ \Lambda_{ij} &= \frac{\mu_0}{a_i a_j}\int_{V_i}\int_{V_j}\left(\hat{t}_i\cdot\hat{t}_j\right)G(\mathbf{r},\mathbf{r}')\,\mathrm{d}^3r\,\mathrm{d}^3r'\end{aligned} \tag{1.21}$$

R_i is the Ohmic loss resistance of the i-th current mesh. V_{si} is the voltage source resulting from the incident wave. The Π_{ij} and Λ_{ij} are complex partial potential coefficient and partial inductance, respectively. They are complex quantities because of the exponential phase delay in the Green's function (1.11). It should be noted that in writing (1.20) we have generalized to including the current meshes of all three dimensions. Current meshes of orthogonal directions have mutual inductance equal to zero, as reflected by the dot product in the definition of Λ_{ij}.

With i going from 1 to n, meaning that we test all the current basis one-by-one, we end up having the matrix equation

$$(\mathbf{R} + j\omega\mathbf{\Lambda})\mathbf{I} = \mathbf{V}_\mathrm{s} + \mathbf{A}^\mathrm{T}\mathbf{\Pi}\mathbf{Q} \tag{1.22}$$

where $\mathbf{I} = [I_1, \ldots, I_n]^\mathrm{T}$, $\mathbf{Q} = [Q_1, \ldots, Q_m]^\mathrm{T}$, $\mathbf{V}_\mathrm{s} = [V_{\mathrm{s}1}, V_{\mathrm{s}2}, \ldots, V_{\mathrm{s}n}]^\mathrm{T}$, $\mathbf{R} = \mathrm{diag}(R_1, \ldots, R_n)$, $\mathbf{\Lambda} = (\Lambda_{ij}) \in \mathbb{C}^{n\times n}$, $\mathbf{\Pi} = (\Pi_{ij}) \in \mathbb{C}^{m\times m}$, and $\mathbf{A} \in \mathbb{R}^{m\times n}$ is the incidence matrix which represents the connections of the current and charge meshes. $A_{ij} = \pm 1$ if charge mesh i is at the source/sink of current mesh j, and 0 otherwise. The superscript T means matrix transpose. From the definitions of partial inductance and potential coefficient in (1.21), we see that the matrices $\mathbf{\Lambda}$ and $\mathbf{\Pi}$ are both symmetric. This property is important for the quasi-static PEEC to be realized as simple circuit elements, as we will see. In (1.22), both $\mathbf{I}$ and $\mathbf{Q}$ are unknowns. To solve the equation we also need the discrete version of charge conservation:

$$\mathbf{A}\mathbf{I} + j\omega\mathbf{Q} = \mathbf{I}_\mathrm{s} \tag{1.23}$$

where $\mathbf{I}_\mathrm{s} = [I_{\mathrm{s}1}, \ldots, I_{\mathrm{s}m}]^\mathrm{T}$ is the vector of external lumped current sources, with positive currents representing currents flowing *into* the corresponding charge meshes. Putting (1.22) and (1.23) together we have the matrix equation

$$\begin{pmatrix} j\omega\mathbf{I}_\mathrm{d} & \mathbf{A} \\ \mathbf{A}^\mathrm{T}\mathbf{\Pi} & -(\mathbf{R} + j\omega\mathbf{\Lambda}) \end{pmatrix} \begin{pmatrix} \mathbf{Q} \\ \mathbf{I} \end{pmatrix} = \begin{pmatrix} \mathbf{I}_\mathrm{s} \\ -\mathbf{V}_\mathrm{s} \end{pmatrix} \tag{1.24}$$

where $\mathbf{I}_\mathrm{d}$ is the identity matrix. The matrix equation (1.24) can be solved algebraically. However, the specialty of PEEC is that these equations are interpreted as circuit elements, which enables the combination with other lumped circuit elements in a direct manner. To see this, we first note that each charge mesh can be associated with a “node”, while each current mesh is regarded as a “branch”. In circuit domain, each node has a unique potential once we assign one node as ground. In PEEC, we let the node potential of the equivalent circuit be the scalar potential $\Phi(\mathbf{r})$ of the EM problem averaged over the corresponding charge mesh. Hence, in the following we will denote the vector of node potentials also as $\mathbf{\Phi}$. Since, according to (1.12), the scalar potential at infinity is zero if all charge are localized, the “ground” node in circuit domain corresponds to the point at infinity. From (1.12) and previous development, we have the relation between $\mathbf{\Phi}$ and the total charge $\mathbf{Q}$ of each charge mesh:

$$\mathbf{\Phi} = \mathbf{\Pi}\mathbf{Q} \tag{1.25}$$

If the potential matrix is invertible, we can rewrite (1.25) as

$$\mathbf{Q} = \mathbf{\Pi}^{-1}\mathbf{\Phi} \tag{1.26}$$

This is recognized to be the equation of a capacitor network, with capacitance matrix $\mathbf{\Pi}^{-1}$. If $\mathbf{\Pi}$ is symmetric, then so is $\mathbf{\Pi}^{-1}$. Then we can define $C_{ij} = -(\mathbf{\Pi}^{-1})_{ij}$ and $C_{ii} = \sum_j [(\mathbf{\Pi}^{-1})_{ij}]$, and the relation (1.26) can be realized by putting a capacitor C_{ij} between the i-th and j-th nodes, and a capacitor C_{ii} between the i-th node and ground. An example realization of four nodes is shown in Fig. 1.2.

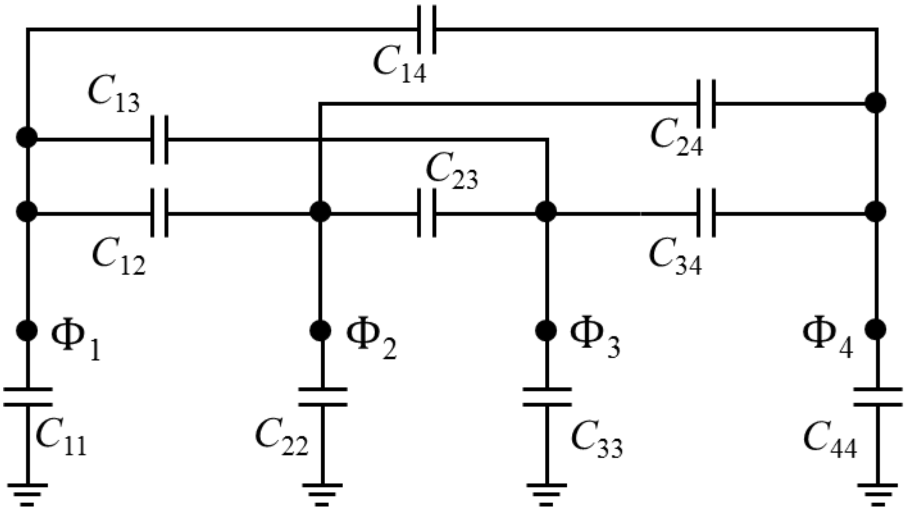

Fig. 1.2. Example realization of the potential coupling between four nodes, using capacitors connected between each pair of nodes and between each node and ground.

For large scale problems, computing matrix inverse is costly and prone to numerical error. There are other circuit realizations of the relation (1.25) that tactically utilize the controlled sources in SPICE to avoid the need to compute $\mathbf{\Pi}^{-1}$. Two methods are shown in Fig. 1.3 and Fig. 1.4, which can be verified to exhibit exact correspondence to (1.25).

doi: 10.6342/NTU201902629

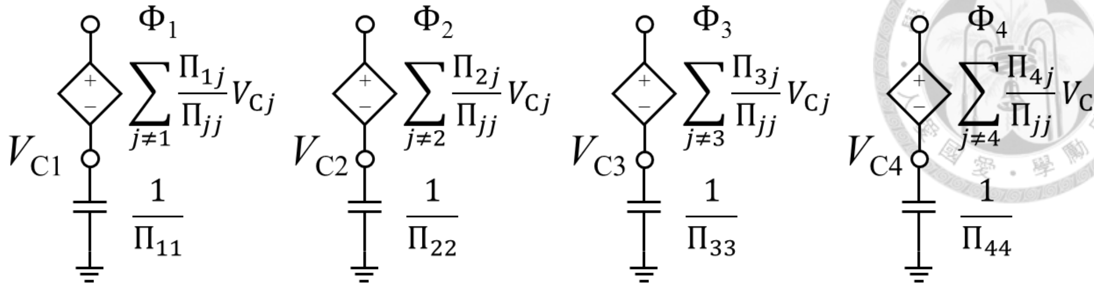

Fig. 1.3. Example realization of the potential coupling of four nodes using VCVS.

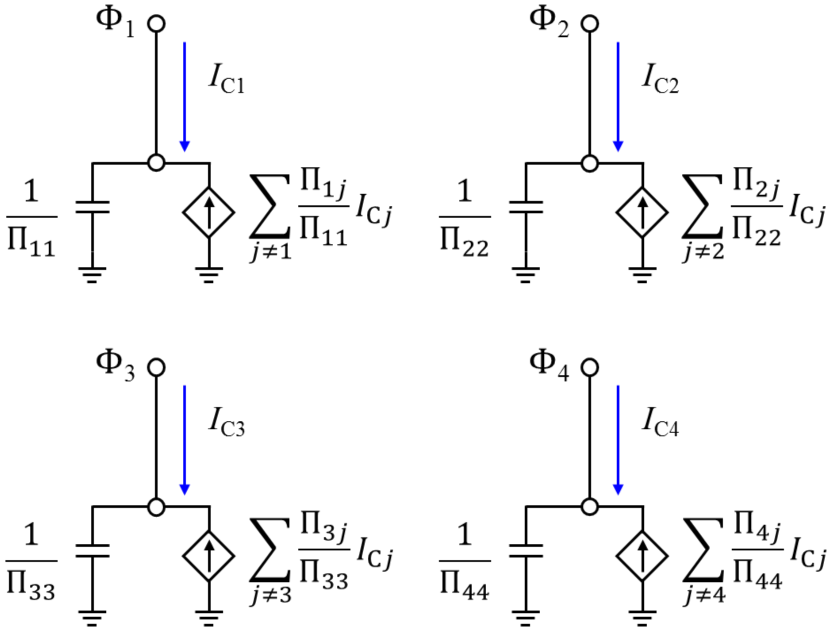

Fig. 1.4. Example realization of potential coupling of four nodes using CCCS.

For practical implementation, these two forms have a subtle difference. Seemingly, the VCVS form introduces one additional node (v_{Cj}) into the circuit for each charge mesh that increases the matrix size and reduces efficiency, whereas the CCCS form doesn't. However, in typical SPICE, to sample the branch current as in the CCCS topology, we need to insert a 0-V voltage source into those branches whose currents we wish to pick out. In addition, under the Modified Nodal Analysis (MNA) formulation which we will briefly describe later, the currents of controlled sources including VCVS and CCCS, as well as the currents of all independent voltage sources, are required to be taken out as independent variables. Consequently, the VCVS form actually introduces one less variable per charge mesh than the CCCS form, when implemented in SPICE. Hence, in Chapters 3 and 4, we will mainly use the VCVS topology for simulation.

The equation governing the behavior of each branch, or current mesh, is (1.22), which comes from enforcing the boundary condition of Ohm’s law at each mesh. Each row of (1.22) is in the form of (1.20). This relation can be realized as equivalent circuit if we recognize the first term in (1.20) as a series resistance, the second term as a mutually-coupled inductor network in series, the third term as a series voltage source, and the last term as the potential difference across the current mesh under consideration, coming from the capacitance network just described. As an example, Fig. 1.6 shows the complete equivalent circuit of a dipole antenna in Fig. 1.5, which is illuminated by an incident wave and at the same time driven by an external current source in parallel with a source resistor Z_0. Each of the two arms of the dipole are partitioned into two charge meshes and one current meshes.

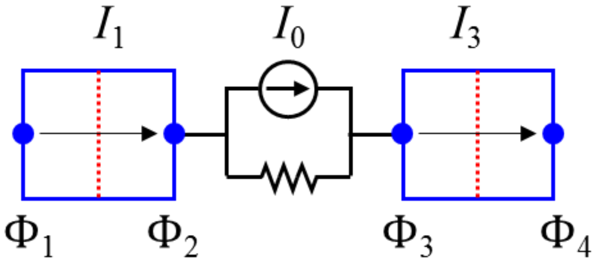

Fig. 1.5. Example of a thin strip dipole antenna.

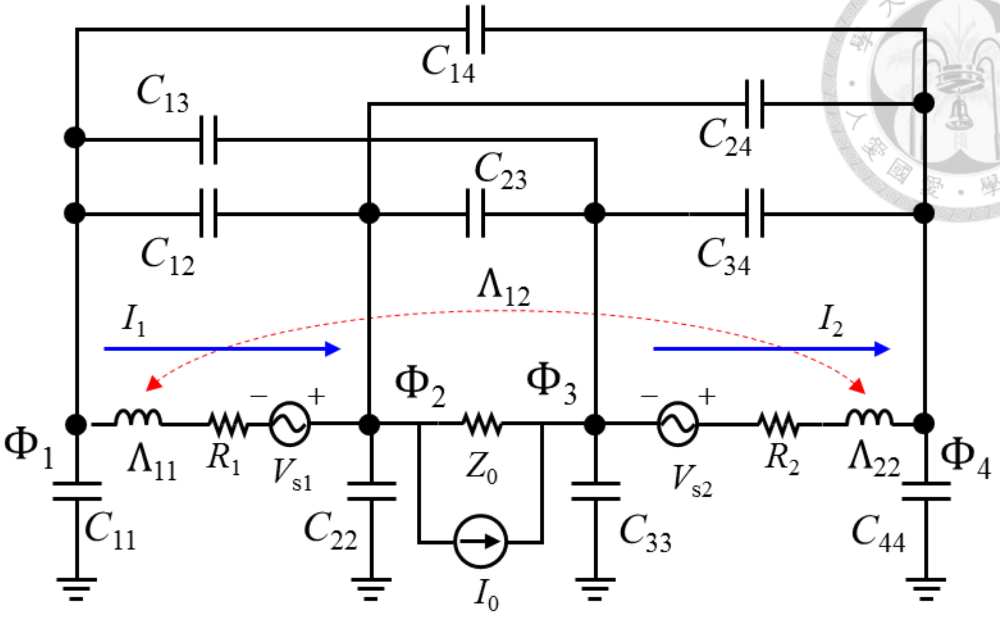

Fig. 1.6. Complete PEEC model of the strip dipole in Fig. 1.5.

Likewise, there are equivalent realizations of the coupled inductor network using controlled sources. Two methods are shown in Fig. 1.7 and Fig. 1.8, both exhibiting exact correspondence to the inductance matrix $\mathbf{\Lambda}$. There is also a subtle difference between these two topologies when running time domain simulation. The CCVS topology takes the currents at the other branches as the control variables, computes their time derivatives (the $j\omega$ in frequency domain), scales, and then adds to the destination branch. However, not every circuit simulators supports the operation of taking time derivative. In addition, careless implementation of the differentiation operation has the potential problem of amplifying numerical errors. The VCVS topology on the other hand cleverly avoids the differentiation by taking the voltage difference across the inductance as control variable, hence being more compatible with circuit simulators. The effect of the differentiation is accomplished by the solver engine of SPICE, whose numerical stability is much more reliable. So in later sections, we will mainly use the VCVS approach.

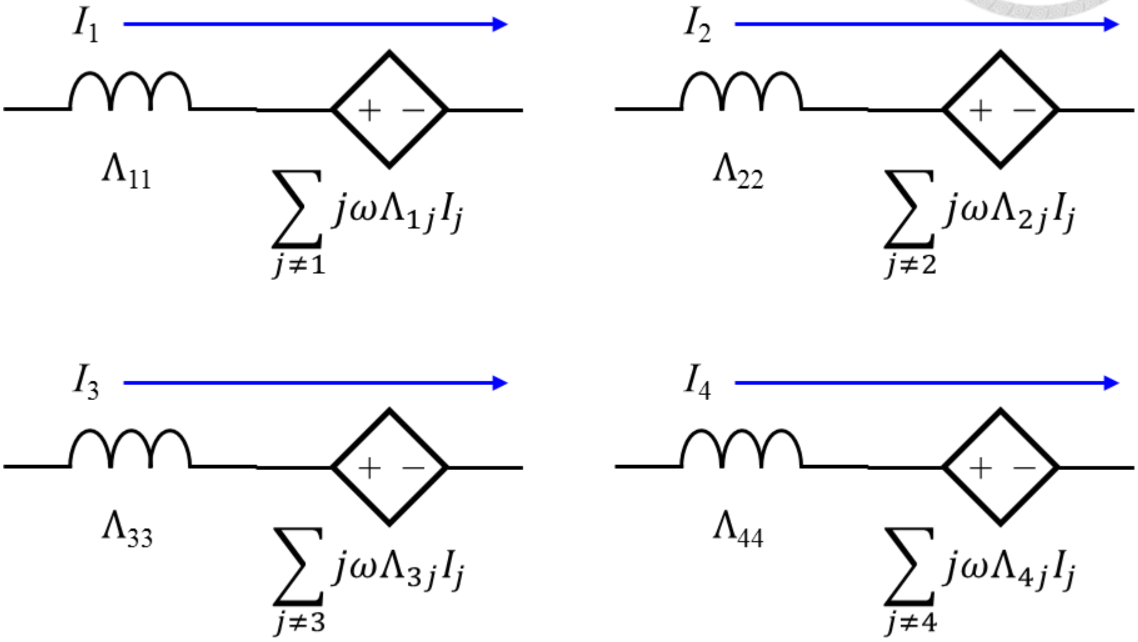

Fig. 1.7. Example realization of the inductive coupling of four branches using CCVS.

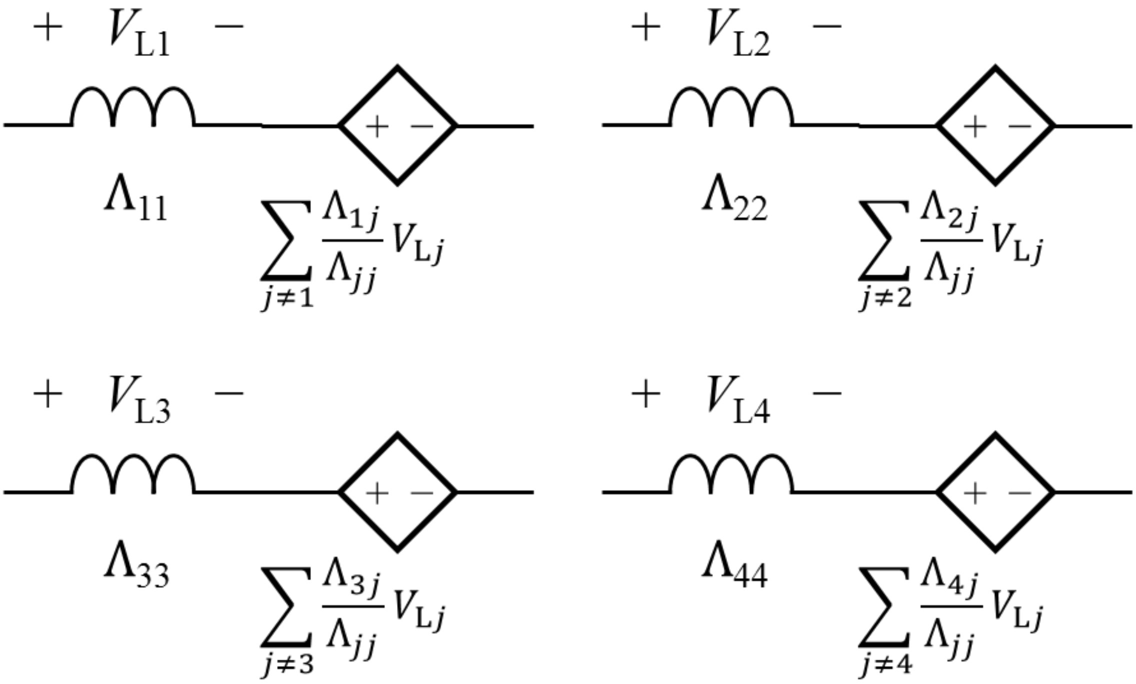

Fig. 1.8. Example realization of the inductive coupling of four branches using VCVS.

Once we build the complete PEEC model for the physical structure, the next step is to solve the circuit. Two common general-purpose algorithms are the Tableau Analysis and the MNA [7]. The principle of Tableau Analysis is to pick out every unknown as independent variable including all node voltages, all branch voltages, and all branch currents, and then write down all available equations, which results in a very large but sparse matrix equation. On the other hand, MNA is based on the nodal analysis, which only identifies the nodal voltages as the primary unknowns. The major equations to be solved are the KCL at each node. When there are components that cannot be described by node voltages only, MNA appends those necessary variables after the nodal voltage vector, together as the independent variables, and adds the governing equations of those branches into the matrix system. For example, the current through a resistor R can be expressed as the difference of the node voltages across it divided by R, so this current will not be included as an unknown. But for an inductor L, its current cannot be described by its terminal voltages. Hence we need to append this current i_L into our vector of unknowns, and add the branch equation $v_\mathrm{L} = L\frac{\mathrm{d}}{\mathrm{d}t} i_\mathrm{L}(t)$ or $V_\mathrm{L}(s) = sLI_\mathrm{L}(s)$ into our system of equation. Normally, the currents flowing through inductors, independent voltage sources, and controlled sources all need to be taken out, because they cannot be described by the node voltages. Still, compared with Tableau Analysis, the MNA matrix is much smaller, and remains quite sparse. The general form of MNA in Laplace domain can be expressed as

$$[\mathbf{T}(s)]\begin{bmatrix}\mathbf{E}\\ \mathbf{I}_2\end{bmatrix}=[\mathbf{U}] \tag{1.27}$$

where $\mathbf{E}$ is the vector of nodal voltages, $\mathbf{I}_2$ is the vector of selected branch currents, $\mathbf{U}$ is the vector of independent sources plus initial conditions, and $\mathbf{T}(s)$ is the MNA matrix. For lumped circuits, each element of $\mathbf{T}(s)$ will be a polynomial in s of order less than or equal to 1. Those elements proportional to s correspond to $\frac{\mathrm{d}}{\mathrm{d}t}$ in time domain. Therefore, for lumped circuits, the time domain MNA equation is given by

$$[\mathbf{T}(D)]\begin{bmatrix}\mathbf{e}(t)\\ \mathbf{i}_2(t)\end{bmatrix}=[\mathbf{u}(t)]$$

where $D = \frac{\mathrm{d}}{\mathrm{d}t}$. For distributed circuits, where terms like $\exp(-s\tau)$ present, the MNA matrix in time domain is not simply $\mathbf{T}(D)$.

The MNA is widely adopted by many circuit simulators. When we put a PEEC model into a SPICE, the solver engine will automatically follow the aforementioned procedure: identify all nodal voltages and necessary branch currents as independent variables, write down corresponding equations, and solve the matrix equation. However, for a PEEC model, we can write down a *reduced* version of the MNA equation by ignoring the *internal nodes* in each branch and the currents through the controlled sources. Specifically, we may use the VCVS topology for mutual inductance coupling. Then each branch would consists of an inductor, a resistor, and a VCVS, resulting in two internal nodes that do not correspond to any charge meshes. For the capacitor network, we may use the VCVS form to realize mutual potential coupling, which results in one internal node between the VCVS

doi: 10.6342/NTU201902629

and the capacitor for each charge mesh. The currents through the VCVS also need to be taken out as unknowns, according to the MNA rule. Consequently, the MNA equation actually being solved by SPICE would be several times larger than the total number of meshes. However, we know that no external lumped circuits will be attached to the internal nodes. As long as we can ensure KCL of the internal nodes, we may safely ignore these nodes in our system of equations. Hence, if we only select the nodes that corresponds to charge meshes, and branch currents of current meshes, as the independent variables, and write down the resulting nodal equations and branch equations, we end up having a very compact form of MNA equation:

$$\begin{pmatrix} j\omega\mathbf{\Pi}^{-1} & \mathbf{A} \\ \mathbf{A}^{\mathrm{T}} & -(\mathbf{R}+j\omega\mathbf{\Lambda}) \end{pmatrix}\begin{pmatrix} \mathbf{\Phi} \\ \mathbf{I} \end{pmatrix} = \begin{pmatrix} \mathbf{I}_{\mathrm{s}} \\ -\mathbf{V}_{\mathrm{s}} \end{pmatrix} \tag{1.28}$$

The upper half of (1.28) are the KCL at each node (excluding the internal nodes), while the lower half are the branch equations. Specifically, the left hand side (LHS) of the upper half equals the total current that *leaves* each node, while the corresponding RHS equals the total current from independent current sources that *enters* each node. This compact form of MNA, as we will see in the ensuing chapters, turns out to be very useful for the purpose of theoretical analysis. We also note that (1.28) is in fact equivalent to (1.24) by a simple change of variable: $\mathbf{\Phi} = \mathbf{\Pi}\mathbf{Q}$.

If lumped resistors are connected to the external nodes of the PEEC model, “external” meaning nodes that correspond to charge meshes, the resulting reduced MNA equation

doi: 10.6342/NTU201902629

would be in the form of

$$\begin{pmatrix} j\omega\mathbf{\Pi}^{-1}+\mathbf{Y} & \mathbf{A} \\ \mathbf{A}^{\mathrm{T}} & -(\mathbf{R}+j\omega\mathbf{\Lambda}) \end{pmatrix} \begin{pmatrix} \mathbf{\Phi} \\ \mathbf{I} \end{pmatrix} = \begin{pmatrix} \mathbf{I}_{\mathrm{s}} \\ -\mathbf{V}_{\mathrm{s}} \end{pmatrix} \tag{1.29}$$

where $\mathbf{Y} \in \mathbb{C}^{m\times m}$ is the node-admittance matrix [7], with $Y_{ii} = \sum_j (1/R_{ij})$, the summation of conductance connected to node i, and $Y_{ij} = 1/R_{ij}$, R_{ij} being the total resistance between nodes i and j. Take Fig. 1.5 as an example. The charge meshes 1 and 2 are the source and sink of current mesh 1 respectively, and charge meshes 3 and 4 are the source and sink of current mesh 2, hence

$$\mathbf{A} = \begin{pmatrix} 1 & -1 & 0 & 0 \\ 0 & 0 & 1 & -1 \end{pmatrix}^{\mathrm{T}}$$

The source resistor Z_0 connects to nodes 2 and 3, hence $\mathbf{Y} \in \mathbb{C}^{4\times 4}$ is zero except $Y_{22} = Y_{33} = 1/Z_0$ and $Y_{23} = Y_{32} = -1/Z_0$. The current source I_0 enters node 3 and leaves node 2, hence $\mathbf{I}_{\mathrm{s}} = (0, -I_0, I_0, 0)^{\mathrm{T}}$.

So far, the PEEC models that we presented have complex circuit elements. The mutual inductance is the complex off-diagonal term of $\mathbf{\Lambda}$, whereas the capacitance comes from the inverse of the complex matrix $\mathbf{\Pi}$. Even with the VCVS realization for $\mathbf{\Pi}$, the scaling coefficients are still complex. The circuit equation (1.29) can be directly solved algebraically by MATLAB. Typical SPICE, however, does not support complex elements. From the definitions of partial coefficients in (1.21), it is clear that the complex nature comes from the exponential phase term, while such phase shift is the result of finite propagation velocity of EM waves. If we let the propagation velocity be infinity, hence

doi: 10.6342/NTU201902629

zero time delay for all mutual couplings, then the exponential terms in (1.21) become unity. Equivalently, it corresponds to the case $\omega = 0$. The resulting inductance matrix $\mathbf{L} = \mathbf{\Lambda}(\omega = 0)$ and potential matrix $\mathbf{P} = \mathbf{\Pi}(\omega = 0)$ are then purely real. Such formulation is called the quasi-static (QS) PEEC, and is completely compatible with SPICE, by whatever realization methods and in both time and frequency domains. In particular, a realization of the inductance matrix **L** using only the basic *linear* controlled source in SPICE has been proposed [16], which is depicted in Fig. 1.9. In this configuration, each destination coupling cell is associated with an intermediate stage consisting of linear voltage-controlled current sources (VCCSs) in parallel, and a 0-V voltage source to sample the sum of these currents. Finally a linear current-controlled voltage source (CCVS) that samples the current-sum is inserted in series with the destination inductor.

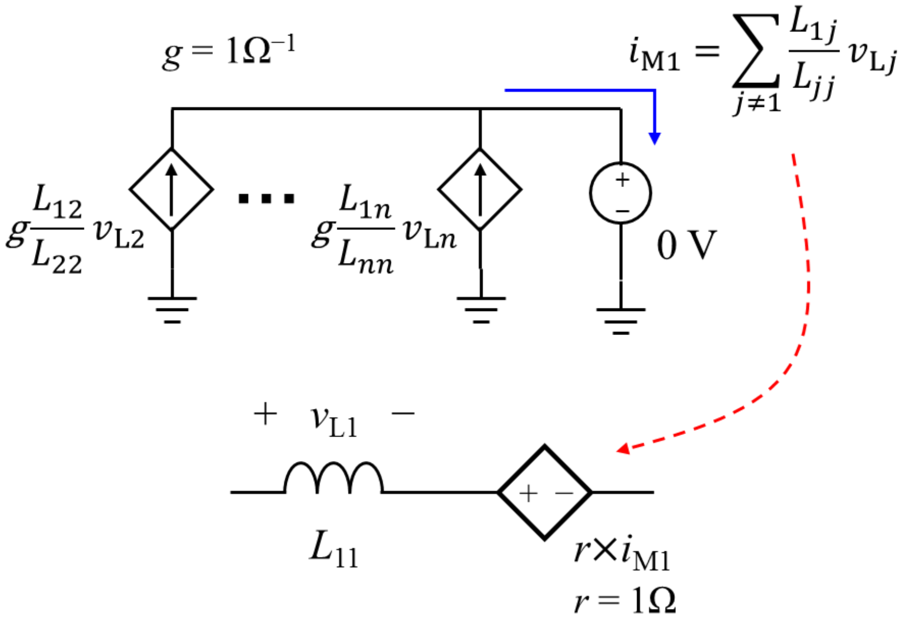

Fig. 1.9. Realization of inductive coupling in QS PEEC using linear VCCSs and CCVS, proposed by [16].

Because time delay is ignored, QS PEEC is applicable mainly for problems where the structures are electrically small, i.e., the largest physical dimension is much smaller than the shortest wavelength of interest, or when the return currents of all signals are *known* to be in close proximity such as in tightly coupled transmission lines [17]. In such case the mutual coupling effects can be approximated as being instantaneous. QS PEEC has found fruitful applications in power electronics modeling [18], [19].

For high frequency problems, where the object is no longer electrically small, the QS PEEC model is inaccurate [20]. Finite propagation velocity must be taken into account. To distinguish from QS PEEC, the PEEC model considering finite delay is called full-wave (FW).

In the above formulation, we note that the exponential phase term, the only frequency-dependent factor, is inside the integration of (1.21). Consequently, the resulting Λ_{ij} and Π_{ij} would vary with frequency in a geometry-dependent manner. In time domain, it corresponds to complicated and distinct convolution operation for each mutual coupling. If the goal is only to obtain the frequency response of the circuit, we can calculate Λ_{ij} and Π_{ij} for every frequency and solve the matrix equation (1.24) or (1.29) algebraically. If, however, transient simulation is desired, then the frequency dependencies of Λ_{ij} and Π_{ij} must be approximated by ones such that their time domain behavior can be handled in a simple manner. The classic method, adopted by Ruehli in his original paper on PEEC [1],

doi: 10.6342/NTU201902629

is called the center-to-center approximation:

$$\Pi_{ij} \cong \bar{P}_{ij} = \frac{e^{-jkR_\mathrm{c}}}{4\pi\varepsilon_0 S_i S_j}\int_{S_i}\int_{S_j}\frac{1}{|\mathbf{r}-\mathbf{r}'|}\mathrm{d}^2r\mathrm{d}^2r' = P_{ij}e^{-jkR_\mathrm{c}}$$

$$\Lambda_{ij} \cong \bar{L}_{ij} = \frac{\mu_0 e^{-jkR_\mathrm{c}}}{4\pi a_i a_j}\int_{V_i}\int_{V_j}\frac{\left(\hat{t}_i\cdot\hat{t}_j\right)}{|\mathbf{r}-\mathbf{r}'|}\mathrm{d}^3r\mathrm{d}^3r' = L_{ij}e^{-jkR_\mathrm{c}} \tag{1.30}$$

where R_c is the center-to-center distance between the respective meshes. We denote L_{ij} and P_{ij} as the real-valued quasi-static Λ_{ij} and Π_{ij}, i.e. by setting $\omega = 0$, and denote $\bar{L}_{ij}$ and $\bar{P}_{ij}$, with overhead bars, as the complex-valued center-to-center approximation of Λ_{ij} and Π_{ij}. The corresponding matrices are denoted as $\mathbf{L}$, $\mathbf{P}$, $\bar{\mathbf{L}}$, and $\bar{\mathbf{P}}$, respectively. In particular, we can write $\bar{\mathbf{P}} = \mathbf{P} \circ \exp(-j\omega\mathbf{T}_\mathrm{P})$ and $\bar{\mathbf{L}} = \mathbf{L} \circ \exp(-j\omega\mathbf{T}_\mathrm{L})$, where $\circ$ is the Hadamard product, i.e., entrywise multiplication, and $\exp(-j\omega\mathbf{T}_\mathrm{P})$ is the entrywise exponential (not the matrix exponential). Here, $\mathbf{T}_\mathrm{P}$ and $\mathbf{T}_\mathrm{L}$ are matrices, of the same sizes as $\mathbf{P}$ and $\mathbf{L}$, whose diagonal elements are all zero and off-diagonal elements the time delay between the respective charge or current meshes. Comparing (1.21) and (1.30), we see that this approximation is valid when $R_\mathrm{c} \ll \lambda$, such that the exponential term roughly equals unity, or when the sizes of the two coupling meshes are both much smaller than wavelength, so that the exponential factor does not vary greatly as the integration variables move around the integration domain. Obviously, if the charge and current meshes are discretized in a manner such that at the highest frequency of interest, denoted as f_m hereafter, they remain much smaller than the corresponding wavelength $\lambda_\mathrm{m} = c\ /\ f_\mathrm{m}$, then the center-to-center approximation will be accurate up to the frequency f_m. Conventionally, the meshing scheme of PEEC follows the λ_m / 20 rule, which means that the largest dimension of the meshes is not greater than λ_m / 20.

The advantage of the center-to-center approximation is twofold. First, the coupling coefficients L_{ij} and P_{ij} are frequency independent, so we only have to calculate them once. For different frequencies of evaluation, we simply multiply them by the exponential factor. Hence, frequency sweep simulation can be greatly sped up, compared with solving the equations in $\mathbf{\Lambda}$ and $\mathbf{\Pi}$ (1.29). In addition, for certain canonical geometries, in particular rectangular meshes, there are closed form solutions for the partial coefficients L_{ij} and P_{ij} [5], which further reduces the effort in building the matrices. Second, the frequency behaviors of $\bar{L}_{ij}$ and $\bar{P}_{ij}$ permit a simple inverse Fourier transform into the time domain—ideal time delay. Specifically, for the *i*-th current mesh, and the *i*-th charge mesh, we have

$$\begin{aligned} v_i(t) &= \sum_{j=1}^{n} L_{ij} \frac{\mathrm{d}}{\mathrm{d}t} i_j\left(t-\tau_{ij}\right) \\ \phi_i(t) &= \sum_{j=1}^{m} P_{ij} q_j\left(t-\hat{\tau}_{ij}\right) \end{aligned} \tag{1.31}$$

where v_i is the branch voltage across the *i*-th inductor, and τ_{ij} and $\hat{\tau}_{ij}$ the time delays between the respective meshes. The self-delay equals zero, i.e., $\tau_{ii} = \hat{\tau}_{ii} = 0$. In time domain, the circuit variables are denoted in lower case letters. Note that for *each* branch current, there are $O(n)$ distinct delay values, where $O(.)$ is the big-O notation. So for each branch current, $O(n)$ of its historical values need to be read out each time the solver marches in time. The corresponding time domain MNA equation would be too complicated to be written out completely, even for a fair amount of meshes. The circuit realization of (1.31), however, can be *descriptively* constructed as in Fig. 1.10. In the figure, only one branch and two nodes are shown. By “descriptive”, we emphasize that even at present, there is no such delay-scale-summation controlled source in most SPICEs. It means that, although Fig. 1.10 is an exact realization of (1.31), it is still not SPICE-compatible. In the past, researchers have to find other means to conduct transient simulation of a FW PEEC model. A review of these methods, along with our proposed method, will be given in Chapter 3.

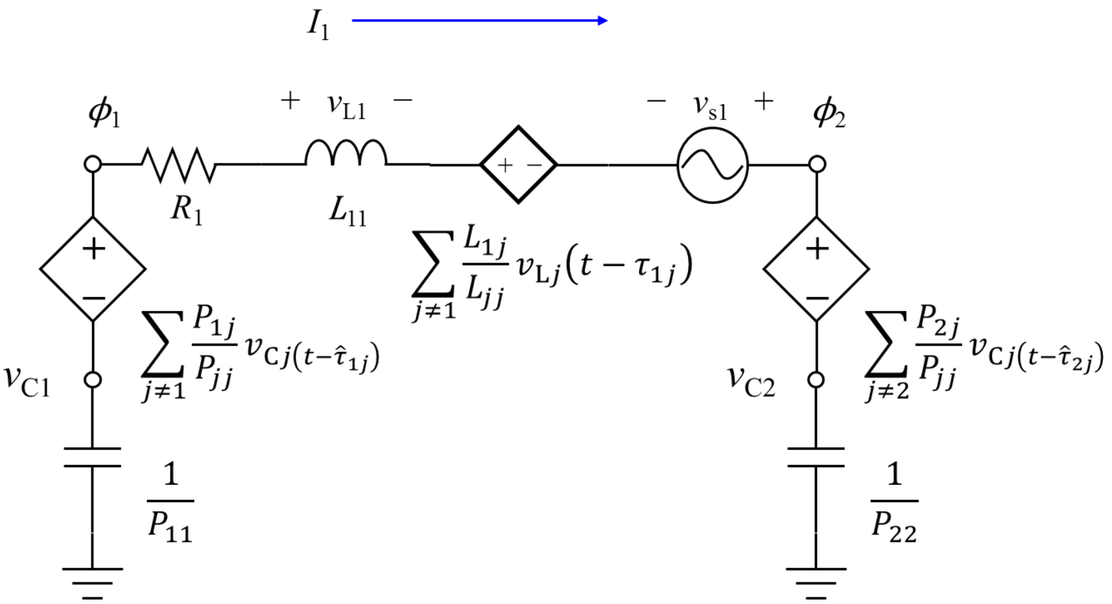

Fig. 1.10. A unit cell of FW PEEC model in time domain, showing two nodes and one branch. The mutual couplings are realized both using VCVS topology.

At this point, we have introduced the most fundamental ingredients of the PEEC method. The review of the issue of time domain stability of PEEC will be postponed to Chapter 4. Before leaving this section, we list several classical and recent applications of PEEC, which include interconnect modeling [21], [22], power integrity analysis [23], transient lightning modeling [24], transient ESD simulation [25], power electronics [26], antenna analysis [27], and modeling of magnetic materials [28]. For an in-depth treatment of PEEC, the readers are referred to the monograph by Kochetov [19], the book by Nitsch, Gronnwald, and Wollenberg [18], and the recent book by Ruehli, Antonini, and Jiang [15].

1.3 Dissertation Outline

From the development presented in the previous section, we see that in frequency domain, FW PEEC has complex inductances and potential coefficients. The physical meaning of these complex coupling coefficients is the main topic of Chapter 2. In Chapter 3, we study the methods to simulate a FW PEEC model in time domain. Specifically, we propose a method to cast a FW PEEC into a truly SPICE-compatible form, so that the equivalent circuit can be solved by a standard circuit simulator. The transient simulation results, however, are often found to be unstable, which means that the time domain waveform, instead of reaching a steady state, diverges with an exponentially-increasing amplitude. This then motivates the study of the stability properties of FW PEEC, which is the main subject of Chapter 4. Because of the heterogeneous nature of these topics, specific literature reviews will be provided separately in sections 2.1, 3.1, 4.1, 4.2.1, 4.3.1, and 4.4.1. The contents of Chapter 2 and Chapter 3 are mainly based on two of our published papers [29], [30]. □

doi: 10.6342/NTU201902629

THIS PAGE INTENTIONALLY LEFT BLANK.

Chapter 2 Radiation Resistance in FW FD PEEC

2.1 Literature Review and Motivation

For QS PEEC, the inductance and potential matrices, **L** and **P**, are real. The corresponding impedance matrices $\mathbf{Z}_{\mathrm{L}} = j\omega\mathbf{L}$ and $\mathbf{Z}_{\mathrm{P}} = \mathbf{P} / j\omega$ are then both purely imaginary. According to circuit theory, the average real power consumed in the **L** matrix is

$$P_{\mathrm{L}} = \mathrm{Re}\left\{\frac{1}{2}\mathbf{I}^{\mathrm{H}}\mathbf{V}\right\} = \mathrm{Re}\left\{\frac{1}{2}\mathbf{I}^{\mathrm{H}}\mathbf{Z}_{\mathrm{L}}\mathbf{I}\right\} = \mathrm{Re}\left\{\frac{j\omega}{2}\mathbf{I}^{\mathrm{H}}\mathbf{L}\mathbf{I}\right\} = -\frac{\omega}{2}\mathrm{Im}\{\mathbf{I}^{\mathrm{H}}\mathbf{L}\mathbf{I}\}$$

where the superscript H means conjugate transpose. Here, the vector **I** is the vector of branch currents, while **V** is the vector of branch voltages, across the inductors. Since **L** is symmetric, a basic property from linear algebra concludes that $\mathbf{I}^{\mathrm{H}}\mathbf{L}\mathbf{I}$ is always real, and thus $P_{\mathrm{L}} = 0$. Similarly, if **P** is constructed such that it is symmetric, then the time-averaged power consumption on the **P** matrix equals zero. Hence, for QS PEEC, the **L** and **P** are no different from the conventional inductors and capacitors in circuit theory, in that they only consume reactive power but no real power.

For FW PEEC, however, the situation is different. Due to the exponential phase delay, which is frequency dependent and mostly complex, $\mathbf{I}^{\mathrm{H}}\bar{\mathbf{L}}\mathbf{I}$ is no longer real, and $P_{\mathrm{L}} \neq 0$ in general. Then a series of questions naturally arises: What is this real power consumption? Does it corresponds to physical quantities? What is its implication and application?

It appears that Wollenberg and Kochetov [31] are the first group that study this problem. They conjecture that the total real power consumption on the PEEC model, including the power on $\bar{\mathbf{L}}$ and $\overline{\mathbf{P}}$, equals the power loss due to radiation plus resistive heating. Since the Ohmic loss is known to be restrictively associated with the series resistor of each branch, the radiation loss seems to be the most logical explanation for the power loss on the $\bar{\mathbf{L}}$ and $\overline{\mathbf{P}}$ matrices. This conjecture is verified in [31] by numerical simulation. Specifically, first the PEEC model of a physical object is built and solved. Then the total power consumed by the $\bar{\mathbf{L}}$ and $\overline{\mathbf{P}}$ matrices, in the circuit domain, is computed and compared against the total radiated power obtained from far field integration, where the fields are calculated, as a post processing, from the currents on the structure solved by the PEEC model. Similar verifications are presented by Cao, Jiang, and Ruehli [32]. The agreement therein is indicative of the correctness of the conjecture. However, no formal proof has ever been proposed. As for application, Wollenberg points out that the information of radiated power is important for antenna and EMC analysis.

Another discovery that is closely related to this conjecture is presented by Yeung and Wu [33]. They formulated a modified PEEC in which the difference between $\mathbf{\Pi}$ and $\mathbf{P}$ is transferred to the inductance matrix through careful application of the continuity equation, so that the potential matrix is quasi-static and purely real, while the inductance matrix consists of the original $\mathbf{\Lambda}$ plus some additional complex terms. Then, the resulting complex inductance L_{Hz} of a simple example—the Hertzian dipole, with one current mesh and two charge meshes only, is derived analytically. The discovery is that

$$\omega \mathrm{Im}\{L_{\mathrm{Hz}}\} = 80\pi^2 \left(\frac{l}{\lambda}\right)^2 = R_{\mathrm{rad}}$$

which is exactly the radiation resistance of a short dipole with length $2l$, as given in many antenna textbooks [34]. This again indicates that the power loss associated with the complex inductance and potential matrices in FW PEEC has close connection with radiation. Similarly, however, no rigorous justification is given in [33].

Motivated by these discoveries, in this dissertation we provide a formal proof based on the fundamental laws, that the total power dissipated on the complex $\mathbf{\Lambda}$ and $\mathbf{\Pi}$ is identical to the total radiated power. What is different from the previous discoveries is that, based on our derivation, we can predict that when the physical object is illuminated by an incident wave, instead of being excited internally, the power loss on $\mathbf{\Lambda}$ and $\mathbf{\Pi}$ then represents the total *scattered* power. This situation is not discussed in the aforementioned papers. Simulation results will be provided in section 2.3 as a *support* of the proposed proof, yet the proof is self-contained and needs no simulation to *justify* it. Physical implication will also be addressed in section 2.4.

2.2 Proposed Proof

Poynting's theorem of an object in free space reads [12]

$$-\frac{1}{2}\int_V \mathbf{E}\cdot\mathbf{J}^* \mathrm{d}^3 r = \oint_S \frac{1}{2}\mathbf{E}\times\mathbf{H}^*\cdot\hat{n}\,\mathrm{d}a + j\omega\int_V \left(\frac{\mu_0}{2}|H|^2 - \frac{\varepsilon_0}{2}|E|^2\right)\mathrm{d}^3 r \tag{2.1}$$

where V is any volume that is large enough to contain all the currents, and that the surface of V, S, can be considered in the far field of all the sources. At far field, the Poynting vector is purely real, thus

$$\mathrm{Re}\left[-\frac{1}{2}\int_V \mathbf{E}\cdot\mathbf{J}^*\mathrm{d}^3r\right]=\frac{1}{2}\oint_S \mathbf{E}\times\mathbf{H}^*\cdot\hat{n}\,\mathrm{d}a$$

where the right-hand-side is the total radiated power:

$$P_{\mathrm{rad}}=\frac{1}{2}\oint_S \mathbf{E}\times\mathbf{H}^*\cdot\hat{n}\,\mathrm{d}a \tag{2.2}$$

By (1.7), we have

$$P_{\mathrm{rad}}=\mathrm{Re}\left[-\frac{1}{2}\int_V \mathbf{E}\cdot\mathbf{J}^*\mathrm{d}^3r\right]=\mathrm{Re}\left[\frac{1}{2}\int_V(j\omega\mathbf{A}+\nabla\Phi)\cdot\mathbf{J}^*\mathrm{d}^3r\right] \tag{2.3}$$

Next, the potentials are expressed in terms of current and charge integrals as in (1.10) and (1.12), giving

$$\begin{aligned}P_{\mathrm{rad}}&=\mathrm{Re}\left[\frac{1}{2}j\omega\int_V\int_V\mu_0\,\mathbf{J}(\mathbf{r}')G(\mathbf{r},\mathbf{r}')\cdot\mathbf{J}^*(\mathbf{r})\,\mathrm{d}^3r'\mathrm{d}^3r\right]\\&+\mathrm{Re}\left[\frac{1}{2}\int_V\int_V\frac{1}{\varepsilon_0}\,\rho(\mathbf{r}')\nabla G(\mathbf{r},\mathbf{r}')\cdot\mathbf{J}^*(\mathbf{r})\,\mathrm{d}^3r'\mathrm{d}^3r\right]\end{aligned} \tag{2.4}$$

By properly using the product rule, divergence theorem, and the charge conservation on the last term of (2.4), we obtain

$$\begin{aligned}\int_V\nabla G(\mathbf{r},\mathbf{r}')\cdot\mathbf{J}^*(\mathbf{r})\mathrm{d}^3r&=\int_V\nabla\cdot\big(G(\mathbf{r},\mathbf{r}')\mathbf{J}^*(\mathbf{r})\big)\,\mathrm{d}^3r-\int_V G(\mathbf{r},\mathbf{r}')\nabla\cdot\mathbf{J}^*(\mathbf{r})\,\mathrm{d}^3r\\&=\oint_S G(\mathbf{r},\mathbf{r}')\mathbf{J}^*(\mathbf{r})\cdot\hat{n}\,\mathrm{d}a-j\omega\int_V G(\mathbf{r},\mathbf{r}')\rho^*(\mathbf{r})\,\mathrm{d}^3r\end{aligned}$$

The surface integral vanishes because there is no current at infinity. Then (2.4) becomes

$$\begin{aligned}P_{\mathrm{rad}}&=\mathrm{Re}\left[\frac{1}{2}j\omega\int_V\int_V\mu_0\,\mathbf{J}(\mathbf{r}')G(\mathbf{r},\mathbf{r}')\cdot\mathbf{J}^*(\mathbf{r})\,\mathrm{d}^3r'\mathrm{d}^3r\right]\\&-\mathrm{Re}\left[\frac{1}{2}j\omega\int_V\int_V\frac{1}{\varepsilon_0}\,\rho(\mathbf{r}')G(\mathbf{r},\mathbf{r}')\,\rho^*(\mathbf{r})\,\mathrm{d}^3r'\mathrm{d}^3r\right]\end{aligned} \tag{2.5}$$

It is clear from (1.11) that $G(\mathbf{r},\mathbf{r}') = G(\mathbf{r}',\mathbf{r})$, that is, both the real and imaginary parts of G are symmetric. It can then be verified that

$$P_{\text{rad}} = -\frac{1}{2}\omega \int_V \int_V \mu_0\, \mathbf{J}(\mathbf{r}') G_i(\mathbf{r},\mathbf{r}') \cdot \mathbf{J}^*(\mathbf{r})\, \mathrm{d}^3r' \mathrm{d}^3r$$

$$+\frac{1}{2}\omega \int_V \int_V \frac{1}{\varepsilon_0}\, \rho(\mathbf{r}') G_i(\mathbf{r},\mathbf{r}')\, \rho^*(\mathbf{r})\, \mathrm{d}^3r' \mathrm{d}^3r \tag{2.6}$$

where G_i is the imaginary part of G. Hence P_{rad} is related to the imaginary part of G by (2.6). Before going further, it is worth mentioning that the current density $\mathbf{J}$ can be expressed as the sum of *impressed* (source) current $\mathbf{J}_{\text{imp}}$ and *induced* current $\mathbf{J}_{\text{ind}}$ [12]. For radiation problem, the current penetrating the air between the two end points of the feeding port is $\mathbf{J}_{\text{imp}}$, while the current on conductor is $\mathbf{J}_{\text{ind}}$. The integration in (2.3), when evaluated at $\mathbf{J}_{\text{imp}}$, represents the real power going from $\mathbf{J}_{\text{imp}}$ to the fields, while when evaluated at $\mathbf{J}_{\text{ind}}$, represents the negative of the power loss on the conductor due to finite conductivity. Hence, the physical meaning of (2.3) can be thought of as that the total radiated power equals the input power supplied from the feeding port subtracting the Ohmic loss on the conductors. For scattering problem, the interpretation is slightly different. Basically, all the currents should be $\mathbf{J}_{\text{ind}}$ because they are induced by the incident wave. However, by substituting the $\mathbf{E}$ field as the integral of current and charge densities as in (2.4), we essentially restrict ourselves to considering only the scattered fields generated by these $\mathbf{J}_{\text{ind}}$, and ignore the effects of $\mathbf{E}_{\text{inc}}$. The Poynting theorem (2.1) is in fact used to describe the *associated* problem in which the current exactly equals $\mathbf{J}_{\text{ind}}$ of the original scattering problems, but flows in free space with no conductors and no incident wave. Consequently, the P_{rad} in (2.3) corresponds to the total scattered power. Note that, for scattering problem, the Ohmic loss is not relevant to (2.4) to (2.6).

In PEEC model, the real power consumed in the inductor network is given by

$$P_{\mathrm{L}} = \mathrm{Re}\left[\tfrac{1}{2} j\omega \mathbf{I}^{\mathrm{H}}\mathbf{\Lambda}\mathbf{I}\right] = -\tfrac{1}{2}\omega\mathbf{I}^{H}(\mathrm{Im}[\mathbf{\Lambda}])\mathbf{I} \tag{2.7}$$

Similarly, the real power consumed in the potential network $\mathbf{\Pi}$ is

$$\begin{aligned} P_{\mathrm{P}} &= \mathrm{Re}\left[\frac{1}{2}\mathbf{I}_{\mathrm{in}}^{\mathrm{H}}\mathbf{\Phi}\right] = \mathrm{Re}\left[\frac{1}{2}\mathbf{I}_{\mathrm{in}}^{\mathrm{H}}\mathbf{\Pi}\mathbf{Q}\right] \\ &= \mathrm{Re}\left[-\tfrac{1}{2} j\omega\mathbf{Q}^{\mathrm{H}}\mathbf{\Pi}\mathbf{Q}\right] = \tfrac{1}{2}\omega\mathbf{Q}^{\mathrm{H}}(\mathrm{Im}[\mathbf{\Pi}])\mathbf{Q} \end{aligned} \tag{2.8}$$

where $\mathbf{I}_{\mathrm{in}}$ is the total current flowing into each charge mesh. The total real power consumed in the complex $\mathbf{\Lambda}$ and $\mathbf{\Pi}$ network is (P_{L}+P_{P}) given by

$$P_{\mathrm{L}} + P_{\mathrm{P}} = -\tfrac{1}{2}\omega\mathbf{I}^{\mathrm{H}}(\mathrm{Im}[\mathbf{\Lambda}])\mathbf{I} + \tfrac{1}{2}\omega\mathbf{Q}^{\mathrm{H}}(\mathrm{Im}[\mathbf{\Pi}])\mathbf{Q} \tag{2.9}$$

It is then recognized that (2.9) is the numerical approximation of the integration (2.6). In particular, if we substitute the current discretization (1.15) into the first term of the RHS of (2.6), we will have

$$-\tfrac{1}{2}\omega\sum_{i=1}^{n}\sum_{j=1}^{n} I_i^* I_j \int_{V_i}\int_{V_j}\mu_0 \frac{(\hat{t}_i\cdot\hat{t}_j)}{a_i a_j} G_i(\mathbf{r},\mathbf{r}')\,\mathrm{d}^3 r'\mathrm{d}^3 r$$

which, by recalling the definition of Λ_{ij} in (1.21), is found to be exactly the same as P_{L}. Similar procedure can be applied to charge density to show that P_{P} equals the discretized version of the second term of the RHS of (2.6).

In PEEC, the current discretization (1.15) only accounts for currents that originally flow on “physical objects”, here the conductors. For radiation problem, the $\mathbf{J}_{\mathrm{imp}}$ at the feeding port is not considered in (2.9). For scattering problem, the $\mathbf{J}_{\text{ind}}$ at the external lumped components is not considered in (2.9). However, the contribution of these currents to the integration (2.6) will be small if the area of the feeding port and lumped components is small. As a result, disregarding the little error from these currents, the total real power consumed in the $\mathbf{\Lambda}$ and $\mathbf{\Pi}$ networks, ($P_{\text{L}} + P_{\text{P}}$), is proved to be the numerical approximation of the total power radiated or scattered to infinity (2.6), i.e., $P_{\text{rad}} \approx P_{\text{L}} + P_{\text{P}}$.

It should not be confused that, for radiation problem, saying the $\mathbf{J}_{\text{imp}}$ is not considered in (2.9) contradicts the statement that P_{rad} equals the input power minus the Ohmic loss. Indeed, the feeding area is not current-meshed, but the two ends of the feeding area is charge-meshed. Hence, the input power is actually accounted for in the P_{P} (2.8), and the summation (2.9) also approximates the input power minus the Ohmic loss, thus P_{rad}. This possible confusion arises from a key difference between (2.3) and (2.4): the contribution of $\mathbf{J}_{\text{imp}}$ to (2.3), which represents the input power, is elemental no matter how small the volume occupied by $\mathbf{J}_{\text{imp}}$ is, while the contribution of $\mathbf{J}_{\text{imp}}$ to the first term of (2.4) is proportional to its volume. The input power, after the transformation, is absorbed into the second term of (2.4).

At low frequencies, where the meshes are much smaller than wavelength, the center-to-center approximation is valid. Hence, the above proof applies to the $\bar{\mathbf{L}}$ and $\bar{\mathbf{P}}$ case. Also, discussion of the results of [33], i.e., the Hertzian dipole, can be found in [29].

2.3 Verification

To verify the proposed proof, simulation results of a strip dipole excited by two different mechanisms are presented. One is internally excited by a current source, while the other is externally illuminated by a uniform plane wave with various incident angles. The geometry of the dipole and the orientation of the incident wave are shown in Fig. 2.1 (a), (b), respectively. The computed results by PEEC are compared with that obtained from ANSYS HFSS. The conductors are assumed to be PEC. The partial inductances and potential coefficients are first computed according to (1.30), where the closed-form formula in [5] are applied to compute the QS coupling coefficients including both the self ($i = j$) and mutual ($i \neq j$) terms. (Note that because we do not numerically compute the double integral, the problem of singularity for self-terms is avoided.) The whole circuit is then solved on MATLAB by the reduced MNA introduced in Chapter 1. Here, each arm of the dipole is divided into $N/2$ uniform current meshes and ($N/2+1$) charge meshes. To illustrate the convergence, the results for $N = 20$ and 32 will be displayed for comparison.

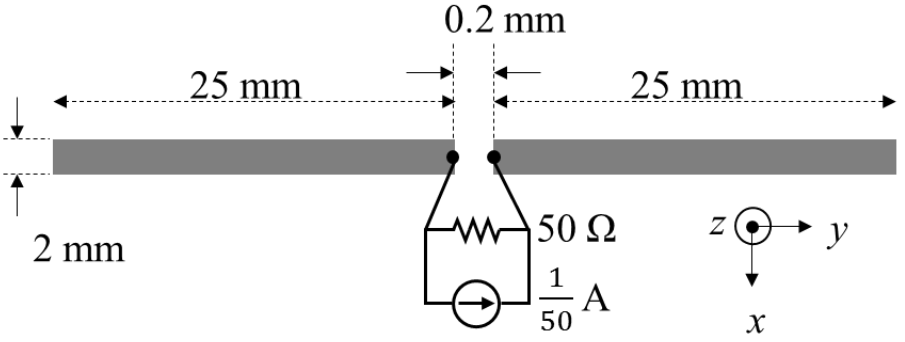

(a)

doi: 10.6342/NTU201902629

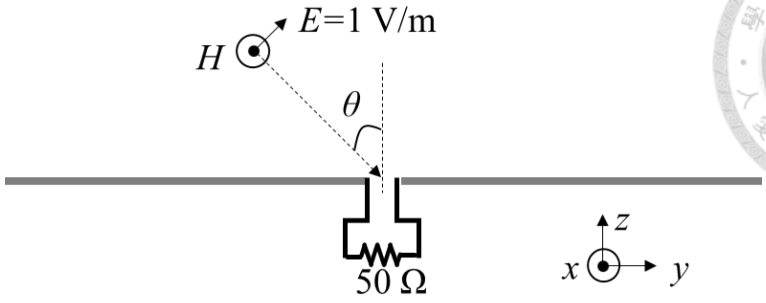

(b)

Fig. 2.1. (a) Geometry of a PEC thin strip dipole. (b) Orientation of the incident wave.

For the radiation case, we note that the current source has an equivalent Thevenin topology, which is simply a 1-V voltage source in series with the 50-Ω resistor. The Norton form is preferred because the corresponding MNA is simpler, as described in Chapter 1. In contrast, if the Thevenin form is used, we not only have to introduce an additional node into the MNA, which is the node between the voltage source and the source resistor, but we also have to include the current flowing through the independent voltage source into the vector of unknowns, according to the MNA rule.

To calculate S parameters, we need to separate the incident voltage from the total voltage. Here, all port impedances are real, so we use the voltage-wave definition of S parameters. Let the total voltage and current flowing into the network at some particular port be V_{port} and I_{port}, respectively. Then the incident wave at this port is given by

$$V^{+} = \frac{V_{\text{port}} + Z_0 I_{\text{port}}}{2}$$

The reflected wave can be obtained by subtracting V^{+} from V_{port}. For the matched source as in Fig. 2.1 (a), it can be verified that $V^{+} = 0.5$ V.

Fig. 2.2 shows the magnitude and phase of S_{11} of the strip dipole computed from PEEC and HFSS. Good agreement between PEEC and HFSS is observed, verifying the accuracy of the model. Also, the results for $N = 20$ and $N = 32$ are close to each other. This then indicates the convergence of the model.

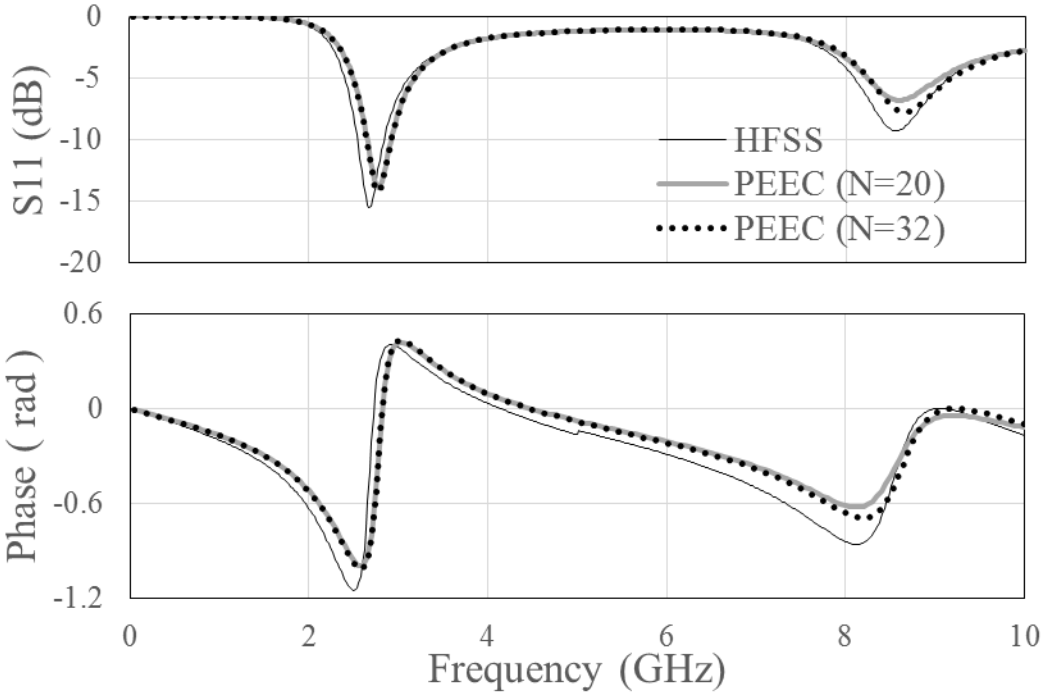

Fig. 2.2. The magnitude and phase of S_{11} of the strip dipole in Fig. 2.1 (a) computed from HFSS and PEEC.

The total radiated power normalized by the incident power $P_{\mathrm{in}} = |V^{+}|^2 / 2Z_0 = 2.5$ (mW) is shown in Fig. 2.3. Note that in HFSS simulation, the conductor is assumed to be lossless. Therefore, the total radiated power can be computed by using $P_{\mathrm{rad}} = P_{\mathrm{in}}(1 - |S_{11}|^2)$. In PEEC, the total radiated power is obtained by computing (2.9). As shown in the figure, good agreement between them is observed. The small deviation around 8.5 GHz is due to the insufficient discretization in PEEC for both the x and y directions

doi: 10.6342/NTU201902629

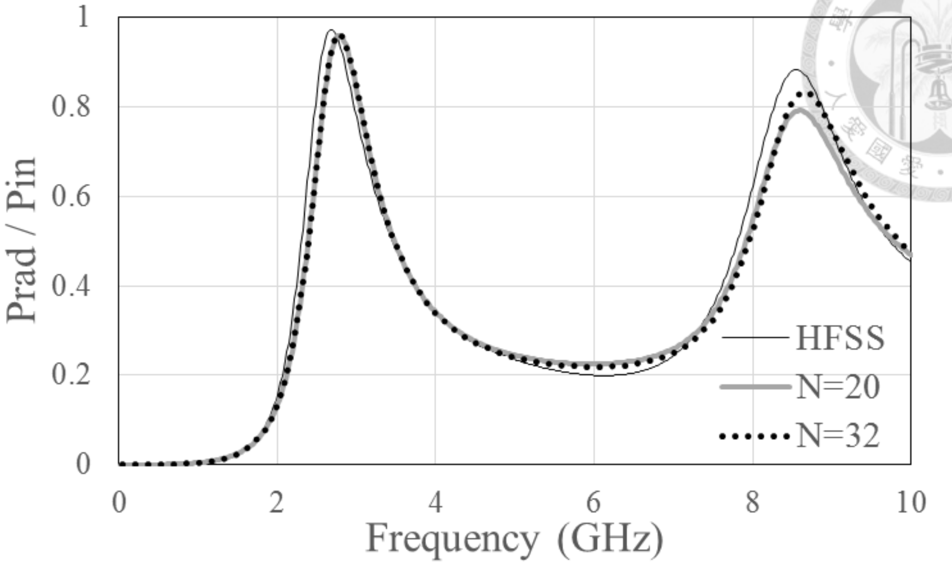

Fig. 2.3. The total radiated power normalized by the incident power computed from HFSS and PEEC. For PEEC, the total radiated power is calculated from (2.9).

For the scattering problem, a voltage source is inserted into each current mesh to represent the electromotive force of the incident electric field. The polarization of incident E field is in the *y* and *z* directions. Its magnitude is given by $E_0 = 1$ V/m. Therefore, the *y* component of the incident field is given by

$$E_y = E_0 \cos\theta \, e^{-jk(z\cos\theta + y\sin\theta)}$$

Since the dipole is along the *y* direction, it does not see the variation of the field along the *z* direction. Thus, we may set $z = 0$ for convenience. Because all the meshes are much smaller than wavelength, we approximate the values of the series voltage sources as

$$V_{si} = \frac{1}{a_i}\int_{V_i} \hat{t}_i \cdot \mathbf{E}_{\mathrm{inc}} d^3r' \cong E_0 l_i \cos\theta \, \mathrm{e}^{-jky_i \sin\theta} \tag{2.10}$$

where l_i and y_i are the length and center location along the *y* axis of the *i*-th mesh, respectively.

doi: 10.6342/NTU201902629

To compare the results, we observe the scattering efficiency defined by [35]

$$Q_s = \frac{\sigma_\mathrm{s}}{\sigma_\mathrm{g}}$$

where σ_s is the scattering cross section, i.e., the total scattered power normalized by the incident power density, while σ_g is the geometric cross section, in this example $\cos(\theta)\times10^{-4}$ (m^2). In HFSS, the total scattered power is obtained by computing the boundary box integration of radiated power, while in PEEC it is calculated by the above formula. The results of normal incidence with different frequencies are shown in Fig. 2.4 (a), while the results of oblique incidence for 2.75 GHz and 8.5 GHz are shown in Fig. 2.4 (b). Good agreement is observed.

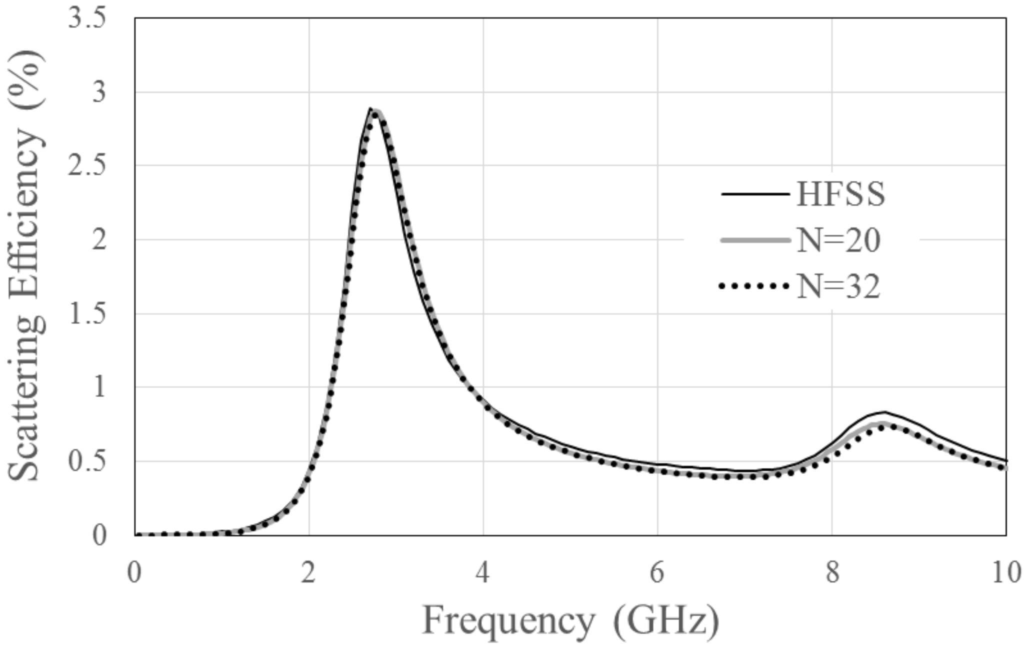

(a)

doi: 10.6342/NTU201902629

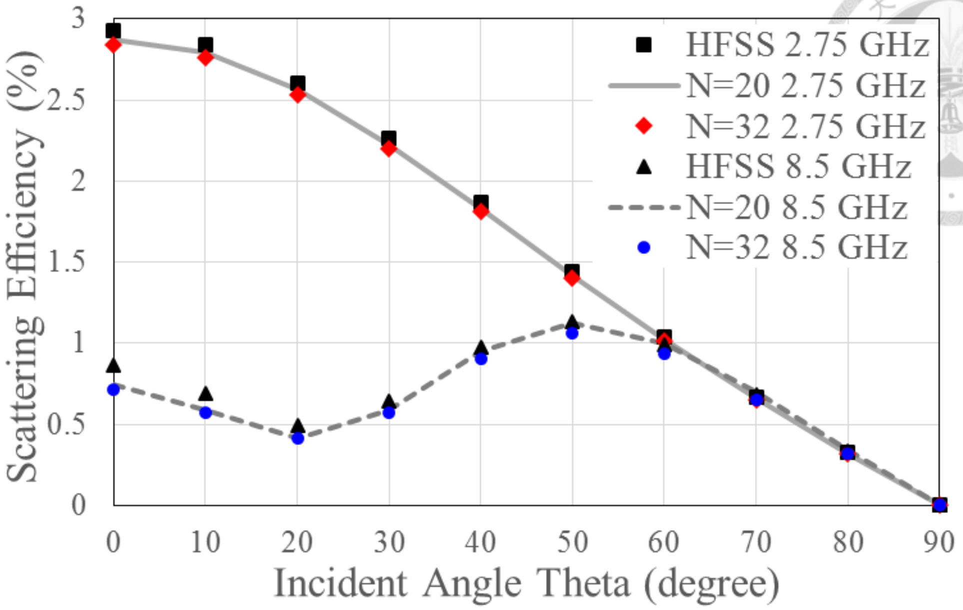

(b)

Fig. 2.4. (a) Scattering efficiency of the strip dipole for normal incidence. (b) Scattering efficiency at 2.75 GHz and 8.5 GHz for various incident angles.

2.4 Discussion

What we have proved in Section 2.2 is that the total real power dissipated on the $\mathbf{\Lambda}$ and $\mathbf{\Pi}$ matrices, or $\bar{\mathbf{L}}$ and $\bar{\mathbf{P}}$ matrices, are the total radiated power for radiation problem, and the total scattered power for scattering problem. This then implies the physical meaning that the imaginary parts of the $\mathbf{\Lambda}$ and $\mathbf{\Pi}$ matrices in PEEC together represent a mutually coupled radiation resistance network. It is in contrast to the usual terminal-based radiation modeling for antennas [34], where a single resistance is placed at the feeding port. PEEC represents a way of *distributed* radiation modeling, where the effect of radiation are nonuniformly distributed along the entire structure. This concept of modeling dates back to Schelkunoff in his classic paper [36]. Schelkunoff formulates a transmission-line model for conical antenna in which the per unit length series *R* precisely accounts for the effect of radiation. In his model, the radiation resistors are *continuously* distributed along the whole radiator, which is similar to PEEC in bearing the idea that “radiation takes place continuously along the antenna,” quoted from [36]. Contrary to Schelkunoff’s method which is not easy to extend to other shapes of radiator, the PEEC can be straightforwardly generalized to arbitrary structures.

Another special characteristic of PEEC implied by the proof is that in PEEC we can *directly* calculate the total radiated or scattered power from power consumed by the circuits, which is a *near-field* quantity. This is in contrast to other full-wave methods such as FEM that requires the field integration on a boundary box, which is a far-field method. It is also possible to compute the total radiated power in the near-field for FEM, by subtracting the total dissipated power on lossy conductors and dielectric from the input power. However, it is an *indirect* method. In PEEC, the information of far-field power is directly represented by, or transformed to, near-field circuit quantities. No any far field or boundary integration is required. The underlying theory justifying this far-to-near field transform is exactly (2.6), and that the PEEC, by considering both the vector potential and the scalar potential, is just the model that implements (2.6) into its formulation. □

Chapter 3 Simulation of FW PEEC Using Standard SPICE

As mentioned in Chapter 1, although the PEEC method features the capability of representing an EM problem as an equivalent circuit, the resulting circuit is not compatible with most circuit simulators except for the QS case, where time delay is ignored. Under the center-to-center approximation, the equations of the retarded mutual coupling (1.31) is repeated here:

$$v_i(t) = \sum_{j=1}^{n} L_{ij} \frac{\mathrm{d}}{\mathrm{d}t} i_j\big(t - \tau_{ij}\big)$$

$$\phi_i(t) = \sum_{j=1}^{m} P_{ij} q_j\big(t - \hat{\tau}_{ij}\big) \tag{3.1}$$

In standard SPICEs, there is no delayed mutual inductance nor delayed capacitance. Researchers in the past have thus developed various methods to overcome this difficulty. The major efforts will be reviewed here. Then, the proposed method will be presented in section 3.2, followed by simulation verification in section 3.3. The focus will be put on transient simulation instead of frequency response, though, because the real specialty of PEEC is its capability of co-simulation with external nonlinear components. Since nonlinear circuit permits no Fourier transform, in such situation we ultimately require transient simulation.

doi: 10.6342/NTU201902629

3.1 Review of Simulation Methods for FW PEEC

The PEEC model with delay has been solved by different kinds of approaches in the literature, which can be classified into two groups: FD-first and direct-TD. In the FD-first group, the FD responses are solved at several predefined ports, and then the TD responses at these ports are obtained by means of inverse Fourier transform [25], convolution [15], or macromodeling [21], [24], [15]. In the Fourier transform approach, we first compute the transform of the input signal to be fed to the circuit. The Fourier domain output is obtained simply by multiplying the input with the transfer function. The time domain output is then obtained by the inverse transform. The problem of this method is that the time domain input cannot be long-lasting, e.g. a pseudorandom bit sequence (PRBS), such that the transform of the input doesn’t exist, or requires an impractically fine frequency spacing. In [25], this method was applied to electrostatic discharge (ESD) simulation whose waveform decays significantly within 100 ns, indeed short-lasting. Another problem of the transform method is that it cannot be applied to cases when there are nonlinear circuits connected to the ports. When nonlinearity presents, we must resort to time domain methods. The convolution method, on the contrary, does not transform the input. Instead, the impulse response of the system is calculated from the transfer function and convoluted with the input signal. A commonly encountered problem of the convolution method is that, if the transfer function violates the requirements for being a

doi: 10.6342/NTU201902629

passive network, the output of convolution may suffer from unstable resonance. The macromodeling approach, different from the above methods, first interpolates the FD response using rational functions. The rational representation is then converted to standard linear circuits based on the poles and residues [37], and the resulting macromodel can be put in SPICE for co-simulation with other linear or nonlinear circuits. In addition, techniques exist to enforce passivity if the macromodel fails to be passive or even stable in the first place. The macromodeling approach is a common practice in industry and academy, and there are commercial software dedicated to this purpose.

Although these FD-first methods can successfully enable transient simulation of FW PEEC, they share a common problem which is the loss of detailed information at every space and time point except at the few selected ports. There are situations as pointed out in [21] where detailed solution of the original structure provides insightful design guides, such as the current distribution on a power plane for decoupling capacitor placement, and the current distribution on an interconnect for EMI diagnosis. Unless a large number of ports are defined throughout the structure, this kind of information will be lost. Another difficulty of FD-first methods is the inclusion of incident wave excitation. In PEEC, the incident wave is represented by a series voltage source at each branch. To apply the macromodeling approach, for example, we have to declare *each* branch as a port. The resulting number of ports in the macromodel can easily exceed several hundreds, which

doi: 10.6342/NTU201902629

would make the model extraction very difficult, if not totally intractable, even with today's advanced macromodeling software.

In the direct-TD group, the delayed differential equation presented by the TD FW PEEC is solved directly using classical numerical techniques such as backward Euler, where the retarded coupling is achieved by the use of a history table [16], [17], [38-40]. The history mechanism has been implemented in the ASTAP simulator in [17], while a modified SPICE is written in [16]. Contrary to the FD-first counterpart, these methods retain the detailed current information at every point, which can be extracted for further analysis. The major problem of these methods considered here is the need for a *modified* or even *homemade* SPICE, instead of using a *standard* SPICE. By *standard*, we mean those that are commercially available such as HSPICE. Modification of a well-packaged commercial SPICE to the level of including retarded coupling may not always be possible, whereas a researcher's homemade SPICE is not equipped with the various sophisticated device libraries that are part of a standard SPICE. In addition, writing a numerically stable and efficient solver for the delayed differential equation is a highly nontrivial task. It makes clear, then, that a method for solving FW PEEC using a standard SPICE is of great convenience. Based on a special function in current standard SPICEs, we found that this objective is achievable.

3.2 Casting FW PEEC in SPICE

As described in Chapter 1, the FW PEEC can be conceptually constructed as in Fig. 1.10. The problem is that in most standard SPICEs, the controlled sources cannot be assigned to have delay, scaling, and summation at the same time. However, we note that it is possible to have the controlled source evaluating the delayed and scaled value of a single input. In typical SPICE language, in particular HSPICE [41], this kind of controlled source has the general input line

```
Gxxx n+ n− DELAY in+ in− TD=val SCALE=val
```

where G stands for voltage-controlled current source (VCCS), `n+` and `n−` are the nodes of the VCCS, `DELAY` is an indicator for time delay, `in+` and `in−` are the nodes of the controlling voltage, and the last two arguments specify the delay value and scaling coefficient. For other types of controlled sources, only the first character 'G' needs to be changed. For example, the voltage-controlled voltage source (VCVS) has the starting character 'E'.

With this kind of controlled source, the delayed mutual coupling (3.1) can be realized as in Fig. 3.1 (a), where we take the voltage across inductor 1 as an example. The $(N-1)$ *intermediate* VCVSs are used to implement delay as well as scaling, while a polynomial VCVS is connected in series with L_{11} to sum up the intermediate voltages.

doi: 10.6342/NTU201902629

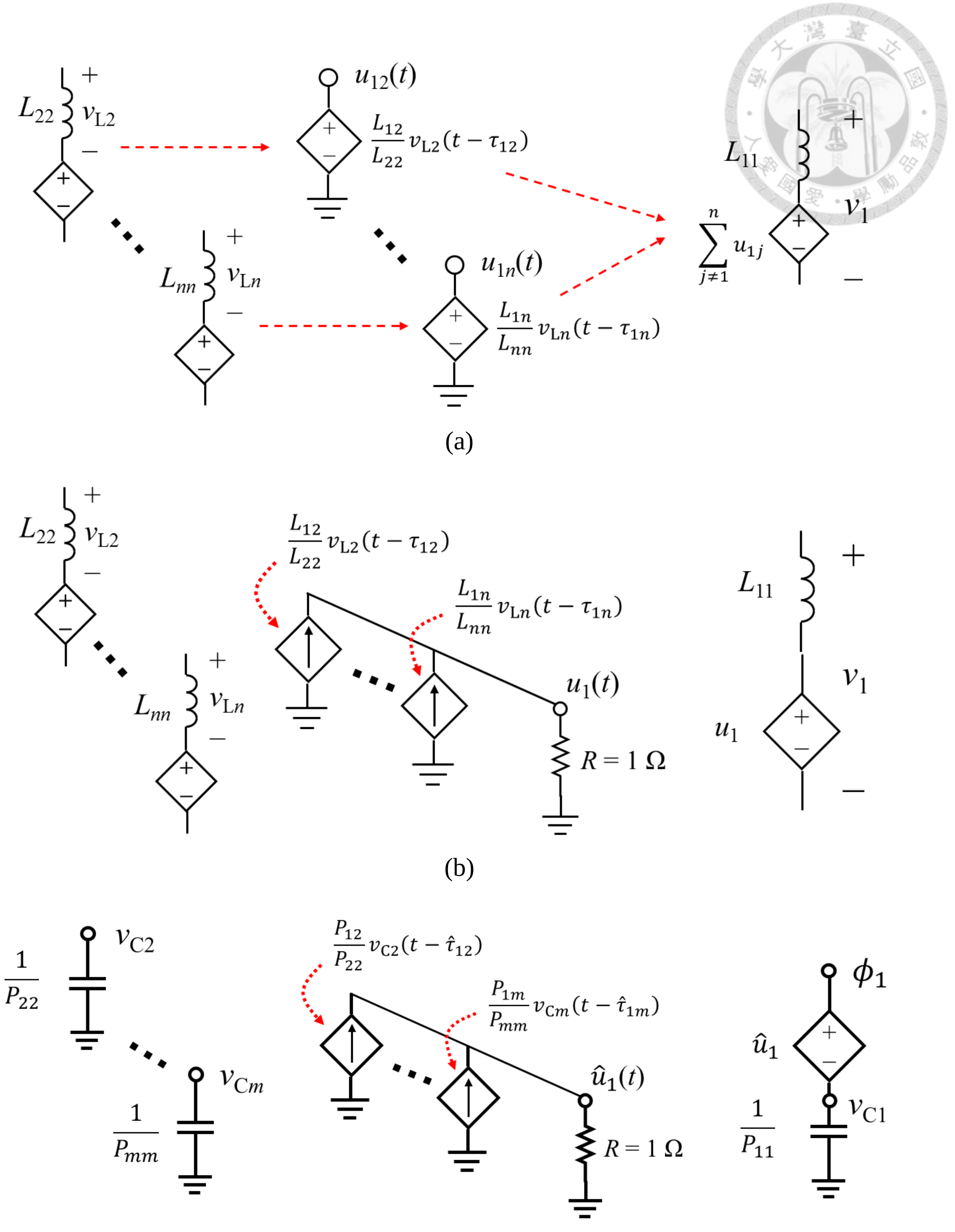

Fig. 3.1. (a) VCVS realization of delayed inductive coupling, (b) VCCS realization of delayed inductive coupling, and (c) VCCS realization of delayed potential coupling.

The drawback of this VCVS topology is the need for $O(N)$ additional nodes in the intermediate stages for *each* destination cell, resulting in $O(N^2)$ extra nodes in total. To reduce the node count, an improved arrangement shown in Fig. 3.1 (b) connects the $(N-1)$ delayed-scaling VCCSs in parallel in the intermediate stage such that the voltage across the 1-Ω resistor forms the immediate summation of the individual components in (3.1), without the need for a polynomial controlled source. Compared with Fig. 3.1 (a), fewer computation resources are needed in this configuration, because only one additional node is required for each destination coupling cell, resulting in N extra nodes in total. A similar circuit for the capacitive coupling from all other charge meshes to node 1 is shown in Fig. 3.1 (c).

It can be observed that this topology is a modification of the quasi-static PEEC structure in Fig. 1.9 proposed by [16]. Specifically, the linear controlled source in the intermediate stage is changed to the delay-scale controlled source as supplied by SPICE, and the 0-V voltage source in Fig. 1.9, originally intended to sample the sum of currents, is replaced with a 1-Ω resistor. The subsequent CCVS in Fig. 1.9 is changed to a unit-gain VCVS. The delay-scale VCCS is just an application of the delay function offered by SPICE, while the replacement of the 0-V voltage source by a 1-Ω resistor, although seemingly a trivial modification, in fact enables the implementation of *stabilizers* into the mutual coupling, which will be discussed in detail in Chapter 4.

Next we consider the incident waves. Suppose there are k different angles of incidence, with E fields polarized in the directions $\hat{e}_{\text{inc}1}$ to $\hat{e}_{\text{inc}k}$, respectively. Recall

doi: 10.6342/NTU201902629

Fig. 1.10. The effects of incident waves are represented as a series voltage source at each branch. From the expressions of these voltage sources (1.21) and (2.10), and again utilizing the technique of parallel-VCCS in the intermediate stages, we can realize the incident-wave-voltage-sources as in Fig. 3.2, where branch 1 is taken as the coupling target for illustration.

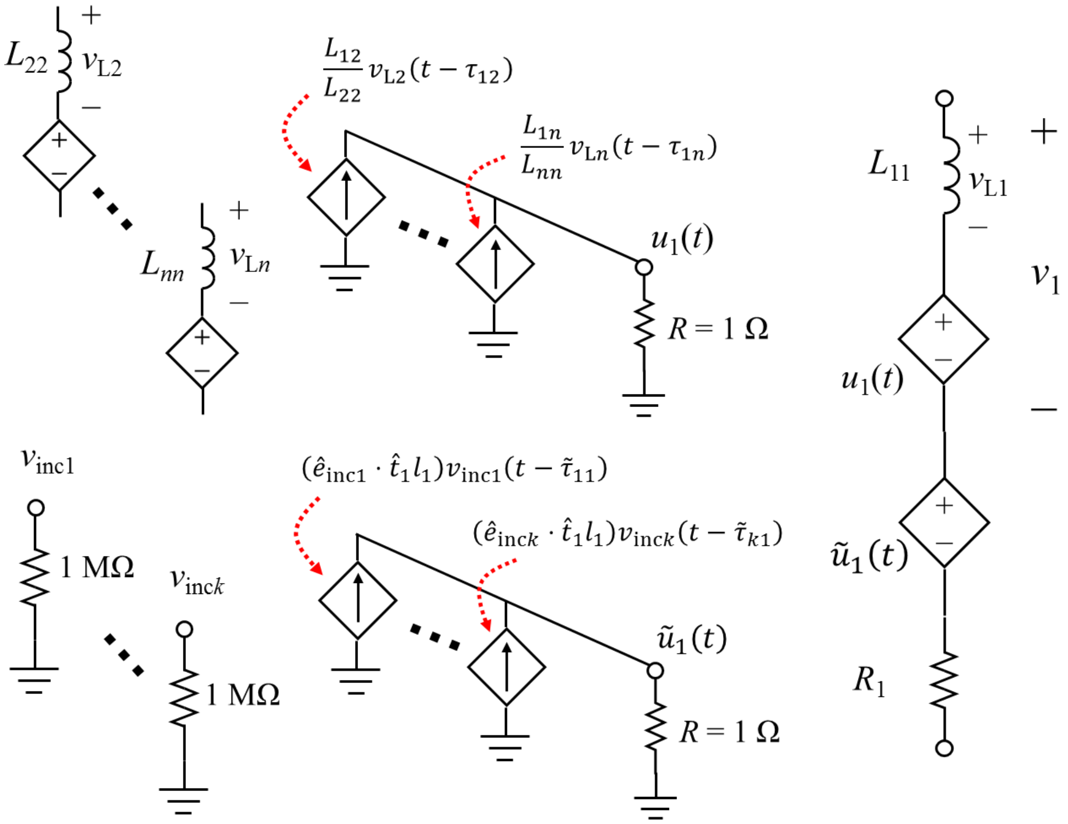

Fig. 3.2. VCCS realization of the incident wave coupling.

In the complete circuit, there will be *k* nodes whose voltages correspond to the incident E field strengths. They can be floating, or connected to ground by an arbitrary resistance, say, 1 MΩ, the latter sometimes giving better SPICE stability. Each branch is associated with an intermediate stage consisting of *k* delay-scaling VCCSs in parallel and a 1 Ω resistor to ground. The VCCS linking the i-th branch to the j-th incident angle has the scaling factor $(\hat{e}_{\mathrm{inc}j} \cdot \hat{t}_i l_i)$, while its associated time delay (unnormalized) is given by $\tilde{\tau}_{ji} = \frac{1}{\omega}(\vec{k}_j \cdot \vec{r}_i) = \frac{1}{c}(x_i \sin\theta_j \cos\phi_j + y_i \sin\theta_j \sin\phi_j + z_i \cos\theta_j)$, where ($x_i$, y_i, z_i) is the center location of the i-th branch, (θ_j, ϕ_j) is the j-th angle of incidence, and c is the speed of light. This delay is called unnormalized because it can be negative. A normalized set of delays can be obtained if we subtract each delay by the smallest value among the set of unnormalized delays (which may be negative). Accordingly, the normalized delays are all positive and the minimum delay is zero second.

Note that the intermediate stages of the incident waves can in fact be joined with the intermediate stages of the mutual inductive coupling, by simply connecting all the VCCSs in parallel. This combination will eliminate n nodes of the circuit and thus improve the efficiency. However, when *stabilizers* are added to the intermediate stages of mutual inductive coupling, as we will discuss in detail in Chapter 4, we need to separate these two different kinds of intermediate stages. Specifically, the mutual inductive coupling may be damped at the intermediate stages, while the incident waves shall not be damped.

As a concrete example, consider the thin strip dipole antenna made of copper as shown in Fig. 2.1 (a) of the previous chapter. If we partition each arm of the dipole into two charge meshes and one current mesh, and suppose there are incident waves coming from two distinct angles, then the overall PEEC model is as shown in Fig. 3.3, with eight

doi: 10.6342/NTU201902629

intermediate stages. The two nodes v_{inc1} and v_{inc2} are to be connected to the external voltage sources that represent the waveforms of the incident waves. This circuit is completely SPICE-compatible.

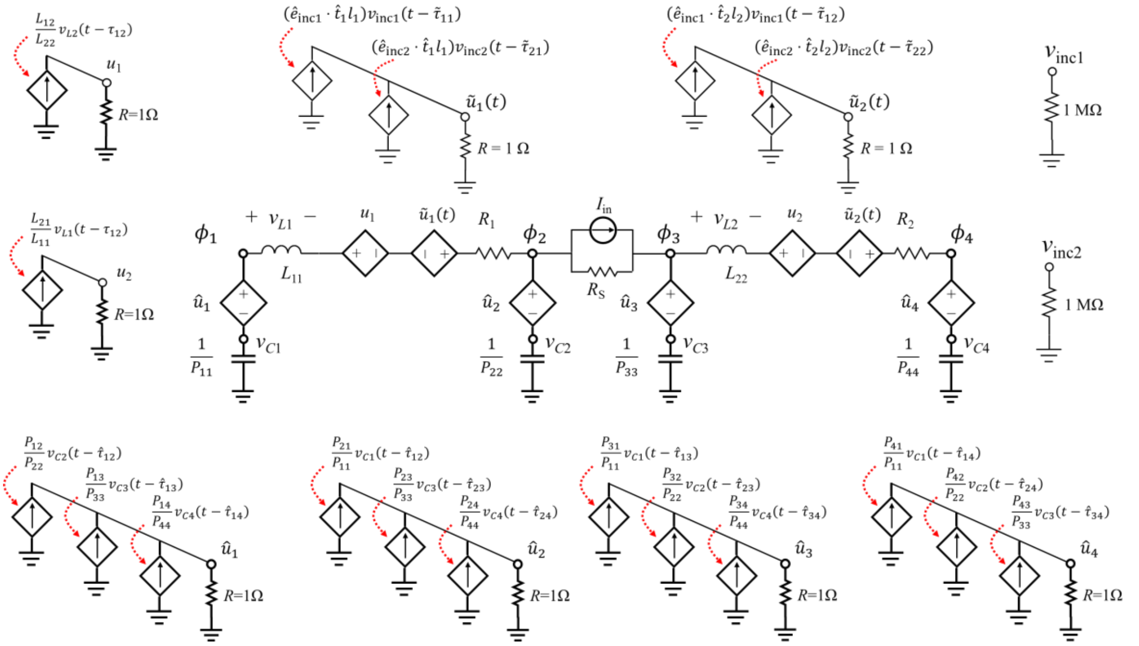

Fig. 3.3. Complete PEEC model of the strip dipole with four nodes and two branches using the VCCS topology, including incident waves coming from two different angles.

3.3 Verification

Simulation results of the dipole antenna in Fig. 2.1 (a) are provided. Here, the dipole is discretized into 20 current meshes and 22 charge meshes along the *y* direction, while the other directions are not meshed for simplicity. We consider the radiation mode, i.e., there is no incident wave. The PEEC subcircuit, based on the VCCS topology, are generated by MATLAB as a text file and loaded into Keysight ADS by its HSPICE compatibility wizard. It is found that ADS is able to perform both TD and FD simulation for such delayed controlled sources. So we first compare the S11 as shown in Fig. 3.4 with that from ANSYS HFSS as reference. Good agreement is observed, verifying the accuracy of the PEEC models. The complete netlist file of this PEEC subcircuit is documented in Appendix A.

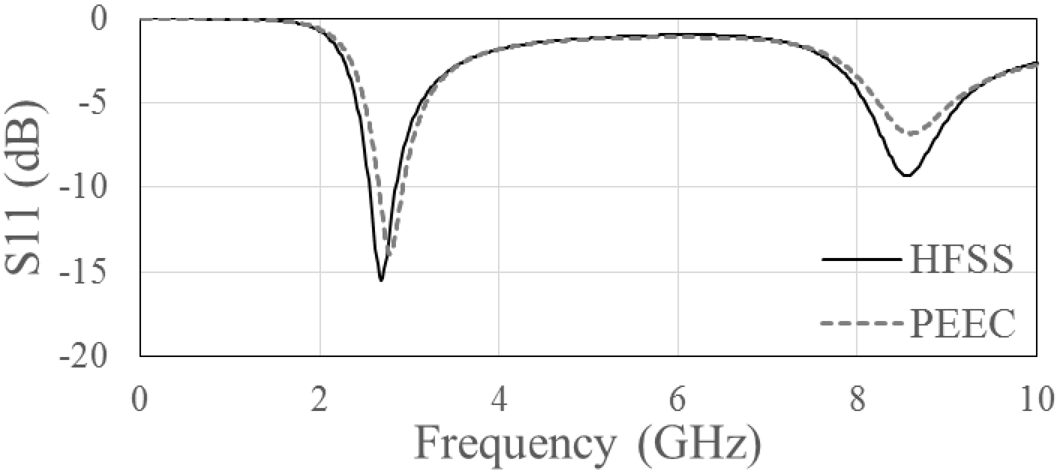

Fig. 3.4. S11 of the strip dipole by HFSS and PEEC with 20 branches and 22 nodes.

Next, time domain simulation is conducted. The input signal is a 2.8 GHz sinusoidal wave with 2 V amplitude and 1 ns delay, which means the sine wave starts from 1 ns. The input impedance at this frequency is 75 Ω plus a minor imaginary part according to FD simulation, giving the steady state amplitude 1.2 V across the input port. Fig. 3.5 shows the simulated port voltage by ADS. As can be seen, the steady state value is as predicted. However, after about 40 ns, the waveform no longer remains in a steady state. Instead, we observe a high-frequency oscillation with an exponentially divergent envelope, which is the typical response when the system has an unstable pole. The enlarged waveforms at 0~5 ns and 49~50 ns are shown in the bottom of Fig. 3.5. Indeed, the unexpected oscillation after 40 ns is at a much higher frequency than the input, roughly 40 GHz. If

doi: 10.6342/NTU201902629

the transient simulation continues, the response of the dipole will be completely masked by this anomalous resonance, and ADS will soon report the error *internal time step too small* and terminate automatically.

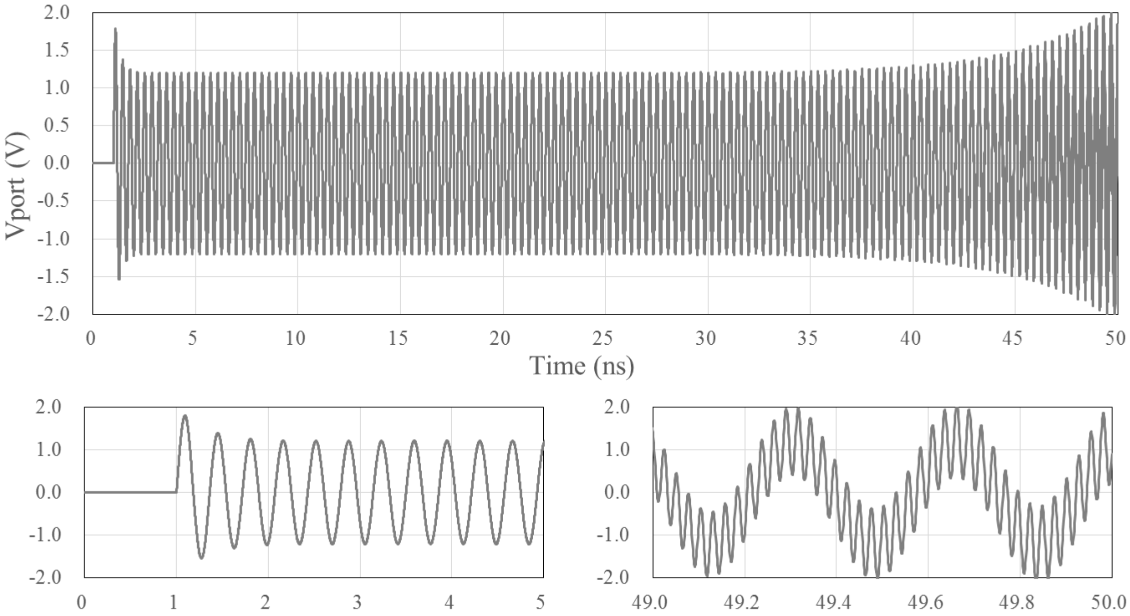

Fig. 3.5. Transient simulation results of the strip dipole PEEC model by ADS.

In summary, in this chapter we presented a method to solve a FW PEEC model in both frequency and time domain using a standard SPICE. The key element in the proposed approach was the delayed controlled source that has become an essential component in current SPICEs. Intermediate stages as proposed by [16] were modified to efficiently realize the massive delayed couplings in a typical PEEC model, as well as the incident waves. FD simulation has verified the validity of the proposed approach, while TD simulation unveiled a deeper issue: the stability of PEEC model, which is the main subject of Chapter 4. □

Chapter 4　Stability of FW PEEC

When obtaining a result like Fig. 3.5, we may suspect two things are going wrong. The first is, of course, that the model itself is unstable. The second possibility is that the method that we used to solve the transient behavior of the model is unstable. We shall distinguish this two aspects. The first issue, which we call model stability, is related to the behavior of the model only, and does not depend on any numerical methods that were adopted to solve the model. For example, a linear model is said to be unstable if there is at least a pole in the right half plane (RHP). On the other hand, the second issue, called numerical stability, is the property solely of the numerical method. The distinction between these two aspects can be best illustrated by a classic example: the RC discharge. Suppose we have a capacitor C in parallel with a resistor R. The voltage across the capacitor is denoted by $v(t)$, with initial value v_0. The governing equation is

$$\frac{d}{dt}v(t) = \frac{-1}{RC}v(t)$$

The analytic solution is well known: $v(t) = v_0 \exp\left(-\frac{t}{RC}\right)$. If both R and C are positive, we say the *model* is stable. If $C > 0$ but $R < 0$, then the *model* is unstable. On the other hand, we may use a numerical procedure to solve the differential equation. For example, first consider the Forward Euler method:

$$\frac{v(t_{k+1}) - v(t_k)}{\Delta t} = -\frac{1}{RC}v(t_k)$$

which gives the solution

$$v(t_{k+1}) = \left(1 - \frac{\Delta t}{RC}\right) v(t_k) = \left(1 - \frac{\Delta t}{RC}\right)^{k+1} v(t_0)$$

where we have assumed uniform time step. Here we observe a geometric sequence with common ratio (1 − Δt / RC). Obviously, if Δt is larger than two times of the RC time constant, the resulting solution will diverge, even if the *model* is stable. In such case we say the *numerical method* is unstable. For Forward Euler, to ensure stability, the time step must not be too large, which usually compromises the efficiency significantly.

Next we consider using Backward Euler to solve the same problem. The algorithm looks very similar, but the result is drastically different:

$$\frac{v(t_{k+1}) - v(t_k)}{\Delta t} = -\frac{1}{RC} v(t_{k+1})$$

which gives

$$v(t_{k+1}) = \frac{v(t_k)}{\left(1 + \frac{\Delta t}{RC}\right)} = \frac{v(t_0)}{\left(1 + \frac{\Delta t}{RC}\right)^{k+1}}$$

The difference is evident. For Backward Euler, no matter how large Δt is, the solution will never diverge, unless the *model* is unstable.

We have seen that the model stability and numerical stability are completely two different issues. In general, a stable model may exhibit an unstable response if the numerical method is unstable, and an unstable model may give a stable (yet inaccurate) solution if the method has a strong *numerical damping* that suppresses the unstable resonance of the model unintentionally. This often occurs if the time step is several orders of magnitude larger than the period of the resonance. In the following, we will focus on

doi: 10.6342/NTU201902629

the *model stability* of PEEC, instead of the numerical stability of the solver. Since all the PEEC models will be solved by Keysight ADS based on the method described in Chapter 3, instead of using our homemade SPICE, we can trust that the numerical stability is always well guaranteed.

The phenomenon in Fig. 3.5 is not uncommon in PEEC simulation. At the beginning everything goes well; the transient waveform evolves in the way it should be. Certain time later, however, the whole circuit turns wild. Every node voltage and branch current engages in a gigantic resonance with an exponentially increasing envelope. This unstable behavior has two characteristics: first, it often shows up not at the beginning of the simulation, but instead at a certain period later, which gives it the name *late-time instability* in the literature [18]. Second, the frequency of oscillation is usually much higher than the maximum frequency of interest, f_{m}, that the discretization is based on. As in the example of Fig. 3.5, the resonance is roughly at 40 GHz, while the discretization has maximum dimension 2.5 mm, giving $f_{\mathrm{m}} = 6$ GHz according to the $\lambda_{\mathrm{m}} / 20$ rule. Based on these observations, if the numerical method used by SPICE is stable, we would expect the model itself has an unstable pole at a frequency $\gg f_{\mathrm{m}}$ whose residue may be quite small. Numerous examples in the literature have demonstrated this high-frequency late-time instability of FW PEEC, to name a few [15], [39]. Kochetov in his monograph [19] even states that: “as a rule, the FW-PEEC method has an unstable solution if we do not apply special techniques for its improvement.”

For such a stability problem, we could ask three questions. First, when we have a PEEC model, how do we *test* its stability? The goal is to know if the model is stable or unstable without conducting transient simulation. Second, if the model is unstable, what is the source of its instability? After all, the PEEC model seems to be consisted of inductors, capacitors, and resistors. We may wonder where is the energy source that drives it unstable. Third, if the model is unstable, how do we fix it? What tools are available that could improve or restore stability without significantly compromising efficiency and accuracy? These three questions are the main subjects of this chapter, and will be covered in sections 4.2 to 4.4. For each part, a survey of what has been done in the literature will be given, followed by the results of our study. Before restricting ourselves to the stability problem of PEEC, we will first review the stability concepts in various related fields, including control theory and circuit theory. The contents of section 4.1 are mainly based on the books by Khalil [42], Franklin, Powell, and Emami-Naeini [43], Gu, Kharitonov, and Chen [44], and Chua, Desoer, and Kuh [7].

4.1 Review of Stability Concepts

Consider a time-invariant system, with no time delay, described by the vector differential equation

doi: 10.6342/NTU201902629

$$\dot{\mathbf{x}} = f(\mathbf{x})$$

where $\mathbf{x}$ is the vector of state variables and the function f is assumed to have certain good properties that ensure the existence and uniqueness of the solution [42]. Without loss of generality, assume $\mathbf{x} = 0$ is an equilibrium point of the system, i.e., $f(0) = 0$. The equilibrium point said to be *stable* in the sense of Lyapunov if $\forall\, \varepsilon > 0$, $\exists\, \delta > 0$ such that if $\|\, \mathbf{x}(0) \,\| < \delta$, then $\|\, \mathbf{x}(t) \,\| < \varepsilon$, $\forall\, t \geq 0$. It is *unstable* if it is not stable. It is *asymptotically stable* if it is stable, and also $\|\, \mathbf{x}(0) \,\| < \delta$ implies $\lim_{t\to\infty} \mathbf{x}(t) = 0$. In other words, if the solution is close enough to a stable equilibrium, it will stay close to it in all future times; if it is close enough to an asymptotically stable equilibrium point, then it will not only stay nearby, but also approaches the equilibrium point as time goes to infinity.

For the special case of a *linear* time-invariant (LTI) delayless system:

$$\dot{\mathbf{x}} = \mathbf{F}\mathbf{x} \tag{4.1}$$

if $\det(\mathbf{F}) \neq 0$, the only equilibrium is at $\mathbf{x} = 0$, the origin. To determine the stability of the origin, we note that the solution of (4.1) can be written as $\mathbf{x}(t) = \exp(\mathbf{F}t)\,\mathbf{x}(0)$ for a given initial condition $\mathbf{x}(0)$, where $\exp(\mathbf{F}t)$ is in matrix exponential sense. If $\mathbf{F}$ is diagonalizable, we can write $\mathbf{F} = \mathbf{P}\mathbf{D}\mathbf{P}^{-1}$, where $\mathbf{D}$ is a diagonal matrix containing the eigenvalues of $\mathbf{F}$. Then $\exp(\mathbf{F}t) = \mathbf{P}\exp(\mathbf{D}t)\mathbf{P}^{-1}$. Hence, the stability of the origin can be characterized by the eigenvalues of $\mathbf{F}$. Specifically, if all eigenvalues are in the open left-half plane (LHP), which means they have strictly negative real parts, then $\exp(\mathbf{D}t)$ will

doi: 10.6342/NTU201902629

tend to 0, and thus the origin is an asymptotically stable equilibrium point. If all eigenvalues have negative real part except some on the imaginary axis with multiplicity one, then the origin is stable but not asymptotically stable. If at least one eigenvalue is in RHP, then the origin is unstable. The case for eigenvalues on the imaginary axis with multiplicity greater than 1 is slightly complicated. See Khalil [42] for detail. In short, if the matrix **F** is diagonalizable, then the system will be stable. In other words, if for eigenvalues of multiplicity greater than one there exists independent eigenvectors with corresponding number, then the system is stable.

The meaning of the eigenvalues of **F** can be presented in another way. For the system (4.1), we seek for a solution of the form $\mathbf{x}(t) = \mathbf{x}_0 \exp(s_i t)$, where $\mathbf{x}_0 = \mathbf{x}(0)$ is a constant initial-condition vector, and s_i is an unknown constant. Since the system is not driven by external inputs, if such solution exists, we call the s_i the *natural frequency*, or *pole*, of the system. Substituting this expression into (4.1) gives

$$\mathbf{F}\mathbf{x}_0 = s_i \mathbf{x}_0$$

which shows that the eigenvalues of **F** are exactly the natural frequencies of the system, or poles.

Now suppose the system is driven by an input **u**, and the output **y** that we observe is a linear function of **x** and **u**. Then the state-space description of the system can be written as:

doi: 10.6342/NTU201902629

$$\dot{\mathbf{x}} = \mathbf{F}\mathbf{x} + \mathbf{G}\mathbf{u}$$

$$\mathbf{y} = \mathbf{H}\mathbf{x} + \mathbf{J}\mathbf{u} \tag{4.2}$$

where **F**, **G**, **H**, and **J** are all constant matrices. Taking Laplace transform of (4.2) and assuming zero initial-condition, i.e., $\mathbf{x}(0) = 0$, we can obtain the relation between the input and output as

$$\mathbf{Y}(s) = [\mathbf{H}(s\mathbf{I}_{\mathrm{d}} - \mathbf{F})^{-1}\mathbf{G} + \mathbf{J}]\, \mathbf{U}(s)$$

where the matrix in the square bracket is the transfer function matrix. From the Cramer's rule in linear algebra, we know that the denominator of every element of the transfer function matrix is exactly $\det(s\mathbf{I}_{\mathrm{d}} - \mathbf{F})$. Therefore, we see that although the exact form of the transfer function is dependent on the selected inputs and outputs, all the poles of the transfer function are the natural frequencies of the system, which further manifests the meaning of "natural frequency".

When particular inputs and outputs are defined, we also have the notion of bounded-input-bounded-output (BIBO) stability. An input-output system is BIBO stable if every bounded input **u** results in a bounded output **y**, where the boundedness is defined based on the infinity norm [42]:

$$\|\mathbf{u}\|_{\mathcal{L}_\infty} = \sup_{t \geq 0} \|\mathbf{u}(t)\| < \infty$$

In other words, the input **u** is bounded if there exists a constant bound for $\|\, \mathbf{u}(t)\, \|$ for all time *t*. For a single-input-single-output LTI system, it can be proved that it is BIBO stable

doi: 10.6342/NTU201902629

if and only if its impulse response is absolutely integrable [43]. Since the poles of the transfer function are all natural frequencies of the system, asymptotic stability implies BIBO stability. A system only being stable but not asymptotically stable, however, is not BIBO stable: when the input is exactly in the form of the natural response of the pole on the imaginary axis, i.e., the input just *hits* at the pole, the output will be unbounded. Hence, for LTI systems, we usually demand asymptotic stability, not just stability. For simplicity, in the remaining sections of this chapter, we will refer to an asymptotically stable system simply as “stable”.

The above concepts of stability and natural frequency parallel those in circuit theory. Consider a linear lumped circuit described by the time domain MNA as

$$\mathbf{T}(D)\mathbf{w}(t) = \mathbf{u}(t) \tag{4.3}$$

where $\mathbf{w}(t) = \begin{bmatrix} \mathbf{e}(t) \\ \mathbf{i}_2(t) \end{bmatrix}$ is the vector of nodal voltages and selected branch currents. We ask: when there is no independent sources, i.e., $\mathbf{u}(t) = 0$ and that all responses are caused by the initial condition, is it possible that the solution is of the form $\mathbf{w}(t) = \mathbf{w}_0 \exp(s_i t)$, where $\mathbf{w}_0$ is a constant nontrivial vector? Substituting into (4.3) and noting that all elements of $\mathbf{T}(D)$ are polynomials of D of order less than or equal to 1, we have

$$\mathbf{T}(D)\mathbf{w}_0 e^{s_i t} = \mathbf{T}(s_i)\mathbf{w}_0 e^{s_i t} = 0$$

or simply $\mathbf{T}(s_i)\mathbf{w}_0 = 0$. Since $\mathbf{w}_0$ is nonzero, it means that we must have

$$\det \mathbf{T}(s_i) = 0$$

doi: 10.6342/NTU201902629

We define $p(s) = \det \mathbf{T}(s)$ the *characteristic polynomial* of the circuit, and any zero of $p(s)$ is called a *natural frequency* of the circuit, or *pole*. This definition of pole is consistent with that introduced previously based on the state-space description, in fact more general: the linear system $s\mathbf{x} = \mathbf{F}\mathbf{x} + \mathbf{G}\mathbf{u}$ can be rewritten as $(s\mathbf{I}_\mathrm{d} - \mathbf{F})\mathbf{x} = \mathbf{G}\mathbf{u}$, which is then in an MNA-like form. In addition, although the natural frequency is defined based on MNA here, we would have identical results if the circuit were analyzed by the Tableau Analysis. The concepts are the same, and the resulting poles are consistent. The equivalence of the two methods is demonstrated in [7].

According to this definition, we can interpret the natural frequency of a circuit as follows. In Laplace domain, a pole of a system is a complex value that makes the MNA matrix, $\mathbf{T}(s)$, singular. In time domain, s_i is a natural frequency of the circuit if and only if the LTI circuit with no independent sources exists a solution described by $\mathbf{w}(t) = \mathbf{w}_0\exp(s_i t)$. When the response of the circuit is exactly $\mathbf{w}(t) = \mathbf{w}_0\exp(s_i t)$, we say the *mode* s_i has been set up. The stability property of the circuit follows immediately. If all natural frequencies have strictly negative real parts, then the *zero-input response*, the response of the circuit driven by initial condition but not independent sources, will tend to zero. In such case the origin is an asymptotically stable equilibrium point. The other cases parallel those in the state-space model.

The constant vector $\mathbf{w}_0$, though not identically zero, may have some components

doi: 10.6342/NTU201902629

equal to zero. The significance of this situation is that at the corresponding circuit quantities, either nodal voltages or branch currents, this mode is not *observable*. If the Tableau Analysis is used to define natural frequency, we may also find some *branch voltages* that cannot observe this mode. A simple example given by [7] is repeated here, as shown in Fig. 4.1.

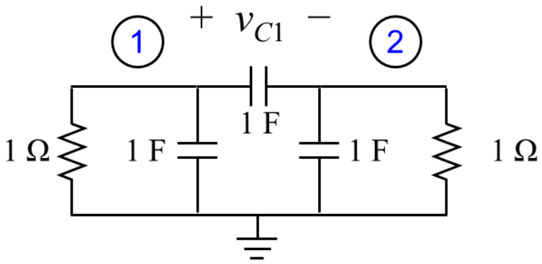

Fig. 4.1. An example from [7] demonstrating the observability issue.

MNA gives $\begin{pmatrix} 2s+1 & -s \\ -s & 2s+1 \end{pmatrix}\begin{pmatrix} E_1 \\ E_2 \end{pmatrix} = \begin{pmatrix} 0 \\ 0 \end{pmatrix}$. The natural frequencies are −1 and −1/3. However, by subtracting the two equations in MNA, we have the equation for the branch voltage V_{C1}: $(3s + 1)V_{C1} = 0$. Hence, the −1 mode is not observable at v_{C1}.

The observability issue is important when the circuit has unstable poles. Since usually we do not observe all components of the state vector, **w**, i.e., we do not probe all the node voltages and branch currents, at the selected observation points we may not observe the responses of the unstable poles. However, SPICE does. The result is that, according to the data we observe, we might think the circuit is going well, while at a certain instance SPICE suddenly quits, reporting an error message indicating the circuit is going wrong. The observability is a theoretical issue, and is something we have to argue

doi: 10.6342/NTU201902629

when we design the *damping* to improve stability based on the port description of the circuit, to be detailed in section 4.4.

When independent sources present in the circuit, the solution of MNA is given by

$$\mathbf{W}(s) = \mathbf{T}(s)^{-1}\mathbf{U}(s)$$

Similar to the state-space version, according to Cramer's rule, the characteristic polynomial $\det\mathbf{T}(s)$ will appear at the denominator. Consequently, no matter which circuit variables are designated as input and output, all the poles of the transfer function will be poles of the circuit, i.e., natural frequencies. The converse, however, does not necessarily hold. It is possible that some natural frequencies of the circuit do not appear as poles of a particular transfer function. The observability issue just mentioned is one case. If a mode is not observable at the selected output, then it will not appear as a pole in the transfer function. The other case is when the mode is not *excitable* from the selected input, e.g., a resonator physically separated from the other parts of the circuit. Examples of these cases can be found in [7]. Mathematically, there will be a pole-zero cancellation in the transfer function. When an unstable mode does not appear in the input-output relation of the system, we say there is an *unstable hidden mode*.

Based on these discussions, we see that if all natural frequencies of an LTI system are in the open LHP, then the BIBO stability for arbitrary inputs and outputs can be guaranteed. If, however, some natural frequencies are in RHP, then even if they may not

doi: 10.6342/NTU201902629

appear in the transfer function of a particular input-output set, the circuit might still diverge, and the SPICE transient simulation will eventually fail. Hence, the safest way to study the stability property of a system is to deal with the natural frequencies, instead of any particular input-output relation.

An important property of natural frequencies is that, because they are the roots of det$\mathbf{T}(s)$, where $\mathbf{T}(s)$ is the MNA matrix of the *whole circuit*, the natural frequencies are also the characteristic of the *whole circuit*. It implies that, even if only a tiny part of the circuit is altered, in general all natural frequencies will change. A directly related notion is the open-circuit stability and short-circuit stability for linear N-ports [7]. Roughly speaking, if an N-port network is stable when its ports are excited by independent current (voltage) sources, then it is called open- (short-) circuit stable. A circuit that is open-circuit stable does not imply it is short-circuit stable, and vice versa. For example, suppose the N-port has an impedance matrix representation, $\mathbf{Z}(s)$. Then it is open-circuit stable if the *poles* of each element of $\mathbf{Z}(s)$ are in the LHP. Now, if this network is excited by voltage sources, then the resulting port currents would be $\mathbf{I}(s) = \mathbf{Z}(s)^{-1}\mathbf{V}(s)$. Thus the short-circuit stability is now determined by the *zeros* of $\det(\mathbf{Z}(s))$, which are not necessarily in the LHP. Another way to appreciate the difference between open-short-circuit stability is by considering the MNA matrix. Independent current sources appear at the RHS and do not affect the natural frequencies. Independent voltage sources, however, would modify the

doi: 10.6342/NTU201902629

MNA matrix by adding additional description lines, hence giving different stability properties.

So far we have mainly considered systems with no time delay, where the definitions of stability, characteristic polynomial, and natural frequency were introduced. As it turns out, these definitions carry over to delay systems, with some necessary modification. However, some stability properties are drastically different. In particular, for a delay-free system, the number of natural frequencies is at most the order of its characteristic polynomial, which is finite. But for a time delay system, however, due to the presence of exponential in the characteristic "polynomial", which is in fact a transcendental function, the number of roots is usually infinite. Consequently, to ensure stability of the system, we need stronger conditions.

A certain type of time-invariant system with time delay can be described by the following *functional differential equation* (FDE):

$$\dot{\mathbf{x}} = f(\mathbf{x}_t)$$

where $\mathbf{x}_t(\theta) = \mathbf{x}(t + \theta)$, $-r \le \theta \le 0$, for some constant maximum delay r. The initial condition of the state vector is a given function $\mathbf{x}(\theta) = \phi(\theta)$, $-r \le \theta \le 0$. Because $\mathbf{x}_t(\theta)$ is a function, instead of a single scalar, each component of f is a function of function, thus the name *functional*. The above type of system has the special property that, in the mathematical model, the term with highest order time derivative ($\dot{\mathbf{x}}$) does not have any

doi: 10.6342/NTU201902629

time delay. To distinguish from the more general delay systems, this type is called the *retarded functional differential equation* (RFDE) in the literature [44].

Definitions of stability are very similar to the delay-free case. Assume $\mathbf{x} = 0$ is an equilibrium point of the system. The equilibrium point is said to be *stable* if $\forall\, \varepsilon > 0$, $\exists\, \delta > 0$ s.t. if $\|\mathbf{x}_0\|_C < \delta$, then $\|\, \mathbf{x}(t)\, \| < \varepsilon$, $\forall\, t \geq 0$. It is *asymptotically stable* if it is stable, and also $\|\mathbf{x}_0\|_C < \delta$ implies $\lim_{t\to\infty} \mathbf{x}(t) = 0$. The difference is at the continuous norm: $\|\mathbf{x}_0\|_C \triangleq \max_{-r\leq\theta\leq 0} \|\mathbf{x}(\theta)\|$.

A special case of RFDE is the LTI system with *pointwise*, or *concentrated*, delays:

$$\dot{\mathbf{x}} = \mathbf{A}_0\mathbf{x} + \sum_{k=1}^{K} \mathbf{A}_k \mathbf{x}(t - r_k)$$

where the square matrices $\mathbf{A}_0$ and $\mathbf{A}_k$ are given, and the delays $0 = r_0 \leq r_1 \leq \ldots \leq r_K = r$. For such an LTI system, we seek, as previously, a solution of the form $\mathbf{x}(t) = \mathbf{x}_0\exp(s_i t)$ with initial condition $\phi(\theta) = \mathbf{x}_0\exp(s_i\theta)$, where $\mathbf{x}_0$ is a constant nontrivial vector. Substituting the trial solution into the RFDE, we obtain

$$\left(s_i\mathbf{I}_\mathrm{d} - \sum_{k=0}^{K} \mathbf{A}_k e^{-s_i r_k}\right)\mathbf{x}_0 = 0$$

For this equation to hold, the scalar s_i must be the value such that the matrix

$$\Delta(s) = \left(s\mathbf{I}_\mathrm{d} - \sum_{k=0}^{K} \mathbf{A}_k e^{-s r_k}\right)$$

becomes singular, or, equivalently, $\det\Delta(s) = 0$. The matrix $\Delta(s)$ is called the *characteristic matrix* of the RFDE, and the expression $\det\Delta(s)$ is called the *characteristic function*, also called the *characteristic quasipolynomial*. Strictly speaking, it is not a polynomial in s due to the presence of e^{-sr}. The roots of $\det\Delta(s) = 0$ are, likewise, the natural frequencies or poles of the system.

The arguments can also be presented based on Laplace transform. For a given initial condition $\phi(\theta)$, we define

$$\Phi_{r_k}(s) = \int_{r_k}^{0} \phi(\theta) e^{-s\theta} d\theta$$

We note that since r_k is finite, Φ_{rk} is an entire function, provided the given $\phi(\theta)$ is well-behaved. Then, the Laplace transform of the RFDE can be expressed as

$$s\mathbf{X} - \phi(0) = \mathbf{A}_0\mathbf{X} + \sum_{k=1}^{K} \mathbf{A}_k e^{-sr_k}\left(\mathbf{X} + \Phi_{r_k}\right)$$

Or

$$\left(s\mathbf{I}_\mathrm{d} - \sum_{k=0}^{K} \mathbf{A}_k e^{-sr_k}\right)\mathbf{X} = \Delta(s)\mathbf{X} = \phi(0) + \sum_{k=1}^{K} \mathbf{A}_k e^{-sr_k}\Phi_{r_k}$$

Note that the RHS is also an entire function in s, thus has no poles. Then, based on Cramer’s rule, the denominators of the state vector **X** will be $\det\Delta(s)$. Again, we see that the natural frequencies will determine the stability property of the system.

What is different from delayless systems is that, since the characteristic quasipolynomial is transcendental, it generally has an infinite number of roots. Yet, because $\det\Delta(s)$ is an entire function, there can only be a finite number of roots within any compact set [44]. As a result, we can expect that most of the poles of the system will go to infinity, either far left, far right, or at very high frequency (far upward). Far-left

doi: 10.6342/NTU201902629

poles have no influence on the stability of the system. Very-high-frequency poles, from the viewpoint of circuit simulation, will be suppressed by numerical damping, and thus have no impact on stability either. Far-right poles, in contrast, will cause the system to break down in an ultra-short time. However, carefully looking at the definition of $\Delta(s)$, we can argue that there will be no far-right poles, nor far-upward poles, as follows.

A pole is a complex value that makes $\Delta(s)$ singular, or equivalently, makes $\Delta(s)$ has 0 as one of its eigenvalues. The Gershgorin Circle Theorem in linear algebra [45] states that the eigenvalues of an arbitrary $n\times n$ matrix will all lie in the union of n circles in the complex plane, whose centers are the diagonal elements of the matrix and radii given by the sum of absolute values of the off-diagonal elements of each row. For a system with only positive delay, i.e., no time advance, e^{-sr} goes to zero as s goes right, which means the radii of the Gershgorin's circles become increasingly small, while the centers move right steadily. Consequently, there will be a vertical threshold such that for all s with real part larger than this threshold, no Gershgorin disks will encircle the origin, hence excluding 0 as an eigenvalue. Therefore, $\Delta(s)$ has no far-right poles. On the other hand, if s moves upward indefinitely while keeping its real part unchanged, then the absolute value of e^{-sr} remains constant, which means the radii of the Gershgorin circles do not shrink. However, the centers of the disks will move upward, unbounded. So similarly there will be a horizontal threshold such that for s with imaginary part greater than the

doi: 10.6342/NTU201902629

threshold, no Gershgorin disks will encircle the origin.

Based on these arguments, a property follows immediately: for any real constant γ, the number of poles of the RFDE system with real parts larger than γ is finite, counting their multiplicities. This property characterizes the distribution of any LTI RFDE system. In view of this, we may define

$$\sigma = \max\{\mathrm{Re}(s) | \det \Delta(s) = 0\}$$

which is called the *stability exponent* of the system. The stability of the RFDE system can be determined based on σ, according to the following theorem [44].

Theorem The RFDE system is asymptotically stable if and only if $\sigma < 0$. Furthermore, σ is a continuous function of the delays $r_k \geq 0$, $k = 1, 2, \ldots, K$.

This theorem is not much different from the delay-free case. The determination of the stability of a system becomes the mathematical procedure of finding the characteristic roots and checking their real parts. The continuity property of σ on the other hand enables a lot of frequency sweeping tests [44]. The basic idea is, if the system is asymptotically stable when all delays are set to zero, then the continuity property ensures that there will be a range of delays $r_k \in [0, \beta]$ in which the RFDE remains asymptotically stable.

Apart from RFDE, a more general class of delay systems is called the *neutral functional differential equation* (NFDE), whose distinct feature is that the time derivative terms also contain delay. We only consider LTI NFDE with pointwise delays, whose

doi: 10.6342/NTU201902629

general form is given by:

$$\dot{\mathbf{x}} - \sum_{k=1}^{K} \mathbf{B}_k \dot{\mathbf{x}}(t - r_k) = \mathbf{A}_0 \mathbf{x} + \sum_{k=1}^{K} \mathbf{A}_k \mathbf{x}(t - r_k) \tag{4.4}$$

By similar derivation to the RFDE case, we define the characteristic quasipolynomial, or characteristic function, of the NFDE as the determinant of the characteristic matrix, $\Delta(s)$:

$$\det \Delta(s) = \det\left(s\left(\mathbf{I}_{\mathrm{d}} - \sum_{k=1}^{K} \mathbf{B}_k e^{-r_k s} \right) - \sum_{k=0}^{K} \mathbf{A}_k e^{-r_k s} \right) \tag{4.5}$$

The roots of the characteristic quasipolynomial are likewise called the natural frequencies, or poles, or characteristic roots, of the NFDE system. The number of poles is generally infinite as well, and is finite in any compact set. Based on similar Gershgorin arguments, we know that there will be no poles at far right. However, it is no longer the case that no poles are at far upward, due to the presence of the term

$$\Delta_0(s) = \left(\mathbf{I}_{\mathrm{d}} - \sum_{k=1}^{K} \mathbf{B}_k e^{-r_k s} \right)$$

which is the characteristic matrix of the *associated difference equation* (ADE):

$$\mathbf{x}(t) - \sum_{k=1}^{K} \mathbf{B}_k \mathbf{x}(t - r_k) = 0$$

Consider the definitions of $\Delta(s)$ and $\Delta_0(s)$. If $\det\Delta_0(s)$ remains bounded from 0 while s continuously moving upward, with a fixed real part, then based on Gershgorin theorem we know $\Delta(s)$ will also be nonsingular. The opposite of this statement is that, if there is a

doi: 10.6342/NTU201902629

pole of $\Delta(s)$ at far upward, deep into very high frequency, then near such pole $\Delta_0(s)$ must be close to singular. Now suppose at $s = s_0$, $\det\Delta_0(s_0) = 0$. Then on the vertical line $\mathrm{Re}(s) = \mathrm{Re}(s_0)$, due to the periodicity of e^{-sr} along the vertical direction, there will be an infinite number of points such that $\Delta_0(s)$ is close to singular, and near which $\Delta(s)$ has the chance to be singular. A theorem can be rigorously established as follows [46], [47]: If s_0 is a root of $\det\Delta_0(s)$, then there exists a series of poles, s_k, of the NFDE with $|s_k| \to \infty$ and $\mathrm{Re}(s_k) \to \mathrm{Re}(s_0)$, i.e., they asymptotically approach the vertical line $\mathrm{Re}(s) = \mathrm{Re}(s_0)$. An illustration of this pole distribution behavior is shown in Fig. 4.2.

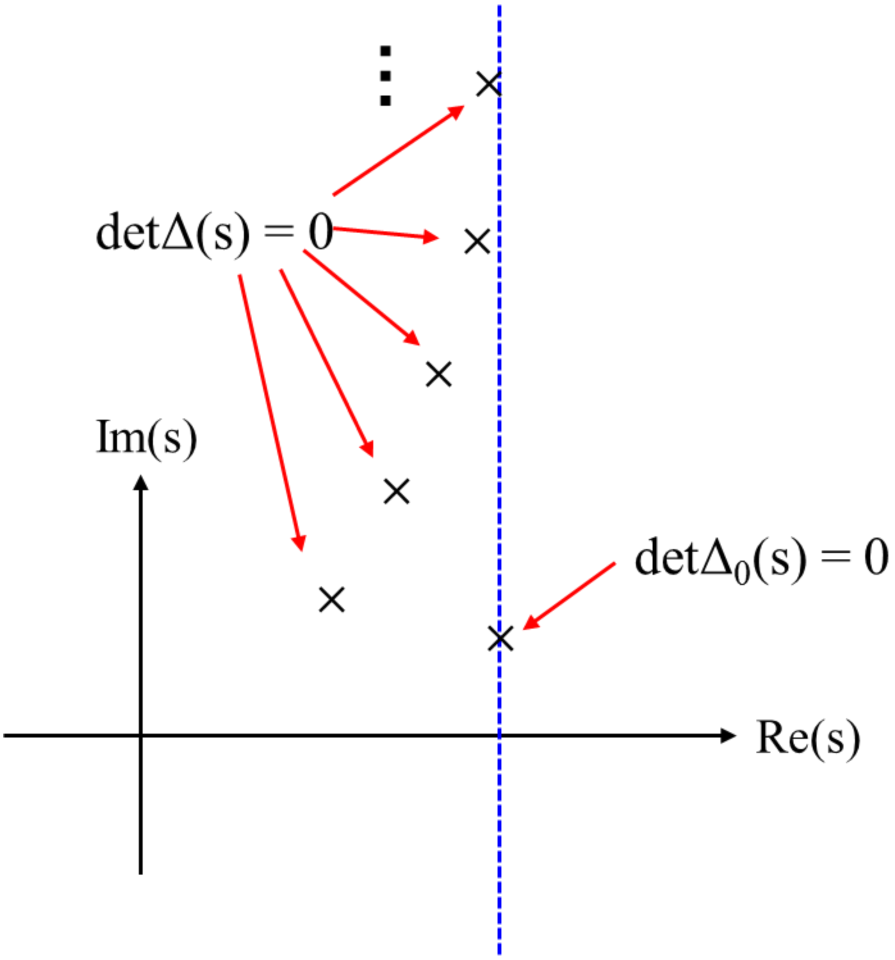

Fig. 4.2. Illustration of the pole distribution of NFDE.

In view of this, the *stability exponent* for an NFDE system has to be defined differently:

$$\sigma = \sup\{\mathrm{Re}(s) \mid \det \Delta(s) = 0\}$$

The main difference from the RFDE case is the replacement of maximum with supremum. From the discussion above, we know that σ is finite. A stability theorem for NFDE systems based on σ is given below [44].

Theorem The NFDE system is asymptotically stable if $\sigma < 0$.

Different from RFDE, all poles of an NFDE system lying in the open LHP is only a necessary condition for asymptotic stability, but not sufficient. The associated difference equation of the NFDE plays a crucial role. If $\det\Delta_0(s)$ has a root on the imaginary axis, then there may be a series of LHP poles of the NFDE system asymptotically approaching the imaginary axis, which makes the stability property difficult to assess. On the other hand, if $\det\Delta_0(s)$ has a root on the RHP, then we know that the NFDE system is unstable.

An example from Datko [48] clearly illustrates the importance of the ADE. Consider the scalar system

$$\dot{x}(t) + \frac{1}{2}\dot{x}\left(t - \frac{\pi\alpha}{2}\right) - \frac{1}{2}\dot{x}(t - \pi\alpha) + x(t) + \frac{1}{2}x\left(t - \frac{\pi\alpha}{2}\right) - \frac{1}{2}x(t - \pi\alpha) = 0$$

where α is a real sweeping parameter controlling the amount of delays. Simple calculation shows that

$$\Delta(s) = (s+1)\Delta_0(s) = (s+1)\left(1 + \frac{1}{2}e^{-s\frac{\alpha\pi}{2}} - \frac{1}{2}e^{-s\alpha\pi}\right)$$

The associated difference equation has a characteristic root at $s = 2j/\alpha$, which is on the

doi: 10.6342/NTU201902629

imaginary axis. When $\alpha = 0$, $\Delta(s) = (s + 1)$, thus $\sigma = -1 < 0$, and the delay-free system is asymptotically stable. However, for α arbitrarily small but nonzero, $\Delta(2j/\alpha) = 0$, thus $\sigma = 0$. In this case the stability exponent has a jump from −1 to 0 when arbitrarily small delays are introduced. In other words, the stability exponent here is not *robust* to time delays.

Datko [48] has provided a theorem giving sufficient conditions for the continuity of the stability exponent. Consider the modified characteristic matrix of the NFDE:

$$\Delta^{(\alpha)}(s) = \left(s\left(\mathbf{I}_{\mathrm{d}} - \sum_{k=1}^{K} \mathbf{B}_k e^{-\alpha r_k s}\right) - \sum_{k=0}^{K} \mathbf{A}_k e^{-\alpha r_k s}\right) \tag{4.6}$$

where the delay-sweeping parameter α is introduced.

Theorem The stability exponent σ is a continuous function of α on $(0, \infty)$. Furthermore, if all roots of $\det\Delta_0(s)$ lies in the left half plane $\mathrm{Re}(s) \in (-\infty, -\beta)$, for some $\beta > 0$, then σ is also continuous at $\alpha = 0$.

It is worth comparing the pole distribution of RFDE and NFDE when small delays are introduced to the system. For a delay-free system, there are only a finite number of poles on the complex plane. We call these poles the “ground poles” of the system. When arbitrarily small delays are introduced, the number of poles suddenly becomes infinite. We call those new poles the “sky poles”, in contrast to the ground poles that the system originally possesses when there is no delay. Since the delays are small, the ground poles will not move greatly, i.e., they will be close to their delay-free locations. The sky poles,

doi: 10.6342/NTU201902629

on the other hand, depends on the system type. For RFDE, all the sky poles occur at far left, and hence the stability property is dominated by the ground poles. As the values of delay gradually increase, the sky poles may move right, and finally contribute to the determination of stability. For NFDE, however, there are two classes of sky poles. Some sky poles will occur at far left as in RFDE, and thus have less impact on stability initially. Some sky poles will occur at far upward, near the vertical lines determined by the ADE, and may have significant impact on stability if these vertical lines are close to the imaginary axis. If one of the vertical lines is in the RHP, then the NFDE system is unstable for arbitrarily small delays, even if the delay-free system is stable.

In this section, we have reviewed the relevant stability concepts and properties in the fields of control theory and circuit theory. Equipped with this knowledge, we are now ready to tackle the stability of full-wave PEEC model. Studies of PEEC stability in the literature will be reviewed in later sections. As an end of this section, we point out that a FW PEEC model, not including possible external nonlinear circuits, is an LTI NFDE system with pointwise delays. The fact that it is an NFDE instead of the benign RFDE can be easily seen from the mutual inductive coupling:

$$v_i(t) = \sum_{j=1}^{n} L_{ij} \frac{\mathrm{d}}{\mathrm{d}t} i_j\big(t - \tau_{ij}\big)$$

Note that the current at the j-th branch is both delayed and differentiated in order to couple to the i-th branch. This then represents the general NFDE form.

doi: 10.6342/NTU201902629

4.2 Stability Test

When we have a PEEC model, how do we know whether it is a stable model or not? To be specific, what we have at hand are the matrices $\bar{\mathbf{P}}$, $\bar{\mathbf{L}}$, $\mathbf{R}$, and $\mathbf{Y}$, and the source vectors $\mathbf{I}_\mathrm{s}$ and $\mathbf{V}_\mathrm{s}$. In other words, we can write down the complete reduced-MNA equation:

$$\begin{pmatrix} s\bar{\mathbf{P}}^{-1} + \mathbf{Y} & \mathbf{A} \\ \mathbf{A}^\mathrm{T} & -(\mathbf{R} + s\bar{\mathbf{L}}) \end{pmatrix} \begin{pmatrix} \mathbf{\Phi} \\ \mathbf{I} \end{pmatrix} = \begin{pmatrix} \mathbf{I}_\mathrm{s} \\ -\mathbf{V}_\mathrm{s} \end{pmatrix}$$

Note that the center-to-center approximation is adopted, because we aim at performing time domain simulation. Of course, the Galerkin matrices $\mathbf{\Pi}$ and $\mathbf{\Lambda}$ are also available.

The simplest way to check the stability would be just putting the model in SPICE and running transient simulation, to see if the response diverges. This heuristic method has some drawbacks: transient simulation is time-consuming; the simulation time required to observe an unstable resonance is never known in advance; the response of the circuit is also subjected to the numerical stability and numerical damping of the SPICE engine, making the results not very conclusive; and finally from the transient outcome we gain little insight about the PEEC model. In this section, we will review the stability tests in the literature, and propose our own method.

4.2.1 Review of Stability Tests for PEEC

Ruehli, Miekkala, and Heeb [49] consider the MNA equation

$$\mathbf{T}(s) \begin{pmatrix} \mathbf{\Phi} \\ \mathbf{I} \end{pmatrix} = \begin{pmatrix} \mathbf{I}_\mathrm{s} \\ -\mathbf{V}_\mathrm{s} \end{pmatrix}$$

From section 4.1, we know that the roots of det**T**(s) = 0 are the natural frequencies, or poles, of the NFDE system, and their locations determine the stability of the system. In [49], they analytically solve the transcendental equation det**T**(s) = 0 for the special case that consists of only three nodes and two branches, which has only three distinct delays. However, although the resulting **T**(s) is only 5×5, the determinant of **T**(s) is still too complicated to handle, so that the authors have to take the Taylor expansion for all $e^{-s\tau}$ terms to first order. An immediate consequence of this approximation is that det**T**(s) is no longer transcendental, and the number of roots is finite. When the delays are small, it is very likely that the solutions are close to the *ground poles* of the system, while the sky poles are all ignored. Still, the resulting approximated pole location permits the *root locus* study, where one of the three delays was taken as the bifurcation parameter while the other two fixed. Because only a finite subset of the poles are checked, it is a necessary-condition test for stability.

One of the major problem of their approach is that the 1st-order Taylor expansion is valid only for low-frequency and small-scale problems. If, on the other hand, higher-order Taylor terms are retained, the resulting det**T**(s), though a polynomial, would not be any simpler than its original transcendental version.

Garrett, Ruehli, and Paul [50] consider the real part of the input impedance of a one-port PEEC model. According to network theory, if the input resistance is negative at some

doi: 10.6342/NTU201902629

frequencies, then it indicates the model is nonpassive, and thus has the *potential* to be unstable. The one-ports in [50] are all antennas, e.g., patch, loop, and ribbon antenna. This approach, based on checking port responses, can be applied to arbitrary large-scale problems, and the efficiency of the test is very high because frequency response of a circuit can be solved in a very short time. It is, however, not without problems. From the theoretical point of view, passivity of a network will guarantee stability, but failure to be passive does not necessarily imply instability. Hence, it is a (usually very conservative) sufficient-condition test. In addition, the port impedance being a passive response does not necessarily imply the whole network is stable, unless all the natural modes of the circuit are observable at the ports. The observability of a PEEC model from its ports is often assumed *a priori*, because all nodes are capacitively coupled and all branches are inductively coupled together. However, the example in section 4.1 regarding observability shows that even if all components are physically connected, there may still exist some circuit variables such as a particular branch voltage that do not observe all the natural modes. Therefore, a rigorous justification of the observability from the ports is necessary in order to infer network stability from port passivity. This is not a trivial task.

Bellen, Guglielmi, and Ruehli [38] study a model with one single delay, and propose a sufficient condition test based on checking some matrix-norm inequalities. If the inequalities are fulfilled, then the model is stable; else, we know nothing about its stability.

doi: 10.6342/NTU201902629

Sufficient conditions are good for damping design, in that if they are satisfied then stability is guaranteed. However, the method in [38] only considers one single delay, which corresponds to the simplest PEEC model with two nodes and one branch.

Kochetov and Wollenberg [39] propose a transformation approach. As introduced in section 4.1, stability of a delay-free LTI system can be assessed by evaluating the eigenvalues of the system matrix of the state-space description. For a FW PEEC model, Kochetov first transforms all the time delay into an equivalent delayless lumped approximation, specifically lowpass filters. Then the state-space representation of the delay-free approximated model is formulated. The lowpass filter approximation for an ideal delay was

$$e^{-s\tau} \cong \left(\frac{n/\tau}{s+n/\tau}\right)^{n} = \left(1+\frac{s\tau}{n}\right)^{-n}$$

The order n is selected as high as 38 in [39] to make the approximation accurate. Once the state-space model is built, eigenvalues are computed. If there is one eigenvalue in the RHP, then we know the system is unstable. Consequently, it is a necessary-condition test.

Although this method puts no restriction on the number of delays in the model as in [38] and [49], the fact that *each* delay needs a 38th-order lowpass approximation, which roughly enlarge the matrix size by $38n^2$ times, prohibits the application of this method to even medium-scale problems. This may be the reason that the largest example in [39] has only six current cells. In addition, since the state-space matrix is much larger than the

MNA matrix, a lot of fictitious eigenvalues will present, which has little physical meaning.

There are some control-theoretic approaches based on the Lyapunov theorems, to name a few, Yue and Han [51], Antonini and Pepe [52], and Zhang and Han [53]. The basic idea is to seek for a Lyapunov functional for the system, which can be thought of as a generalized energy function that satisfies certain requirements. If a Lyapunov function can be found, then the system is proved to be stable. If we failed to find such a function, however, we know nothing about the stability of the system, which means that it is a sufficient-condition test. The searching of the Lyapunov function is usually put in the form of a linear matrix inequality (LMI). Existing algorithms are then applied to solve the LMI, which can be accomplished by, e.g., the LMI toolbox in MATLAB.

Applying these methods to real PEEC models would encounter the same problem with [39]: computational complexity. First of all, solving a large-scale LMI is computationally expensive. To make the situation worse, the size of the LMI is usually proportional to the *product* of the number of distinct delays and the number of state variables (nodes and branches), which greatly limits on the scalability of these methods. All the examples given in these papers contain only a few number (<15) of distinct delays. Another problem of these approaches is that because the Lyapunov theorem is applicable to general nonlinear systems, the methods often become too mathematically involved that blocks the physical insight. For example, the result of the LMI does not provide any

doi: 10.6342/NTU201902629

information regarding the poles of the PEEC model.

The table below summarizes the key properties of the aforementioned methods. The second column is a brief description of their key spirits, the third column indicates whether their tests are sufficient or necessary for stability, and the fourth column lists the scale of problem that each method is applicable for.

TABLE 4.1
SUMMARY OF EXISTING STABILITY TESTS FOR FW PEEC

Method	Description	Sufficient or Necessary Condition	Applicable Problem Scale
[49]	Analytic pole	Necessary	Small scale
[50]	Input resistance	Sufficient under observability assumption	General large scale
[38]	Matrix-norm inequality	Sufficient	Small scale
[39]	State-space eigenvalue	Necessary	Small to medium scale
[51-53]	Linear matrix inequality	Sufficient	Small to medium scale

We shall distinguish the usage of necessary and sufficient conditions. If we suspect a model is unstable, a necessary-condition test can help us verify that it is indeed unstable, while a sufficient-condition test, if failed, does not provide any conclusive answer. On the other hand, in designing the *damping* to ensure the stability of the model, a sufficient-condition test is preferred, because passing a necessary-condition test does not guarantee stability. It would be best, of course, to have a test that is both sufficient and necessary. However, such tests are scarce. In fact, as pointed out by [44], “many such results merely

doi: 10.6342/NTU201902629

fall into a restatement—in one form or another—of the definition of stability, thus rendering the conditions of little use.”

From the standpoint of PEEC, according to Kochetov’s conjecture [19] that a FW PEEC model is generally unstable if we do not add any damping, a necessary-condition test is preferred for a *raw* PEEC model to reveal its instability, while a sufficient-condition test may be useful for the design of damping. For the first part, i.e., for a raw PEEC model, it is obvious that there is a lack of a necessary-condition test that is applicable for general large-scale problems. Our proposed method in section 4.2.2, indeed, just fulfills this need. For the second part, i.e., the design of damping, the Garrett’s method [50] seems to be a good choice. However, in [50] they only consider one-port networks, and the detailed conditions for being a passive immittance network are not studied. The general method of enforcing stability by passivity will be explored in section 4.4.

4.2.2 Proposed Methodology

The proposed stability test is to numerically find out all the ground poles of the PEEC model. As introduced in Section 4.1, a pole of a PEEC model is a complex number s such that $\det\mathbf{T}(s) = 0$, where $\mathbf{T}(s)$ is the MNA matrix. A ground pole is a pole that also presents in the delay-free model, i.e., by setting all delays equal to zero. When delays are introduced, these ground poles will move, hopefully continuously, around its delay-free

doi: 10.6342/NTU201902629

locations. For the delay-free model, we first put the MNA equation into an eigendecomposition form, and solve the ground poles by conventional matrix diagonalization algorithm. Next, delays are introduced bit by bit, and the ground pole locations are updated accordingly. When the full actual delays are reached, we then have the final values of the ground poles of the FW PEEC model, and any ground poles in the RHP will conclude the instability of the model. It is the fundamental idea of the proposed approach.

The MNA of QS PEEC reads

$$\mathbf{T}_{\mathrm{QS}}(s)\begin{pmatrix}\boldsymbol{\Phi}\\ \mathbf{I}\end{pmatrix} = \begin{pmatrix} s\mathbf{P}^{-1}+\mathbf{Y} & \mathbf{A}\\ \mathbf{A}^{\mathrm{T}} & -(\mathbf{R}+s\mathbf{L})\end{pmatrix}\begin{pmatrix}\boldsymbol{\Phi}\\ \mathbf{I}\end{pmatrix} = \begin{pmatrix}\mathbf{I}_{\mathrm{s}}\\ -\mathbf{V}_{\mathrm{s}}\end{pmatrix}$$

where **P** and **L** are all real matrices. The natural frequencies are where det$\mathbf{T}_{\mathrm{QS}}(s) = 0$. However, this determinant equation is difficult to solve directly. Hence, we make the following transformation:

$$\begin{pmatrix} s\mathbf{P}^{-1}+\mathbf{Y} & \mathbf{A}\\ \mathbf{A}^{\mathrm{T}} & -(\mathbf{R}+s\mathbf{L})\end{pmatrix}\begin{pmatrix}\boldsymbol{\Phi}\\ \mathbf{I}\end{pmatrix} = \begin{pmatrix} s\mathbf{I}_{\mathrm{d}}+\mathbf{YP} & \mathbf{A}\\ \mathbf{A}^{\mathrm{T}}\mathbf{P} & -(\mathbf{R}+s\mathbf{L})\end{pmatrix}\begin{pmatrix}\mathbf{P}^{-1}\boldsymbol{\Phi}\\ \mathbf{I}\end{pmatrix}$$

$$= \begin{pmatrix} -\mathbf{YP}-s\mathbf{I}_{\mathrm{d}} & \mathbf{AL}^{-1}\\ -\mathbf{A}^{\mathrm{T}}\mathbf{P} & -\mathbf{RL}^{-1}-s\mathbf{I}_{\mathrm{d}}\end{pmatrix}\begin{pmatrix}-\mathbf{P}^{-1}\boldsymbol{\Phi}\\ \mathbf{LI}\end{pmatrix} = \left[\begin{pmatrix} -\mathbf{YP} & \mathbf{AL}^{-1}\\ -\mathbf{A}^{\mathrm{T}}\mathbf{P} & -\mathbf{RL}^{-1}\end{pmatrix} - s\mathbf{I}_{\mathrm{d}}\right]\begin{pmatrix}-\mathbf{Q}\\ \mathbf{LI}\end{pmatrix}$$

where we note **Φ** = **PQ**. In this transformation, we need the QS **L** matrix to be invertible. The last equation is in the eigendecomposition form. Define

$$\mathbf{F}_0 = \begin{pmatrix} -\mathbf{YP} & \mathbf{AL}^{-1}\\ -\mathbf{A}^{\mathrm{T}}\mathbf{P} & -\mathbf{RL}^{-1}\end{pmatrix}$$

Then an s makes det$\mathbf{T}_{\mathrm{QS}}(s) = 0$ if and only if it is an eigenvalue of $\mathbf{F}_0$. This result shows that a PEEC model with m charge meshes and n current meshes will have $m + n$ ground poles, counting multiplicity. Because $\mathbf{F}_0$ is a real matrix, complex poles will occur in conjugate pairs. Thus, in the following we will ignore poles with negative imaginary parts.

The MNA of FW PEEC reads

$$\mathbf{T}(s)\begin{pmatrix}\mathbf{\Phi}\\ \mathbf{I}\end{pmatrix} = \begin{pmatrix} s\bar{\mathbf{P}}^{-1} + \mathbf{Y} & \mathbf{A} \\ \mathbf{A}^{\mathrm{T}} & -(\mathbf{R} + s\bar{\mathbf{L}})\end{pmatrix}\begin{pmatrix}\mathbf{\Phi}\\ \mathbf{I}\end{pmatrix} = \begin{pmatrix}\mathbf{I}_{\mathrm{s}}\\ -\mathbf{V}_{\mathrm{s}}\end{pmatrix}$$

The ground poles for the QS case would be taken as the initial guesses to solve the FW case: $\det\mathbf{T}(s) = 0$. The determinant of a large matrix can be easily computed numerically by, e.g., MATLAB subroutine. If we treat the determinant of $\mathbf{T}(s)$ as a single-input-single-output function, $f(s) = \det\mathbf{T}(s)$, then there are numerous root-finding algorithms in the literature that we may apply. One of the most classic method is the Newton's iteration:

$$s_{k+1} = s_k - \frac{f(s_k)}{f'(s_k)}$$

It is known that near a simple root of $f(s)$, i.e., not a repeated root, there exists a region in which the Newton iteration converges to the solution quadratically [54]. Specifically, denote the error of the k-th iteration as $e_k = x_k - x^*$, where x^* is the true solution. Then for e_k sufficiently small, the Newton iteration will have

$$e_{k+1} \cong K e_k^2$$

where K is a constant. For example, if after one iteration, we gain one digit of accuracy. Then after another iteration, we gain two extra digits, resulting in three digits of accuracy. Yet after another iteration, we gain four extra digits, giving total seven digits of accuracy, and so on. Practically, quadratic convergence is considered very fast and desirable.

doi: 10.6342/NTU201902629

To apply Newton's method, however, the exact derivative of $f(s)$ is needed. In our case, since $f(s)$ involves the determinant of a large matrix, the closed-form expressions for $f(s)$ and $f'(s)$ are nearly impossible to obtain. Consequently, although we could numerically compute $f(s)$ by e.g., LU decomposition, we have no access to $f'(s)$. In the literature, the most classic alternative to Newton that does not require the exact derivative of $f(s)$ is the secant method:

$$s_{k+1} = s_k - f(s_k)\frac{s_k - s_{k-1}}{f(s_k) - f(s_{k-1})}$$

Essentially, the secant method approximates $f'(s)$ with the finite difference computed from the last two iterations. Theoretical analysis reveals that the convergence rate of the secant method is superlinear [54]. Specifically, for e_k sufficiently small,

$$e_{k+1} \cong K e_k^{\gamma}$$

where $\gamma = \left(1 + \sqrt{5}\right)/2 \cong 1.618$ is the golden ratio. Consequently, the secant method is still much faster than other linear-convergence methods, though slower than Newton.

For the current problem, we can directly apply the secant method to find the natural frequencies. Indeed, this kind of quasi-Newton methods are often applied to waveguide problems in MoM, in which we also encounter the mathematical form $\det\mathbf{M}(k_c) = 0$, where k_c is the unknown cutoff wavenumber [3], [55]. Here, however, we propose a different approach, whose distinct advantages will be discussed later.

First we note that in the MNA matrix $\mathbf{T}(s)$, the potential matrix $\overline{\mathbf{P}}$ appears in its

doi: 10.6342/NTU201902629

inverse, which prohibits any symbolic manipulation. Therefore, as in the QS case, the following transformation is made:

$$\begin{pmatrix} s\overline{\mathbf{P}}^{-1} + \mathbf{Y} & \mathbf{A} \\ \mathbf{A}^{\mathrm{T}} & -(\mathbf{R} + s\bar{\mathbf{L}}) \end{pmatrix} \begin{pmatrix} \mathbf{\Phi} \\ \mathbf{I} \end{pmatrix} = \begin{pmatrix} s\mathbf{I}_{\mathrm{d}} + \mathbf{Y}\overline{\mathbf{P}} & \mathbf{A} \\ \mathbf{A}^{\mathrm{T}}\overline{\mathbf{P}} & -(\mathbf{R} + s\bar{\mathbf{L}}) \end{pmatrix} \begin{pmatrix} \overline{\mathbf{P}}^{-1}\mathbf{\Phi} \\ \mathbf{I} \end{pmatrix}$$

We note that $\overline{\mathbf{P}}^{-1}\mathbf{\Phi} = \mathbf{Q}$, the charge vector. Hence we call this form the “QI formulation” because the independent variables are **Q** and **I**. This transformation can be interpreted in another way. Suppose in the beginning we take **Q** and **I** as the unknowns, instead of **Φ** and **I** as by MNA. Then the resulting equations would naturally involve no $\overline{\mathbf{P}}^{-1}$, and will be consistent with the standard form of NFDE (4.4). In this regard, the invertibility of the matrix $\overline{\mathbf{P}}$ over the entire RHP becomes irrelevant. Now define

$$\mathbf{F}(s) = \begin{pmatrix} s\mathbf{I}_{\mathrm{d}} + \mathbf{Y}\overline{\mathbf{P}} & \mathbf{A} \\ \mathbf{A}^{\mathrm{T}}\overline{\mathbf{P}} & -(\mathbf{R} + s\bar{\mathbf{L}}) \end{pmatrix}$$

Then, similarly, *s* is a natural frequency if and only if det**F**(*s*) = 0. Here, instead of directly solving det**F**(*s*) = 0, we seek for a scalar *s* and a *normalized* vector **X** such that

$$\mathbf{F}(s)\mathbf{X} = 0$$

If this relation holds, then such *s* makes **F** singular, and is thus a pole. The way we normalize **X** deserves some concern. Since **X** is complex, the natural choice would be $||\mathbf{X}||_2^2 = \mathbf{X}^{\mathrm{H}}\mathbf{X} = 1$. However, the complex conjugate operation is not a holomorphic function, rendering such normalization not complex-differentiable. Hence, we adopt the following less stable but differentiable normalization:

$$\mathbf{e}_K^{\mathrm{T}}\mathbf{X} = 1$$

where $\mathbf{e}_K$ is the K-th standard basis vector, i.e., its K-th component is 1 and all other components 0. This normalization means that we enforce the K-th component of $\mathbf{X}$ to be 1. With this choice, we can write the following system of equation:

$$\mathbf{f}(\mathbf{y}) = \begin{pmatrix} \mathbf{F}(s)\mathbf{X} \\ \mathbf{e}_K^{\mathrm{T}}\mathbf{X} - 1 \end{pmatrix} = 0$$

where $\mathbf{y} = \begin{pmatrix} s \\ \mathbf{X} \end{pmatrix}$. We then apply the *multivariable* Newton's method to solve $\mathbf{f}(\mathbf{y}) = 0$:

$$\mathbf{y}_{k+1} = \mathbf{y}_k - \mathbf{J}(\mathbf{y}_k)^{-1}\mathbf{f}(\mathbf{y}_k)$$

where $\mathbf{J}(\mathbf{y})$ is the Jacobian of $\mathbf{f}(\mathbf{y})$, given by

$$\mathbf{J}(\mathbf{y}) = \left(\frac{\partial f_i}{\partial y_j}\right) = \begin{pmatrix} \dfrac{\partial \mathbf{F}}{\partial s}\mathbf{X} & \mathbf{F}(s) \\ 0 & \mathbf{e}_K^{\mathrm{T}} \end{pmatrix}$$

where $\frac{\partial \mathbf{F}}{\partial s}$ is in elementwise sense. The benefit of the above QI formulation and normalization becomes obvious: we can write down the analytic expression for $\mathbf{J}(\mathbf{y})$, which enables the exact Newton iteration and hence quadratic convergence.

Three conditions are checked sequentially for each $\mathbf{y}_k$ to determine if the Newton iteration can be terminated:

$$\begin{gathered} \frac{\|\mathbf{f}(\mathbf{y}_k)\|_2}{\|\mathbf{F}(s_k)\|_{\mathrm{Fro}}} \leq \varepsilon_1 \\ \frac{\|\mathbf{y}_k - \mathbf{y}_{k-1}\|_2}{\|\mathbf{y}_{k-1}\|_2} \leq \varepsilon_2 \\ k > M \end{gathered}$$

The first condition indicates that $\mathbf{y}_k$ is sufficiently close to the true solution. The relative error is used as the index instead of the absolute value $\|\mathbf{f}(\mathbf{y}_k)\|_2$, because the elements in the matrix $\mathbf{F}(s)$ may be very large, e.g., of order 10^{12}. Due to the inevitable rounding errors, it is more reasonable to require the relative error to be smaller than a tolerance. The Frobenius norm is chosen for the denominator simply because its computation is much faster than the matrix 2-norm. The second condition indicates that the consecutive iterates do not change greatly. The third condition means the number of iteration exceeds a predefined limit. In all the examples to be presented, both ε_1 and ε_2 are about 10^{-9}, while M is roughly 50. However, in most cases, the first condition is fulfilled within only 3 to 6 iterations, due to the rapid convergence of Newton.

Practically, the **P** matrix is in the order of 10^{12}, the **L** matrix is 10^{-9}, and the incidence matrix **A** is of order 1. Thus the **F** matrix has components of significantly different orders of magnitude. To avoid possible numerical error, the following scaling is applied before the Newton iteration:

$$s \to s' = as$$

$$\bar{\mathbf{L}} \to \bar{\mathbf{L}}' = \frac{\bar{\mathbf{L}}}{a}$$

$$\bar{\mathbf{P}} \to \bar{\mathbf{P}}' = a\bar{\mathbf{P}}$$

$$\mathbf{Q} \to \mathbf{Q}' = \frac{\mathbf{Q}}{a}$$

$$\mathbf{T}_\mathrm{P}' = \frac{\mathbf{T}_\mathrm{P}}{a}$$

$$\mathbf{T}_\mathrm{L}' = \frac{\mathbf{T}_\mathrm{L}}{a}$$

where a choice for the scaling coefficient a is

$$a = \sqrt{L_{11}/P_{11}}$$

doi: 10.6342/NTU201902629

The resulting equation to be solved is

$$\mathbf{F}'(s')\mathbf{X}' = \begin{pmatrix} s'\mathbf{I}_\mathrm{d} + \mathbf{Y}\bar{\mathbf{P}}' & \mathbf{A} \\ \mathbf{A}^\mathrm{T}\bar{\mathbf{P}}' & -(\mathbf{R} + s'\bar{\mathbf{L}}') \end{pmatrix} \begin{pmatrix} \mathbf{Q}' \\ \mathbf{I} \end{pmatrix} = 0$$

The termination conditions are modified accordingly. In our program, we all use the scaled parameters, instead of the actual parameters. The $\mathbf{F}_0$ matrix in the QS case, on the other hand, does not need scaling, because $\mathbf{P}$ and $\mathbf{L}^{-1}$ are not very much different in magnitude.

As mentioned earlier, the ground poles of the QS case would be taken as the initial guesses. For the secant method, the pole values are sufficient. But for the proposed multivariate Newton, we also need the initial guesses for the mode vector $\mathbf{X}$. If we denote the computed eigenvectors for the QS case as $\mathbf{X}_\mathrm{QS}$, then the corresponding initial trial for the FW case is given by

$$\mathbf{X}'_0 = \begin{pmatrix} \mathbf{Q}' \\ \mathbf{I} \end{pmatrix}_0 = \begin{pmatrix} -\mathbf{I}_\mathrm{d}/a & 0 \\ 0 & \mathbf{L}^{-1} \end{pmatrix} \mathbf{X}_\mathrm{QS} = \begin{pmatrix} -\mathbf{I}_\mathrm{d}/a & 0 \\ 0 & \mathbf{L}^{-1} \end{pmatrix} \begin{pmatrix} -\mathbf{Q}_\mathrm{QS} \\ \mathbf{L}\mathbf{I}_\mathrm{QS} \end{pmatrix}$$

The initial pole is simply $s'_0 = a s_\mathrm{QS}$.

As mentioned earlier, the normalization $\mathbf{e}_K^\mathrm{T}\mathbf{X} = 1$ is considered less numerically stable. The reason is that if the K-th component of $\mathbf{X}$ happens to be zero, or several orders of magnitude smaller than all the other components, then this normalization may induce significant numerical errors. To avoid this problem, we choose K as the index of the maximum component of the initial mode vector $\mathbf{X}'_0$, i.e.,

$$K = \underset{i}{\operatorname{argmax}}\ |(\mathbf{X}'_0)_i|$$

From experience, this choice of K seldom causes numerical instability.

Theoretically, the Newton's method will converge to a root if the initial guess is sufficiently close to it. However, we never know in advance the exact size of the region of attraction. As a result, to find the poles of the FW PEEC, we add delays into the model gradually, bit by bit. To this end, we introduce the delay-sweeping parameter t, $0 \le t \le 1$,

$$t = \frac{\text{Vacuum speed of light}}{\text{Assumed speed of light}}$$

When $t = 0$, it corresponds to the QS case because the speed of light is assumed to be ∞, and when $t = 1$, it is the FW case. Then, all delays τ_{ij} are replaced with $t\tau_{ij}$. The function of t is exactly the α in (4.6), described in the NFDE part of section 4.1. But for PEEC, it has the special interpretation as the adjustment of the speed of light.

An example choice is $t = 0 : 0.1 : 1$, which means t has a uniform step of 0.1 between 0 and 1. At the beginning, $t = 0$, we solve the eigenvalue and eigenvector of the QS case. Then $t = 0.1$, and the results of QS case are taken as the initial guess for the Newton iteration. Because t is small, i.e., the assumed speed of light is very fast, the *accelerated* FW PEEC is not much different from the QS PEEC, and the resulting ground poles are expected to be close to their QS locations. In such case, Newton iteration will quickly converge to the answer. Next, t marches to 0.2, and the poles and mode vectors for $t = 0.1$ are taken as the initial guess for a new round of Newton iteration. The whole process moves on until $t = 1$. In this manner, we obtain the *root loci* of the ground poles from QS

doi: 10.6342/NTU201902629

PEEC to FW PEEC. The complete algorithm is summarized below.

```
========== Algorithm: Newton Pole Search ==========

Define scaling coefficient $a = \sqrt{L_{11}/P_{11}}$, and $\varepsilon_1 = \varepsilon_2 = 10^{-9}$

Compute $\mathbf{P}' = a\mathbf{P}$, $\mathbf{L}' = \mathbf{L}/a$, $\mathbf{T}_\mathrm{P}' = \frac{\mathbf{T}_\mathrm{P}}{a}$, and $\mathbf{T}_\mathrm{L}' = \frac{\mathbf{T}_\mathrm{L}}{a}$

Form $\mathbf{F}_0 = \begin{pmatrix} -\mathbf{YP} & \mathbf{AL}^{-1} \\ -\mathbf{A}^\mathrm{T}\mathbf{P} & -\mathbf{RL}^{-1} \end{pmatrix}$. Compute its eigenvalues $s_\mathrm{QS}$ and eigenvectors $\mathbf{X}_\mathrm{QS}$.

Discard eigenvalues with negative imaginary parts.

For each eigenvalue and corresponding eigenvector, do

    Compute $s_0' = a s_\mathrm{QS}$, $\mathbf{X}'_0 = \begin{pmatrix} -\mathbf{I}_\mathrm{d}/a & 0 \\ 0 & \mathbf{L}^{-1} \end{pmatrix} \mathbf{X}_\mathrm{QS}$, and $\mathbf{y}_0' = \begin{pmatrix} s_0' \\ \mathbf{X}_0' \end{pmatrix}$

    Compute $K = \underset{i}{\operatorname{argmax}} \ |(\mathbf{X}'_0)_i|$

    For $t$ = 0.1 : 0.1 : 1, do

        Form $\bar{\mathbf{P}}' = \mathbf{P}' \circ \exp(-s_0' t \mathbf{T}_\mathrm{P})$ and $\bar{\mathbf{L}}' = \mathbf{L}' \circ \exp(-s_0' t \mathbf{T}_\mathrm{L})$

        Form $\mathbf{F}_0' = \begin{pmatrix} s_0' \mathbf{I}_\mathrm{d} + \mathbf{Y}\bar{\mathbf{P}}' & \mathbf{A} \\ \mathbf{A}^\mathrm{T}\bar{\mathbf{P}}' & -(\mathbf{R} + s_0' \bar{\mathbf{L}}') \end{pmatrix}$

        Form $\mathbf{f}_0' = \begin{pmatrix} \mathbf{F}'(s_0')\mathbf{X}_0' \\ \mathbf{e}_K^\mathrm{T}\mathbf{X}_0' - 1 \end{pmatrix}$

        For $k$ = 1 : $M$, do

            Form $\mathbf{J}_{k-1}' = \begin{pmatrix} \frac{\partial \mathbf{F}'}{\partial s'}\Big|_{s_{k-1}'} \mathbf{X}_{k-1}' & \mathbf{F}_{k-\mathbf{1}}' \\ 0 & \mathbf{e}_K^\mathrm{T} \end{pmatrix}$

            Solve $\begin{pmatrix} \Delta s \\ \Delta \mathbf{X} \end{pmatrix} = -(\mathbf{J}_{k-1}')^{-1} \mathbf{f}_{k-1}'$

            Store $s_k' = s_{k-1}' + \Delta s$, $\mathbf{X}_k' = \mathbf{X}_{k-1}' + \Delta \mathbf{X}$, and $\mathbf{y}_k' = \begin{pmatrix} s_k' \\ \mathbf{X}_k' \end{pmatrix}$

            Form $\bar{\mathbf{P}}' = \mathbf{P}' \circ \exp(-s_k' t \mathbf{T}_\mathrm{P})$ and $\bar{\mathbf{L}}' = \mathbf{L}' \circ \exp(-s_k' t \mathbf{T}_\mathrm{L})$
```

Form $\mathbf{F}_k' = \begin{pmatrix} s_k'\mathbf{I}_\mathrm{d} + \mathbf{Y}\overline{\mathbf{P}}' & \mathbf{A} \\ \mathbf{A}^\mathrm{T}\overline{\mathbf{P}}' & -(\mathbf{R} + s_k'\overline{\mathbf{L}}') \end{pmatrix}$

Form $\mathbf{f}_k' = \begin{pmatrix} \mathbf{F}'(s_k')\mathbf{X}_k' \\ \mathbf{e}_K^\mathrm{T}\mathbf{X}_k' - 1 \end{pmatrix}$

If one of the following conditions is satisfied, then break.

$$\frac{\|\mathbf{f}_k'\|_2}{\|\mathbf{F}_k'\|_\mathrm{Fro}} \leq \varepsilon_1$$

$$\frac{\|\mathbf{y}_k' - \mathbf{y}_{k-1}'\|_2}{\|\mathbf{y}_{k-1}'\|_2} \leq \varepsilon_2$$

Store $s_0' \leftarrow s_k'$, $\mathbf{X}_0' \leftarrow \mathbf{X}_k'$, and $\mathbf{y}_0' = \begin{pmatrix} s_0' \\ \mathbf{X}_0' \end{pmatrix}$

Rescale back: $s_\mathrm{pole} = \frac{s_0'}{a}$ and $\begin{pmatrix} \mathbf{\Phi} \\ \mathbf{I} \end{pmatrix}_\mathrm{mode} = \begin{pmatrix} \overline{\mathbf{P}}' & 0 \\ 0 & \mathbf{I}_\mathrm{d} \end{pmatrix}\mathbf{X}_0'$

========== End of Newton Pole Search ==========

For completeness, we also document the expression for $\frac{\partial \mathbf{F}}{\partial s}$:

$$\frac{\partial \mathbf{F}'}{\partial s'} = \begin{pmatrix} \mathbf{I}_\mathrm{d} - \mathbf{Y}(\overline{\mathbf{P}}' \circ \mathbf{T}_\mathrm{P}'t) & 0 \\ -\mathrm{A}^\mathrm{T}(\overline{\mathbf{P}}' \circ \mathbf{T}_\mathrm{P}'t) & -\overline{\mathbf{L}}' + s'(\overline{\mathbf{L}}' \circ \mathbf{T}_\mathrm{L}'t) \end{pmatrix}$$

4.2.3 Verification

The proposed algorithm is written in MATLAB. To verify the correctness of the program, we consider the following situation. If a FW PEEC model has only one pair of complex conjugate poles in the RHP, denoted as $s_0 = \sigma_0 \pm j\omega_0$, then ultimately the time domain response of any circuit variable, of any input, will be dominated by

$$x(t) \to A_0 e^{\sigma_0 t}\cos(\omega_0 t + \phi_0)$$

for some constant A_0 and ϕ_0. In such case, we can estimate ω_0 from the period of oscillation in time domain, and estimate σ_0 from the rate of increase of the envelope. It is important that only one pair of poles are in RHP. If there are more than one pair, then the time domain response will be the mixing of their natural responses, making the estimation more difficult.

We consider the example of a coplanar strip transmission line shown in Fig. 4.3. The characteristic impedance is 305 Ω calculated by ANSYS 2D Extractor. Here in PEEC, each strip is partitioned into N current meshes and N+1 charge meshes. Both ends of the transmission line are terminated by 100 Ω resistors. In fact, this example is the third test case in [52], in which the authors have verified through their Lyapunov functional that this structure is stable for $N = 1$. Taking this result as reference, we first plot the ground poles of the coplanar strips also for $N = 1$, as shown in Fig. 4.4. The horizontal and vertical axes are the real and imaginary parts of the poles, respectively. Their units are in fact the same. However, by convention we denote the unit of the real part as Nepers-per-second, while for the imaginary part it is rad-Hz.

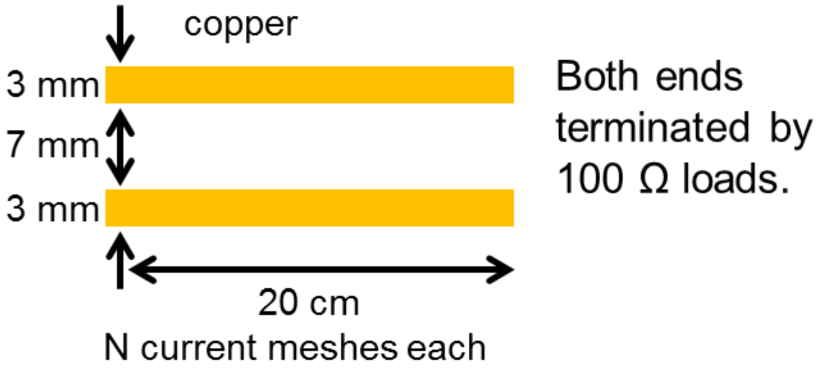

Fig. 4.3. Coplanar strip transmission line.

doi: 10.6342/NTU201902629

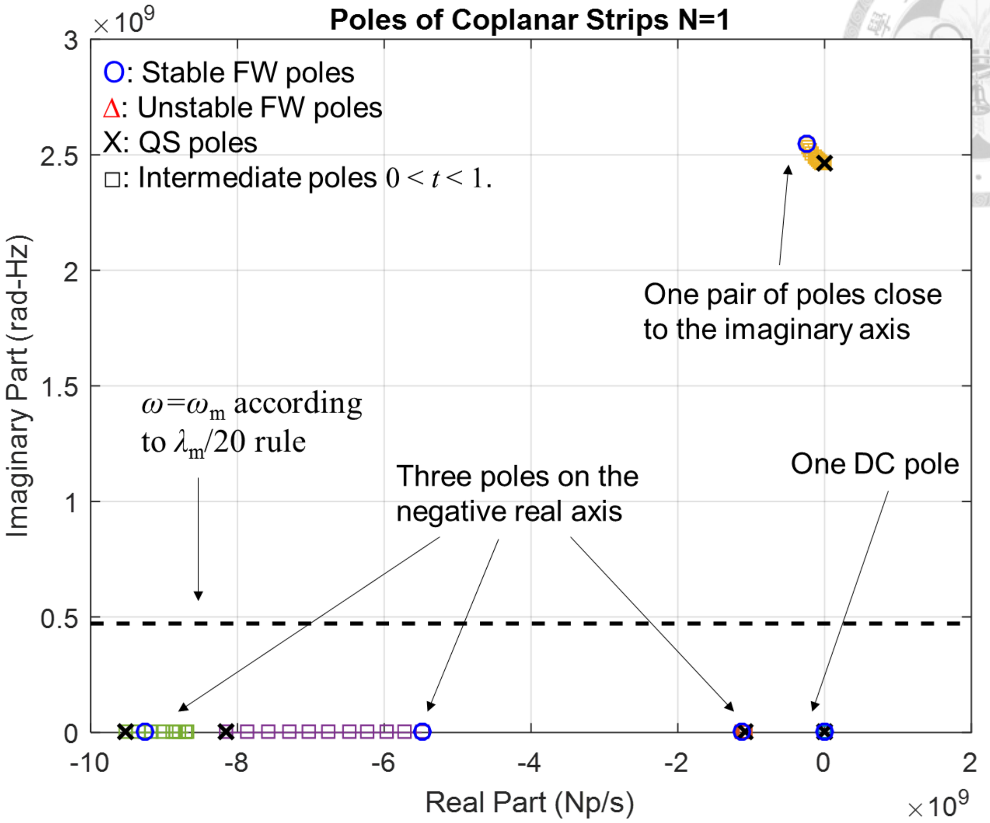

Fig. 4.4. Ground poles of the coplanar strip transmission line with $N = 1$.

For $N = 1$, the L matrix is 2-by-2 and the P matrix is 4-by-4. Thus there are only six ground poles. As shown in the figure, we find three poles on the negative real axis, one DC pole, and one pair of poles close to the imaginary axis. The horizontal dashed line indicates the maximum frequency of interest $\omega = \omega_m$, according to the $\lambda_m/20$ rule. The QS poles are denoted as a thick X, while the FW poles are either an O or a Δ, which indicate stable (in LHP) or unstable (in RHP) poles, respectively. The □'s between QS and FW poles indicate the intermediate poles obtained during $0 < t < 1$. In other words, they form the root loci of the poles. For the $N = 1$ case, all ground poles are stable, which is consistent with the Lyapunov results of [52]. The proposed method only takes 0.027 s to obtain all the ground poles, on a PC with Intel i7-2600 CPU and 16 GB RAM. Although a direct comparison of computation time is absolutely unfair, we still point out that it took 4.25 s to solve the LMI in [52], for the same structure.

Next, we consider the case N = 10, which gives 42 ground poles. MATLAB takes 0.38 s to obtain the results shown in Fig. 4.5, where 19 pairs of conjugate poles and 4 real poles are found. Only two real poles are shown in the figure, because the other two are deep into LHP. In this case, there is one pair of RHP poles located at $\sigma_0 \pm j\omega_0$ = 2.459e7 ± j 2.97e10. If the calculation is correct, we would expect to see unstable resonance in transient simulation.

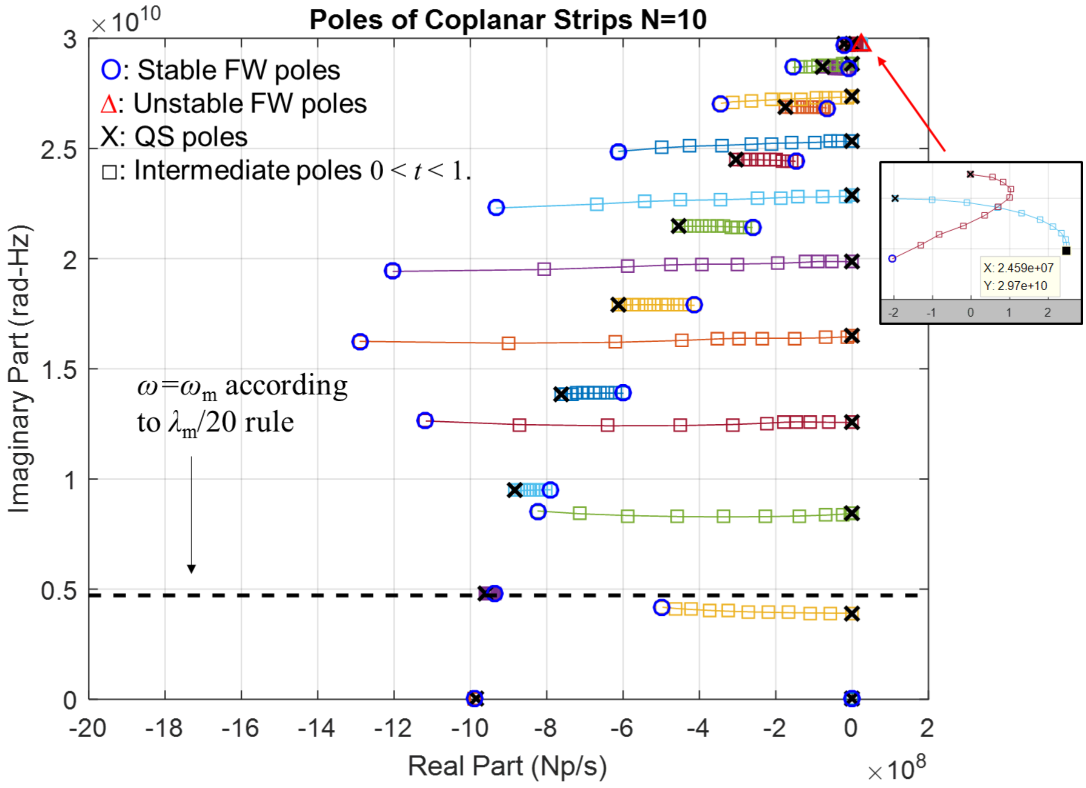

Fig. 4.5. Ground poles of the coplanar strips with N = 10.

doi: 10.6342/NTU201902629

To verify the above results, the *N* = 10 PEEC model is exported into a subcircuit file using the method described in Chapter 3, and loaded into Keysight ADS, as shown in the following figure. A short pulse current source with pulsewidth 1 ns and rise/fall time 0.1 ns is used to excite the circuit. The maximum time step is set to be 10 ps so that the poles at the GHz band can reveal themselves.

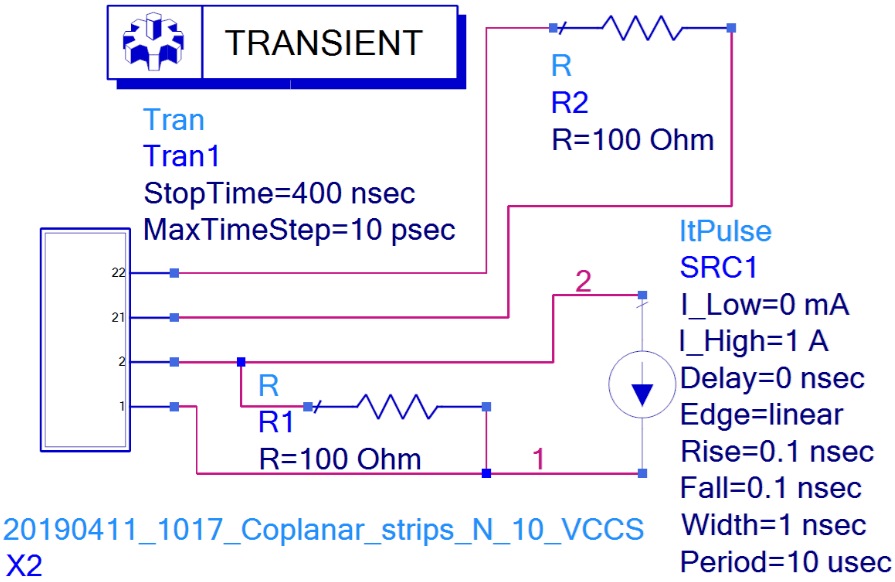

Fig. 4.6. ADS simulation setup of the coplanar strips with *N* = 10.

The voltage difference between nodes 1 and 2 labeled in the above figure is shown in Fig. 4.7 (a), along with the input voltage of an ideal 305 Ω transmission line with the same load impedances and excitation for comparison. Good agreement is observed, verifying the accuracy of the PEEC model. Up to 10 ns, there seems no sign for instability, so we continue transient simulation to 400 ns. The voltage of node 1 is shown in Fig. 4.7 (b). Indeed, the late-time instability strikes.

doi: 10.6342/NTU201902629

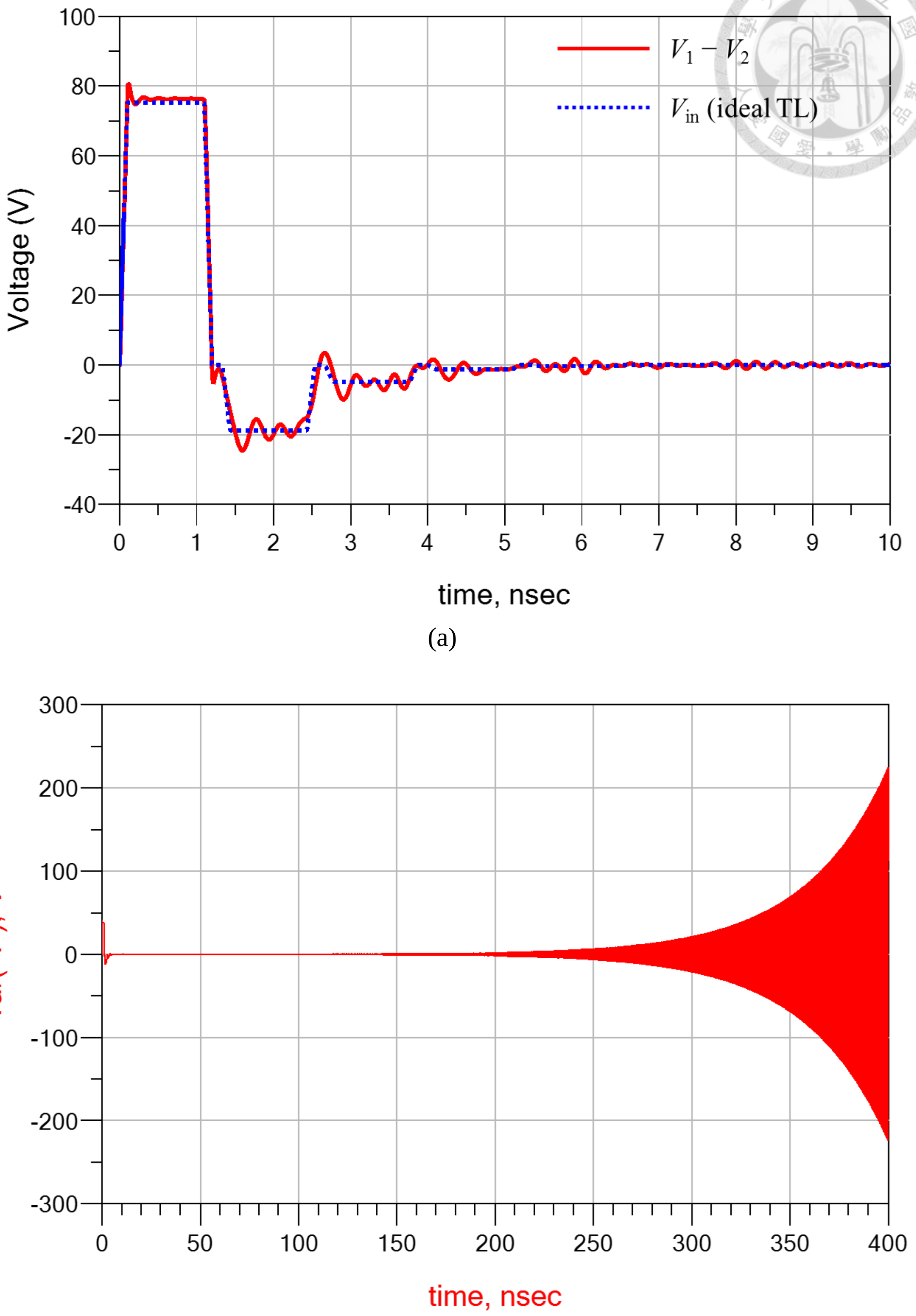

(a)

(b)

Fig. 4.7. (a) Transient ($V_1 - V_2$) of the coplanar strips with $N = 10$, in comparison with the input voltage of an ideal 305 Ω transmission line up to 10 ns. (b) Transient voltage of node 1 of the coplanar strips with $N = 10$ up to 400 ns.

doi: 10.6342/NTU201902629

The real and imaginary parts of the RHP pole, if there is only one RHP pole pair, can be estimated from the waveform between 200 ns and 400 ns. We first enlarge the waveform between 200 ns and 203 ns as shown in Fig. 4.8. The duration for ten periods of oscillation is read out to estimate ω_0, which gives ω_0 = 2.936e10 rad-Hz. Compared with the predicted value by Newton search, the error is only 1.16 %.

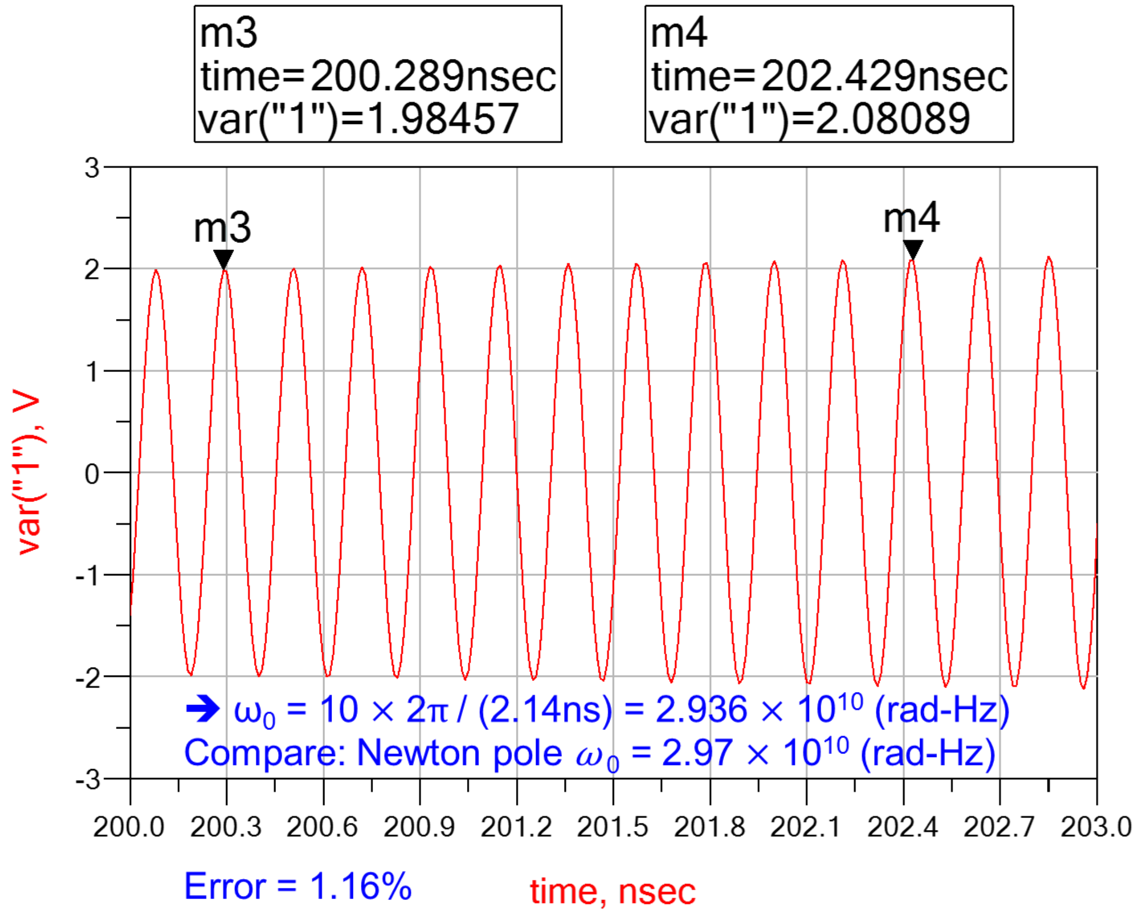

Fig. 4.8. Transient voltage of node 1 of the coplanar strips between 200 and 203 ns.

Next, we take the natural logarithm of the absolute value of the waveform, whose slope corresponds to σ_0. The result is shown in Fig. 4.9. The error is only 3.8 %.

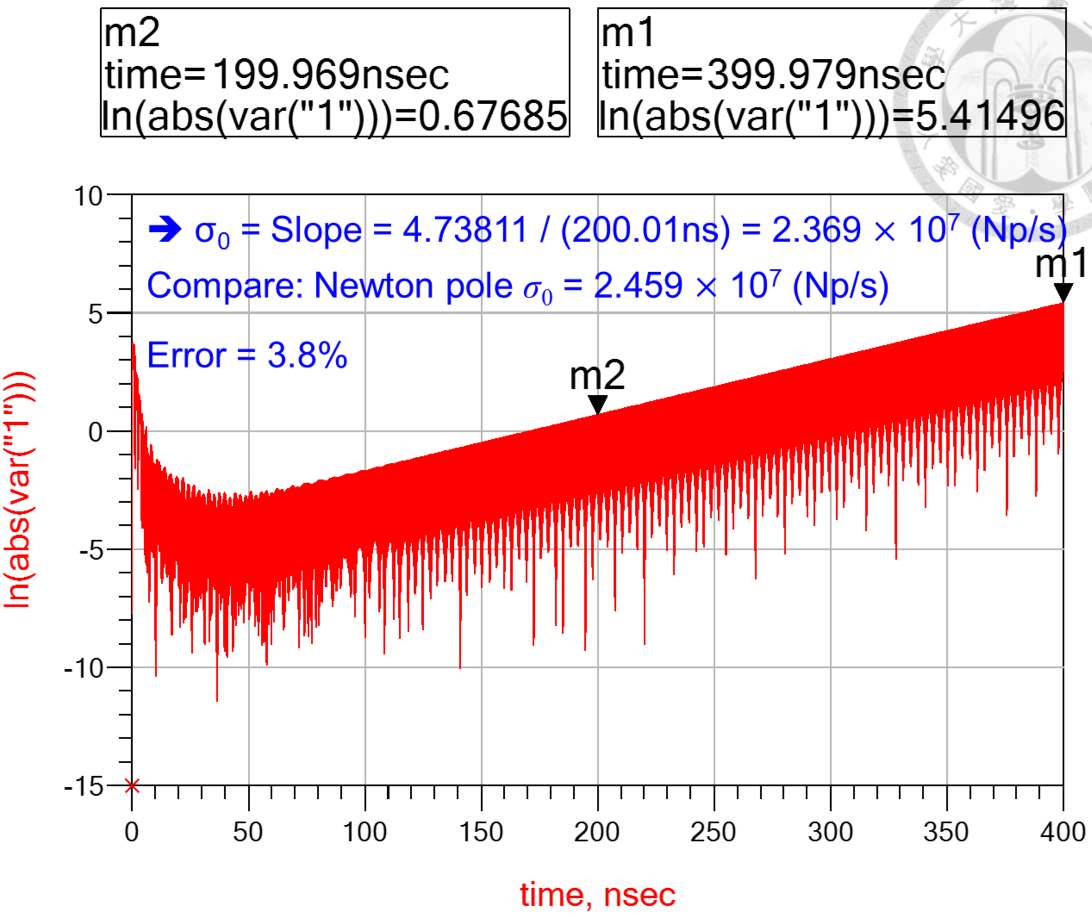

Fig. 4.9. Log-abs value of transient voltage of node 1 of the coplanar strips.

In summary, the above example has verified that the proposed Newton search algorithm produces reliable pole locations, and can be used to judge the stability of the FW PEEC model.

This $N = 10$ case is also useful to exemplify the effect of numerical damping that was mentioned in section 4.1. As previously verified, it is an unstable model. However, suppose we deliberately increase the maximum timestep of transient simulation to 100 ns, which is 10000 times larger than our previous simulation, as shown in Fig. 4.10. The current source is slowed down accordingly. Then we find out that the unstable pole is completely suppressed out and the waveform is far from unstable even up to 10 us. This clearly demonstrates the effect of numerical damping.

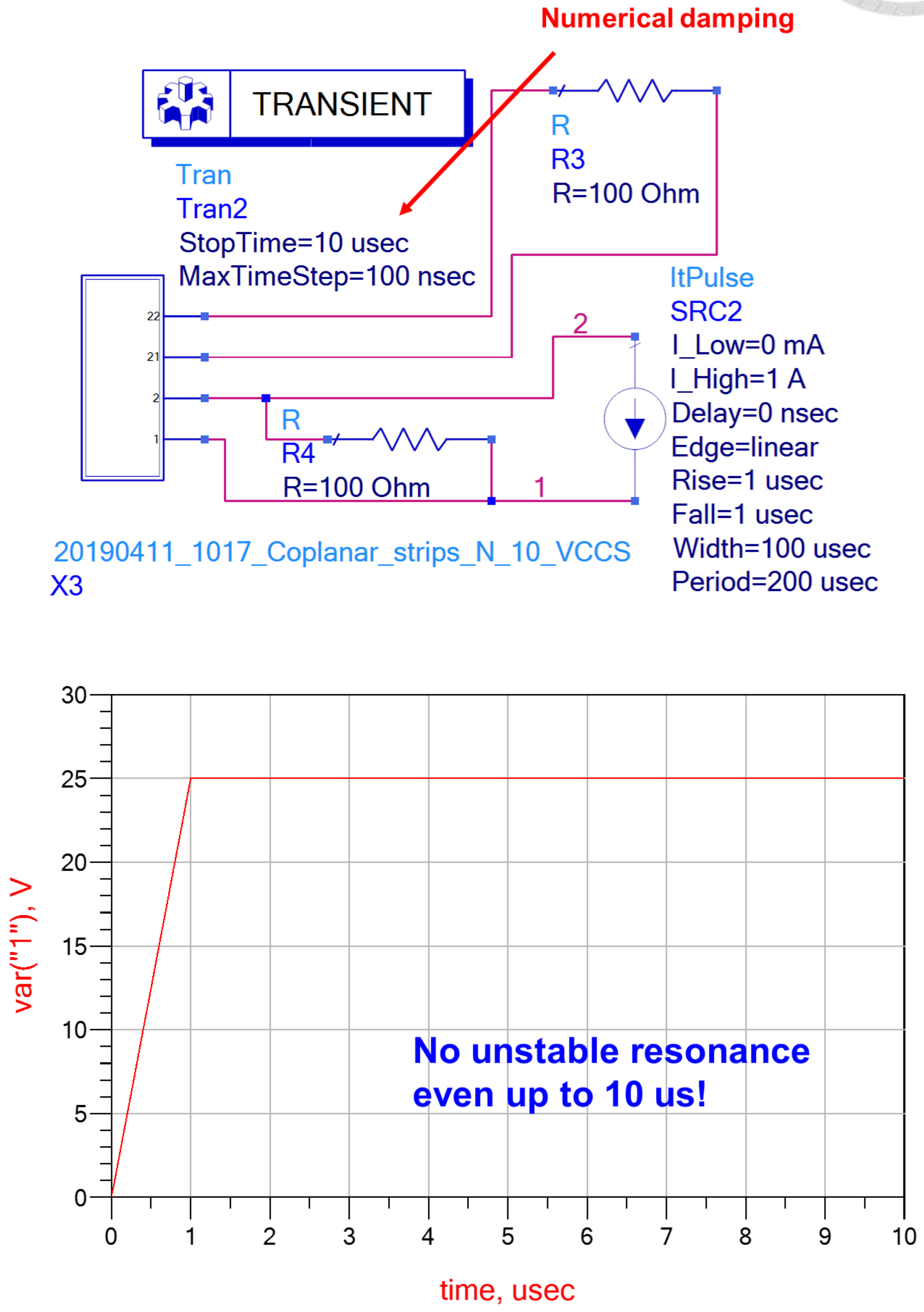

Fig. 4.10. ADS simulation of the coplanar strips with $N = 10$ demonstrating the effect of numerical damping achieved by very large time step.

doi: 10.6342/NTU201902629

4.2.4 Examples and Discussion

In this section, several pole plots will be displayed, in an attempt to provide a basic understanding of the stability property of an undamped FW PEEC model. First, we continue considering the coplanar strip transmission line. It is known that it is stable for N = 1, unstable for N = 10. What if we keep increasing the discretization? The ground poles with N = 100 are shown in Fig. 4.11, which takes MALTAB 138.19 s to complete. Again, some poles far to the left are not shown in the figure. In this case, the MNA matrix is 402×402, and there are more than 200 different delay values. In the literature, except Garrett’s indirect method [50], there has been no any approaches that could determine the stability for models of such a scale.

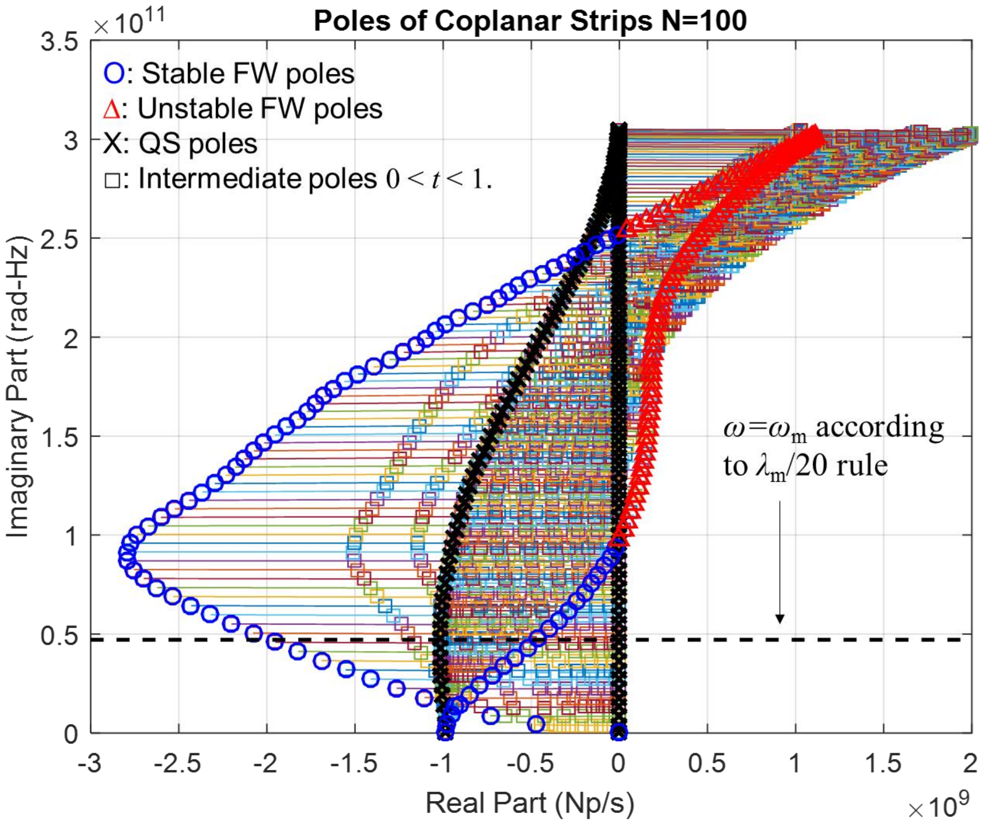

Fig. 4.11. Ground poles of the coplanar strips with N = 100.

The results clearly show that the model is unstable, in fact, extremely unstable: a considerable number of poles are in RHP. When delays are introduced, we observe some QS poles move left, while some move right. For low frequency poles, most of them go left, but for frequency higher than f_m, a lot of poles go right in the first place. If their QS locations happen to be close to the imaginary axis, they might go into RHP even with tiny delays.

It is conjectured by Kochetov and Wollenberg [39] that "increasing the discretization precision will never help to obtain a stable solution." The coplanar strip example presented here supports this statement. A detailed discussion for this behavior will be left to the next section.

The theory of NFDE says that there is an infinite number of poles, and together they determine the stability of the system. In addition, the characteristic roots of the associated difference equation will present vertical lines of attraction, toward which some NFDE poles (in particular, sky poles) asymptotically approach. From the proposed method, we do not know where the sky poles locate, and we do not consider the roots of the ADE. However, we see that for a FW PEEC model with little damping, very often the ground poles already cause instability.

By "damping", we mean those additional unphysical resistors or lowpass filters added to the model that aim merely at improving the stability, to be studied in detail in

doi: 10.6342/NTU201902629

section 4.4. The conductor loss **R** and port resistors **Y** in the coplanar strip example, though provide a certain amount of *damping*, turn out not be able to pull all the ground poles left, not to mention the sky poles.

It is worth considering the associated difference equation of a FW PEEC model. From the MNA equation

$$\begin{pmatrix} s\bar{\mathbf{P}}^{-1}+\mathbf{Y} & \mathbf{A} \\ \mathbf{A}^{\mathrm{T}} & -(\mathbf{R}+s\bar{\mathbf{L}}) \end{pmatrix}\begin{pmatrix} \mathbf{\Phi} \\ \mathbf{I} \end{pmatrix}=\begin{pmatrix} \mathbf{I}_{\mathrm{s}} \\ -\mathbf{V}_{\mathrm{s}} \end{pmatrix}$$

due to the presence of $\bar{\mathbf{P}}^{-1}$, we cannot easily identify its characteristic quasipolynomial. However, from the QI formulation,

$$\mathbf{F}(s)\begin{pmatrix} \mathbf{Q} \\ \mathbf{I} \end{pmatrix}=\begin{pmatrix} s\mathbf{I}_{\mathrm{d}}+\mathbf{Y}\bar{\mathbf{P}} & \mathbf{A} \\ \mathbf{A}^{\mathrm{T}}\bar{\mathbf{P}} & -(\mathbf{R}+s\bar{\mathbf{L}}) \end{pmatrix}\begin{pmatrix} \mathbf{Q} \\ \mathbf{I} \end{pmatrix}=\begin{pmatrix} \mathbf{I}_{\mathrm{s}} \\ -\mathbf{V}_{\mathrm{s}} \end{pmatrix}$$

we readily see that the characteristic quasipolynomial is given by det**F**(s). Further, rewrite

$$\det\begin{pmatrix} s\mathbf{I}_{\mathrm{d}}+\mathbf{Y}\bar{\mathbf{P}} & \mathbf{A} \\ \mathbf{A}^{\mathrm{T}}\bar{\mathbf{P}} & -(\mathbf{R}+s\bar{\mathbf{L}}) \end{pmatrix}=\det\left[s\begin{pmatrix} \mathbf{I}_{\mathrm{d}} & 0 \\ 0 & -\bar{\mathbf{L}} \end{pmatrix}+\begin{pmatrix} \mathbf{Y}\bar{\mathbf{P}} & \mathbf{A} \\ \mathbf{A}^{\mathrm{T}}\bar{\mathbf{P}} & -\mathbf{R} \end{pmatrix}\right]$$

Compared with (4.5) in section 4.1, we conclude that the characteristic equation of the ADE is given by

$$\det\Delta_0(s)=\det\begin{pmatrix} \mathbf{I}_{\mathrm{d}} & 0 \\ 0 & -\bar{\mathbf{L}} \end{pmatrix}=\det(-\bar{\mathbf{L}})=0$$

In other words, the characteristic equation of the ADE is simply the determinant of the inductance matrix! From the definition of $\bar{\mathbf{L}}$ and the Gershgorin theorem, we immediately know that the ADE will not have deep RHP poles. In fact, all poles will be on the left of a particular vertical line, which can be determined from the off-diagonal row sums and the diagonal elements, according to Gershgorin. However, for large scale problems where **L** is not diagonally dominant, this vertical line is still in RHP, and we cannot guarantee its stability just from Gershgorin arguments. Note that the characteristic equation is in the same form of det**F**(s) = 0. Hence, we can apply the same Newton iteration to find the roots. The difficulty, however, is that we do not have a good initial guess. When the delays are zero, **L** is a constant matrix, independent of s. Thus we have no way of knowing where the poles and mode vectors approximately locate. To implement Newton, we can only use random initial trials. Nevertheless, as long as the algorithm converges, we can still obtain some characteristic roots of the ADE, which also serves as a necessary condition test for the stability of the NFDE system. For the coplanar strip example with N = 10, we select 100 random mode vectors as the initial guesses, while the initial poles are all in the RHP. The results of Newton search is shown in Fig. 4.12. In this run, 41 of the 100 trials converge, which means that they satisfy the condition

$$\frac{\left\| \begin{pmatrix} \bar{\mathbf{L}}(s_k)\mathbf{X}_k \\ \mathbf{e}_K^{\mathrm{T}}\mathbf{X}_{\boldsymbol{k}} - \mathbf{1} \end{pmatrix} \right\|_2}{\|\bar{\mathbf{L}}(s_k)\|_{\mathrm{Fro}}} \leq \varepsilon_1$$

All converged poles are stable, as indicated from the figure.

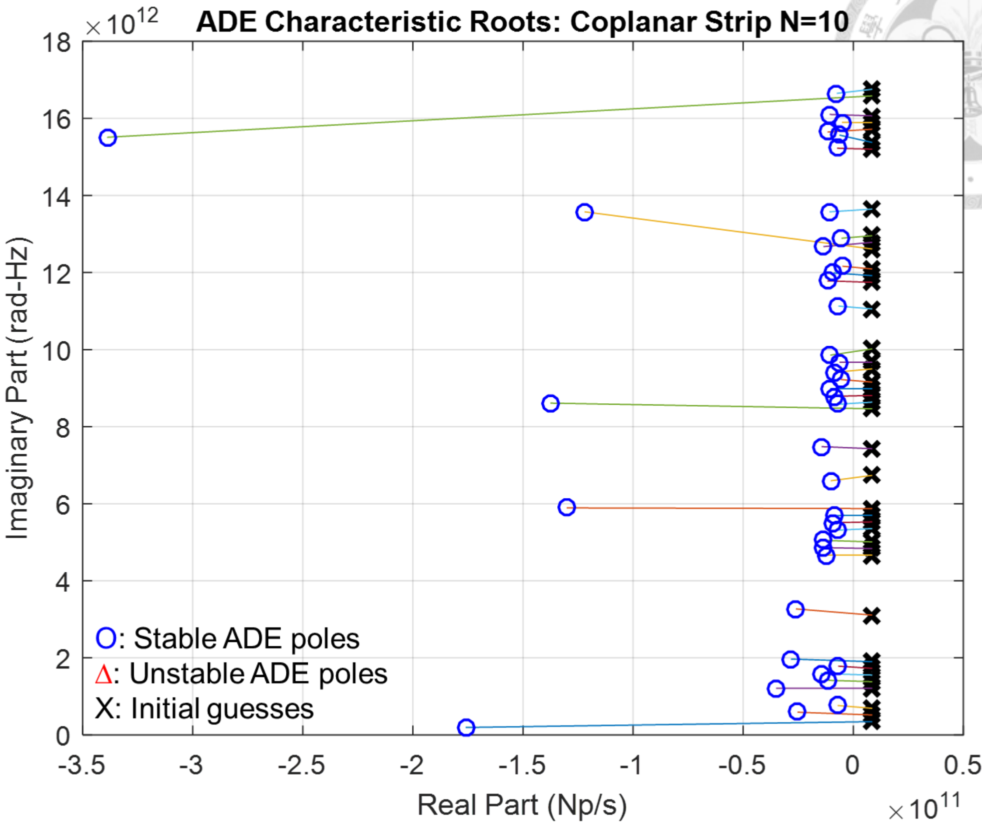

Fig. 4.12. Characteristic roots of the associated difference equation of the coplanar strips with $N = 10$.

Although the ADE pole search is a necessary condition test for the NFDE stability, in the following we will not consider the ADE anymore, except when unstable ADE poles are found. From experience, for an undamped PEEC model, the ground poles are usually the main cause of instability, instead of the sky poles.

We now go back to the NFDE poles. Before considering a new example, we take a look at the locations of the QS poles, which are the eigenvalues of $\mathbf{F}_0$. In the coplanar strip example, roughly half of the QS poles are close to the imaginary axis, while the other half inside LHP. In fact, when the model is lossless, i.e., both $\mathbf{R} = 0$ and $\mathbf{Y} = 0$, all the poles will be exactly on the imaginary axis, i.e., all the eigenvalues of $\mathbf{F}_0$ have zero real

doi: 10.6342/NTU201902629

parts. This is a subtle point that cannot be seen easily from the form of $\mathbf{F}_0$. To show this, we recall that a natural frequency of a circuit is such that there exists a solution of the form $\mathbf{x}(t) = \mathbf{x}_0\exp(s_i t)$. Now, a lossless QS model can be represented as real inductors and capacitors. For such a circuit, we cannot have all node voltages and branch currents decay in magnitude at the same time, nor amplify. Consequently, the only possible values of the natural frequencies would be purely imaginary, resulting in an oscillation with constant amplitude. For a lossy model, **R** represents conductor loss, while **Y** represents additional lumped resistors. If the conductor is copper, then **R** is usually too small such that the presence of **R** only slightly shift the ground poles into LHP, but still close to the imaginary axis. The lumped resistors **Y**, though may be as large as 50 Ω, is usually very sparse, i.e., only a few lumped resistors are connected to a few nodes of the model. In the coplanar strip example, the addition of **Y** causes some poles to appear on the negative real axis and some move left, while leaving half of the poles to remain close to the imaginary axis. Consequently, when delays are introduced, the directions of moving of those poles that are initially close to the imaginary axis become very important. As it turns out, some poles may go right ever from the beginning, into the RHP, and result in instability.

As a verification, the case $N = 10$ with $\mathbf{R} = 0$ and $\mathbf{Y} = 0$ is shown in Fig. 4.13. Indeed, all the QS poles are on the imaginary axis, and the highest-frequency one goes to RHP in the beginning.

doi: 10.6342/NTU201902629

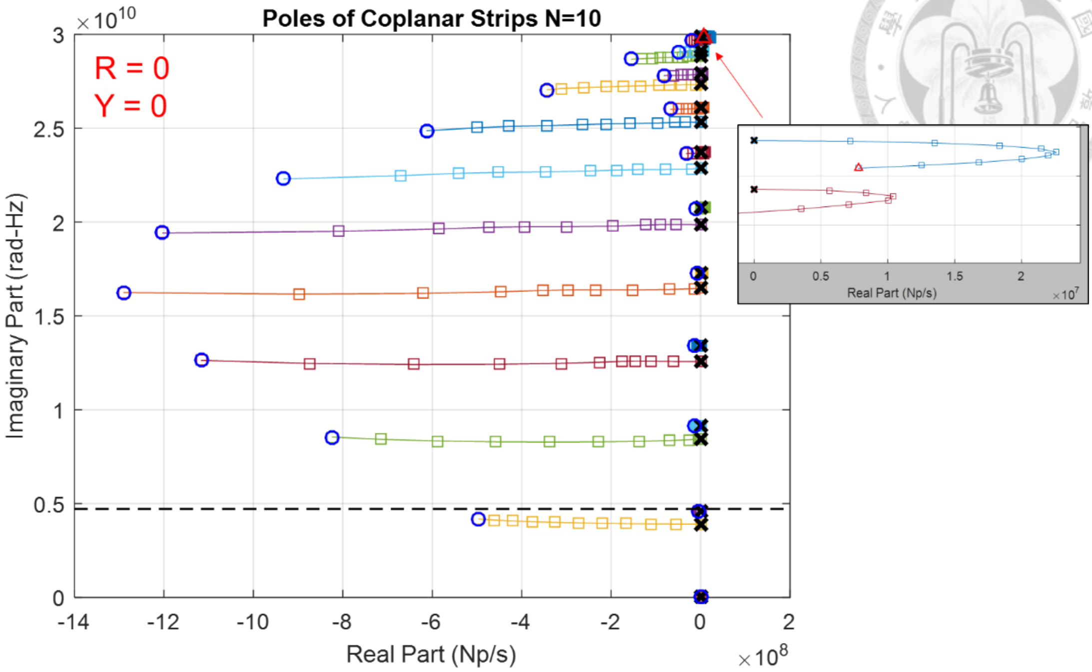

Fig. 4.13. Ground poles of the coplanar strips with $N = 10$, lossless ($\mathbf{R} = 0$), and no termination ($\mathbf{Y} = 0$).

The same case when $\mathbf{R} \neq 0$, but $\mathbf{Y}$ is still 0, is shown in Fig. 4.14. Compared with the R = 0 case, very little difference can be observed. Each QS pole only assumes a very small real part.

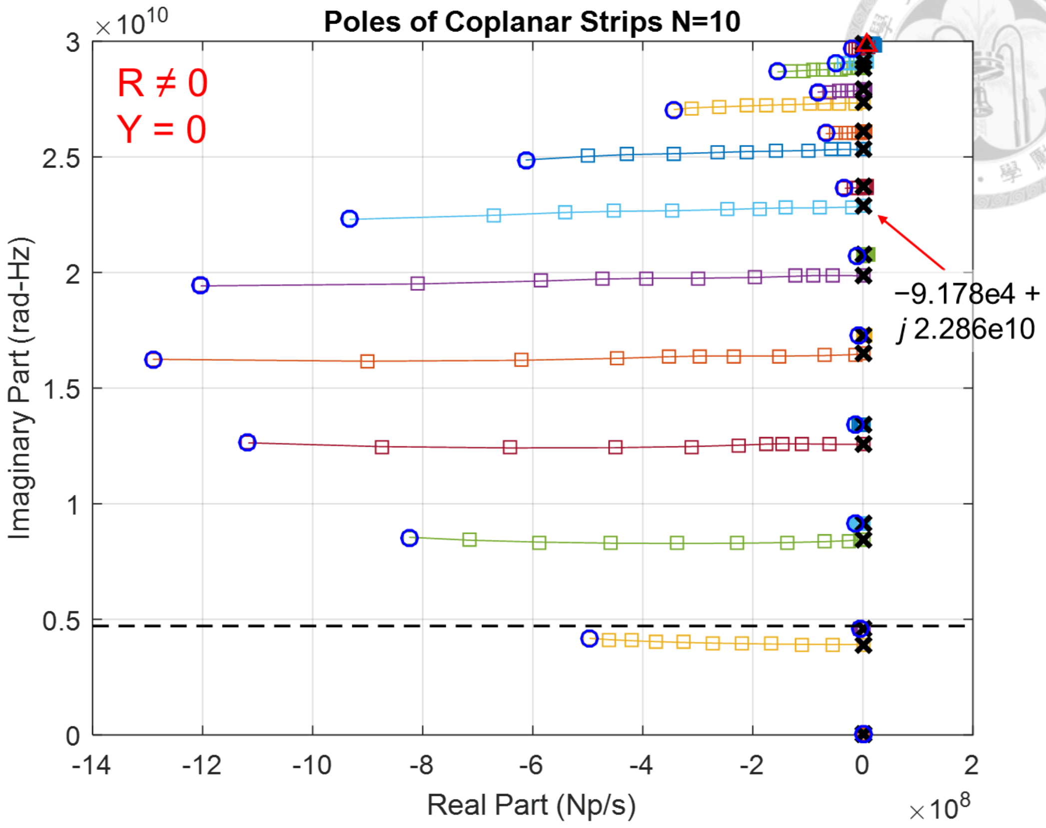

Fig. 4.14. Ground poles of the coplanar strips with N = 10 and no termination (**Y** = 0).

There is one point worth comparing between Fig. 4.5 and Figs. 4.13 and 4.14: the DC pole. In Fig. 4.13 as well as 4.14, there is a double pole at DC (s = 0), while in Fig. 4.5, there is a simple pole at DC and a pole at negative real axis. As pointed out by Chua [7], there are three possible situations that a circuit may have a DC pole. The first one is when the circuit has a capacitor *cut set*. The second is when the circuit has an inductor *loop*. The third one is for certain controlled-source topologies. The PEEC model here belongs to the first category. A *cut* is a partition of the nodes of the circuit into two disjoint subsets. A *cut set* is a set of branches of the circuit that forms a cut, with the endpoints of each branch in the cut set belonging to different subsets. Recall the definition of pole, or

doi: 10.6342/NTU201902629

natural frequency: s is a pole if there exists a nontrivial $\mathbf{w}_0$ such that the circuit has the response $\mathbf{w}_0\exp(st)$. If there is a cut set formed by capacitors, then there is a natural mode in which one subset of the nodes assumes one single voltage and the other subset assumes another voltage. Because at DC, capacitors are open, such voltage distribution can sustain, thus forming a *mode*. Now, for the PEEC model, there is at least one capacitor cut set, which is the partition between the ground node and all the other nodes. If the coplanar strips are not terminated by resistors, i.e., $\mathbf{Y} = 0$, then there is another capacitor cut set, which is the partition between the two strips. These two capacitor cut sets are reflected by the double poles at DC in Figs. 4.13 and 4.14. For the terminated case in Fig. 4.5, one DC pole is moved to the negative real axis, which corresponds to RC discharge between the two strips. The other DC pole remains, which corresponds to the mode where both strips have the same nonzero voltage. This behavior can be verified by observing the mode vectors $\begin{pmatrix}\boldsymbol{\Phi}\\ \mathbf{I}\end{pmatrix}_{\mathrm{mode}}$ obtained as a byproduct of the Newton pole search. Also, since this behavior does not depend on the presence of time delay, these DC poles does not form root loci during the light speed sweep. Finally, we remind that double poles on the imaginary axis do not necessarily imply instability. Since there are obvious independent vectors of voltage distribution corresponding to the DC poles, these multiple imaginary-axis poles will not destabilize the system.

Next, we consider the strip dipole antenna presented in Chapters 2 and 3. It was found to be an unstable circuit through SPICE simulation in Chapter 3. Here, the ground poles for the $N = 20$ case are calculated through the Newton search, as shown in Fig. 4.15. Two unstable poles are found, one at $f = 37.8$ GHz and the other slightly higher. This is consistent with the transient simulation results in Chapter 3. In this example, we see that low frequency poles go left when delays are introduced. In other words, delay induces power loss. As studied in Chapter 2, the lost power goes to radiation. This is, however, not the case for high frequency poles. Most high frequency poles go right, and the two highest frequency ones stay in RHP.

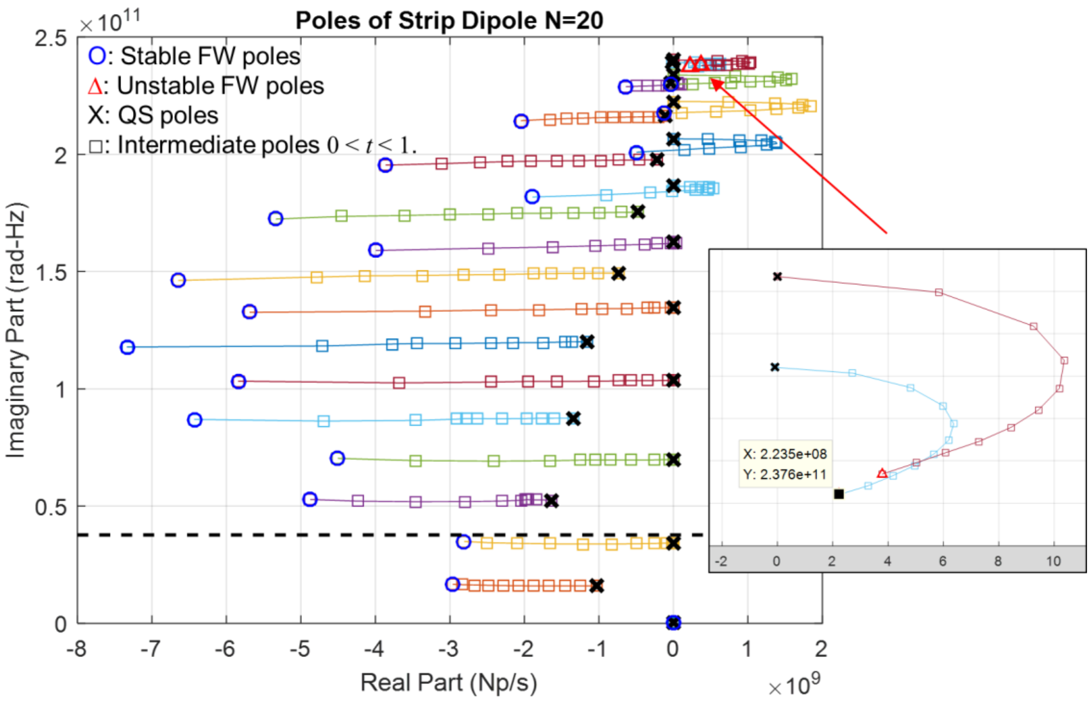

Fig. 4.15. Ground poles of the strip dipole antenna with $N = 20$.

We also plot the poles of strip dipole for the $N = 32$ case, as shown in Fig. 4.16. Again, we see that increasing discretization does not improve the stability: more RHP poles come out. It is also interesting to note that, in all the examples presented so far, most of the unstable poles tend to occur in the frequency range $3f_{\mathrm{m}}$ to $6f_{\mathrm{m}}$, where f_{m} is based on the $\lambda_{\mathrm{m}}/20$ rule. At $f = 5f_{\mathrm{m}}$, the distance between neighboring meshes reaches $\lambda/4$, i.e., quarter wavelength.

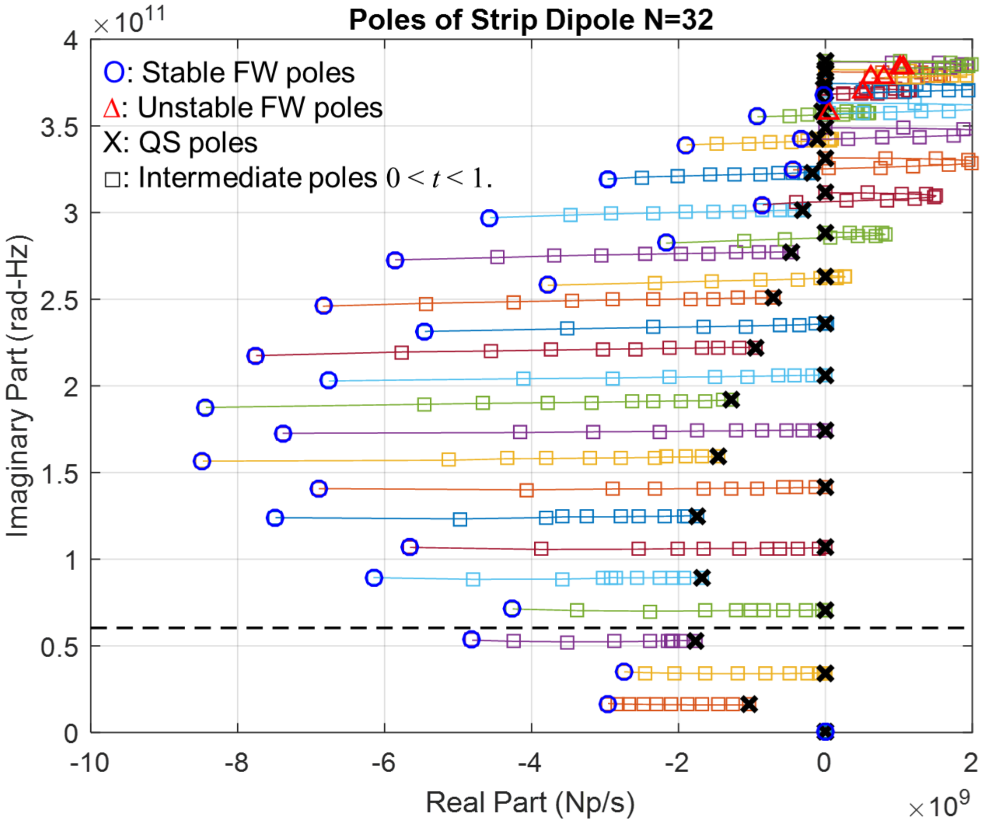

Fig. 4.16. Ground poles of the strip dipole antenna with $N = 32$.

Before ending this section, we give some comparison between the proposed Newton method and the classic secant method as described in Section 4.2.2, in terms of computational complexity, numerical stability, and the ability to resolve two closely-spaced poles.

First, we compare the complexity of the two methods. In each Newton iteration, a linear equation has to be solved: $\mathbf{J}(\mathbf{y}_k)(\mathbf{y}_{k+1} - \mathbf{y}_k) = \mathbf{f}(\mathbf{y}_k)$, which takes up most of the computation time of the algorithm. In practice, we do not explicitly form the inverse of the Jacobian matrix. Instead, methods such as LU decomposition will be adopted, which generally requires $O(n^3)$ operations. For the secant method, the most costly operation is to compute the determinant of a matrix. In MATLAB, the 'det' function also uses LU decomposition to find the determinant. Consequently, the Newton method and the secant method have the same order of computational complexity. From our test implementation of the secant method, we find that the secant method is slightly faster. The Newton method, however, permits further acceleration. For large scale problems, the linear equation may be solved by iterative methods such as the successive over-relaxation or Krylov subspace methods, which have the potential of reducing the computing time to $O(\gamma\, n^2)$, for some constant γ. Another acceleration approach, applicable to both Newton and secant, is to compute only the few highest frequency poles. As shown in the examples, the unstable poles are often the highest frequency ones. As a necessary-condition test, we can simply focus on these suspicious poles, and leave aside the low frequency ones.

Next, in terms of numerical stability, the secant method is inferior in that the computation of matrix determinant is prone to numerical errors. We can use two simple examples to demonstrate this aspect. In the first example, we ask MATLAB to compute the determinant of a 200×200 random matrix, whose elements are all between 0 and 20, by the statement: `det(20*rand(200,200))`. The answer returned by MATLAB is

doi: 10.6342/NTU201902629

always either `Inf` or `-Inf`, which means that MATLAB is unable to calculate the exact determinant for matrices of such a scale or larger. The second example is to calculate the determinant of a matrix that is close to singular. We first generate a random 50×50 matrix whose elements are in [0, 20] by `A=20*rand(50,50)`. Then we rewrite the 50-th column as its 49-th column plus a random 50×1 vector whose elements are of order 10^{-15}, i.e., close to machine precision: `A(:,50) = A(:,49) + (1e-15)*rand(50,1)`. Since the last two columns of **A** are nearly parallel, **A** is close to singular. However, the determinant of **A** as returned by MATLAB is 3.3769e+56, an extremely large number! These two examples show that the determinant operation as needed by the secant method is numerically unstable. On the other hand, solving a linear equation of the size 200×200, or even several times larger, is a trivial and numerically stable task for MATLAB.

The third aspect is the resolvability of closely-spaced poles. In any root-finding algorithms, we require the initial guess to be "sufficiently" close to the actual root. The closeness to the root depends on the behavior of the function as well as the algorithm. For the current pole-finding problem, the only variable in the secant method is s, while in the Newton method there is an additional mode vector **X**. Consequently, if there are two poles close to each other, "close" on the complex plane $\mathbb{C}$, the secant method may fail to distinguish them, i.e., two different initial guesses converge to the same pole while leaving the other pole undiscovered. But for the Newton method, if the mode vectors of

doi: 10.6342/NTU201902629

these two poles are sufficiently different, i.e., sufficiently separated in the complex *space* $\mathbb{C}^n$, Newton will be able to resolve these two poles. From our test implementation of the secant method, we sometimes see two root loci merge into one, which indicates the aforementioned problem. The only solution the secant method can apply is to set the bifurcation parameter t to have a finer step, e.g., $t = 0 : 0.01 : 1$, so that for each iteration the initial guess is closer to the actual root. This, however, will inevitably increase the computation time. On the other hand, the Newton method does not have this problem.

Finally, we note that in the Newton method, sometimes MATLAB will report the Jacobian matrix being ill-conditioned and thus the solution may be inaccurate. This situation often occurs for real poles deep into LHP because the term $\exp(-s\tau)$ increases exponentially and can easily become too large to be accurately represented under double precision storage. Nevertheless, for the current application, since deep LHP poles have no impact on stability, we can just ignore their loci.

4.3 Sources of Instability

In this section, we investigate the sources of instability. First of all, the physical structure being modelled by PEEC is passive, and hence always stable. Thus, the problem is in the formulation of PEEC. Next, under certain conditions the QS PEEC can be realized by resistors, inductors, and capacitors, which are all passive and guarantee stability. Therefore we could say the instability is caused by the delay, or, more precisely, by how we introduce delay into the model. Then the questions would be: how does delay affect stability? What is the weakness of the way we introduce delay?

From the examples in the previous section, we have seen that some PEEC models with delay are stable, while some are unstable. Consequently, when we say something is the general cause for the instability, it is always a *qualitative* description. It may be quantitative to some extent, but cannot be absolutely quantitative, for such a statement would be equivalent to a stability test, and is certainly case-by-case.

4.3.1 Literature Review

First we consider the QS PEEC. As described in Chapter 1, the **P** matrix can be realized as a capacitor network, in which there is a capacitor between each node whose value is calculated from the inverse of **P**, provided **P** is symmetric. The **L** matrix, on the other hand, is readily realized by mutual inductors: each diagonal element corresponds to a self-

doi: 10.6342/NTU201902629

inductor and each off-diagonal element corresponds to a mutual inductor, provided $\mathbf{L}$ is symmetric. For an inductor network, the stored energy equals

$$E_{\mathrm{L}}(t)=\int_0^t \mathbf{i}(t')^{\mathrm{T}}\mathbf{v}(t')\mathrm{d}t'=\int_0^t \mathbf{i}(t')^{\mathrm{T}}\mathbf{L}\frac{\mathrm{d}}{\mathrm{d}t'}\mathbf{i}(t')\mathrm{d}t'$$
$$=\int_0^t \frac{\mathrm{d}}{\mathrm{d}t'}\left(\frac{1}{2}\mathbf{i}(t')^{\mathrm{T}}\mathbf{L}\mathbf{i}(t')\right)\mathrm{d}t'=\frac{1}{2}\mathbf{i}(t)^{\mathrm{T}}\mathbf{L}\mathbf{i}(t)$$

Consequently, the stored energy is always positive if and only if **L** is nonnegative definite. Similarly, the stored energy in the capacitor network is

$$E_{\mathrm{P}}(t)=\int_0^t \mathbf{i}(t')^{\mathrm{T}}\boldsymbol{\Phi}(t')\mathrm{d}t'=\int_0^t \left(\frac{\mathrm{d}}{\mathrm{d}t'}\mathbf{q}(t')^{\mathrm{T}}\right)\mathbf{P}\mathbf{q}(t')\mathrm{d}t'$$
$$=\int_0^t \frac{\mathrm{d}}{\mathrm{d}t'}\left(\frac{1}{2}\mathbf{q}(t')^{\mathrm{T}}\mathbf{P}\mathbf{q}(t')\right)\mathrm{d}t'=\frac{1}{2}\mathbf{q}(t)^{\mathrm{T}}\mathbf{P}\mathbf{q}(t)$$

Thus, the stored energy is always positive if and only if **P** is nonnegative definite. In fact, it can be verified that the nonnegative-definiteness of **P** and **L** will ensure that they represent *positive-real* immitance networks [56], and are hence *passive*. On the other hand, if **P** and **L** fail to be positive semidefinite, then under certain input conditions, the circuit will continuously generate energy, and produce unstable response.

It has been studied by Ekman, Antonini, Orlandi, and Ruehli [57] that the sources that lead to the nondefiniteness of the **P** and **L** matrices are inaccurate calculation of partial coefficients and inappropriate discretization. The former problem manifests itself when the meshes are of irregular shapes that require numerical integration for the Green’s function double integral. The problem of inappropriate discretization typically arises when there are meshes of significantly different sizes that are close to each other.

Examples are provided in [57] showing the impact of poor meshing on the $\mathbf{C} = \mathbf{P}^{-1}$ matrix. A discretization guideline, called “projection meshing”, is also proposed to avoid this problem.

If proper numerical procedures are applied, such that the **P** and **L** matrices are positive definite, the QS PEEC model will be stable. In such case, however, the model may still be unstable when delays are introduced. As an example, consider the strip dipole antenna presented in Chapter 3. The current meshes are uniform, which is deemed ideal. The **L** matrix has the following eigenvalues calculated by MATLAB: {0.406, 0.41, 0.43, 0.44, 0.46, 0.48, 0.51, 0.54, 0.59, 0.62, 0.68, 0.73, 0.8, 0.87, 0.97, 1.1, 1.2, 1.4, 1.6, 2.2} (nH), which are all positive. Similarly, the eigenvalues of **P** are all positive. Hence the QS PEEC model is passive and stable, yet the FW model, as demonstrated in Chapter 3, is unstable. Therefore, we could say the delay is the main cause for the instability. Indeed, Garrett [50] has already pointed out that “PEEC model without delays are passive and stable. Hence, it is evident that the instabilities are caused by the delays between the partial inductances and the coefficients of potential.” The next question naturally arises: how does delay cause instability?

From the theory of control system, we learn that a time delay system is fundamentally difficult to analyze, to stabilize, and to design. An RFDE system already has an infinite number of poles. For an NFDE system we also have to take care its

doi: 10.6342/NTU201902629

associated difference equation. Furthermore, if the values of the delays are incommensurate, which means that they do not have rational relationships, then the general problem of delay-independent stability has been proved to be NP-hard [44]. Therefore, as a first answer, we could say it is not at all a surprise to find a delayed PEEC model unstable.

There are more PEEC-specific answers, though. From the results of transient simulation, researchers have observed that the unstable resonance usually occurs at a frequency much higher than the maximum frequency of interest, f_m, that the discretization is based on [50]. In section 4.2 we have explicitly demonstrated this phenomenon through the proposed Newton method. These high frequency poles, however, is definitely unphysical. Why do they occur?

The first explanation for the occurrence of these high frequency poles [15], [50] is that, although at $f = f_m$, the meshing is 20-cells/λ, which gives fairly accurate results, at $f \gg f_m$, say, $f = 10f_m$, the meshing is only 2-cells/λ, which is absolutely insufficient for an accurate modeling. Then, it gives no surprise that RHP poles occur in this frequency range.

Of course, saying that f_m is the "maximum frequency of interest", it makes no sense to have an accurate modeling for $f \gg f_m$. However, a time domain simulation differentiates from a frequency domain simulation in that the behavior of the model at frequencies far beyond $f = f_m$ cannot be neglected, because the excitation signal will contain spectral

doi: 10.6342/NTU201902629

components extended to $f \gg f_m$, even if very small. Nitsch, Gronwald, and Wollenberg [18] have pointed out that

> “for the transient analysis of TD-PEEC models the frequency spectra of signals cannot be limited on the range up to f_m. Thus, the system analysis and, implied, the stability analysis have to take place in an extended frequency range, theoretically up to infinity.”

Considering the numerical damping of the SPICE engine, though, we need not carry out the analysis to infinite frequency. Still, frequencies below $100f_m$, especially below $10f_m$, are crucial to the stability analysis.

The explanation we have thus reached is that the high frequency unstable poles are the result of insufficient discretization at $f \gg f_m$. This line of reasoning, in a sense, can never be rejected, for if we have sufficient meshing at $10f_m$, there would not be unstable poles below $10f_m$. However, will the stability problem be solved if we really increase discretization up to $10f_m$? Not at all. Obviously, the discretization would then be insufficient for $f = 100f_m$, and RHP poles may occur in this frequency range. As demonstrated in Section 4.2, increasing meshing will never help to obtain a stable model. Consequently, insufficient discretization is not considered a very satisfying answer.

Kochetov and Wollenberg [39] have a different thought. Recall the development of PEEC as we presented in Chapter 1. In the beginning, it is a frequency domain

doi: 10.6342/NTU201902629

formulation, just as the conventional MoM. Kochetov then asks a question: how does the ideal time delay come into the formulation? The answer is the center-to-center approximation of the partial coefficients. The equations in Chapter 1 are repeated here:

$$\Pi_{ij}=\frac{1}{4\pi\varepsilon_0 S_i S_j}\int_{S_i}\int_{S_j}\frac{e^{-jkR_\mathrm{c}}}{|\mathbf{r}-\mathbf{r}'|}d^2r d^2r'$$

$$\Lambda_{ij}=\frac{\mu_0}{4\pi a_i a_j}\int_{V_i}\int_{V_j}\frac{\left(\hat{t}_i\cdot\hat{t}_j\right)e^{-jkR_\mathrm{c}}}{|\mathbf{r}-\mathbf{r}'|}d^3r d^3r'$$

$$\Pi_{ij}\cong\bar{P}_{ij}=\frac{e^{-jkR_\mathrm{c}}}{4\pi\varepsilon_0 S_i S_j}\int_{S_i}\int_{S_j}\frac{1}{|\mathbf{r}-\mathbf{r}'|}d^2r d^2r'=P_{ij}e^{-jkR_\mathrm{c}}$$

$$\Lambda_{ij}\cong\bar{L}_{ij}=\frac{\mu_0 e^{-jkR_\mathrm{c}}}{4\pi a_i a_j}\int_{V_i}\int_{V_j}\frac{\left(\hat{t}_i\cdot\hat{t}_j\right)}{|\mathbf{r}-\mathbf{r}'|}d^3r d^3r'=L_{ij}e^{-jkR_\mathrm{c}}$$

As described in Chapter 1, this approximation is valid if the mesh sizes are much smaller than wavelength. Apparently, this approximation fails for $f \gg f_\mathrm{m}$, where wavelength becomes comparable to mesh sizes. Kochetov and Wollenberg are the first ones that have the insight to recognize the detrimental effect of the center-to-center approximation on time domain simulation. They point out that, when the exponential term is inside the integral, the partial coefficients Λ_{ij} and Π_{ij} have an intrinsic damping at high frequencies, namely, they have a lowpass response; but when the exponential term is taken outside the integral, the partial coefficients $\bar{P}_{ij}$ and $\bar{L}_{ij}$ have an allpass response up to $f \to \infty$, i.e., they have no damping. This distinction also applies to self-coupling coefficients, i.e., $\bar{P}_{ii}$ and $\bar{L}_{ii}$. As an example, consider a 1cm×1cm thin square strip, which corresponds to f_m = 1.5 GHz. Its self-inductance from 1 to 100 GHz is shown Fig. 4.17 which is calculated

doi: 10.6342/NTU201902629

through numerical integration. Indeed, for $f > f_\mathrm{m}$, the magnitude of the self-inductance drops significantly. When we make the center-to-center approximation, however, the magnitude of self-inductance remains constant.

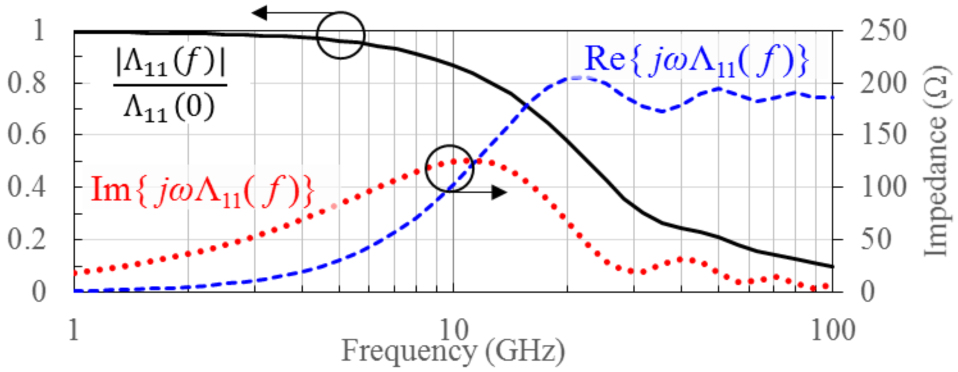

Fig. 4.17. Self-inductance and impedance of a 1cm×1cm square patch.

In short, Kochetov and Wollenberg suggest that the center-to-center approximation is the main cause for instability, because it removes the intrinsic damping of the model. In view of this, the fix to the stability problem proposed by Kochetov is to add back the damping to each self and mutual coupling, which we will describe in detail in Section 4.4.

As a historical note, we point out that the original version of PEEC proposed by Ruehli in his 1974 classic paper was a time domain formulation, instead of frequency domain as we presented in Chapter 1. The center-to-center approximation from the Galerkin matching to the delayed-static coupling was not explicitly written out. Hence, it should be appreciated that the recognition of the center-to-center approximation as the reason for time domain instability is really a remarkable and ingenious discovery of Kochetov and Wollenberg.

In this dissertation, we further strengthen the argument of Kochetov and Wollenberg. Indeed, the center-to-center approximation is deemed the origin of the stability problem. However, as we will show immediately, the harmful effect of the center-to-center approximation is not just the removal of damping, but also the introduction of a huge power bank into the circuit. With such an energy spring, the FW PEEC model is far from being passive. With this understanding, we can appreciate the ubiquitous occurrence of unstable resonance in the various examples in the literature.

4.3.2 Passivity of FW PEEC

We say that an LTI n-port network is passive if [56]

$$\int_{-\infty}^{t} \mathbf{i}^{\mathrm{T}}(\tau)\mathbf{v}(\tau)d\tau \geq 0$$

for any values of t and all possible port voltages $\mathbf{v}(t)$ and port currents $\mathbf{i}(t)$. Assume it has an impedance representation $\mathbf{Z}(s)$ in the Laplace domain (or admittance representation $\mathbf{Y}(s)$). Then, according to Wohlers [56], it is a passive network if and only if $\mathbf{Z}(s)$ is positive-real, which means that

1. Each element of $\mathbf{Z}(s)$ is analytic in $\mathrm{Re}(s) > 0$.
2. $\mathbf{Z}(s^*) = \mathbf{Z}^*(s)$.
3. $(\mathbf{Z}^{\mathrm{H}} + \mathbf{Z}) \succcurlyeq 0$ in $\mathrm{Re}(s) > 0$.

The first condition excludes any RHP poles for each element of $\mathbf{Z}$. The second condition

doi: 10.6342/NTU201902629

ensures that the time domain impulse response is real. The matrix ($\mathbf{Z}^{\mathrm{H}}$ + $\mathbf{Z}$)/2 is called the Hermitian part of $\mathbf{Z}$, denoted by $\mathbf{Z}^{(\mathrm{H})}$, and the third condition requires the Hermitian part to be positive semidefinite in the RHP. (The divided-by-two operation is irrelevant to the positive-definiteness.) For reciprocal networks, the Hermitian part of an immittance matrix equals its real part. From this theorem, we see that a QS PEEC model is passive if both the **P** and **L** matrices are positive semidefinite.

Now, for a FW PEEC model, the impedance matrix $\mathbf{Z}_{\mathrm{L}}$ associated with the inductor network $\bar{\mathbf{L}}$, under the center-to-center approximation, is given by

$$\mathbf{Z}_{\mathrm{L}} = s\bar{\mathbf{L}} = s\begin{bmatrix} L_{11} & L_{12}e^{-s\tau_{12}} & \cdots & L_{1n}e^{-s\tau_{1n}} \\ L_{12}e^{-s\tau_{12}} & L_{22} & \cdots & L_{2n}e^{-s\tau_{2n}} \\ \vdots & \vdots & \ddots & \vdots \\ L_{1n}e^{-s\tau_{1n}} & L_{2n}e^{-s\tau_{2n}} & \cdots & L_{nn} \end{bmatrix}$$

Our goal is to show that this $\mathbf{Z}_{\mathrm{L}}$ is in general far from being passive. For simplicity, we only consider $s = j\omega$, i.e., s is on the imaginary axis. Since each element of $\mathbf{Z}_{\mathrm{L}}$ is continuous in s, the restriction $s = j\omega$ can be thought of as the limiting case of $\mathrm{Re}(s) \to 0^+$. On the other hand, the results of $s = j\omega$ correspond to the sinusoidal steady state, where the input $\mathbf{i}(t)$ and output $\mathbf{v}(t)$ are all sine waves of the frequency ω, with different amplitudes and phases. In such case, we can interpret the third condition, namely the positive definiteness of the Hermitian part, in the following way. Suppose the port voltages and currents are given by the vectors $\mathbf{V}(j\omega)$ and $\mathbf{I}(j\omega)$, respectively. Then the power consumed in the impedance network is given by

doi: 10.6342/NTU201902629

$$P_{\text{in}} = \frac{1}{2}\text{Re}\{\mathbf{I}^{\text{H}}\mathbf{V}\} = \frac{1}{2}\text{Re}\{\mathbf{I}^{\text{H}}\mathbf{Z}\mathbf{I}\} = \frac{1}{2}\left[\frac{\mathbf{I}^{\text{H}}\mathbf{Z}\mathbf{I} + (\mathbf{I}^{\text{H}}\mathbf{Z}\mathbf{I})^{\text{H}}}{2}\right] = \frac{1}{2}\mathbf{I}^{\text{H}}\left(\frac{\mathbf{Z} + \mathbf{Z}^{\text{H}}}{2}\right)\mathbf{I} = \frac{1}{2}\mathbf{I}^{\text{H}}\mathbf{Z}^{(\text{H})}\mathbf{I}$$

Hence, we see that if $\mathbf{Z}^{(\text{H})}$ is positive definite, the power consumption will always be positive, and if $\mathbf{Z}^{(\text{H})}$ has negative eigenvalues, then P_{in} may be negative, which means that this impedance network generates energy back into the system.

Since $\mathbf{Z}_{\text{L}}$ is reciprocal, the Hermitian part of $\mathbf{Z}_{\text{L}}(j\omega)$ is its real part, given by

$$\mathbf{Z}_{\text{L}}^{(\text{H})} = \omega\begin{bmatrix} 0 & L_{12}\sin\omega\tau_{12} & \cdots & L_{1n}\sin\omega\tau_{1n} \\ L_{12}\sin\omega\tau_{12} & 0 & \cdots & L_{2n}\sin\omega\tau_{2n} \\ \vdots & \vdots & \ddots & \vdots \\ L_{1n}\sin\omega\tau_{1n} & L_{2n}\sin\omega\tau_{2n} & \cdots & 0 \end{bmatrix} = \omega\{\mathbf{L}\circ\sin(\omega\mathbf{T}_{\text{L}})\}$$

First of all, because any principal 2×2 minor has negative determinant, we immediately know that $\mathbf{Z}_{\text{L}}^{(\text{H})}$ is not positive semidefinite, for any frequency $\omega > 0$. By this simple argument, we have shown that the impedance matrix associated with the inductive coupling in FW PEEC is nonpassive, i.e., energy-generating. This conclusion applies to any physical structure modeled by PEEC.

We can go further beyond the passive/nonpassive classification. Specifically, because a positive eigenvalue of $\mathbf{Z}_{\text{L}}^{(\text{H})}$ means power dissipation, while a negative eigenvalue corresponds to power generation, we would like to know the magnitudes of the positive and negative eigenvalues, and the distribution of eigenvalues. We do not specify any particular structure in order to keep the results general.

First we consider the low frequency limit: $\omega \to 0^+$. The sine function can be approximated by $\sin(x) \approx x$. Hence,

doi: 10.6342/NTU201902629

$$\mathbf{Z}_{\mathrm{L}}^{(\mathrm{H})} \approx \omega^2 \begin{bmatrix} 0 & L_{12}\tau_{12} & \cdots & L_{1n}\tau_{1n} \\ L_{12}\tau_{12} & 0 & \cdots & L_{2n}\tau_{2n} \\ \vdots & \vdots & \ddots & \vdots \\ L_{1n}\tau_{1n} & L_{2n}\tau_{2n} & \cdots & 0 \end{bmatrix} = \omega^2[\mathbf{L} \circ \mathbf{T}_{\mathrm{L}}]$$

Recall the definition of partial mutual inductance:

$$L_{ij} = \frac{\mu_0(\hat{t}_i \cdot \hat{t}_j)}{4\pi a_i a_j} \int_{V_i} \int_{V_j} \frac{1}{|\mathbf{r} - \mathbf{r}'|} \mathrm{d}^3 r \mathrm{d}^3 r'$$

For simplicity, we restrict ourselves to considering parallel meshes, i.e., $\hat{t}_i \cdot \hat{t}_j = 1$. For current meshes with center-to-center distance R_{c} much larger than the mesh size, we could approximate L_{ij} as

$$L_{ij} \approx \frac{\mu_0}{4\pi a_i a_j} \frac{1}{R_{\mathrm{c}}} \int_{V_i} \int_{V_j} \mathrm{d}^3 r \mathrm{d}^3 r' = \frac{\mu_0}{4\pi} \frac{l_i l_j}{R_c}$$

where l_i and l_j are the lengths of the meshes. But, the time delay τ_{ij} equals R_{c}/c. Thus,

$$L_{ij}\tau_{ij} \approx \frac{\mu_0}{4\pi} \frac{l_i l_j}{c}$$

which is independent of R_{c}! Although this approximation is valid only for distant cells, the value of $L_{ij}\tau_{ij}$ would be of the same order of magnitude for closely-spaced meshes. If we further assume all current meshes have identical length, l, then we have

$$\mathbf{Z}_{\mathrm{L}}^{(\mathrm{H})} \approx \omega^2 \frac{\mu_0}{4\pi} \frac{l^2}{c} \begin{bmatrix} 0 & 1 & \cdots & 1 \\ 1 & 0 & \cdots & 1 \\ \vdots & \vdots & \ddots & \vdots \\ 1 & 1 & \cdots & 0 \end{bmatrix} = \omega^2 \frac{\mu_0}{4\pi} \frac{l^2}{c} \left(\underline{\mathbf{1}} - \mathbf{I}_{\mathrm{d}}\right) = \omega^2 \frac{\mu_0}{4\pi} \frac{l^2}{c} (\mathbf{I}_{\mathrm{od}})$$

where we denote $\underline{\mathbf{1}}$ as the matrix of all elements equal to 1, and $\mathbf{I}_{\mathrm{od}} = (\underline{\mathbf{1}} - \mathbf{I}_{\mathrm{d}})$ as the matrix of all off-diagonals equal to 1 and 0 on the diagonals. Because rank($\underline{\mathbf{1}}$) = 1, the eigenvalues of $\underline{\mathbf{1}}$ are n with multiplicity 1 and 0 with multiplicity $(n-1)$. Then, the eigenvalues of $\mathbf{I}_{\mathrm{od}}$ are $(n-1)$ with multiplicity 1 and (-1) with multiplicity $(n-1)$. Thus, we see that the center-to-center approximation of FW PEEC results in an inductive coupling impedance matrix that has most of its eigenvalues negative even at very low frequencies, $f \ll f_\mathrm{m}$, while the only positive eigenvalue is about n times larger than the negative eigenvalues, where n being the number of meshes. In other words, the delayed inductive coupling is nonpassive ever since $\omega = 0^+$.

As an example, consider the strip dipole in Chapter 2 with 20 current meshes, i.e., $n = 20$. Each mesh has length $l = 2.5$ mm, giving $\frac{\mu_0}{4\pi}\frac{l^2}{c} = 2.08 \times 10^{-21}$. The twenty exact eigenvalues of $[\mathbf{L} \circ \mathbf{T}_\mathrm{L}]$ are calculated by MATLAB. Nineteen of them are found to be located between (-1.31×10^{-21}) and (-2.64×10^{-21}), while one eigenvalue is 40.4×10^{-21}, which is indeed about 20 times the magnitude of the negative eigenvalues. This example confirms the eigenvalue estimation presented above.

Next we consider the general case $\omega > 0$, where $\mathbf{Z}_\mathrm{L}^{(\mathrm{H})} = \omega\{\mathbf{L} \circ \sin(\omega\mathbf{T}_\mathrm{L})\}$. The exact eigenvalues are impossible to quantify if no specific structure is given. However, we observe that the diagonal elements of $\mathbf{Z}_\mathrm{L}^{(\mathrm{H})}$ are all zero, while the off-diagonal elements are all sine functions of ω, which are periodic in ω with period $\omega_{ij} = 2\pi/\tau_{ij}$. Now, if all ω_{ij} are commensurable, i.e., their ratios form rational numbers, then there exists a least common multiple of ω_{ij}, denoted as ω_LCM, which will be the period of the $\mathbf{Z}_\mathrm{L}^{(\mathrm{H})}$. Because $\sin(\omega\tau_{ij})$ takes on positive values for half period and negative values for the other half, the eigenvalues of $\mathbf{Z}_\mathrm{L}^{(\mathrm{H})}$ can be expected to be symmetrically distributed between positive

doi: 10.6342/NTU201902629

values and negative values, for $0 < \omega < \omega_{\mathrm{LCM}}$. Thus, although at low frequencies the dominant eigenvalue is positive, there will always exist a frequency such that the dominant eigenvalue becomes negative. Even if the ω_{ij} are incommensurable, because rational numbers are dense, there will still exist an approximated ω_{LCM}, after which $\mathbf{Z}_{\mathrm{L}}^{(\mathrm{H})}$ approximately repeats. This general observation indicates that, considering the frequency range $0 < \omega < \omega_{\mathrm{LCM}}$, we could say the delayed inductive coupling results in an impedance matrix $\mathbf{Z}_{\mathrm{L}}$ that is equally power-dissipating and power-generating. Putting such a network into a circuit, though will not necessarily incur unstable resonance, is certainly very dangerous.

We can further give an estimate for ω_{LCM}. Among all ω_{ij}, the longest period corresponds to the smallest τ_{ij}, namely, the shortest time delay, which would correspond to the delay between adjacent current meshes, denoted as τ_{adj}. If the aspect ratios of current meshes are near 1, i.e., the mesh is not too *thin* ($w \ll l$), then the $\tau_{\mathrm{adj}} \approx l/c$, where l is the mesh length. Writing $l = \lambda_{\mathrm{m}}/20$, we have $\omega_{\mathrm{adj}} = 2\pi/\tau_{\mathrm{adj}} \approx 2\pi c/l = 20\omega_{\mathrm{m}}$. Now, if all τ_{ij} are close to integer multiples of τ_{adj}, then $\omega_{\mathrm{LCM}} \approx \omega_{\mathrm{adj}} \approx 20\omega_{\mathrm{m}}$. This simple calculation reveals that we will be able to find $\mathbf{Z}_{\mathrm{L}}$ significantly power-generating before $f = 20f_{\mathrm{m}}$, which is not a very high frequency that we could rely on numerical damping to stabilize the circuit.

As a representative structure, consider a 1cm×10cm rectangular strip divided into 10 uniform current meshes. Each mesh is 1cm×1cm, corresponding to f_{m} = 1.5 GHz. All

doi: 10.6342/NTU201902629

delays are exactly integer multiples of τ_{adj}, hence $\omega_{\mathrm{LCM}} = \omega_{\mathrm{adj}} = 20\omega_{\mathrm{m}}$. Fig. 4.18 shows all the ten eigenvalues of the matrix $\{\mathbf{L} \circ \sin(\omega \mathbf{T}_{\mathrm{L}})\}$ versus frequency. In this case, it turns out that $\omega_{\mathrm{LCM}} = \omega_{\mathrm{adj}}/2 = 10\omega_{\mathrm{m}}$. Indeed, in the frequency range $0 < f < f_{\mathrm{LCM}}$ the eigenvalues are evenly distributed between positive and negative values. Thus, we could not say this $\mathbf{Z}_{\mathrm{L}}$ is mainly power-dissipating. As we have pointed out, it is equally power-dissipating and power-generating.

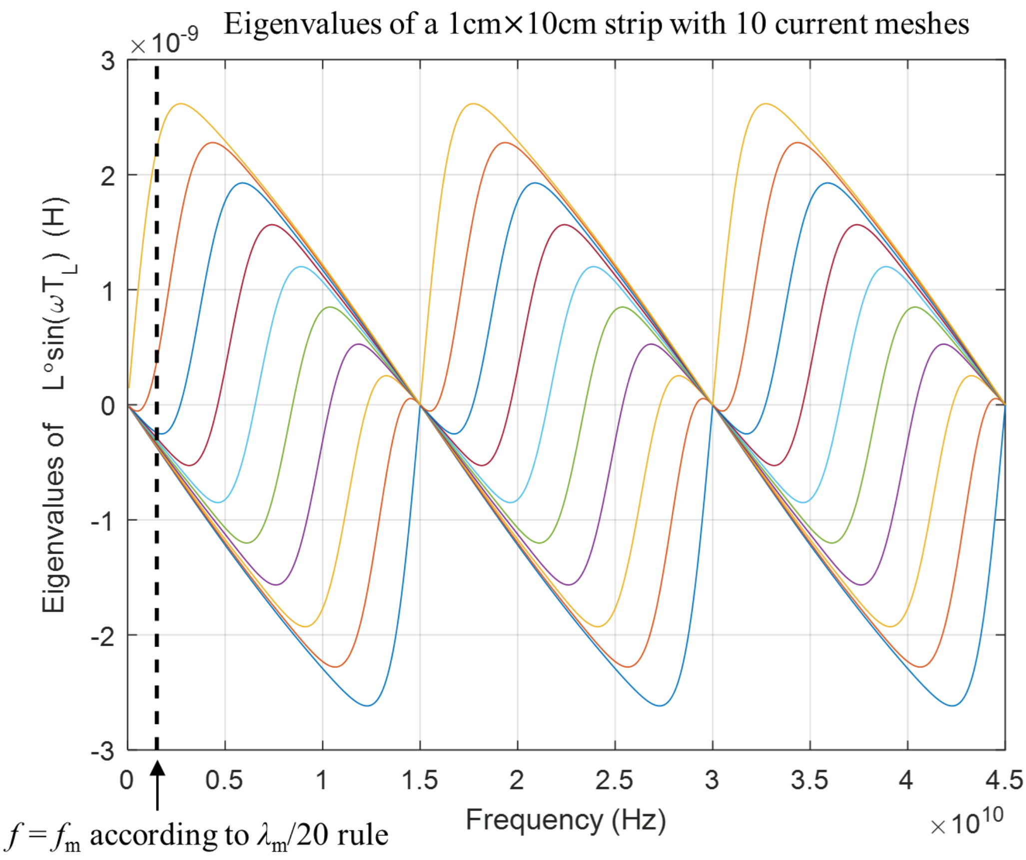

Fig. 4.18. Eigenvalues of $\{\mathbf{L} \circ \sin(\omega \mathbf{T}_{\mathrm{L}})\}$ for a 1cm×10cm strip with 10 current meshes.

The exact eigenvalues of $\mathbf{Z}_{\mathrm{L}}^{(\mathrm{H})}$ are shown in Fig. 4.19. Because the curves are modulated by ω, they become smaller at low frequencies and gradually increase as f increases. Nevertheless, the implication of this result is the same: this inductor network is far from passive, in fact power-generating.

This result also shows that the negative eigenvalues are proportional to ω. Therefore, we cannot rely on any constant series resistor, i.e., Ohmic loss, to lift the eigenvalues back to positive. No matter how low the conductivity is, the impedance matrix $\mathbf{R} + j\omega\bar{\mathbf{L}}$ will always be nonpassive. Instead, we need a damping method that changes the behavior of **L** matrix, so that the negative eigenvalues of $\mathbf{Z}_\mathrm{L}^{(\mathrm{H})}$ all the way to $f \rightarrow \infty$ can be eliminated.

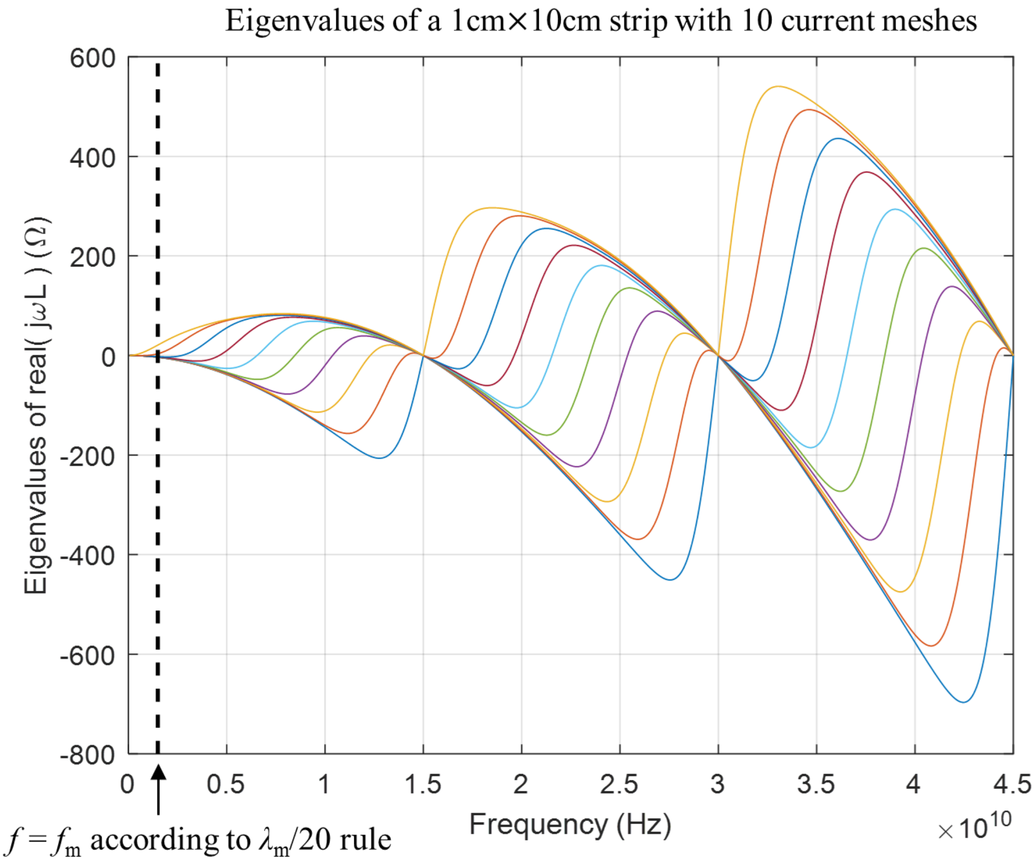

Fig. 4.19. Eigenvalues of real($j\omega\bar{\mathbf{L}}$) for a 1cm×10cm strip with 10 current meshes.

Next we consider the strip dipole that we have studied many times. For the $N = 20$ case, each mesh is 2.5mm long, corresponding to f_m = 6 GHz. In this example some delays are not integer multiples of τ_adj, hence the exact ω_LCM would be greater than $\omega_\mathrm{adj} = 20\omega_\mathrm{m}$.

The eigenvalues of the matrix $\{\mathbf{L} \circ \sin(\omega\mathbf{T}_\mathrm{L})\}$ versus frequency are plotted in Fig. 4.20 (a), and the eigenvalues of $\mathbf{Z}_\mathrm{L}^{(\mathrm{H})}$ are shown in Fig. 4.20 (b). As it turns out, just as the previous strip example, the frequency $f = 10f_\mathrm{m}$ is still quite a watershed, after which the distribution of eigenvalues roughly repeats, though not exactly. In the frequency range $0 < f < 10f_\mathrm{m}$, positive and negative eigenvalues are equally pervasive. In particular, in the range $5f_\mathrm{m} < f < 10f_\mathrm{m}$, the magnitudes of negative eigenvalues are larger than the positive ones, indicating a strong power-generating capability of the impedance network. Recall the pole distribution presented in Fig. 4.15. Two unstable poles are found to be around 37.8 GHz, which corresponds to $6.3f_\mathrm{m}$, just inside the *active* range of the impedance network. It is quite a satisfying consistency between the two results.

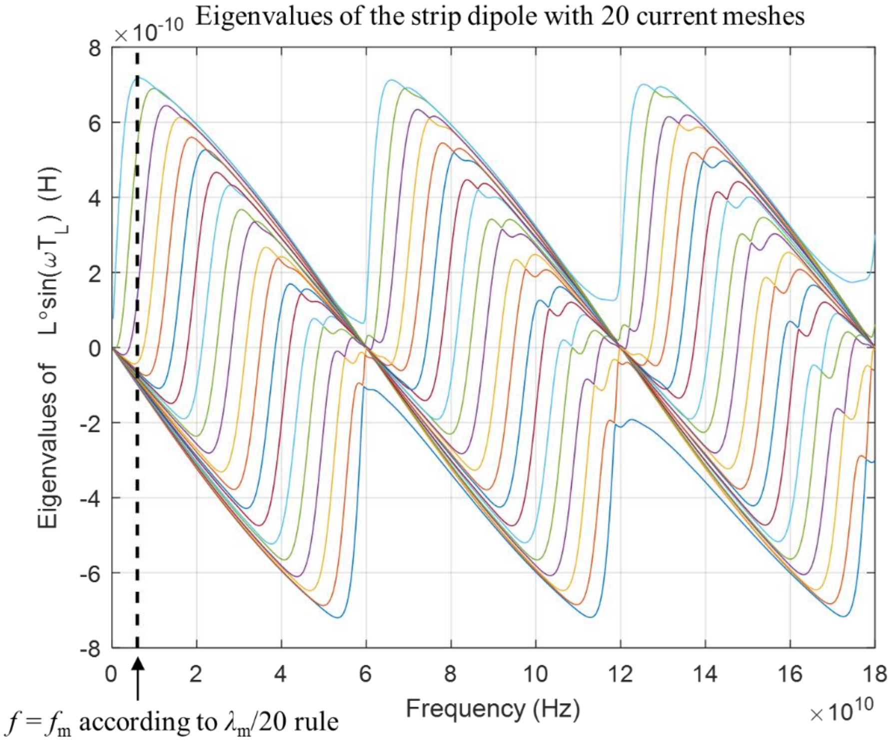

(a)

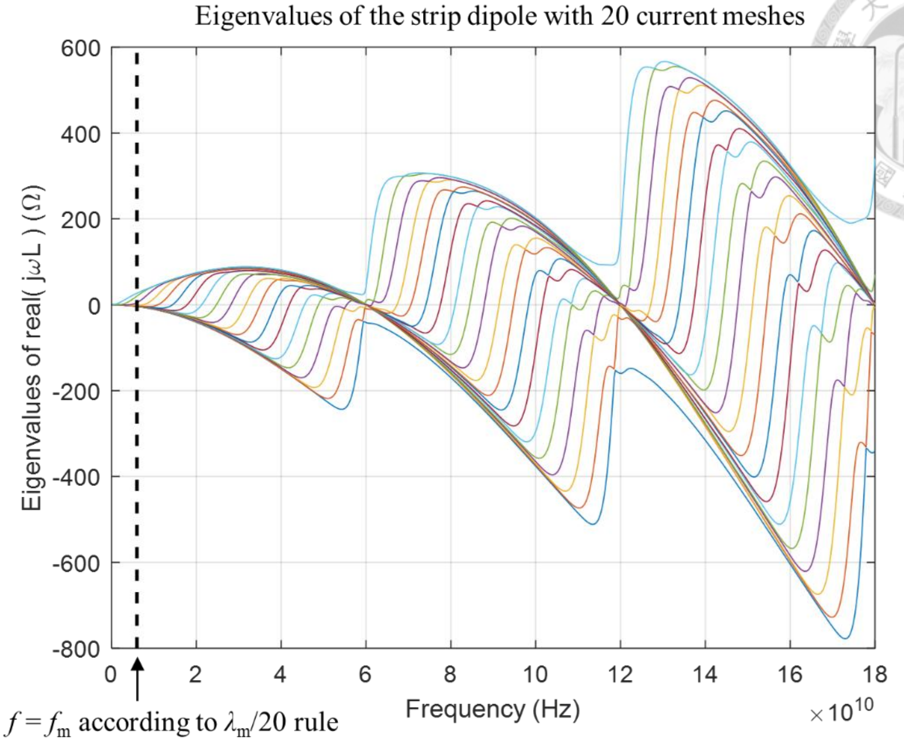

(b)

Fig. 4.20. Eigenvalues of (a) $\{\mathbf{L} \circ \sin(\omega \mathbf{T}_\mathrm{L})\}$ and (b) real$(j\omega\bar{\mathbf{L}})$ for the strip dipole antenna with 20 current meshes.

So far we have mainly considered inductive coupling. The results for capacitive coupling are mathematically similar. The impedance matrix $\mathbf{Z}_\mathrm{P}$ for the potential coupling is given by

$$\mathbf{Z}_\mathrm{P} = \frac{\bar{\mathbf{P}}}{s} = \frac{1}{s}\begin{bmatrix} P_{11} & P_{12}e^{-s\tau_{12}} & \cdots & P_{1m}e^{-s\tau_{1m}} \\ P_{12}e^{-s\tau_{12}} & P_{22} & \cdots & P_{2m}e^{-s\tau_{2m}} \\ \vdots & \vdots & \ddots & \vdots \\ P_{1m}e^{-s\tau_{1m}} & P_{2m}e^{-s\tau_{2m}} & \cdots & P_{mm} \end{bmatrix}$$

Through an abuse of notation, we also denote the time delay between charge meshes as τ_{ij}. The Hermitian part of $\mathbf{Z}_\mathrm{P}$ along the $s = j\omega$ axis is given by

$$\mathbf{Z}_\mathrm{P}^{(\mathrm{H})} = \frac{-1}{\omega}\begin{bmatrix} 0 & P_{12}\sin\omega\tau_{12} & \cdots & P_{1m}\sin\omega\tau_{1m} \\ P_{12}\sin\omega\tau_{12} & 0 & \cdots & P_{2m}\sin\omega\tau_{2m} \\ \vdots & \vdots & \ddots & \vdots \\ P_{1m}\sin\omega\tau_{1m} & P_{2m}\sin\omega\tau_{2m} & \cdots & 0 \end{bmatrix} = \frac{-1}{\omega}\{\mathbf{P} \circ \sin(\omega\mathbf{T}_\mathrm{P})\}$$

This has the same form as $\mathbf{Z}_\mathrm{L}^{(\mathrm{H})}$, except that here $\mathbf{Z}_\mathrm{P}^{(\mathrm{H})}$ is proportional to $1/\omega$. By the same argument, we immediately know that $\mathbf{Z}_\mathrm{P}$ is equally power-dissipating and power-generating in the frequency range $0 < f < f_\mathrm{LCM}$.

Next, we consider both $\mathbf{Z}_\mathrm{P}$ and $\mathbf{Z}_\mathrm{L}$ together. Recall the reduced-form MNA (1.29). After applying the center-to-center approximation, we have

$$\begin{pmatrix} s\bar{\mathbf{P}}^{-1}+\mathbf{Y} & \mathbf{A} \\ \mathbf{A}^\mathrm{T} & -(\mathbf{R}+s\bar{\mathbf{L}}) \end{pmatrix} \begin{pmatrix} \mathbf{\Phi} \\ \mathbf{I} \end{pmatrix} = \begin{pmatrix} \mathbf{I}_\mathrm{s} \\ -\mathbf{V}_\mathrm{s} \end{pmatrix}$$

In Chapter 2 of [15], the authors present two formulations that further reduce the MNA equations. The first one, which we call “node form”, is obtained by eliminating the variable $\mathbf{I}$ through the lower half of the MNA equation: $\mathbf{I}=(\mathbf{R}+s\bar{\mathbf{L}})^{-1}(\mathbf{A}^\mathrm{T}\mathbf{\Phi}+\mathbf{V}_\mathrm{s})$. Substituting into the upper half equation, we obtain

$$[(s\bar{\mathbf{P}}^{-1}+\mathbf{Y})+\mathbf{A}(\mathbf{R}+s\bar{\mathbf{L}})^{-1}\mathbf{A}^\mathrm{T}]\mathbf{\Phi}=\mathbf{Y}_\mathrm{node}\mathbf{\Phi}=\mathbf{I}_\mathrm{s}-\mathbf{A}(\mathbf{R}+s\bar{\mathbf{L}})^{-1}\mathbf{A}^\mathrm{T}\mathbf{V}_\mathrm{s}$$

In this formulation, the only unknowns are the node potentials $\mathbf{\Phi}$. We denote the matrix in the square bracket as $\mathbf{Y}_\mathrm{node}$. If there is no incident wave excitation, i.e., $\mathbf{V}_\mathrm{s}=0$, then $\mathbf{Y}_\mathrm{node}$ represents a node admittance matrix.

The second formulation, which we call “branch form”, is obtained by eliminating the variable $\mathbf{\Phi}$ through the upper half equation: $\mathbf{\Phi}=(s\bar{\mathbf{P}}^{-1}+\mathbf{Y})^{-1}(\mathbf{I}_\mathrm{s}-\mathbf{A}\mathbf{I})$. Substituting into the lower half, we have

$$[(\mathbf{R}+s\bar{\mathbf{L}})+\mathbf{A}^\mathrm{T}(s\bar{\mathbf{P}}^{-1}+\mathbf{Y})^{-1}\mathbf{A}]\mathbf{I}=\mathbf{Z}_\mathrm{branch}\mathbf{I}=\mathbf{V}_\mathrm{s}+\mathbf{A}^\mathrm{T}(s\bar{\mathbf{P}}^{-1}+\mathbf{Y})^{-1}\mathbf{I}_\mathrm{s}$$

In this formulation, the only unknowns are the branch currents $\mathbf{I}$. We denote the matrix in the square bracket as $\mathbf{Z}_{\text{branch}}$. If there is no independent current source, i.e., $\mathbf{I}_{\text{s}} = 0$, then $\mathbf{Z}_{\text{branch}}$ represents an impedance matrix.

At frequencies sufficiently high, $\mathbf{Y}_{\text{node}} \approx s\bar{\mathbf{P}}^{-1} = \mathbf{Z}_{\text{P}}^{-1}$, and $\mathbf{Z}_{\text{branch}} \approx s\bar{\mathbf{L}} = \mathbf{Z}_{\text{L}}$. Hence, we see that the non-passivity of $\mathbf{Z}_{\text{P}}$ and $\mathbf{Z}_{\text{L}}$ spreads through $\mathbf{Y}_{\text{node}}$ and $\mathbf{Z}_{\text{branch}}$.

To summarize, in this section we have shown that the delayed inductive coupling and delayed capacitive coupling in FW PEEC are far from being passive, in fact equally power-dissipating and power-generating. This non-passivity is a direct consequence of the center-to-center approximation that transforms the Galerkin-matching coefficient into a delayed-coupling form that permits simple transient simulation. With such a power source inserted into the circuit, it can be appreciated that an undamped FW PEEC model is usually unstable. Further, this phenomenon will never be removed by increasing discretization, because the forms of $\mathbf{Z}_{\text{P}}$ and $\mathbf{Z}_{\text{L}}$ remain unchanged, and thus they remain being strong power sources. Guided by this understanding, in the next section we will study the methods that help to stabilize the FW PEEC model.

doi: 10.6342/NTU201902629

4.4 Designs of Damping

The general goal of damping is to stabilize the PEEC model, and at the same time keep the solution accuracy and circuit complexity at an acceptable level. From the results in section 4.2, it is seen that the unstable poles often occur at frequencies several times higher than f_m. Consequently, the damping is essentially of a lowpass nature. The pass band should extend up to f_m, while above f_m the suppression can be as large as possible such that the unstable poles are deprived of the required energy source. This basic concept of stabilization, which is not specific for PEEC, is called *amplitude stabilization* in the field of control system design [43].

We shall distinguish two different aspects of damping. The first one is the *damping structure*, which indicates the specific circuit topology that is adopted to give additional power dissipation for the purpose of stabilization. The second aspect is the *damping design*, which refers to the methodology that we apply in order to determine the circuit values or parameters so as to obtain the effect of stabilizing the PEEC model. In short, we could say the first aspect is how we insert a particular lowpass filter (LPF) structure into the PEEC model, and the second aspect is how we design the LPF parameters such as its cutoff frequency.

There are different damping structures in the PEEC literature, while only some of them will be reviewed in section 4.4.1. The selection is based on the ease of analysis and

doi: 10.6342/NTU201902629

design, which is the subjects of sections 4.4.2 and 4.4.3. Those methods not mentioned here can be found in the references, and a thorough discussion can be found in [15]. In section 4.4.1, we also propose one our own damping structure, which is very much motivated by the existing methods in the literature. Yet, as we shall see, the proposed structure has drastically different mathematical description.

Once we have selected a particular damping structure, how should we design the circuit values? The heuristic approach is simply to choose an arbitrary damping level and run time domain simulation. If the transient outcome is unstable, then we add in more damping until it becomes (seemingly) stable. There are several problems with this trial-and-error method, though. First, it does not provide any insight regarding the stabilization effects of the damping structures. Second, from a practical point of view, if the added damping is insufficient but close to sufficient, which means that the unstable poles are very close to the imaginary axis, then it may take a very long simulation time for the instability to show up. If the simulation time is not long enough, we might be deceived by the transient response to consider the model as fully stabilized. Therefore, there should be a systematic design method that could overcome these problems. This issue will be reviewed in section 4.4.1, and our proposed analysis and design method will be presented in sections 4.4.2 to 4.4.4.

4.4.1 Review of Damping Methods

One of the most classic damping structure in PEEC is the damping resistor proposed by Garrett, Ruehli, and Paul [50], as shown in Fig. 4.21. A resistor R_L is inserted in parallel with the inductor of each current branch. At low frequencies, the inductor dominates the branch, while above the cutoff frequency $f_\mathrm{c} = R_\mathrm{L1} / 2\pi L_{11}$, the resistor prevails, thus achieving the effect of power dissipation. Cutoff frequency f_c is usually selected to be several times above f_m, so that the low frequency signal will not be affected by the presence of damping. In [50], the suggestion was $f_\mathrm{c} = kf_\mathrm{m}$, where $k = 10 \ldots 100$. This damping structure has another important advantage: parallel combination of the damping resistor will not increase the MNA matrix size, because no additional nodes are introduced into the circuit. As a result, the circuit complexity is the same as the undamped case, which is very desirable.

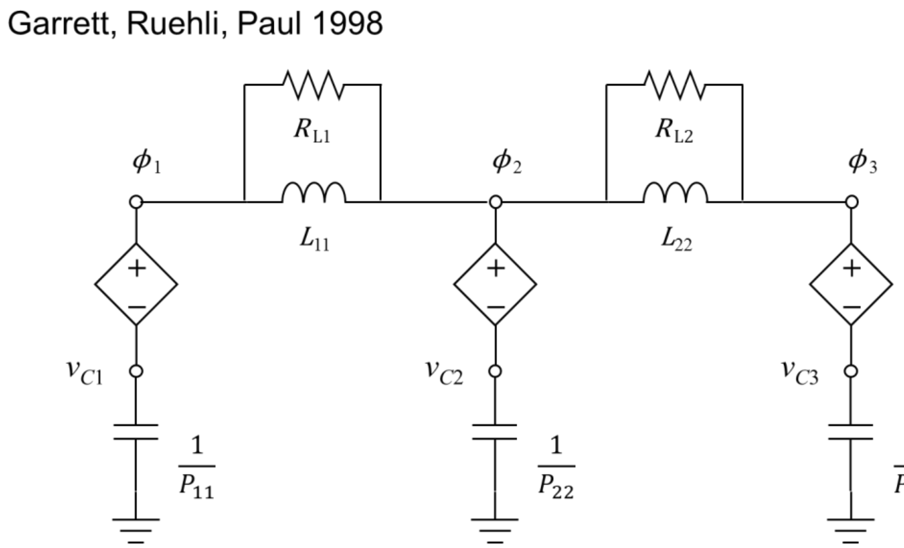

Fig. 4.21. The parallel damping resistor proposed by Garrett, Ruehli, and Paul in [50].

We point out that Fig. 4.21 is an exact reproduction of the original drawing in [50]. Comparing carefully between this damping structure with the undamped structure, e.g., Fig. 1.10, we will note an ambiguity about the exact connection of the damping resistor. In a PEEC branch, there are Ohmic resistor, self-inductor, mutual inductor represented by controlled source, and incident wave voltage source. What exactly should the damping resistor be parallel to?

As it turns out, there are different interpretations of Garrett's method in the literature. Four representatives are shown in Fig. 4.22, including our own interpretation. The first interpretation, by Ekman, Antonini, and Ruehli [58], is that R_L is in parallel with all the branch components, including Ohmic resistor. On the other side, in the interpretation of Kochetov and Wollenberg [40], R_L is in parallel only with the self-inductor, not even including the controlled source for mutual coupling. In a recent publication of Ruehli, Antonini, and Jiang [15], the Ohmic resistor is taken outside the parallel connection, while the location of the controlled source is not clear. In this dissertation, we propose the fourth interpretation, in which the R_L is in parallel with the self-inductor and the controlled source for mutual coupling, but not the Ohmic resistor. The reason is that, if R_L is in parallel with the Ohmic resistor as in Ekman's interpretation, the DC operating point of the circuit will be perturbed by the presence of R_L. The amount of deviation of the DC operating point will be minor if the conductor has high conductivity such as copper, but

doi: 10.6342/NTU201902629

may be significant for low conductivity materials where the Ohmic resistance is not negligibly small. On the other hand, if R_L is not in parallel with the controlled source as in Kochetov's interpretation, then, as we will see in the analysis of section 4.4.2, the damping will be effective only for a limited bandwidth. Putting these reasons together, we think the right implementation of Garrett's method is the fourth interpretation in Fig. 4.22. In the following, we will refer to the damping structure of the fourth interpretation as GRP.

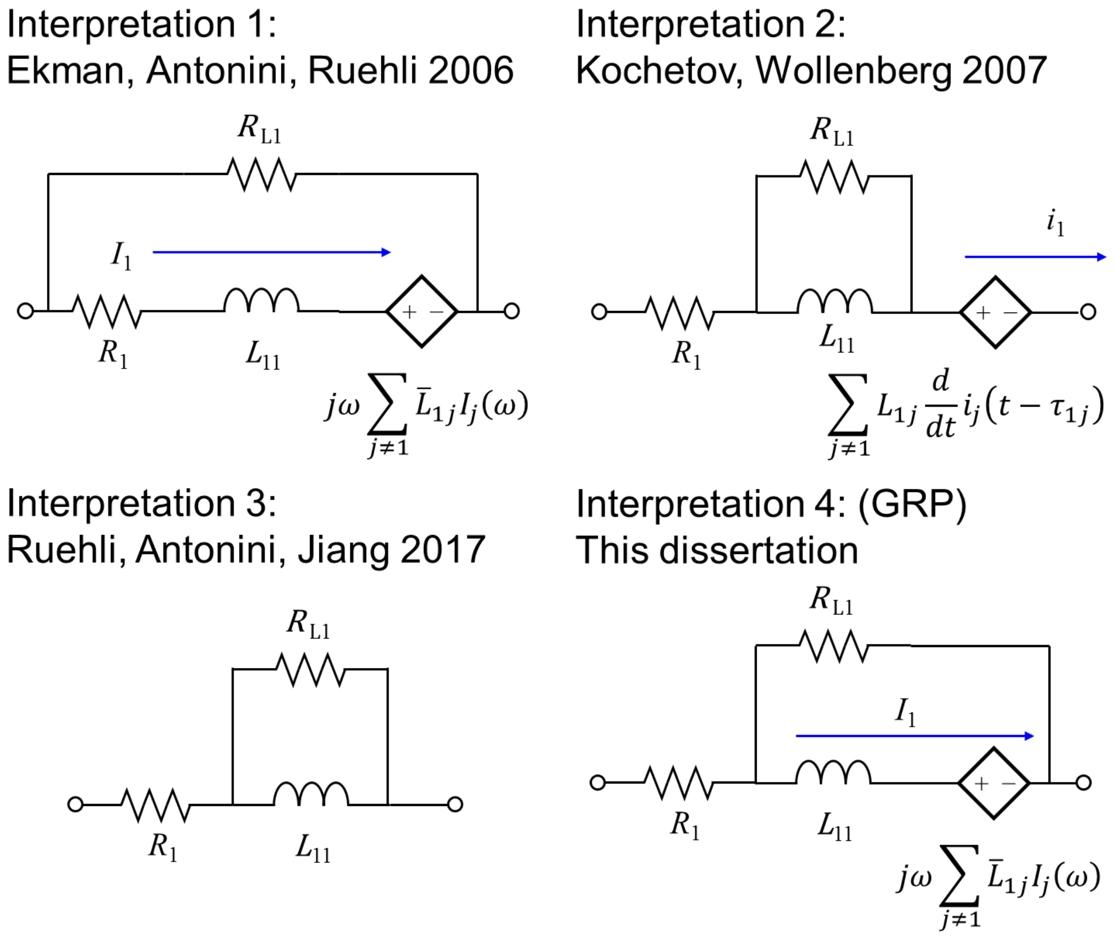

Fig. 4.22. Different interpretations of the damping resistor shown in Fig. 4.21.

Although we will show that the structure of the second interpretation is not effective over a wide bandwidth, we find that a slight modification will greatly change the behavior of the circuit, as shown in Fig. 4.23. In particular, the CCVS in Kochetov's interpretation is replaced with a VCVS. If there were no damping resistor, the structure is identical to the usual realization of mutual inductive coupling as introduced in Fig. 1.8. But when damping resistor is added into the circuit as in Fig. 4.23, the behavior is very different from all the four interpretations of Garrett's method. In fact, the resulting impedance matrix becomes nonreciprocal, as we will see. This proposed topology, which is an intuitive modification of Kochetov and Wollenberg's interpretation for the GRP, will be referred to as MKW in the following. Also, just as GRP, the MKW structure does not increase the circuit complexity because the number of nodes is the same as the undamped case.

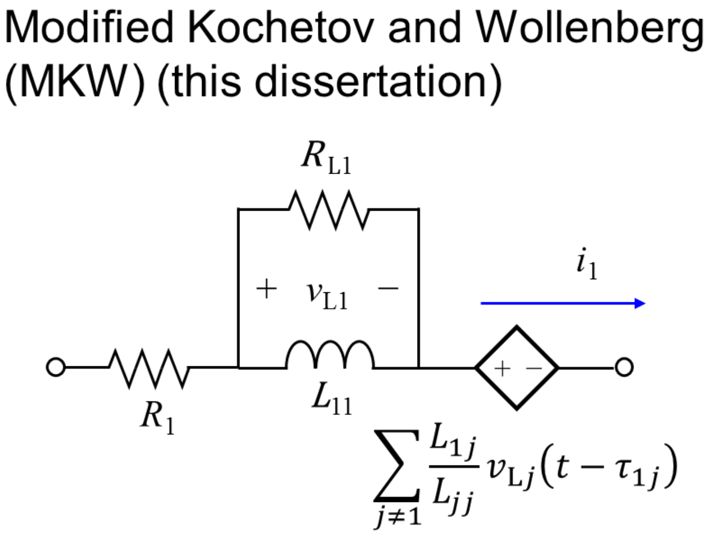

Fig. 4.23. The proposed damping structure, abbreviated as MKW.

In essence, the above methods introduce a first-order LPF into each current branch. Second-order extensions are straightforward. Some topologies proposed by this study are shown in Fig. 4.24. Below the cutoff frequency, 2nd-order damping structures will induce smaller deviation from the undamped case, while above the cutoff frequency it has a sharper falloff. The analysis and design methods are no different from the first-order cases. Hence, in the following, we will not further elaborate these 2nd-order damping structures.

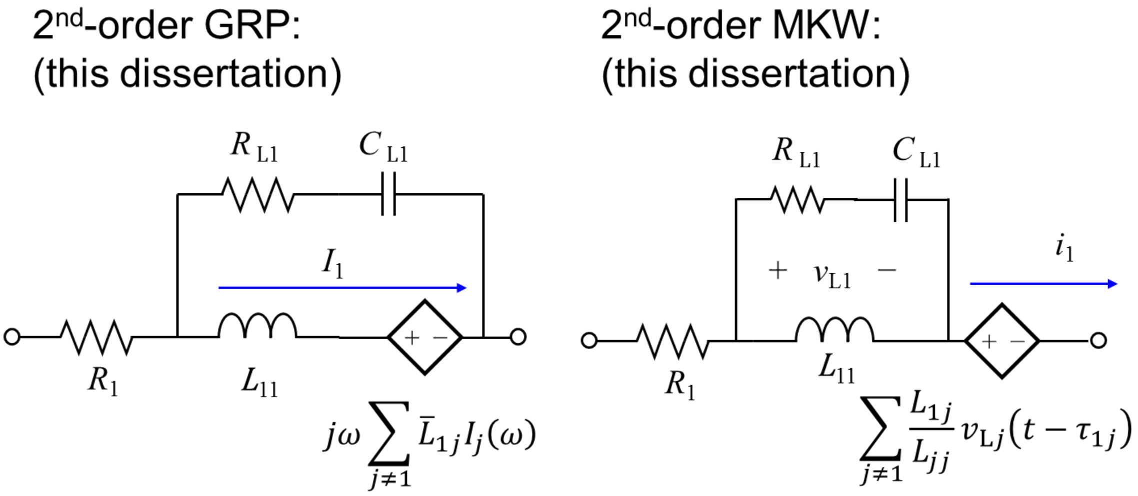

Fig. 4.24. Examples of 2nd-order damping structures.

For the potential coupling, there is also a similar structure proposed by Ekman, Antonini, and Ruehli, as shown in Fig. 4.25 [58]. A resistor R_P is in series with each self-capacitor, so that at low frequencies the capacitor dominates the node, while at frequencies above the cutoff $f_c = P_{11} / 2\pi R_{P1}$, the resistor overwhelms. The original drawing in [58] utilizes the CCCS topology for mutual coupling. An equivalent structure based on the VCVS topology is shown at the lower half of the figure. In the following, we will refer to this damping structure as EAR. Unlike GRP, however, EAR will introduce one additional node for each charge mesh, resulting in *m* additional nodes in total.

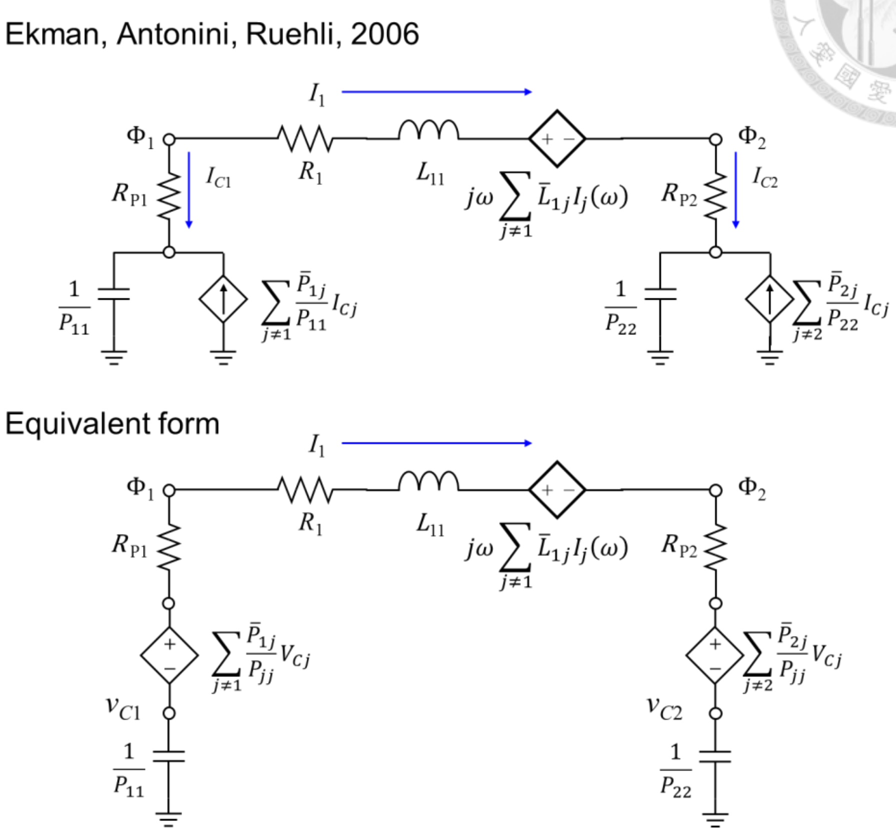
Ekman, Antonini, Ruehli, 2006

Equivalent form

Fig. 4.25. The series damping resistor proposed by Ekman, Antonini, and Ruehli [58].

In [58], there is another damping structure called *split-cap filter*. However, such topology is more difficult to analyze, and does not necessarily outperform the simple series resistor. Hence, we will not consider that structure in this dissertation.

The above-mentioned damping structures can be readily incorporated into a PEEC model. There is yet another classic damping method proposed by Kochetov and Wollenberg [39], [40]. As described in section 4.3, Kochetov considers the center-to-center approximation the main cause of instability, because it removes the intrinsic damping of the coupling coefficients derived from the Galerkin's matching. Accordingly, the cure suggested by Kochetov is to add back the damping to the circuit based on the following equations:

$$\Pi_{ij} \cong \bar{P}_{ij}H(\omega) = P_{ij}e^{-jkR_\mathrm{c}}H(\omega)$$

$$\Lambda_{ij} \cong \bar{L}_{ij}H(\omega) = L_{ij}e^{-jkR_\mathrm{c}}H(\omega)$$

where $H(\omega)$ is the transfer function of some LPF. Essentially, the above equations represent a revised center-to-center approximation, in that the amplitude attenuation at very high frequencies are accounted for by the newly added term $H(\omega)$. We point out that the term $H(\omega)$ applies to both self and mutual coupling coefficients. For self-coupling, $R_\mathrm{c} = 0$ and there is no phase delay, but the lowpass effect of $H(\omega)$ remains. The specific form of $H(\omega)$ used in [39] is

$$H(\omega) = \left(\frac{n\omega_c}{j\omega + n\omega_c}\right)^n$$

where the filter order n is between 1 and 4. Higher orders are considered unnecessary. In [40], a Gaussian filter for $H(\omega)$ is proposed. We note that in [39] and [40], the FW PEEC models are solved by their homemade SPICE, and the LPF $H(\omega)$ is realized by digital signal processing techniques written into their SPICE. Consequently, it didn't matter if $H(\omega)$ is in a circuit-realizable form or not. However, as described in Chapter 3, we would like the PEEC model to be fully compatible with standard SPICEs. As a result, we propose the following topology that efficiently realizes the idea of Kochetov and Wollenberg, as shown in Fig. 4.26. Specifically, the LPF $H(\omega)$ for mutual inductive coupling is inserted

doi: 10.6342/NTU201902629

into each intermediate stage by a shunt capacitor. For second-order LPF, we simply add an additional series inductor. In a similar way we can insert the LPF into the intermediate stages of mutual capacitive coupling. From the viewpoint of circuit complexity, first-order LPF does no increase the number of nodes because the capacitor is in shunt with an existing resistor. It will only increase the density of the MNA matrix. Second-order LPF, on the other hand, will add in ($m + n$) new nodes.

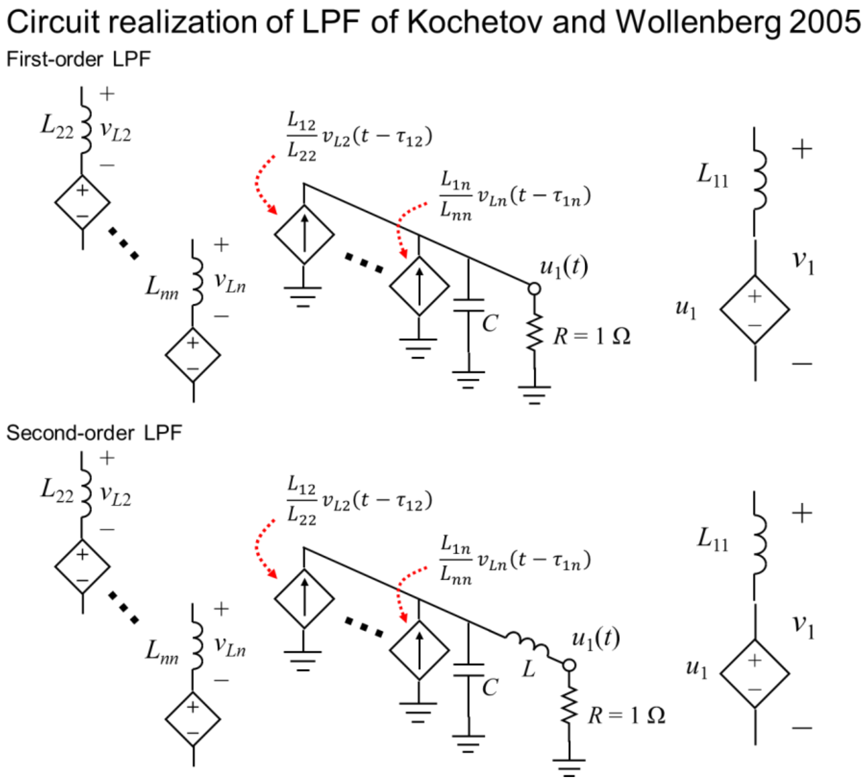

Fig. 4.26. Proposed damping structure in each mutual coupling, which is a circuit realization of the idea proposed by Kochetov and Wollenberg in [39].

We note several difference between this realization and the original form of Koehctov’s method. First, in Kochetov’s proposition, each mutual coupling should be assigned a different $H(\omega)$ whose response depends on the Galerkin’s coefficient. This can be done with the VCVS topology of Fig. 3.1. However, with the VCCS topology, since mutual couplings of the same destination cell are lumped together in the same intermediate stage in order to reduce the number of nodes, we can only assign the same $H(\omega)$ to these couplings. Second, the form of the LPF is fixed. For the first-order case, we have

$$H(s) = \frac{1}{1 + RCs}$$

while for the second-order case,

$$H(s) = \frac{1}{1 + RCs + LCs^2}$$

Since $R = 1\Omega$ to ensure unit DC gain, for the first-order case the only freedom is the cutoff frequency $f_c = 1/2\pi RC$. For the second-order case, we have an additional freedom for shaping the filter. For example, the classic Butterworth response can be realized by setting $L = \frac{R}{\sqrt{2}\omega_c}$ and $C = \frac{\sqrt{2}}{R\omega_c}$. Unlike Kochetov's scheme, we cannot easily implement a Gaussian filter. Third, as mentioned earlier, Kochetov adds the LPF $H(\omega)$ to both self and mutual couplings. For the proposed circuit realization scheme, however, only the mutual coupling terms are lowpass filtered. To achieve lowpass filtering for the self-coupling terms, i.e., self-inductance and capacitance, we need to resort to the GRP, MKW, and EAR methods.

Still, this damping structure provides a mean to control the mutual inductive and capacitive couplings, which, to be demonstrated in later sections, is crucial for the

doi: 10.6342/NTU201902629

enforcement of passivity of the PEEC model. In the following, we will refer to this damping structure simply as KW (although Kochetov and Wollenberg use different methods to realize their LPFs).

There is yet another approach that helps improve the stability and is also physically reasonable: to include the skin effect loss [15]. It is known that at high frequencies, the equivalent resistance of a conductor is proportional to $\sqrt{\omega}$, which is very desirable from the stability point of view. A detailed treatment on the circuit models for skin effect can be found in [10] and [59]. In general, however, the skin effect model will be much more complicated than the above-mentioned GRP, MKW, and EAR, resulting in a larger computational overhead. In addition, the skin effect model as a circuit stabilizer does not apply to the cases with perfect electric conductor (PEC). Hence, we will not further elaborate this idea in this dissertation.

Last but not least, we point out that since the PEEC model will eventually be solved in discrete time steps, digital lowpass filters, either FIR or IIR, can be applied to several preselected nodes and branches [15]. This method does not necessarily correspond to realizable circuits, while its stabilization effect is sometimes useful.

In the ensuing sections, we will focus on the structures of GRP, MKW, EAR, and KW only, all of which are in the form of real circuits, and permit systematic design methodologies. Brief description of them are summarized in the following table. We point

doi: 10.6342/NTU201902629

out that all four structures are useful, capable of stabilizing or passivizing an unstable model. Moreover, except the GRP and MKW are mutually exclusive, all structures can be combined together in the same PEEC model for an improved stabilizing effect.

TABLE 4.2

SUMMARY OF THE FOUR DAMPING STRUCTURES

Damping Structure	Description
GRP Fig. 4.22	Add damping resistor to each current branch, in parallel with self-inductor and mutual inductor represented by controlled source.
MKW Fig. 4.23	Add damping resistor to each current branch, in parallel with the self-inductor only, while the mutual inductive coupling is realized by the VCVS topology.
EAR Fig. 4.25	Add damping resistor to each charge node, in series with the capacitor.
KW Fig. 4.26	Add LPF to each mutual coupling, realized in the intermediate stages. First-order LPF: shunt capacitor. Second-order LPF: shunt capacitor and series inductor.

Next, we turn ourselves to the existing design methods. According to our survey, there seems to be only two kinds of systematic design methods in the literature, not including the heuristic approach mentioned earlier. The first one is to passivize the port input impedance, $Z_{\mathrm{in}}(j\omega)$, for an extended frequency range $f \gg f_{\mathrm{m}}$. This method was implied by Garrett [50] and also in [60]. The second one is to match all the coupling coefficients to that obtained from the Galerkin's procedure in the active frequency range $0 \leq f \leq f_{\mathrm{m}}$. This was first proposed by Kochetov [39] and further developed by Antonini [61].

doi: 10.6342/NTU201902629

Specifically, in the first approach, the real part of $Z_{\text{in}}(j\omega)$ is monitored from DC to a frequency much higher than f_{m}. Any frequency at which Re{ $Z_{\text{in}}(j\omega)$ } < 0 is an indication of the model being nonpassive, and we in turn increase the damping level until Re{ $Z_{\text{in}}(j\omega)$ } > 0, $\forall\omega\in$R. In [60], the target was $|S_{11}(j\omega)| < 1$, $\forall\omega\in$R, instead of Z_{in}. However, since only the values on the imaginary axis are checked, these two targets are in fact equivalent. The concept is that if we can make the circuit passive, then it must also be stable, because a passive circuit will not generate energy from its own.

In the second approach, the design goal is not based on the stability nor passivity of the circuit. Instead, the objective is to add damping to each self and mutual coupling so that they better approximate the original coupling coefficients derived from Galerkin's matching:

$$\Pi_{ij} = \frac{1}{4\pi\varepsilon_0 S_i S_j}\int_{S_i}\int_{S_j}\frac{e^{-jkR_{\text{c}}}}{|\mathbf{r}-\mathbf{r}'|}d^2r d^2r'$$

$$\Lambda_{ij} = \frac{\mu_0}{4\pi a_i a_j}\int_{V_i}\int_{V_j}\frac{\left(\hat{t}_i\cdot\hat{t}_j\right)e^{-jkR_{\text{c}}}}{|\mathbf{r}-\mathbf{r}'|}d^3r d^3r'$$

In this approach, the *belief* is that if we have followed Galerkin, the model would be stable. Sometimes, one or two simple lumped circuits are not sufficient to resemble Π_{ij} and Λ_{ij} accurately. In such case, Antonini [61] proposed to use vector fitting for each Π_{ij} and Λ_{ij} first, and then the resulting rational function fit is converted back to lumped circuits.

Several comments can be made regarding these two design approaches. For the first method, we summarize our study into three points. The first two remarks are theoretical issues, while the last one is a practical consideration.

(1) It is right that a passive model is always stable. However, Re{ $Z_{\text{in}}(j\omega)$ } > 0, $\forall\omega\in$R is merely one of the necessary conditions. In fact, to verify that a model is indeed passive, the first step is actually to verify that it is stable. Recall the three conditions for an immittance matrix to be passive, as stated in the beginning of section 4.3.2. The first condition requires the immittance having no RHP poles, while the third condition asks for a positive real part. The third condition does not imply the first, so both conditions are needed in order to ascertain passivity. In this design method, only the third condition for passivity is checked. The first condition, i.e., the model stability, however, remains unknown. There are pathological one-port networks whose input impedance has positive real parts for all frequencies, while being unstable. As an example, consider the impedance $Z_{\text{in}}(s)=\frac{-1}{s-1}$. The only pole is at s = 1, which is unstable, while Re{ $Z_{\text{in}}(j\omega)$ } = $\frac{1}{\omega^2+1}$ > 0, $\forall\omega\in$R. Consequently, in this design method, we can only *assume* the model is already stabilized when the damping is added to the level that makes Re{ $Z_{\text{in}}(j\omega)$ } > 0.

(2) The second remark is related to the observability issue. Since only the port impedance is monitored, we have to assume that any internal instability will be faithfully reflected to the port impedance, i.e., the whole circuit is observable at the selected port. The port observability is believed in [60] because in PEEC all inductors are

doi: 10.6342/NTU201902629

coupled together, and all charge nodes are coupled together too. In such a tightly coupled circuit, any natural modes should be more or less transparent at the ports. Rigorous justification of the observability, however, is still a subject of study.

(3) Sometimes, we only need a stable model, but not necessarily passive. This situation occurs if we know that the PEEC model is not going be connected with any external circuits, or will be connected with only a few circuits with which we are confident that they will not drive the non-passivity into instability. For example, in a scattering problem, the only excitation is the series voltage sources representing incident waves, and very few external circuits are connected to the model. In such a case, it may suffice to stabilize the model for an accurate transient simulation. If, however, we insist on enforcing passivity, we might run into an overdesign that either increases the complexity by adding too many damping circuits, or decreases the solution accuracy by choosing a damping cutoff frequency too low and too close to f_{m}. That is to say, passivity is a rather *conservative* condition for ensuring stability.

For the second design method, i.e., the Galerkin matching, the major concern is that we do not know this level of damping will guarantee a stable model or not. In the literatures [39], [40], [61], the authors provide transient simulation results as the only mean to demonstrate the stability of the model. However, as we know, if the unstable pole

doi: 10.6342/NTU201902629

is very close to the imaginary axis, it may take a very long simulation time to reveal the instability. Nevertheless, from our experience with the MKW method, to be presented later, we could say that this design method is usually sufficient to stabilize the model, but may not be sufficient to make the model passive.

To summarize the review of this section, we note that various damping structures have been proposed in the literature, while only a few design methods are suggested. In addition, there has been no any design method that directly enforces the stability (not the passivity) of the model. Obviously, this is tightly related to how we determine the stability of the model. If we cannot assess its stability, we will not be able to design the damping that makes it stable. Among the various stability tests reviewed in section 4.2.1, most of them cannot be applied to a damped FW PEEC model without substantial modification. The only exception is the Garrett's input impedance test which, as we described above, is a passivity-based method and has both theoretical and practical issues that should be addressed. On the other hand, the proposed Newton pole search in section 4.2.2 can be straightforwardly extended to the damped case, thus continuing to serve as a very useful necessary-condition test. In section 4.4.2, we will first present our study on all four damping structures listed above. Their corresponding immittance matrices will be analytically derived. From the mathematical forms, we can draw several qualitative conclusions about their behavior, especially their ability to passivize an arbitrary PEEC

doi: 10.6342/NTU201902629

model. Then in section 4.4.3, we will present the modified Newton pole search, which will tell us the final pole locations when damping resistors and capacitors are added into the PEEC model. Based on this information, we can quantitatively determine how much damping we should place in order to stabilize the circuit. Finally, in section 4.4.4 we will discuss the Garrett's method in detail, namely, passivity enforcement of PEEC.

4.4.2 Analysis of Damping Structures

First, consider the GRP structure, i.e., the fourth interpretation in Fig. 4.22. Denote $\mathbf{R}_\mathrm{L}$ = diag($R_{\mathrm{L}1}$, …, $R_{\mathrm{L}n}$), which is a $n \times n$ diagonal matrix with the damping resistor values. Normally, $R_{\mathrm{L}i} \neq 0$ for each i. Thus $\mathbf{R}_\mathrm{L}$ is invertible. Then, note that the inductor network $\bar{\mathbf{L}}$ is in parallel with the damping resistor network $\mathbf{R}_\mathrm{L}$, hence

$$\mathbf{Z}_\mathrm{L} = \left(\frac{\bar{\mathbf{L}}^{-1}}{j\omega} + \mathbf{R}_\mathrm{L}^{-1}\right)^{-1} = j\omega(\bar{\mathbf{L}}^{-1} + j\omega\mathbf{R}_\mathrm{L}^{-1})^{-1}$$

where $\mathbf{Z}_\mathrm{L}$ is the impedance matrix of the combined inductance and damping resistance. For notational convenience in later sections, we denote

$$\mathbf{L}_\mathrm{GRP} = (\bar{\mathbf{L}}^{-1} + s\mathbf{R}_\mathrm{L}^{-1})^{-1}$$

From the expression of $\mathbf{Z}_\mathrm{L}$, we note that if $\bar{\mathbf{L}}(j\omega)$ is invertible for all ω, then above some frequency $\mathbf{Z}_\mathrm{L}(j\omega)$ will be dominated by $\mathbf{R}_\mathrm{L}$. In this case we could say GRP is a *consistent* damping structure, similar to the saying that an estimator is consistent in the field of statistical inference. On the other hand, if $\bar{\mathbf{L}}(j\omega)$ is singular or close to singular for some

doi: 10.6342/NTU201902629

ω, then at these frequencies $\mathbf{Z}_\mathrm{L}(j\omega)$ might not be dominated by $\mathbf{R}_\mathrm{L}$, and the non-passive nature of $\bar{\mathbf{L}}(j\omega)$ may still be reflected to $\mathbf{Z}_\mathrm{L}$, making the damping resistor ineffective. Note that in this subsection, passivity is referred to the impedance matrix $\mathbf{Z}_\mathrm{L}$ only, instead of the whole PEEC model. Consequently, we are studying the ability of the damping structures to make the coupled inductor network passive. The passivity of the complete PEEC model will be addressed in section 4.4.4.

Next, consider the Kochetov's interpretation of GRP (the second one in Fig. 4.22). It can be derived that the corresponding impedance matrix is given by

$$\mathbf{Z}_\mathrm{L} = \frac{j\omega\mathbf{L}_\mathrm{d}\mathbf{R}_\mathrm{L}}{j\omega\mathbf{L}_\mathrm{d} + \mathbf{R}_\mathrm{L}} + j\omega\bar{\mathbf{L}}_\mathrm{od}$$

where $\mathbf{L}_\mathrm{d} = \mathrm{diag}(\mathrm{diag}(\bar{\mathbf{L}}))$, i.e., the diagonal matrix with the diagonal elements of $\bar{\mathbf{L}}$, and $\mathbf{L}_\mathrm{od}$ is the matrix with all off-diagonal elements of $\bar{\mathbf{L}}$, with 0 on its diagonals. Note that since both $\mathbf{R}_\mathrm{L}$ and $\mathbf{L}_\mathrm{d}$ are diagonal matrices, for ease of understanding we have put the matrices in fractional form instead of writing matrix inverse. The cutoff frequency of the i-th branch is $f_{ci} = R_{\mathrm{L}i} / 2\pi L_{\mathrm{d}i}$. For simplicity of design, we always set the cutoff frequencies of all branches identical. Above f_c, the first term of the RHS will become the constant matrix $\mathbf{R}_\mathrm{L}$, while the second term continues to grow proportional to ω. Hence, we immediately see that the eigenvalues of the Hermitian part of $\mathbf{Z}_\mathrm{L}$ will asymptotically approach the undamped case as $\omega \to \infty$. Hence, the KW's interpretation of GRP is not a consistent damping structure. This is the reason why we said in the previous section that

doi: 10.6342/NTU201902629

this damping structure will be effective only for a limited bandwidth. However, it should be clarified that this is not saying it cannot stabilize the PEEC model. Stability and passivity are different properties, and any dissipation added to the circuit may have the effect of stabilizing the model. For the Kochetov's interpretation of GRP, it simply cannot passivize the inductance matrix and hence the PEEC model.

Next, consider the proposed MKW structure in Fig. 4.23. The total voltage drop across the self-inductor and controlled source of the *i*-th branch is $V_i = V_{\mathrm{L}i} + \sum_{j \neq i} \frac{\bar{L}_{ij}}{L_{jj}} V_{\mathrm{L}j} = (j\omega L_{ii} \parallel R_{\mathrm{L}i}) I_i + \sum_{j \neq i} \frac{\bar{L}_{ij}}{L_{jj}} \left(j\omega L_{jj} \parallel R_{\mathrm{L}j}\right) I_j$. Therefore, we have

$$\mathrm{Z_L} = \begin{bmatrix} \dfrac{j\omega L_{11} R_{\mathrm{L}1}}{j\omega L_{11} + R_{\mathrm{L}1}} & \cdots & \dfrac{j\omega \bar{L}_{1n} R_{\mathrm{L}n}}{j\omega L_{nn} + R_{\mathrm{L}n}} \\ \vdots & \ddots & \vdots \\ \dfrac{j\omega \bar{L}_{1n} R_{\mathrm{L}1}}{j\omega L_{11} + R_{\mathrm{L}1}} & \cdots & \dfrac{j\omega L_{nn} R_{\mathrm{L}n}}{j\omega L_{nn} + R_{\mathrm{L}n}} \end{bmatrix} = j\omega \bar{\mathbf{L}} \left(\frac{\mathbf{R}_\mathrm{L}}{j\omega \mathbf{L}_\mathrm{d} + \mathbf{R}_\mathrm{L}} \right)$$

We also denote $\mathbf{L}_{\mathrm{MKW}} = \bar{\mathbf{L}} \left(\frac{\mathbf{R}_\mathrm{L}}{s\mathbf{L}_\mathrm{d} + \mathbf{R}_\mathrm{L}} \right)$. The cutoff frequency is again defined as $f_\mathrm{c} = R_{\mathrm{L}1} / 2\pi L_{11}$, and all branches have the same cutoff. An essential difference of MKW is that it is in general nonreciprocal, due to the asymmetry of $\mathbf{Z}_\mathrm{L}$. Nevertheless, at low frequencies where $\mathbf{L}$ dominates $\mathbf{R}_\mathrm{L}$, $\mathbf{Z}_\mathrm{L} \approx j\omega\mathbf{L}$ and is approximately reciprocal. At high frequencies, $\mathbf{Z}_\mathrm{L} \approx \bar{\mathbf{L}} \frac{\mathbf{R}_\mathrm{L}}{\mathbf{L}_\mathrm{d}}$, so both the diagonal and off-diagonal elements are no longer proportional to ω. The Hermitian part $\mathbf{Z}_\mathrm{L}^{(\mathrm{H})}$ is roughly related to the real part of $\bar{\mathbf{L}}$, instead of the imaginary part as in the undamped case. Since the real part of $\bar{\mathbf{L}}$ usually has strong diagonal, $\mathbf{Z}_\mathrm{L}^{(\mathrm{H})}$ is more likely to be positive definite. However, just like GRP, in general we cannot guarantee MKW is a consistent damping structure.

As an example, consider the 1cm×10cm strip with 10 current meshes that we have studied in section 4.3.2. The eigenvalues of Re{ $\mathbf{Z}_L(j\omega)$ } for the undamped case has been presented in Fig. 4.19. The eigenvalues of $\mathbf{Z}_L^{(H)}$ for GRP, KW's interpretation of GRP, and MKW, with different cutoff frequencies, are shown in Fig. 4.27 for comparison. The figures in the first row are GRP. We see that at high frequencies all the eigenvalues are positive. However, to achieve positive definiteness for all frequencies, we need to set f_c as small as f_m, which may considerably reduce the low frequency accuracy of the model.

The figures in the second row are the results of KW's interpretation of GRP. As mentioned above, it cannot passivize $\mathbf{Z}_L$ for all band. Indeed, when $f_c = 3f_m$ or $f_c = f_m$, only the very low frequency ($f < 3f_m$ or $2f_m$) eigenvalues are made positive. However, for the purpose of stabilization, it may still be useful.

The last row is the MKW case. Similar to GRP, when $f_c = 10f_m$ all high frequency eigenvalues are turned positive. To achieve all band positive definiteness, we need $f_c = 3f_m$, which is slightly better than GRP in terms of low frequency accuracy.

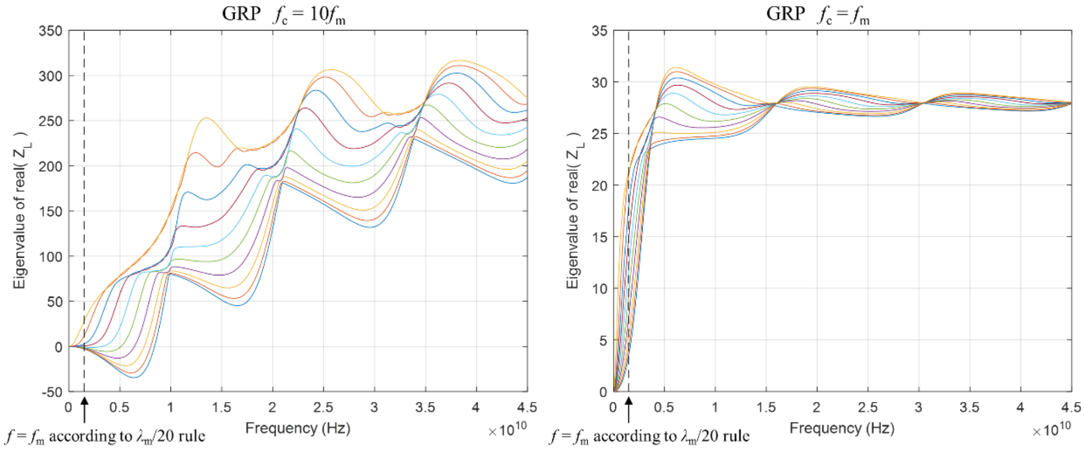

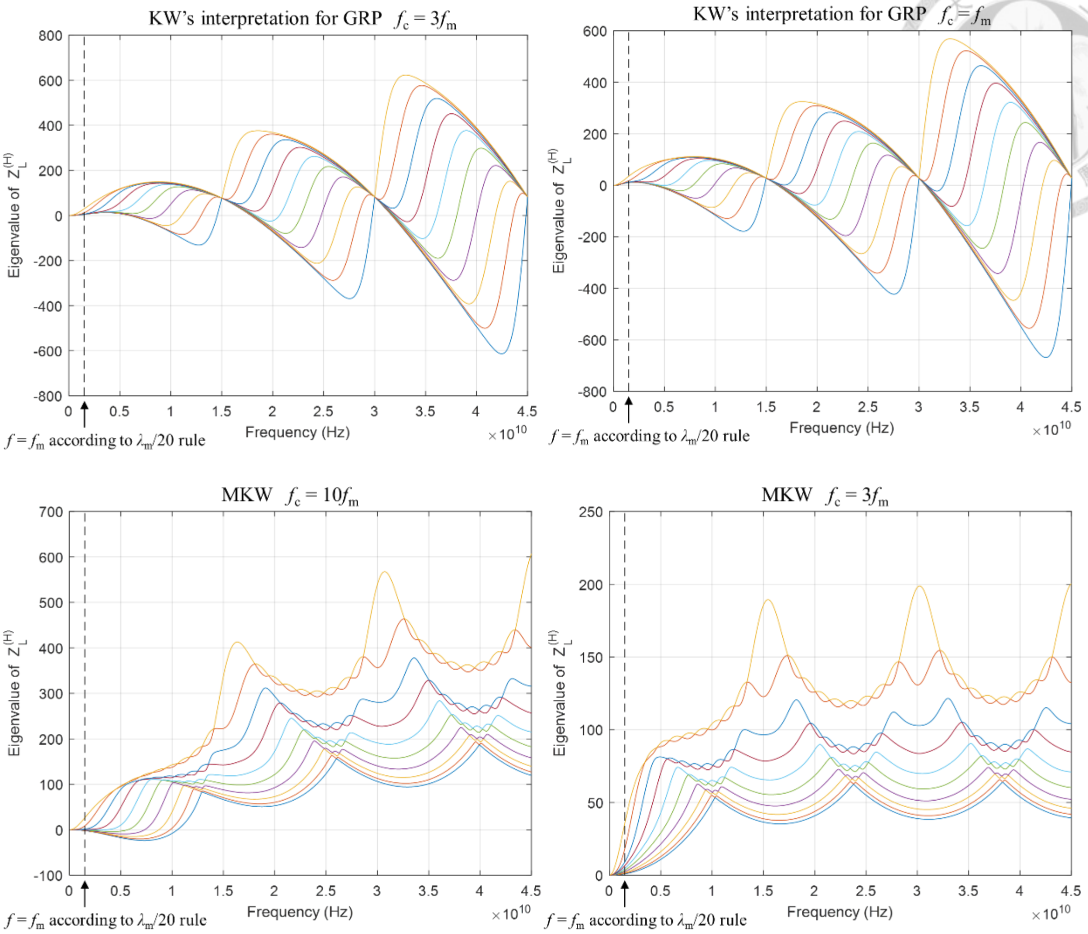

Fig. 4.27. Eigenvalues of $\mathbf{Z}_L^{(H)}$ of the 1cm×10cm strip with 10 meshes, for various damped cases.

Next, consider KW, i.e., the mutual damping in Fig. 4.26. Assume all LPFs in the intermediate stages share the same transfer function $H(j\omega)$, either first or second order. Then the equivalent inductance matrix becomes

$$\mathbf{L}_{\mathrm{KW}} = \bar{\mathbf{L}} \circ \mathbf{I}_{\mathrm{od}} H$$

where $\mathbf{I}_{\mathrm{od}} = (\underline{\mathbf{1}} - \mathbf{I}_{\mathrm{d}})$ is the matrix of all off-diagonals 1 and diagonals 0. The impedance matrix is simply $\mathbf{Z}_L = j\omega\mathbf{L}_{\mathrm{KW}}$. Note that the off-diagonals will saturate above cutoff, while the diagonals continue to grow proportional to ω. However, since the diagonals are still imaginary, the Hermitian part of $\mathbf{Z}_L$ will have zero diagonals, and thus never be positive definite. Consequently, the KW structure shall not be used alone. Instead, it should be combined with GRP, MKW, or EAR. Combination with GRP or MKW is achieved by simply replacing $\bar{\mathbf{L}}$ with $\mathbf{L}_{\mathrm{KW}}$:

$$\mathbf{L}_{\mathrm{GRP+KW}} = (\mathbf{L}_{\mathrm{KW}}^{-1} + s\mathbf{R}_{\mathrm{L}}^{-1})^{-1}$$

$$\mathbf{L}_{\mathrm{MKW+KW}} = \mathbf{L}_{\mathrm{KW}} \frac{\mathbf{R}_{\mathrm{L}}}{s\mathbf{L}_{\mathrm{d}} + \mathbf{R}_{\mathrm{L}}}$$

As described earlier, if $\bar{\mathbf{L}}$ is singular or close to singular at some frequencies, then the corresponding $\mathbf{L}_{\mathrm{GRP}}$ may fail to be passive. The effect of combining KW with GRP is that since the off-diagonal terms are further reduced by the LPF $H(j\omega)$, $\mathbf{L}_{\mathrm{KW}}$ becomes increasingly diagonally dominant as frequency goes higher. According to Gershgorin, it is then guaranteed that above a certain frequency, $\mathbf{L}_{\mathrm{KW}}$ will never be singular, and hence resolving the problem of GRP. Similarly, MKW suffers from the problem of $\mathrm{Re}\{\bar{\mathrm{L}}\}$ not being positive definite for all frequencies. When KW is combined and the off-diagonals of $\bar{\mathbf{L}}$ are filtered, this problem is settled down.

Consider the coplanar strip example of Fig. 4.3. We partition each strip into $N = 50$ current meshes, resulting in a 100×100 inductance matrix. The eigenvalues of $\mathbf{Z}_{\mathrm{L}}^{(\mathrm{H})}$ of various undamped and damped cases are shown in Fig. 4.28, and the absolute values of the eigenvalues of $\frac{\bar{\mathbf{L}}}{L_{11}}$ is shown in the upper-left figure, which reveals the frequencies at which $\bar{\mathbf{L}}$ is singular or close to singular. In this example, we see that $\bar{\mathbf{L}}$ is close to singular around 68 GHz, 80 GHz, 103 GHz, and 115 GHz. Indeed, both GRP ($f_{\mathrm{c}} = 10f_{\mathrm{m}}$)

doi: 10.6342/NTU201902629

and MKW ($f_c = 10f_m$) suffer from or close to passivity violation at these frequencies. On the other hand, if combined with a first-order KW, with the same cutoff frequency, then this kind of “high-frequency surprise” no longer happens.

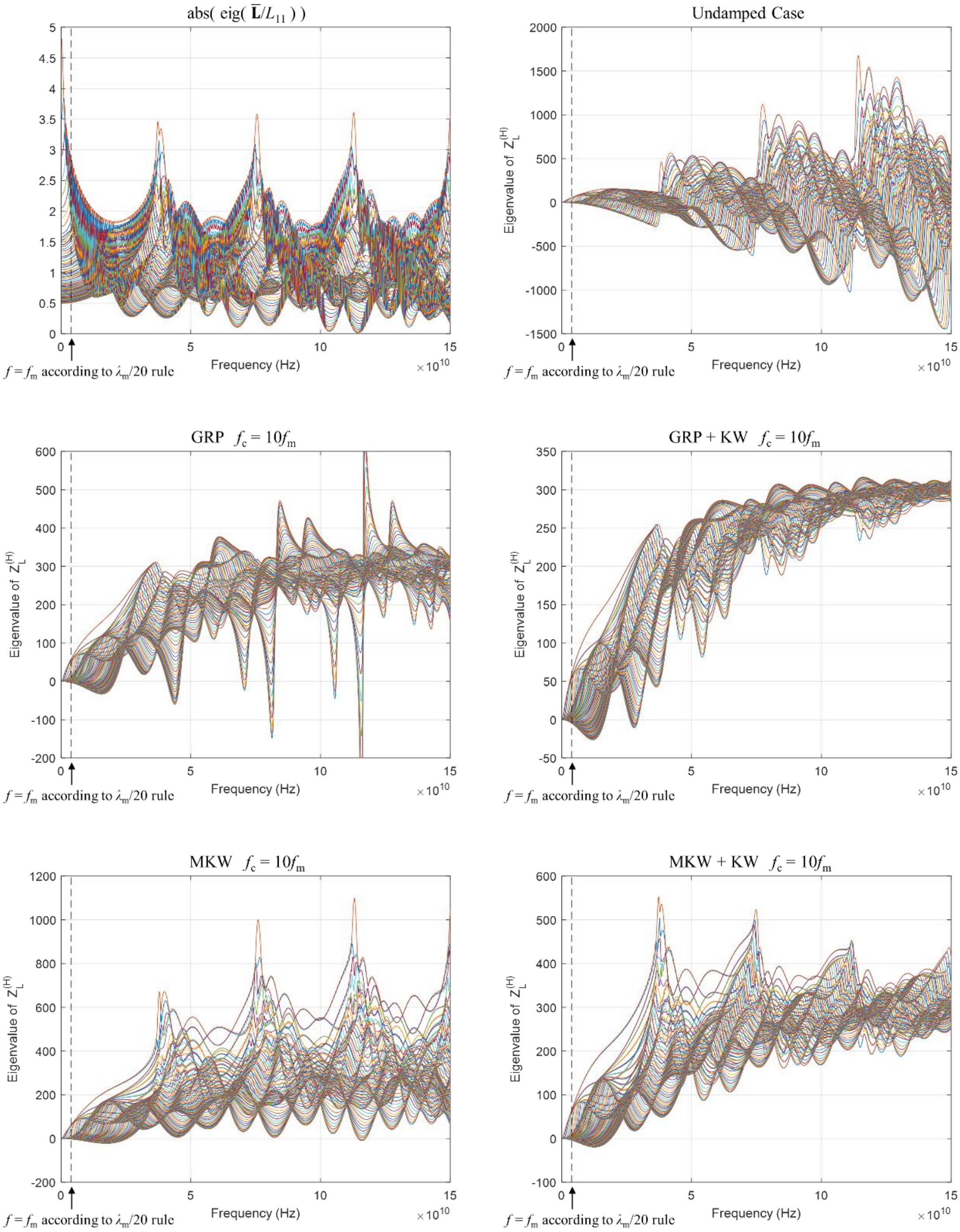

Fig. 4.28. Eigenvalues of normalized $\bar{\mathbf{L}}$, undamped $\mathbf{Z}_{\mathrm{L}}^{(\mathrm{H})}$, and various damped $\mathbf{Z}_{\mathrm{L}}^{(\mathrm{H})}$, for the coplanar strip transmission line example with $N = 50$.

doi: 10.6342/NTU201902629

In the above figures, we see that both GRP+KW and MKW+KW with $f_c = 10f_m$ still have some negative eigenvalues below $f = 10f_m$. They can be removed by further decreasing the cutoff frequency f_c. Here, we would like to discuss the lower limit on f_c that preserves the low frequency accuracy of the circuit at an acceptable level. The MKW structure introduces a first-order lowpass filter to each element of $\mathbf{Z}_L$. Consequently, at the 3-dB cutoff frequency $f = f_c$, each element of $\mathbf{Z}_L$ will deviate from the undamped $\mathbf{Z}_L$ by 3-dB. At $f = f_c / 10$, the deviation of each element will be roughly 10%. If we take the 10% deviation from the undamped case as a criterion, then the lowest acceptable f_c would be $10f_m$. Indeed, in [50] the recommendation by Garrett was $f_c = 10f_m$ to $100f_m$. However, we should note that this conclusion applies exactly to MKW only. For GRP, due to the matrix inverse operation, the amount of deviation from the undamped case is dependent on the determinant of the $\bar{\mathbf{L}}$ matrix. Note that the cutoff frequency for GRP is defined based on the diagonal elements of $\bar{\mathbf{L}}$, i.e., the self-inductances. For small-scale problems, $\bar{\mathbf{L}}$ tends to be diagonally dominant, and the error behavior would be similar to the MKW. However, for large-scale problems with strong off-diagonals, the "cutoff frequency" f_c usually does not represent the exact 3-dB point. Actually, we can expect that if the effect of the off-diagonal terms is to increase $\det(\bar{\mathbf{L}})$, then the exact 3-dB breakpoint, for some elements of $\mathbf{Z}_L$, will be smaller than f_c. Consequently, for GRP, a 10% error criterion would require $f_c > 10f_m$. The exact threshold, however, is hard to quantify analytically.

doi: 10.6342/NTU201902629

This may be considered as an advantage of the proposed MKW over GRP.

There is yet another perspective on the accuracy issue. As described earlier, researchers such as Kochetov [39] and Antonini [61] suggest matching the coupling coefficients to that obtained from Galerkin's method, Π_{ij} and Λ_{ij}. The PEEC system in terms of $\mathbf{\Pi}$ and $\mathbf{\Lambda}$ is considered not just more stable than the system in terms of $\bar{\mathbf{P}}$ and $\bar{\mathbf{L}}$, but also more accurate. The fact that Π_{ij} and Λ_{ij} have an intrinsic high frequency damping, as demonstrated in Fig. 4.17, indicates that we are actually allowed to deviate from $\bar{\mathbf{P}}$ and $\bar{\mathbf{L}}$ to some extent, while not being considered as inducing error. To quantify this idea, consider two *x*-directed inductive cells lying on the *x* axis with dimensions shown in Fig. 4.29, both with infinitesimal thickness. R_c is the center-to-center distance between the two cells. We assume $l_1 \geq l_2$, and all w and l are of the same order of magnitude.

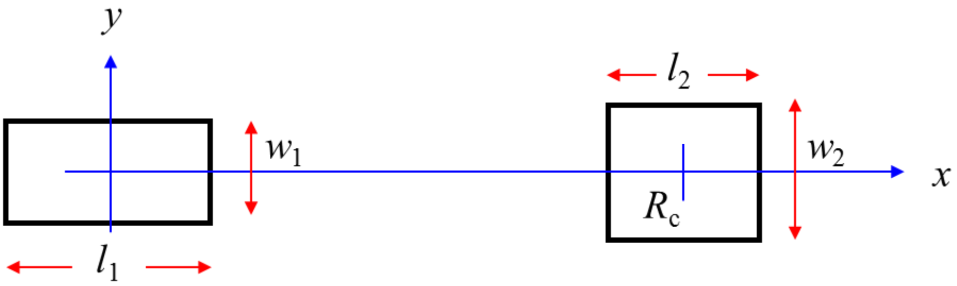

Fig. 4.29. Two *x*-directed inductive meshes lying on the *x* axis.

For one extreme case $R_c \gg l_1$, we can approximate Λ_{12} as

$$\Lambda_{12} \cong \frac{\mu_0}{4\pi}\frac{e^{-jkR}}{w_1 w_2 R}\int_{-\frac{w_1}{2}}^{\frac{w_1}{2}} dy_1 \int_{-\frac{w_2}{2}}^{\frac{w_2}{2}} dy_2 \int_{-\frac{l_1}{2}}^{\frac{l_1}{2}} dx_1 \int_{-\frac{l_2}{2}}^{\frac{l_2}{2}} dx_2 e^{-jk\hat{\mathbf{x}}\cdot(\mathbf{r}_2-\mathbf{r}_1)}$$

$$= \frac{\mu_0}{4\pi}\frac{e^{-jkR_c}}{R_c} l_1 l_2 \operatorname{sinc}\left(\frac{l_1}{\lambda}\right)\operatorname{sinc}\left(\frac{l_2}{\lambda}\right)$$

where the phase term was Taylor expanded to first order, a technique commonly used in far-field integral of antenna currents. An important observation is that the *envelope* of the magnitude of Λ_{ij} decreases as frequency increases, at the rate of $(1 / f^2)$, which corresponds to second-order LPF as in Fig. 4.26. To be quantitative, if $l_1 = l_2 = l$, then the magnitude of Λ_{12} will be 0.707 times its dc value, or 3-dB smaller, when $l = 0.3189\lambda$. Suppose the meshes are discretized according to $\lambda_\mathrm{m}/20$ rule, i.e., $l = \lambda_\mathrm{m} / 20$, then the cutoff frequency of the Galerkin coefficient for distant cells would be $6.4f_m$. The result of this simple model is found to be in good agreement with the numerical integration given in Fig. 3 of [40].

At the other extreme, where the two coupled cells are close to each other, numerical integration has confirmed that the cutoff frequency is higher. Taking a 1cm×1cm square patch as the limiting case, the absolute value of its self-inductance Λ_{11}, as shown in Fig. 4.17, is found to drop to 0.707 times its dc value (3dB smaller) at roughly $10f_m$. Similar behavior was also confirmed by Fig. 3 of [40]. Combining this two extreme cases, we conclude that the cutoff frequency of the Galerkin coupling coefficient, either for distant or closely-spaced meshes, due to its intrinsic damping, is somewhere between $6f_\mathrm{m}$ to $10f_\mathrm{m}$. Consequently, when we set $f_\mathrm{c} = 10f_\mathrm{m}$, although the coupling coefficients at $f = f_\mathrm{m}$ will experience 10% deviation from the undamped case, they are actually closer to the Galerkin's results, i.e., the coefficients before center-to-center approximation. The

doi: 10.6342/NTU201902629

matching would be even better if we use 2nd-order LPF, e.g., MKW + 1st-order KW. In this regard, the cutoff frequency of MKW can be set as small as $6f_\mathrm{m}$ while not being considered as significantly corrupting the low frequency accuracy of the model. Similarly, the cutoff for GRP can also be smaller, but its error is more difficult to quantify.

Finally, we consider the EAR. Since the damping resistor of each node is in series with the capacitor and the VCVS of that node, we conclude that

$$\mathbf{Z}_\mathrm{P} = \frac{\overline{\mathbf{P}}}{j\omega} + \mathbf{R}_\mathrm{P}$$

where $\mathbf{R}_\mathrm{P} = \mathrm{diag}(R_{\mathrm{P}1}, \ldots, R_{\mathrm{P}m})$. We also denote $\mathbf{P}_\mathrm{EAR} = \overline{\mathbf{P}} + s\mathbf{R}_\mathrm{P}$. According to Gershgorin theorem, we know that above a certain frequency, $\mathbf{Z}_\mathrm{P}^{(\mathrm{H})}$ will definitely be positive definite, i.e., the EAR is a consistent damping structure. Different from GRP, there is no matrix-inverse involved, and hence there is no “high-frequency surprise” in EAR. Combination with KW is straightforward:

$$\mathbf{P}_\mathrm{EAR+KW} = \mathbf{P}_\mathrm{KW} + s\mathbf{R}_\mathrm{P}$$

where $\mathbf{P}_\mathrm{KW} = \overline{\mathbf{P}} \circ \mathbf{I}_\mathrm{od} H$.

In this section, we have briefly discussed the general behavior of the damping structures GRP, MKW, KW, and EAR. The focus was on their ability to passivize the inductance or potential matrix, instead of the ability to stabilize a model. Because stability is the property of the whole system, to deal with stability we must consider both the inductance and potential matrices together, under the framework of MNA. As a summary,

doi: 10.6342/NTU201902629

we list the equivalent L or P matrices for these damping structures in the following table, which will be used in the following section.

TABLE 4.3

EQUIVALENT L AND P MATRICES FOR VARIOUS DAMPING STRUCTURE

$\mathbf{L}_{\mathrm{KW}} = \bar{\mathbf{L}} \circ \mathbf{I}_{\mathrm{od}} H$	$\mathbf{P}_{\mathrm{KW}} = \bar{\mathbf{P}} \circ \mathbf{I}_{\mathrm{od}} H$
$\mathbf{L}_{\mathrm{GRP}} = (\bar{\mathbf{L}}^{-1} + s\mathbf{R}_{\mathrm{L}}^{-1})^{-1}$	$\mathbf{P}_{\mathrm{EAR}} = \bar{\mathbf{P}} + s\mathbf{R}_{\mathrm{P}}$
$\mathbf{L}_{\mathrm{GRP+KW}} = (\mathbf{L}_{\mathrm{KW}}^{-1} + s\mathbf{R}_{\mathrm{L}}^{-1})^{-1}$	$\mathbf{P}_{\mathrm{EAR+KW}} = \mathbf{P}_{\mathrm{KW}} + s\mathbf{R}_{\mathrm{P}}$
$\mathbf{L}_{\mathrm{MKW}} = \bar{\mathbf{L}} \left(\frac{\mathbf{R}_{\mathrm{L}}}{s\mathbf{L}_{\mathrm{d}} + \mathbf{R}_{\mathrm{L}}} \right)$	$H(s) = \frac{1}{1+\frac{s}{\omega_{\mathrm{c}}}}$ 1st-order
$\mathbf{L}_{\mathrm{MKW+KW}} = \mathbf{L}_{\mathrm{KW}} \frac{\mathbf{R}_{\mathrm{L}}}{s\mathbf{L}_{\mathrm{d}} + \mathbf{R}_{\mathrm{L}}}$	$H(s) = \frac{1}{1+\frac{\sqrt{2}}{\omega_{\mathrm{c}}}s+\frac{s^2}{\omega_{\mathrm{c}}^2}}$ 2nd-order Butterworth
$\mathbf{L}_{\mathrm{d}} = \mathrm{diag}\big(\mathrm{diag}(\bar{\mathbf{L}})\big)$	$\mathbf{I}_{\mathrm{od}} = \underline{\mathbf{1}} - \mathbf{I}_{\mathrm{d}}$

4.4.3 Damping Design based on Stability

In this section, we propose a damping design method based on stability arguments. Recall that in section 4.2, we presented the Newton algorithm to numerically find out all the ground pole locations of an undamped PEEC. From several examples we have seen that the ground poles are already causing instability, even if we know nothing about the sky poles. Consequently, in order to stabilize the system, a necessary condition is to make those unstable ground poles stable, i.e., move back to LHP. The ground pole locations will be calculated by an extension of the Newton method. When this goal is achieved, then the PEEC model will be stable if all the sky poles are stable. It is the fundamental concept of the proposed design method. Although we cannot ensure the stability of the sky poles, the result still serves to define a minimum required damping level, i.e., a lower bound. There has been no other methods so far in the literature that could provide this information.

The key is to obtain the ground pole locations when damping is added. Recall the QI formulation of the reduced MNA for an undamped PEEC model:

$$\begin{pmatrix} s\mathbf{I}_\mathrm{d} + \mathbf{Y}\bar{\mathbf{P}} & \mathbf{A} \\ \mathbf{A}^\mathrm{T}\bar{\mathbf{P}} & -(\mathbf{R} + s\bar{\mathbf{L}}) \end{pmatrix} \begin{pmatrix} \mathbf{Q} \\ \mathbf{I} \end{pmatrix} = \begin{pmatrix} \mathbf{I}_\mathrm{s} \\ -\mathbf{V}_\mathrm{s} \end{pmatrix}$$

From the study in section 4.4.3, we see that the MNA for a damped PEEC is simply

$$\mathbf{F}(s) \begin{pmatrix} \mathbf{Q} \\ \mathbf{I} \end{pmatrix} = \begin{pmatrix} s\mathbf{I}_\mathrm{d} + \mathbf{Y}\mathbf{P}_\mathrm{eq} & \mathbf{A} \\ \mathbf{A}^\mathrm{T}\mathbf{P}_\mathrm{eq} & -\left(\mathbf{R} + s\mathbf{L}_\mathrm{eq}\right) \end{pmatrix} \begin{pmatrix} \mathbf{Q} \\ \mathbf{I} \end{pmatrix} = \begin{pmatrix} \mathbf{I}_\mathrm{s} \\ -\mathbf{V}_\mathrm{s} \end{pmatrix}$$

where $\mathbf{P}_\mathrm{eq}$ and $\mathbf{L}_\mathrm{eq}$ are the equivalent potential and inductance matrices of the corresponding damping structures, such as $\mathbf{P}_\mathrm{EAR}$ and $\mathbf{L}_\mathrm{MKW}$. If, for example, the potential coupling is not damped, then $\mathbf{P}_\mathrm{eq} = \bar{\mathbf{P}}$. The natural frequencies or poles are the complex scalars *s* such that

$$\det \begin{pmatrix} s\mathbf{I}_\mathrm{d} + \mathbf{Y}\mathbf{P}_\mathrm{eq} & \mathbf{A} \\ \mathbf{A}^\mathrm{T}\mathbf{P}_\mathrm{eq} & -\left(\mathbf{R} + s\mathbf{L}_\mathrm{eq}\right) \end{pmatrix} = 0$$

The mathematical form is not different from the undamped case. Further, if the cutoff frequency $f_\mathrm{c} \gg f_\mathrm{m}$, then at frequencies $f \ll f_\mathrm{c}$, we have $\mathbf{L}_\mathrm{eq} \approx \bar{\mathbf{L}}$ and $\mathbf{P}_\mathrm{eq} \approx \bar{\mathbf{P}}$ for all damping structures. Hence the ground poles for the damped case will be close to the undamped case if $f_\mathrm{c} \gg f_\mathrm{m}$. This property can be exploited to set up an iterative pole search algorithm. As in the undamped case where we defined a delay-sweeping parameter *t* that

doi: 10.6342/NTU201902629

gradually put the delay into the QS PEEC model, here we introduce a damping-sweeping parameter *r* that gradually add the damping into the undamped model. For simplicity, we set the capacitive damping (EAR), inductive damping (GRP and MKW), and mutual damping (KW) all to have the same cutoff frequency f_c. Then, the bifurcation parameter *r* can be expressed as

$$r = \frac{\text{Nominal } f_\mathrm{c}}{\text{Actual } f_\mathrm{c}}$$

The undamped case corresponds to $r = 0$ because the actual $f_\mathrm{c} = \infty$. For $0 < r < 1$, it corresponds to a less damped model, compared with the nominal damping. The equivalent potential and inductance matrices for various cases are modified accordingly, as listed in the following table.

TABLE 4.4

Equivalent L and P Matrices for Various Damping Structure, with the Inclusion of the Bifurcation Parameter *r*

$\mathbf{L}_\mathrm{KW} = \bar{\mathbf{L}} \circ \mathbf{I}_\mathrm{od} H$	$\mathbf{P}_\mathrm{KW} = \bar{\mathbf{P}} \circ \mathbf{I}_\mathrm{od} H$
$\mathbf{L}_\mathrm{GRP} = (\bar{\mathbf{L}}^{-1} + rs\mathbf{R}_\mathrm{L}^{-1})^{-1}$	$\mathbf{P}_\mathrm{EAR} = \bar{\mathbf{P}} + rs\mathbf{R}_\mathrm{P}$
$\mathbf{L}_\mathrm{GRP+KW} = (\mathbf{L}_\mathrm{KW}^{-1} + rs\mathbf{R}_\mathrm{L}^{-1})^{-1}$	$\mathbf{P}_\mathrm{EAR+KW} = \mathbf{P}_\mathrm{KW} + rs\mathbf{R}_\mathrm{P}$
$\mathbf{L}_\mathrm{MKW} = \bar{\mathbf{L}} \left(\frac{\mathbf{R}_\mathrm{L}}{rs\mathbf{L}_\mathrm{d} + \mathbf{R}_\mathrm{L}} \right)$	$H(s) = \frac{1}{1+\frac{rs}{\omega_\mathrm{c}}}$ 1st-order
$\mathbf{L}_\mathrm{MKW+KW} = \mathbf{L}_\mathrm{KW} \frac{\mathbf{R}_\mathrm{L}}{rs\mathbf{L}_\mathrm{d} + \mathbf{R}_\mathrm{L}}$	$H(s) = \left(1 + \frac{\sqrt{2}}{\omega_\mathrm{c}} rs + \frac{(rs)^2}{\omega_\mathrm{c}^2}\right)^{-1}$ 2nd-order
$\mathbf{L}_\mathrm{d} = \mathrm{diag}\big(\mathrm{diag}(\bar{\mathbf{L}})\big)$	$\mathbf{I}_\mathrm{od} = \underline{\mathbf{1}} - \mathbf{I}_\mathrm{d}$

As before, we seek for a scalar *s* and a normalized vector **X**, written together as $\mathbf{y} = \begin{pmatrix} s \\ \mathbf{X} \end{pmatrix}$, that satisfy

$$\mathbf{f}(\mathbf{y}) = \begin{pmatrix} \mathbf{F}(r,s)\mathbf{X} \\ \mathbf{e}_K^{\mathrm{T}}\mathbf{X} - 1 \end{pmatrix} = 0$$

This root-finding equation is then solved by the classic multivariate Newton's method:

$$\mathbf{y}_{k+1} = \mathbf{y}_k - \mathbf{J}(\mathbf{y}_k)^{-1}\mathbf{f}(\mathbf{y}_k)$$

where **J**(**y**) is the Jacobian of **f** (**y**) given by

$$\mathbf{J}(\mathbf{y}) = \left(\frac{\partial f_i}{\partial y_j}\right) = \begin{pmatrix} \dfrac{\partial \mathbf{F}}{\partial s}\mathbf{X} & \mathbf{F}(r,s) \\ 0 & \mathbf{e}_K^{\mathrm{T}} \end{pmatrix}$$

The derivatives of **F** with respect to *s* is

$$\frac{\partial \mathbf{F}}{\partial s} = \begin{pmatrix} \mathbf{I}_{\mathrm{d}} + \mathbf{Y}\dfrac{\partial \mathbf{P}_{\mathrm{eq}}}{\partial s} & 0 \\ \mathbf{A}^{\mathrm{T}}\dfrac{\partial \mathbf{P}_{\mathrm{eq}}}{\partial s} & -\mathbf{L}_{\mathrm{eq}} - s\dfrac{\partial \mathbf{L}_{\mathrm{eq}}}{\partial s} \end{pmatrix}$$

The derivatives of the P and L matrices are documented in the following table.

TABLE 4.5

THE DERIVATIVES OF THE L AND P MATRICES FOR VARIOUS DAMPING STRUCTURES

$\frac{\partial}{\partial s}\mathbf{L}_{\mathrm{KW}} = \frac{\partial \bar{\mathbf{L}}}{\partial s} \circ \mathbf{I}_{\mathrm{od}}H + \bar{\mathbf{L}} \circ \mathbf{I}_{\mathrm{od}}\frac{\partial H}{\partial s}$	$\frac{\partial}{\partial s}\mathbf{P}_{\mathrm{KW}} = \frac{\partial \bar{\mathbf{P}}}{\partial s} \circ \mathbf{I}_{\mathrm{od}}H + \bar{\mathbf{P}} \circ \mathbf{I}_{\mathrm{od}}\frac{\partial H}{\partial s}$
$\frac{\partial}{\partial s}\mathbf{L}_{\mathrm{MKW}} = \frac{\partial \bar{\mathbf{L}}}{\partial s}\left(\frac{\mathbf{R}_{\mathrm{L}}}{rs\mathbf{L}_{\mathrm{d}} + \mathbf{R}_{\mathrm{L}}}\right) - \bar{\mathbf{L}}\frac{r\mathbf{L}_{\mathrm{d}}\mathbf{R}_{\mathrm{L}}}{(rs\mathbf{L}_{\mathrm{d}} + \mathbf{R}_{\mathrm{L}})^2}$	$\frac{\partial}{\partial s}\mathbf{P}_{\mathrm{EAR}} = \frac{\partial \bar{\mathbf{P}}}{\partial s} + r\mathbf{R}_{\mathrm{P}}$
$\frac{\partial}{\partial s}\mathbf{L}_{\mathrm{MKW+KW}} = \frac{\partial \mathbf{L}_{\mathrm{KW}}}{\partial s}\frac{\mathbf{R}_{\mathrm{L}}}{rs\mathbf{L}_{\mathrm{d}} + \mathbf{R}_{\mathrm{L}}} - \mathbf{L}_{\mathrm{KW}}\frac{r\mathbf{L}_{\mathrm{d}}\mathbf{R}_{\mathrm{L}}}{(rs\mathbf{L}_{\mathrm{d}} + \mathbf{R}_{\mathrm{L}})^2}$	$\frac{\partial}{\partial s}\mathbf{P}_{\mathrm{EAR+KW}} = \frac{\partial \mathbf{P}_{\mathrm{KW}}}{\partial s} + r\mathbf{R}_{\mathrm{P}}$
$\frac{\partial}{\partial s}H(s) = \frac{\partial}{\partial s}\left(1 + \frac{rs}{\omega_{\mathrm{c}}}\right)^{-1} = -\frac{r}{\omega_c}H^2$ 1st-order	
$\frac{\partial}{\partial s}H(s) = \frac{\partial}{\partial s}\left(1 + \sqrt{2}\frac{rs}{\omega_{\mathrm{c}}} + \frac{(rs)^2}{\omega_{\mathrm{c}}^2}\right)^{-1} = -\left(\frac{\sqrt{2}r}{\omega_{\mathrm{c}}} + 2\frac{r^2 s}{\omega_{\mathrm{c}}^2}\right)H^2$ 2nd-order Butterworth	

The derivative for $\mathbf{L}_{\mathrm{GRP}}$ is more complicated since it involves matrix inversion. For any invertible matrix $\mathbf{A}$ whose elements are differentiable functions of s, we have

$$0 = \frac{\mathrm{d}}{\mathrm{d}s}\mathbf{I}_{\mathrm{d}} = \frac{\mathrm{d}}{\mathrm{d}s}(\mathbf{A}\mathbf{A}^{-1}) = \frac{\mathrm{d}\mathbf{A}}{\mathrm{d}s}\mathbf{A}^{-1} + \mathbf{A}\frac{\mathrm{d}\mathbf{A}^{-1}}{\mathrm{d}s}$$

Thus $\frac{\mathrm{d}\mathbf{A}^{-1}}{\mathrm{d}s} = -\mathbf{A}^{-1}\frac{\mathrm{d}\mathbf{A}}{\mathrm{d}s}\mathbf{A}^{-1}$. Using this formula, we have

$$\frac{\partial}{\partial s}\mathbf{L}_{\mathrm{GRP}} = -\mathbf{L}_{\mathrm{GRP}}\left[\frac{\partial}{\partial s}(\bar{\mathbf{L}}^{-1} + rs\mathbf{R}_{\mathrm{L}}^{-1})\right]\mathbf{L}_{\mathrm{GRP}} = -\mathbf{L}_{\mathrm{GRP}}\left[-\bar{\mathbf{L}}^{-1}\frac{\partial\bar{\mathbf{L}}}{\partial s}\bar{\mathbf{L}}^{-1} + r\mathbf{R}_{\mathrm{L}}^{-1}\right]\mathbf{L}_{\mathrm{GRP}}$$

$$\frac{\partial}{\partial s}\mathbf{L}_{\mathrm{GRP+KW}} = -\mathbf{L}_{\mathrm{GRP+KW}}\left[-\mathbf{L}_{\mathrm{KW}}^{-1}\frac{\partial\mathbf{L}_{\mathrm{KW}}}{\partial s}\mathbf{L}_{\mathrm{KW}}^{-1} + r\mathbf{R}_{\mathrm{L}}^{-1}\right]\mathbf{L}_{\mathrm{GRP+KW}}$$

The initial guesses for the iteration will be the poles and mode vectors of the undamped case, i.e., the results of section 4.2 with $t = 1$. When r is very small, e.g., $r = 0.1$, the damped pole locations and mode vectors can be expected to be close to the undamped case. Hence, a few iterations would suffice to converge to the solution, usually smaller than five iterations. The termination conditions are identical to that in section 4.2. The scaling coefficient is also the same. Note that the damping resistors, $\mathbf{R}_{\mathrm{L}}$ and $\mathbf{R}_{\mathrm{P}}$, are not scaled, while the cutoff frequency f_{c} is scaled as $f_{\mathrm{c}}' = af_{\mathrm{c}}$.

First we consider again the coplanar strip example with $N = 10$ current meshes for each strip. In section 4.2.3, we have seen that the undamped model has one unstable ground pole, as shown in Fig.4.5. The results of transient simulation suggested that it is the only unstable pole of the system; or, if there is another unstable pole, it must be either too close to the imaginary axis such that it needs an extremely long time to show up, or it is just suppressed by the numerical damping of SPICE because its frequency is too high.

Fig. 4.30 shows the pole loci for EAR with nominal cutoff $f_c = 100f_m = 75$ GHz. As before, 'x' denote the starting QS poles. Squares □ and diamonds ◊ are intermediate poles during delay and damping sweeping, respectively. The final poles are O for stable ones and Δ for unstable ones. In obtaining Fig. 4.30, we used a coarser t: [0, 0.25, 0.5, 0.75, 1]. The damping parameter r is [0.01, 0.02, 0.1, 0.2], which correspond to actual cutoff [10000, 5000, 1000, 500] × f_m. Since the actual cutoff frequencies are all ≫ f_m, the low frequency poles ($f < 3f_m$) almost stand still during the damping sweeping, and we hardly see the diamonds because they are overlapped by the final 'O'. It means that in time domain, the signal of interest will not be much affected by this EAR damping.

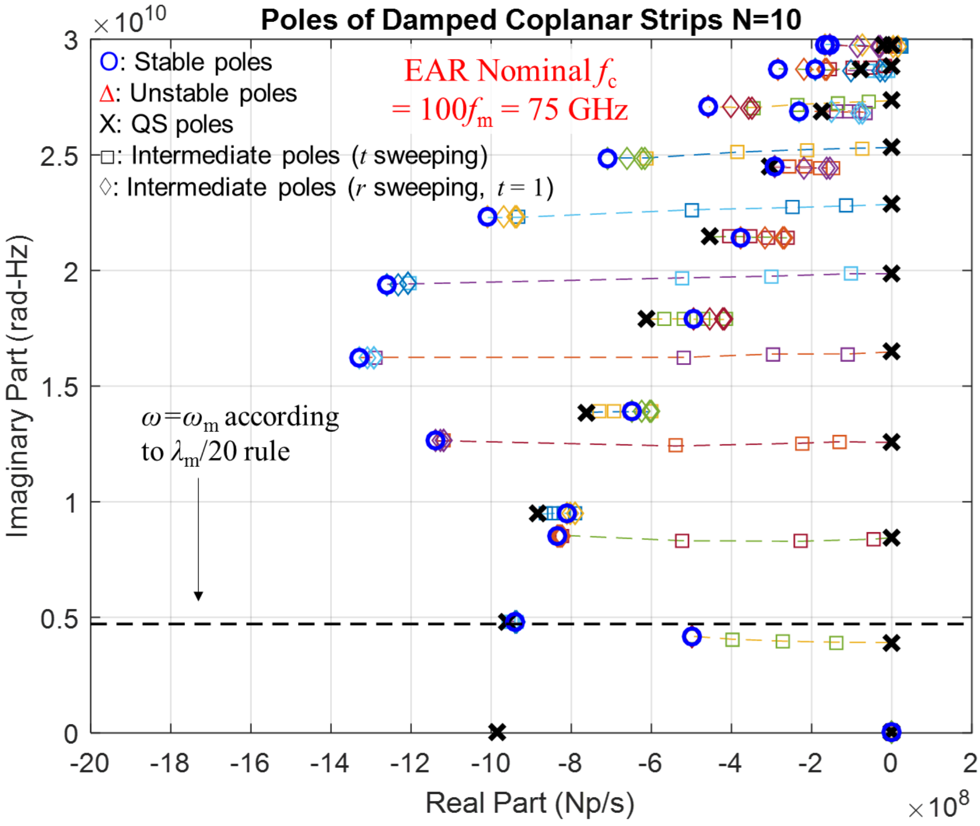

Fig. 4.30. Ground poles of the coplanar strips with N = 10 under EAR damping. The nominal cutoff frequency is $f_c = 100f_m$, while the sweeping parameter r is [0.01, 0.02, 0.1, 0.2], which correspond to the actual cutoff frequencies [10000, 5000, 1000, 500] × f_m.

doi: 10.6342/NTU201902629

The vital part is the locus of the unstable pole, which is enlarged in Fig. 4.31. We clearly see that the unstable pole goes left as EAR is gradually added in. From the figure we can also quantitatively conclude that the model remains unstable if the actual cutoff is 3750 GHz. The pole location is recorded as shown. When the actual cutoff is reduced to 750 GHz, all the ground poles are stable. If there is no unstable sky poles, then the PEEC model is fully stabilized.

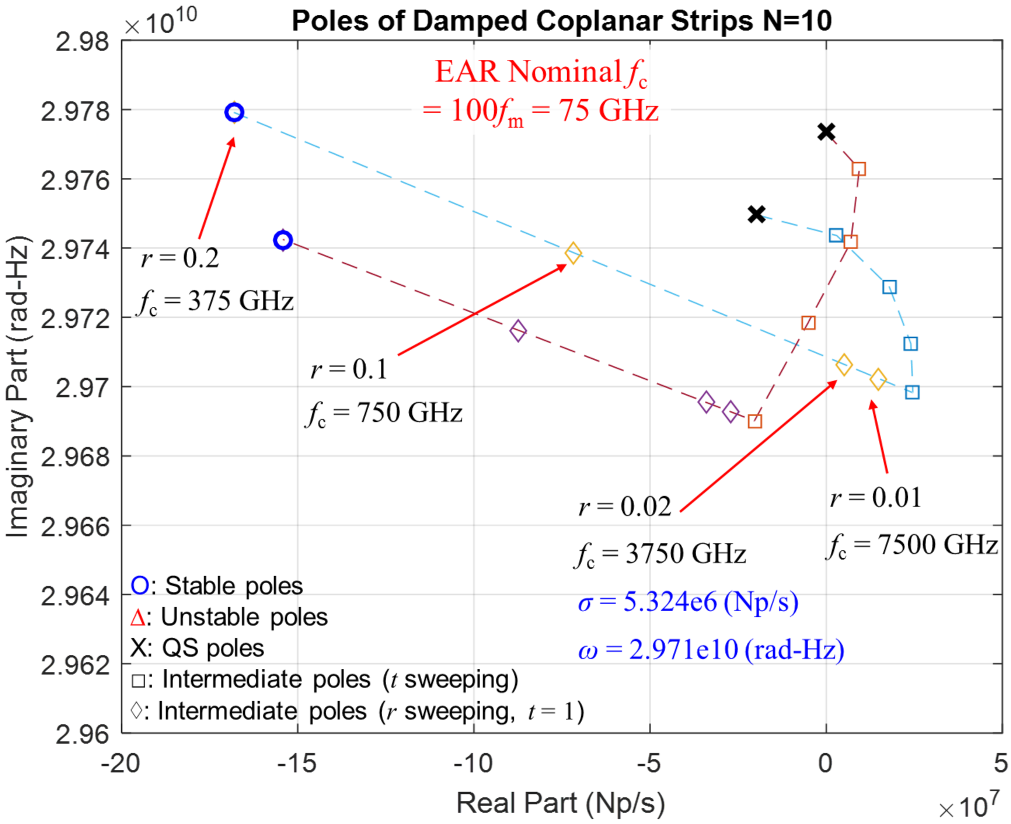

Fig. 4.31. The two highest frequency ground poles of the coplanar strips with N = 10 and EAR damping.

To verify the above result, we resort to the same method as in section 4.2.3. The PEEC model of the r = 0.02 case is exported into a subcircuit file and loaded into ADS. The transient results are shown in Fig. 4.32. Instability shows up as expected. Compared

doi: 10.6342/NTU201902629

with Fig. 4.5, however, we see that because the real part of the pole becomes five times smaller, it takes 600 ns for the amplitude of the resonance to reach 300 mV. From the enlarged response between 550 and 553 ns, we find that the estimated ω is within 0.71% error, and from the log-abs plot, the error of the estimated σ is 12.7%.

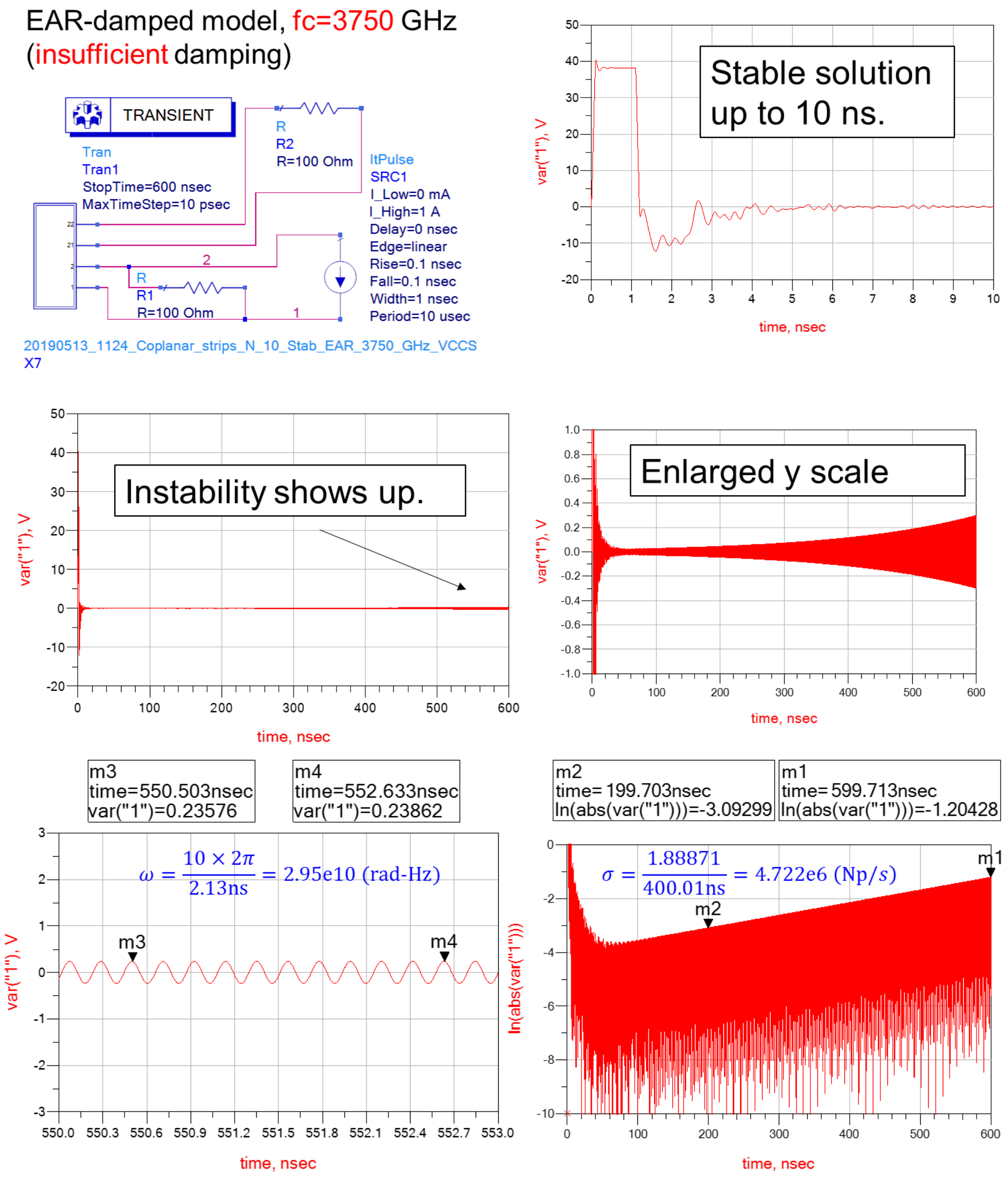

Fig. 4.32. Transient simulation results of the coplanar strip transmission line with $N = 10$, and EAR damping with actual cutoff frequency $f_c = 5000 f_m = 3750$ GHz.

Next, we simulate the $r = 0.1$ case, i.e., $f_c = 1000 f_m = 750$ GHz. The log-abs result is shown in Fig. 4.33, from which we observe stable waveform even up to 1 us. Note that the steady state voltage is roughly around $\exp(-30) \approx 9\times10^{-14}$, which is very close to the limit of double precision storage. From this result, we can almost conclude that the model is stable. At least, if there is any unstable sky poles, they are effectively suppressed by the numerical damping of ADS under the current setting.

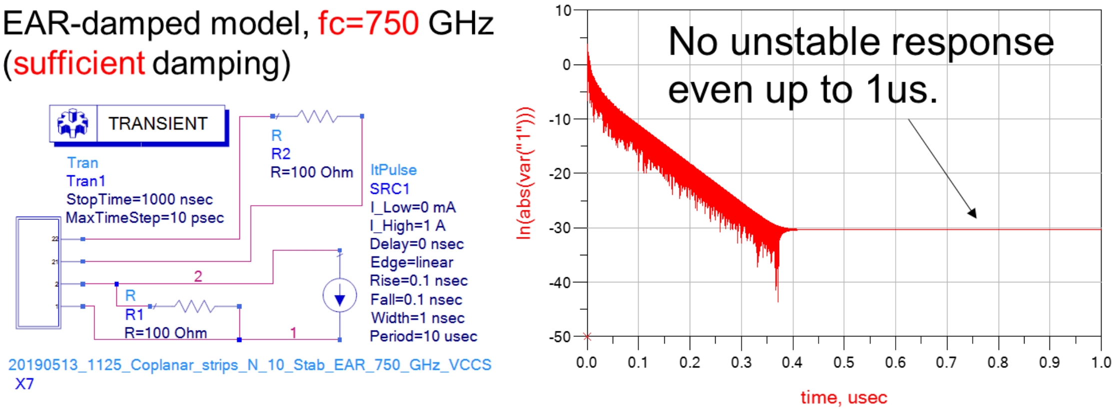

Fig. 4.33. Transient simulation results (log-abs plot) of the EAR-damped coplanar strips (N = 10). The actual cutoff is 750 GHz. According to the calculation of Fig. 4.31, the unstable ground pole is removed.

Next, we test the MKW structure with the same setting. The locus of the unstable pole is shown in Fig. 4.34, which is slightly different from the EAR case. The ADS simulation results for the $f_c = 3750$ GHz case are shown in Fig. 4.35, which verify that it is indeed unstable. The estimated pole location is consistent with the transient waveform as shown.

doi: 10.6342/NTU201902629

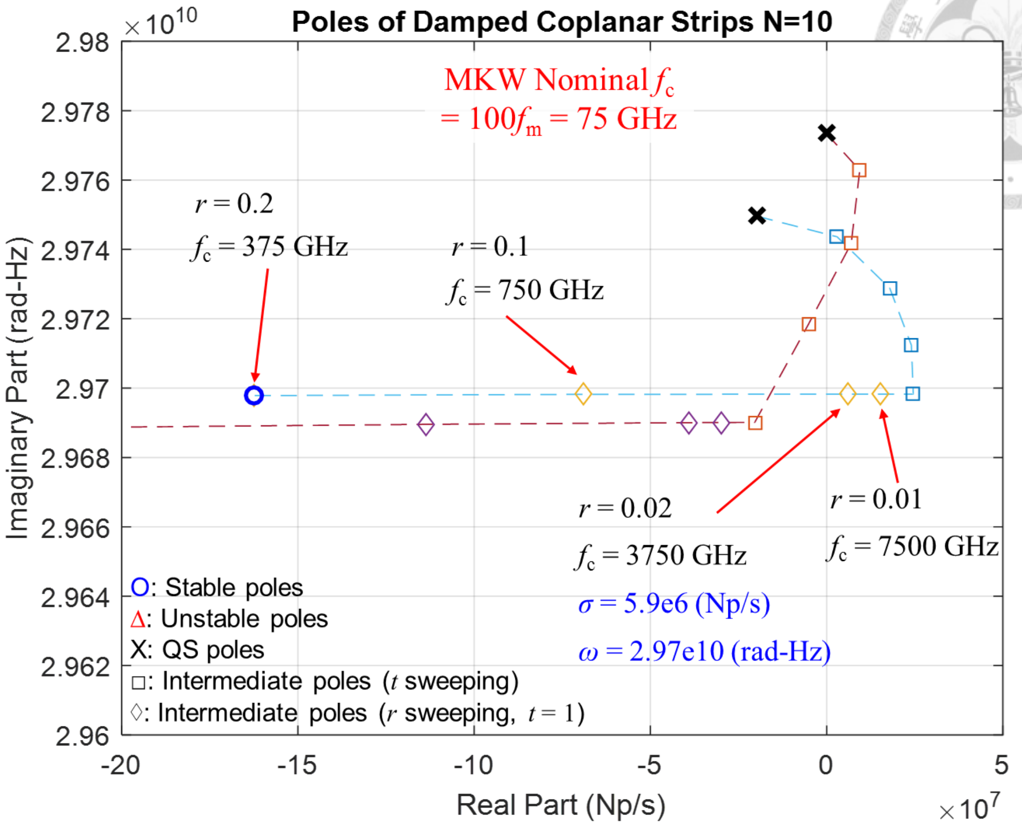

Fig. 4.34. The two highest frequency ground poles of the coplanar strips with $N = 10$ and MKW damping. The damping settings are the same as the EAR case. Nominal $f_c = 100f_m$.

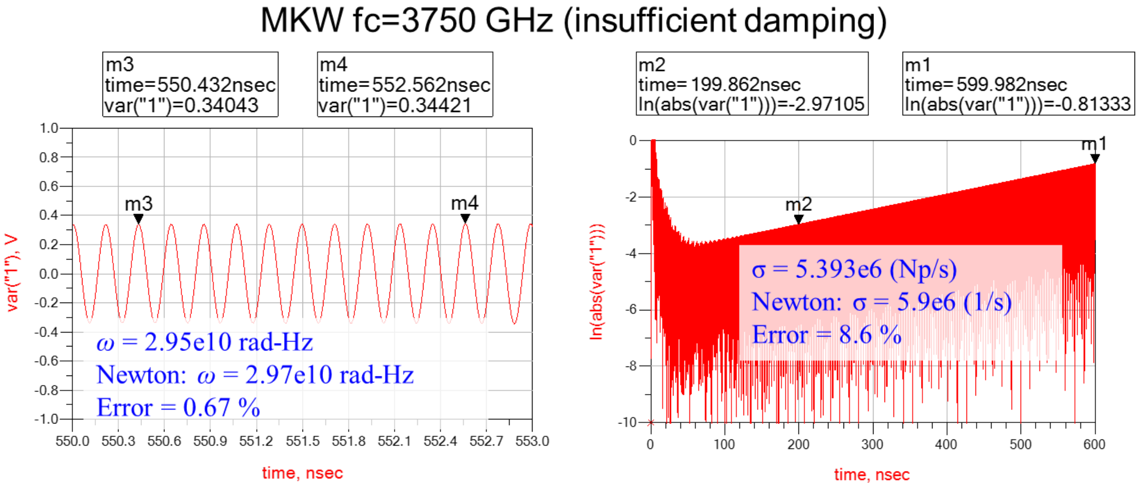

Fig. 4.35. Transient simulation results of the MKW-damped coplanar strips. Actual cutoff $f_c = 3750$ GHz, which is insufficient according to Fig. 4.34.

The result of the f_c = 750 GHz case is shown in Fig. 4.36. Again, the steady state voltage drops to machine precision, indicating there is no any other unstable pole.

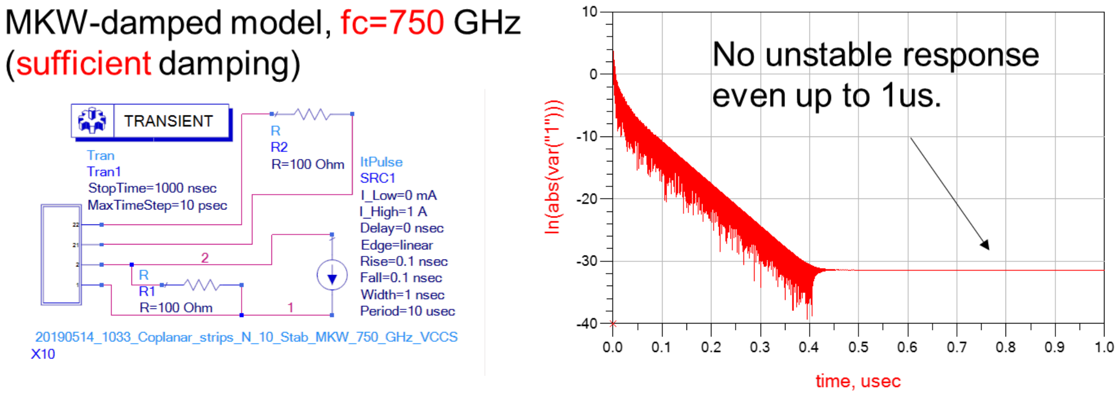

Fig. 4.36. Transient simulation results (log-abs plot) of the MKW-damped coplanar strips with N = 10. The actual cutoff is f_c = 750 GHz, which is sufficient to remove the unstable ground pole according to Fig. 4.34. The time domain waveform further indicates that there is no other unstable sky pole.

Next, we test the GRP structure with the same setting. The locus of the unstable pole is shown in Fig. 4.37, which is again slightly different from the previous two cases. Since the correctness of the algorithm has been verified, we do not perform transient simulation for this case.

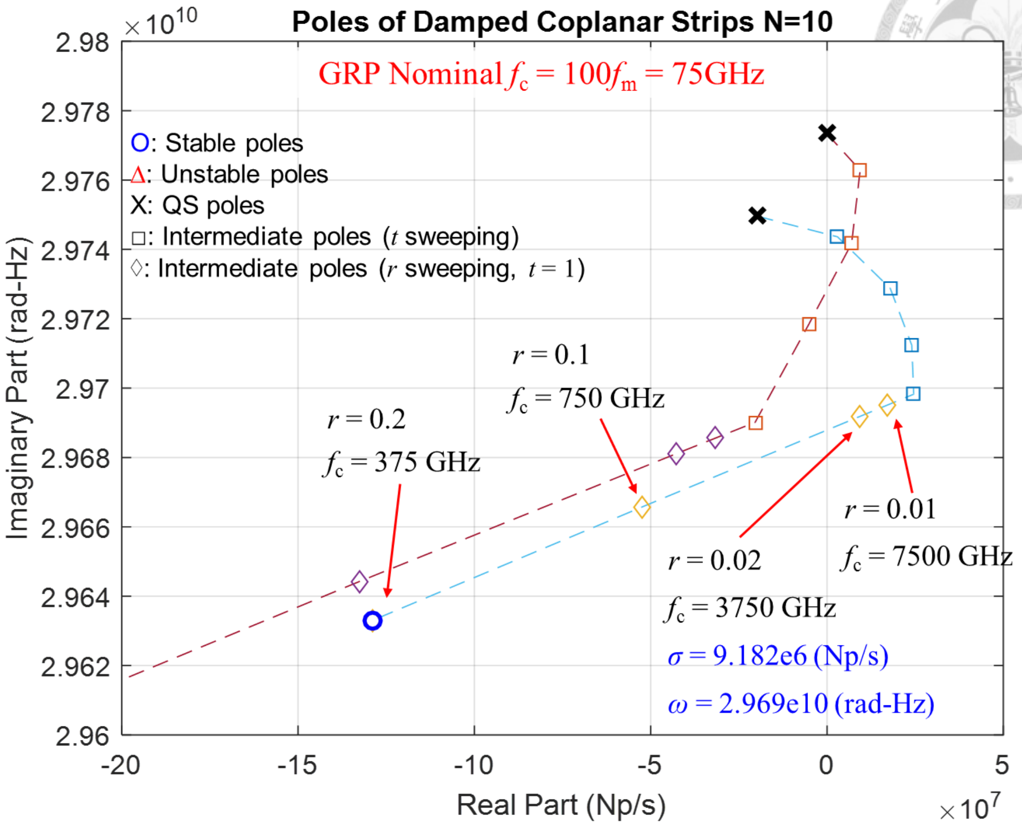

Fig. 4.37. The two highest frequency ground poles of the coplanar strips with N = 10 and GRP damping. The damping settings are the same as the EAR case. Nominal $f_c = 100f_m$.

From the results of EAR, MKW, and GRP, we have several observations. First, any single damping structure may be sufficient to stabilize the circuit. Combination of different damping structures is helpful but not necessary. Second, when damping is added into the circuit, the unstable pole will go left, which is intuitive. Third, it is quite a surprise that, in order to *stabilize* the model, we do not need a very low cutoff frequency. In all cases above, it suffices to set $f_c = 1000f_m$. In contrast, in Garrett's study [50], the suggested cutoff was between $10f_m$ to $100f_m$. Her argument is based on the passivity of the port impedance $\mathbf{Z}_{in}$. Comparing both results, we realize that to *passivize* the model is a much more challenging task than simply to *stabilize* it.

Next, we test the KW structure. The parameter r is still [0.01, 0.02, 0.1, 0.2]. As noted before, the KW should not be used alone. To see this, Fig. 4.38 shows the root locus of the unstable pole when the nominal $f_c = f_m$, a very low cutoff frequency compared with previous cases. The result shows that for the actual cutoff $f_c = 5f_m$, the unstable pole just moves to the imaginary axis, and is still in RHP. This demonstrates that to achieve a better stabilizing effect, KW should be used in conjunction with other damping structures.

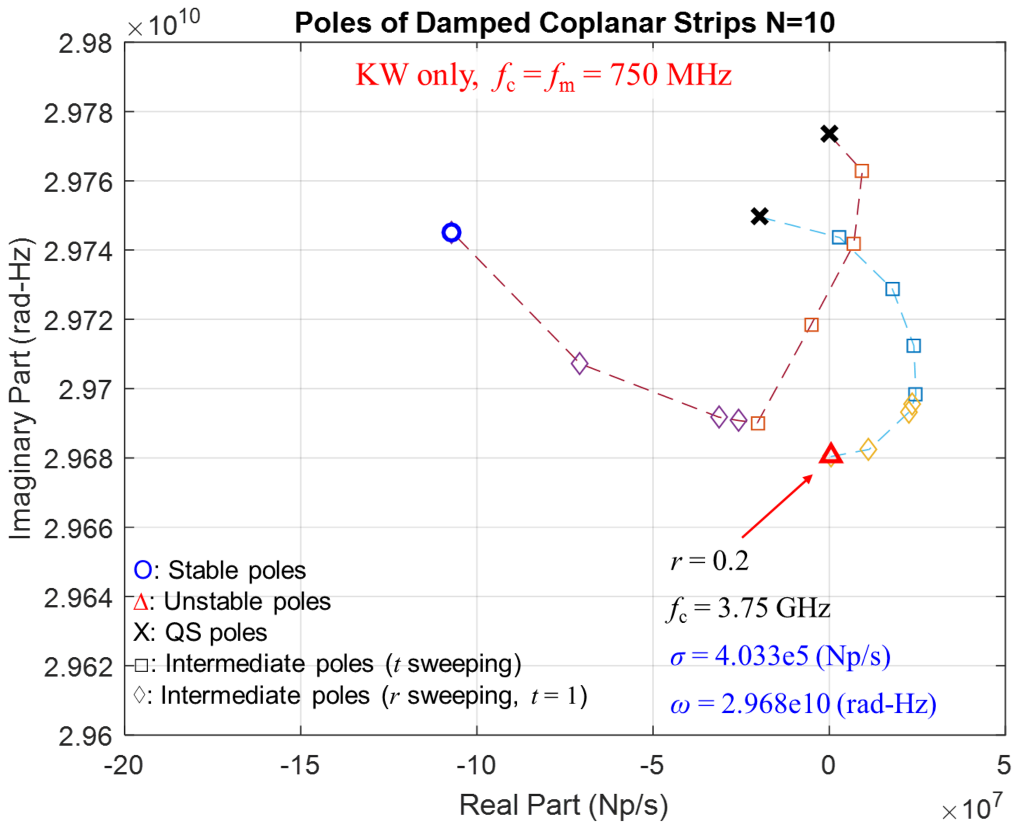

Fig. 4.38. The two highest frequency ground poles of the coplanar strips with N = 10 and KW damping. The damping settings are the same as the EAR case. Nominal $f_c = 100f_m$.

Recall the undamped N = 100 case of the coplanar strips, which exhibits a number of unstable poles as shown in Fig. 4.11. Under the same settings, the MKW and GRP structures are applied to improve the stability. The results are shown in Fig. 4.39, and the loci of the highest frequency poles are enlarged in the bottom figures. Quite remarkably, even for a model with so many unstable poles, it suffices to use $f_c = 500f_m$ ($r = 0.2$ for nominal $f_c = 100f_m$) to achieve stabilization, for both methods. It again exemplifies the difference between stability and passivity. Another point worth comparing is the impact of damping on the low frequency poles. Comparing MKW and GRP, we see that the low frequency poles of GRP tend to travel longer distance than MKW when damping is added in. It means that the MKW may retain a better low frequency accuracy.

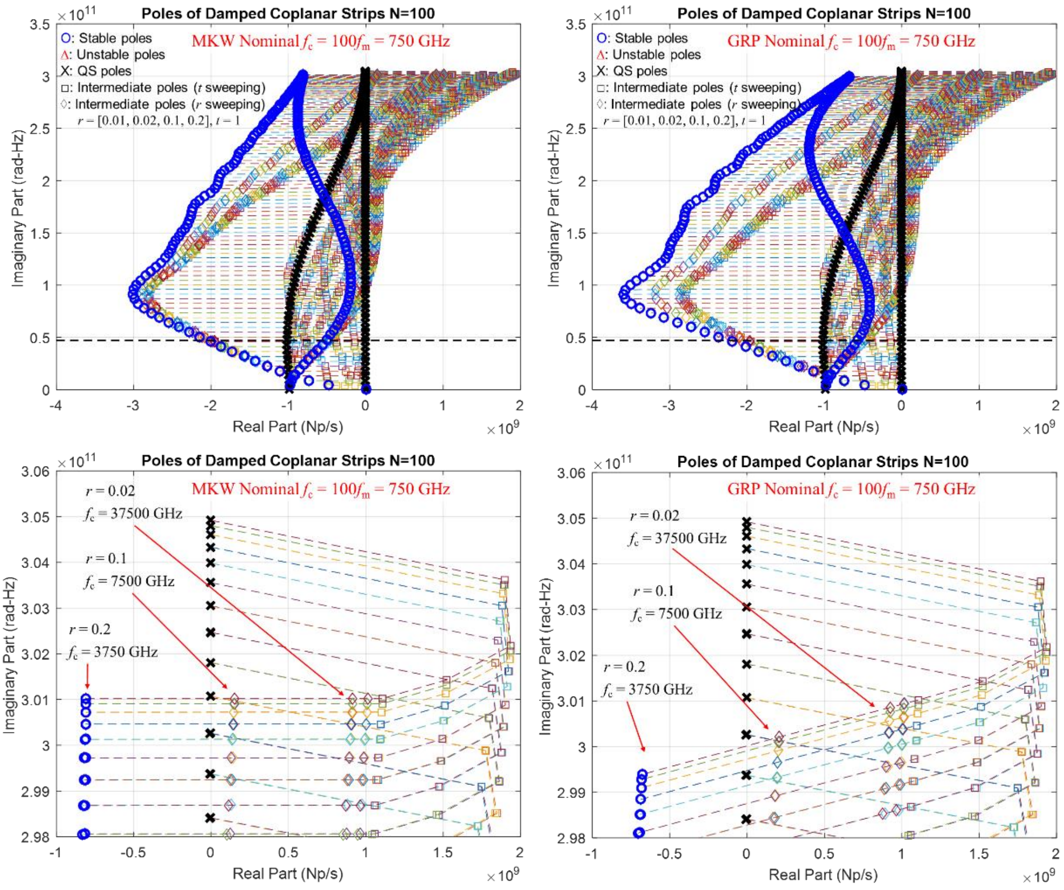

Fig. 4.39. Ground poles of the coplanar strips with $N = 100$ under MKW and GRP damping. Damping settings are the same as previously. Nominal $f_c = 100f_m = 750$ GHz.

In summary, in this subsection we extended the Newton pole algorithm to include various damping structures. With the knowledge of the ground pole locations, we are able to design the damping level to make the model stable, under the assumption that there is no unstable sky poles. This design methodology is different from the passivity-based design method, which we will investigate in detail in the next subsection, in that the required damping level to stabilize the model is usually far less than that required to passivize the model. MATLAB and ADS simulation results have verified that for the cases under study, it suffices to set the cutoff frequency as high as $f_c = 500f_m$ for the purpose of stabilization, which is quite different from model passivization that often need $f_c = 10f_m$ or even smaller.

doi: 10.6342/NTU201902629

4.4.4 Damping Design based on Passivity

The physical structure modelled by PEEC is linear and passive. However, under the standard (undamped) formulation, the model is highly active, as we have seen in section 4.3. Consequently, restoring the passivity of the model by deliberate damping is not only critical for a stable transient simulation, but also physically satisfying. In addition, a passive model can be connected with arbitrary passive circuits and still remains passive and thus stable. On the other hand, a stable but nonpassive model, when connected with other passive circuits, is not guaranteed to be stable [62]. Hence, in the design of damping, the philosophy of passivity-based method [50] [60] is to make the model passive, and thus guaranteed stable under arbitrary passive combination.

In [50] and [60], the passivity indexes are the port impedance Z_{in} and reflection coefficient S_{11} of a one-port model, respectively. A passive one-port should satisfy $\mathrm{Re}\{Z_{\mathrm{in}}(j\omega)\} > 0, \forall\ \omega \in \mathrm{R}$, and $|S_{11}(j\omega)| < 1, \forall\ \omega \in \mathrm{R}$. Any violation of these criterions at any set of frequencies of nonzero measure implies the model is nonpassive. Thus, we could utilize this property to determine the required damping level. In particular, we continue decreasing the cutoff frequency of the damping structure, and/or add in different damping structures, until either criterion is satisfied in an *extended* frequency range, $0 \leq f \leq \beta f_{\mathrm{m}}$, for example $\beta = 1000$, and assume any energy gain due to the non-passivity above βf_{m} will be effectively suppressed by the numerical damping of SPICE.

doi: 10.6342/NTU201902629

In this subsection, we would like to investigate in further detail the passivity issue of a FW PEEC model. The motivation is: what is the proper index of passivity for a general *N*-port? The usual treatment of passivity description of scattering or immittance matrices does not assume any prior knowledge about the interior of the network [56]. The only available information is the port voltages and currents. However, in PEEC we know every construction detail of the model. Can we exploit this information to derive a more thorough passivity index?

Since the energy sources in a FW PEEC is the inductance and potential matrices, $\bar{\mathbf{L}}$ and $\bar{\mathbf{P}}$, an intuitive idea is to separately make both $\mathbf{L}_{\text{eq}}$ and $\mathbf{P}_{\text{eq}}$ passive. We have seen some examples in section 4.4.2 that it is indeed possible to make $\mathbf{L}_{\text{eq}}$ passive, by decreasing the cutoff frequency of GRP or MKW and combining the KW damping. When KW is included, the high frequency passivity is guaranteed because $\mathbf{L}_{\text{KW}}$ will eventually be diagonally dominant. Since the eigenvalue of the inductance matrix is a continuous function of frequency, if we can further show that the negative eigenvalues at $\omega \to 0^+$ can be removed by decreasing cutoff frequency, then we would have essentially prove that the inductance matrix can be fully passivized. The low frequency accuracy is another issue, though.

Recall the low frequency approximation of the Hermitian part of the undamped $\mathbf{Z}_{\text{L}} = j\omega\bar{\mathbf{L}}$, as described in section 4.3.2:

$$\mathbf{Z}_{\mathrm{L}}^{(\mathrm{H})} \approx \omega^2 \frac{\mu_0}{4\pi}\frac{l^2}{c}\begin{bmatrix} 0 & 1 & \cdots & 1 \\ 1 & 0 & \cdots & 1 \\ \vdots & \vdots & \ddots & \vdots \\ 1 & 1 & \cdots & 0 \end{bmatrix} = \omega^2 \frac{\mu_0}{4\pi}\frac{l^2}{c}\left(\underline{\mathbf{1}} - \mathbf{I}_{\mathrm{d}}\right) = \omega^2 \frac{\mu_0}{4\pi}\frac{l^2}{c}\left(\mathbf{I}_{\mathrm{od}}\right)$$

where we assume all current meshes are identical, with the same length *l*. This expression shows that the eigenvalues of $\mathbf{Z}_{\mathrm{L}}^{(\mathrm{H})}$ are roughly $(n-1)\omega^2 \frac{\mu_0}{4\pi}\frac{l^2}{c}$ with multiplicity 1 and $-\omega^2 \frac{\mu_0}{4\pi}\frac{l^2}{c}$ with multiplicity $(n-1)$. Now suppose we apply the MKW structure. The resulting $\mathbf{Z}_{\mathrm{L}}$ is:

$$\mathrm{Z}_{\mathrm{L}} = \begin{bmatrix} \frac{j\omega L_{11} R_{\mathrm{L}1}}{j\omega L_{11} + R_{\mathrm{L}1}} & \cdots & \frac{j\omega \bar{L}_{1n} R_{\mathrm{L}n}}{j\omega L_{nn} + R_{\mathrm{L}n}} \\ \vdots & \ddots & \vdots \\ \frac{j\omega \bar{L}_{1n} R_{\mathrm{L}1}}{j\omega L_{11} + R_{\mathrm{L}1}} & \cdots & \frac{j\omega L_{nn} R_{\mathrm{L}n}}{j\omega L_{nn} + R_{\mathrm{L}n}} \end{bmatrix} = j\omega\bar{\mathbf{L}}\left(\frac{\mathbf{R}_{\mathrm{L}}}{j\omega\mathbf{L}_{\mathrm{d}} + \mathbf{R}_{\mathrm{L}}}\right)$$

At low frequency $\omega \to 0^+$,

$$\mathbf{Z}_{\mathrm{L}} = j\omega\bar{\mathbf{L}}\frac{\mathbf{R}_{\mathrm{L}}}{j\omega\mathbf{L}_{\mathrm{d}} + \mathbf{R}_{\mathrm{L}}} = j\omega\bar{\mathbf{L}}\frac{1}{\mathbf{I}_{\mathrm{d}} + \frac{j\omega\mathbf{L}_{\mathrm{d}}}{\mathbf{R}_{\mathrm{L}}}} \cong j\omega\bar{\mathbf{L}}\left(\mathbf{I}_{\mathrm{d}} - \frac{j\omega\mathbf{L}_{\mathrm{d}}}{\mathbf{R}_{\mathrm{L}}}\right) = j\omega\bar{\mathbf{L}} + \omega^2\bar{\mathbf{L}}\frac{\mathbf{L}_{\mathrm{d}}}{\mathbf{R}_{\mathrm{L}}}$$

By assumption, all self-inductance are identical, and thus $\mathbf{Z}_{\mathrm{L}}$ is reciprocal. Then

$$\mathbf{Z}_{\mathrm{L}}^{(\mathrm{H})} = \mathrm{Re}[\mathbf{Z}_{\mathrm{L}}] \cong -\omega\mathrm{Im}[\bar{\mathbf{L}}] + \omega^2\mathrm{Re}[\bar{\mathbf{L}}]\frac{\mathbf{L}_{\mathrm{d}}}{\mathbf{R}_{\mathrm{L}}}$$

Note that both terms are proportional to ω^2 at low frequencies, and $\mathrm{Re}[\bar{\mathbf{L}}(\omega \to 0^+)] \approx \mathbf{L}$, the QS inductance matrix. Now, if **L** is positive definite, then we can find an $\mathbf{R}_{\mathrm{L}}$ small enough such that all negative eigenvalues of $\mathbf{Z}_{\mathrm{L}}^{(\mathrm{H})}$ at $\omega \to 0^+$ are removed. The positive definiteness of **L** needs to be accomplished by, for example, a proper discretization method such as the projection meshing proposed by [57].

We can further provide an estimate of the required cutoff frequency. Since **L** is positive definite and has strong diagonals (though not necessarily diagonally dominant), the eigenvalues of $\mathbf{L}$ will roughly be around $\mathbf{L}_d$, i.e., its diagonal values. Combining with the results that $\lambda_{\min}(-\omega\text{Im}[\bar{\mathbf{L}}]) \cong -\omega^2 \frac{\mu_0}{4\pi}\frac{l^2}{c}$, we have the following requirement for a positive definite $\mathbf{Z}_L^{(H)}$: $\omega^2 \frac{L_{11}^2}{R_{L1}} > \omega^2 \frac{\mu_0}{4\pi}\frac{l^2}{c}$. Note that typically the self-inductance $L_{11} \cong \frac{\mu_0}{4\pi}\beta l$, where $\beta = O(1)$. Let $l = \lambda_m/20$, and after some manipulation, we have $R_{L1} < 20f_m\beta L_{11} = (10\beta/\pi)\omega_m L_{11}$. It means that to fully passivize the inductance matrix, the ratio of cutoff frequency to f_m, i.e., f_c / f_m, should be around $(10\beta/\pi)$, which is of order 1. Although this estimation is very crude due to the various approximations, it is consistent with MATLAB calculation. For the 1cm×10cm strip in Fig. 4.27, we see that MKW needs $f_c = 3f_m$ to remove all negative eigenvalues. For the coplanar strips example with $N = 50$, we know that $f_c = 10f_m$ is not sufficient to passivize $\mathbf{Z}_L^{(H)}$ according to Fig. 4.28. Instead of further decreasing the cutoff frequencies for both MKW and KW, we find that the negative eigenvalues can be removed if the cutoff for MKW is reduced to $f_c = 2f_m$ while keeping the cutoff of KW at $f_c = 10f_m$, as shown in Fig. 4.40.

doi: 10.6342/NTU201902629

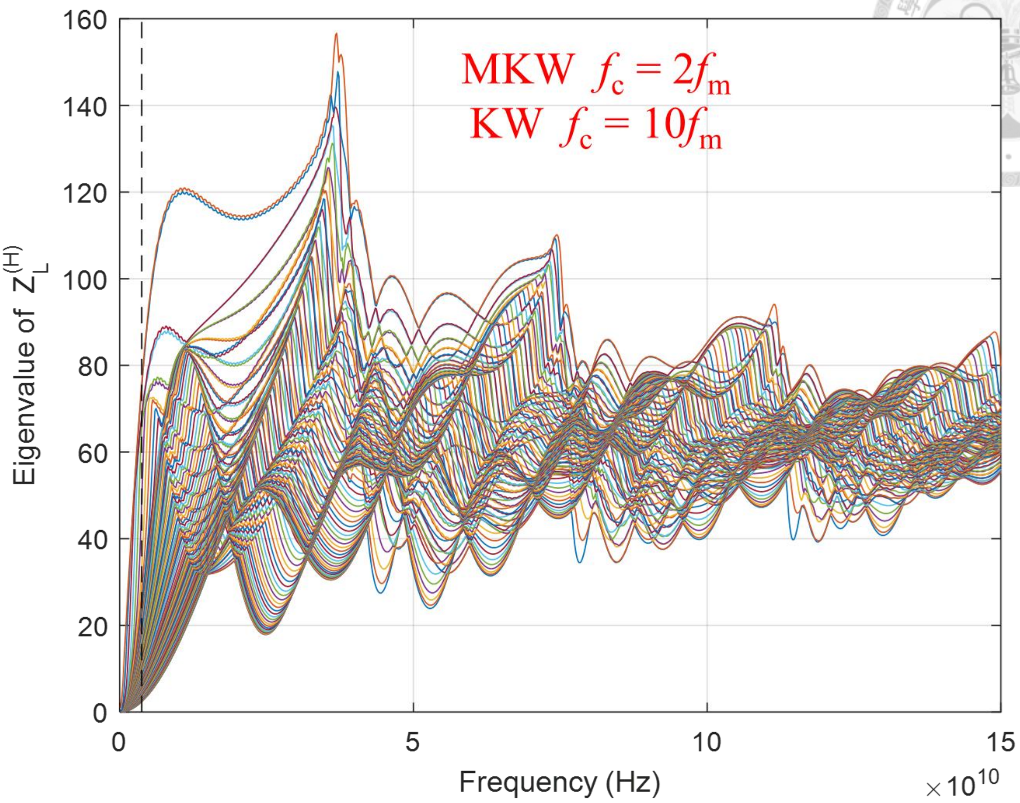

Fig. 4.40. Eigenvalues of $\mathbf{Z}_L^{(H)}$ for the coplanar strips with N = 50 under MKW+KW damping, with cutoff frequencies $2f_m$ and $10f_m$, respectively.

The above discussion shows that the delayed inductive coupling

$$v_i(t) = \sum_{j=1}^{n} L_{ij} \frac{\mathrm{d}}{\mathrm{d}t} i_j\left(t - \tau_{ij}\right)$$

by *itself*, can be made passive by the damping structures, regardless of the potential coupling and other connections in the complete PEEC model. Therefore, these damping structures and corresponding analysis and design have general applicability beyond PEEC. Whenever we encounter a delayed coupling network of the same mathematical form, we may apply the methods here.

The potential matrix $\overline{\mathbf{P}}$, in contrast, is quite different. We saw in section 4.3.2 that

$$\mathbf{Z}_{\mathrm{P}}^{(\mathrm{H})} = \frac{-1}{\omega}\begin{bmatrix} 0 & P_{12}\sin\omega\tau_{12} & \cdots & P_{1m}\sin\omega\tau_{1m} \\ P_{12}\sin\omega\tau_{12} & 0 & \cdots & P_{2m}\sin\omega\tau_{2m} \\ \vdots & \vdots & \ddots & \vdots \\ P_{1m}\sin\omega\tau_{1m} & P_{2m}\sin\omega\tau_{2m} & \cdots & 0 \end{bmatrix} = \frac{-1}{\omega}\{\mathbf{P}\circ\sin(\omega\mathbf{T}_{\mathrm{P}})\}$$

At the low frequency limit $\omega \to 0^+$, $\mathbf{Z}_{\mathrm{P}}^{(\mathrm{H})} \approx -\mathbf{P} \circ \mathbf{T}_{\mathrm{P}}$. Recalling the definition of $\mathbf{P}$ in (1.30), we have $P_{ij}\tau_{ij} \approx \frac{1}{4\pi\varepsilon_0}\frac{1}{R_{\mathrm{c}}}\frac{R_{\mathrm{c}}}{c} = \frac{1}{4\pi\varepsilon_0 c} = \frac{1}{4\pi}\sqrt{\frac{\mu_0}{\varepsilon_0}} = 30\ \Omega$, where R_{c} is the center-to-center distance. Thus $-\mathbf{P} \circ \mathbf{T}_{\mathrm{P}} \approx -30\ \mathbf{I}_{\mathrm{od}}$. The smallest eigenvalue of $\mathbf{Z}_{\mathrm{P}}^{(\mathrm{H})}$ is then $-30(m-1)$, which is proportional to the number of charge meshes! The consequence is that, the more charge meshes we partition, the more negative the DC eigenvalue of $\mathbf{Z}_{\mathrm{P}}^{(\mathrm{H})}$ will be.

For the coplanar strips with $N = 50$, the eigenvalues of $\mathbf{Z}_{\mathrm{P}}^{(\mathrm{H})}$ in the range $0 < f < 4f_{\mathrm{m}}$ is plotted in Fig. 4.41. Since there are total 102 nodes, the estimated negative eigenvalue is $-30(m-1) = -3030$. From the figure, we see that this estimate is quite accurate.

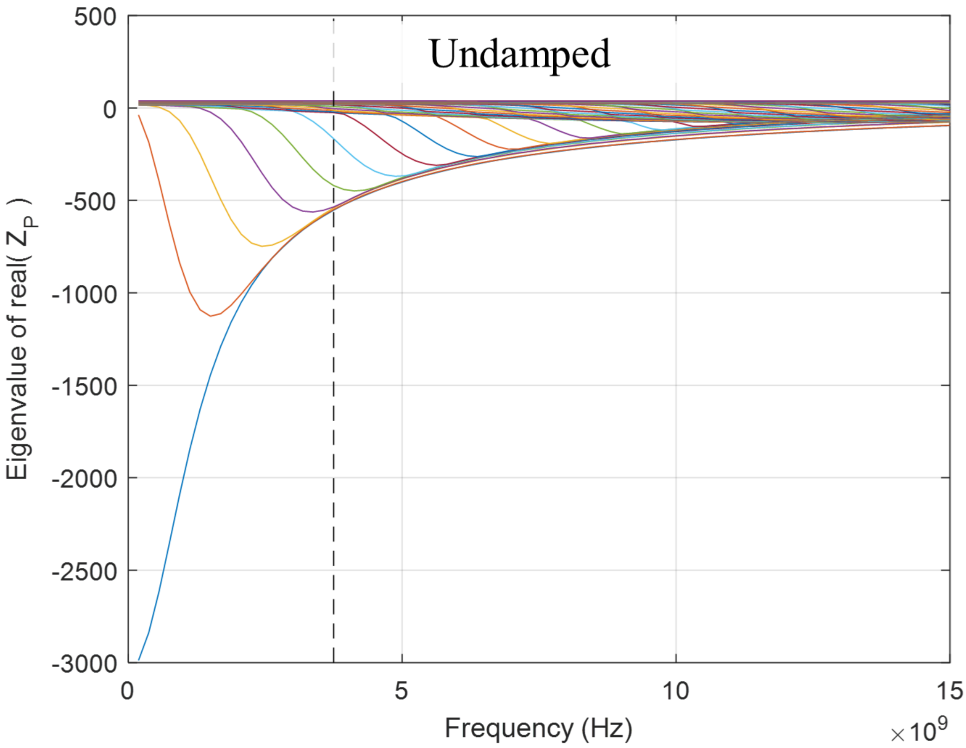

Fig. 4.41. Eigenvalues of undamped $\mathbf{Z}_{\mathrm{P}}^{(\mathrm{H})}$ of the coplanar strips with $N = 50$.

Now, the EAR structure gives $\mathbf{Z}_{\mathrm{P\,(EAR)}} = \overline{\mathbf{P}}/s + \mathbf{R}_{\mathrm{P}}$. Clearly, we can remove the DC negative eigenvalue of $\mathbf{Z}_{\mathrm{P\,(EAR)}}{}^{(\mathrm{H})}$ by choosing $\mathbf{R}_{\mathrm{P}} > 30m\mathbf{I}_{\mathrm{d}}$. However, it will definitely alter the low frequency response greatly. In addition, noting that the dominant eigenvalue of $\mathbf{Z}_{\mathrm{P}}{}^{(\mathrm{H})}$ at low frequency is negative, which is in contrast to $\mathbf{Z}_{\mathrm{L}}{}^{(\mathrm{H})}$, we may wonder: is it really necessary to remove negative eigenvalues of $\mathbf{Z}_{\mathrm{P}}{}^{(\mathrm{H})}$ for all frequencies?

We then recall equation (2.5) in Chapter 2, which relates the total radiated power to the current and charge densities as

$$P_{\mathrm{rad}} = \mathrm{Re}\left[\frac{1}{2} j\omega \int_V \int_V \mu_0\, \mathbf{J}(\mathbf{r}')G(\mathbf{r},\mathbf{r}') \cdot \mathbf{J}^*(\mathbf{r})\, \mathrm{d}^3r'\mathrm{d}^3r\right]$$
$$-\mathrm{Re}\left[\frac{1}{2} j\omega \int_V \int_V \frac{1}{\varepsilon_0}\, \rho(\mathbf{r}')G(\mathbf{r},\mathbf{r}')\, \rho^*(\mathbf{r})\, \mathrm{d}^3r'\mathrm{d}^3r\right]$$

Note that the second term of RHS has a negative sign, contrary to the first term. Consequently, it is in fact reasonable to have $\lambda(\mathbf{Z}_{\mathrm{P}}{}^{(\mathrm{H})}) < 0$ at low frequency, and it makes no sense to enforce $\mathbf{Z}_{\mathrm{P}}{}^{(\mathrm{H})}$ to be positive definite for all frequencies. An important implication of this observation is that the damping for potential coupling should not be designed separately. Instead, we should consider the whole PEEC model together. The question then becomes: what is the right target that we should look at?

In section 4.3.2, two alternative forms of MNA were presented: the branch form and the node form. The equation for the branch form is

$$[(\mathbf{R} + s\overline{\mathbf{L}}) + \mathbf{A}^{\mathrm{T}}(s\overline{\mathbf{P}}^{-1} + \mathbf{Y})^{-1}\mathbf{A}]\mathbf{I} = \mathbf{V}_{\mathrm{s}} + \mathbf{A}^{\mathrm{T}}(s\overline{\mathbf{P}}^{-1} + \mathbf{Y})^{-1}\mathbf{I}_{\mathrm{s}}$$

For a pure scattering problem, $\mathbf{I}_s = 0$, we can interpret $\mathbf{Z}_{\text{branch}}$, the matrix in the square bracket of the LHS, as an impedance matrix that relates the branch currents to the voltage sources of the incident wave. For damped case, we simply replace $\overline{\mathbf{P}}$ and $\overline{\mathbf{L}}$ with $\mathbf{P}_{\text{eq}}$ and $\mathbf{L}_{\text{eq}}$, respectively. Passivity check can be performed on $\mathbf{Z}_{\text{branch}}$. However, due to the following reasons, we seldom need to do so. There are two possible situations for a scattering problem. In the first case, the lumped elements such as resistors and capacitors to be connected with the PEEC model are known and can be represented by the **Y** matrix. In this case, it suffices to ensure the stability of the model for an accurate and stable transient simulation. Passivity enforcement is apparently unnecessary because the *ports* of $\mathbf{Z}_{\text{branch}}$ will not be connected with any external circuits other than the voltage sources. In the second situation, the elements to be connected with the PEEC model are unknown, i.e., undetermined, or they are known but cannot be represented by the **Y** matrix, e.g., nonlinear devices. In this case, making the circuit model passive is the safest way to ensure stable transient simulation. However, the passivity of $\mathbf{Z}_{\text{branch}}$ is not sufficient for this purpose, due to the ignorance of a proper **Y** matrix. As a result, we conclude that $\mathbf{Z}_{\text{branch}}$ is not the right target to ensure passivity.

The equation for the node form is

$$[(s\overline{\mathbf{P}}^{-1} + \mathbf{Y}) + \mathbf{A}(\mathbf{R} + s\overline{\mathbf{L}})^{-1}\mathbf{A}^{\mathrm{T}}]\mathbf{\Phi} = \mathbf{I}_{\mathrm{s}} - \mathbf{A}(\mathbf{R} + s\overline{\mathbf{L}})^{-1}\mathbf{A}^{\mathrm{T}}\mathbf{V}_{\mathrm{s}}$$

When there is no incident wave, $\mathbf{V}_s = 0$, we can interpret $\mathbf{Y}_{\text{node}}$, the matrix in the square

doi: 10.6342/NTU201902629

bracket of the LHS, as an admittance matrix that relates the node voltages to the independent current sources fed into each node. Again, for damped case, we simply replace $\overline{\mathbf{P}}$ and $\overline{\mathbf{L}}$ with $\mathbf{P}_{\mathrm{eq}}$ and $\mathbf{L}_{\mathrm{eq}}$, respectively. Can we take $\mathbf{Y}_{\mathrm{node}}$ as the target for passivity enforcement?

For the coplanar strips example with $N = 50$, the eigenvalues of $\mathbf{Y}_{\mathrm{node}}$ in the frequency range $0 < f < 12f_{\mathrm{m}}$ are plotted in Fig. 4.42. We note a phenomenon in the figure similar to the eigenvalues of undamped $\mathbf{Z}_{\mathrm{P}}$ shown in Fig. 4.41: the low frequency eigenvalues are predominately negative. An immediate consequence is that we can never make the eigenvalues of $\mathbf{Y}_{\mathrm{node}}^{(\mathrm{H})}$ positive without significantly altering the low frequency response of the circuit. The implication of this result is twofold: first, if *each* of the m (external) nodes of the PEEC model is individually treated as a port, then the model cannot be made passive while still maintaining low frequency accuracy. Second, if not all nodes of the circuit are port terminals, then $\mathbf{Y}_{\mathrm{node}}$ is not the right target for passivity enforcement. Instead, we should seek for a smaller matrix that just describes the port behavior such as the input impedance in [50]. This result also reveals the fact that a circuit characterized as “passive” under a particular port description does not necessarily mean its internal construction is passive. On the contrary, a port-passive circuit can have significantly active parts internally. In the standard FW PEEC, we see that at low frequencies, the potential coupling is significantly active, while the inductive coupling is

doi: 10.6342/NTU201902629

much more passive. The combined effect, as we studied in Chapter 2, turns out to be mainly passive at low frequencies because of the associated power loss (radiation) instead of power gain. However, the more number of ports defined, the more difficult to make the PEEC model passive by adding damping.

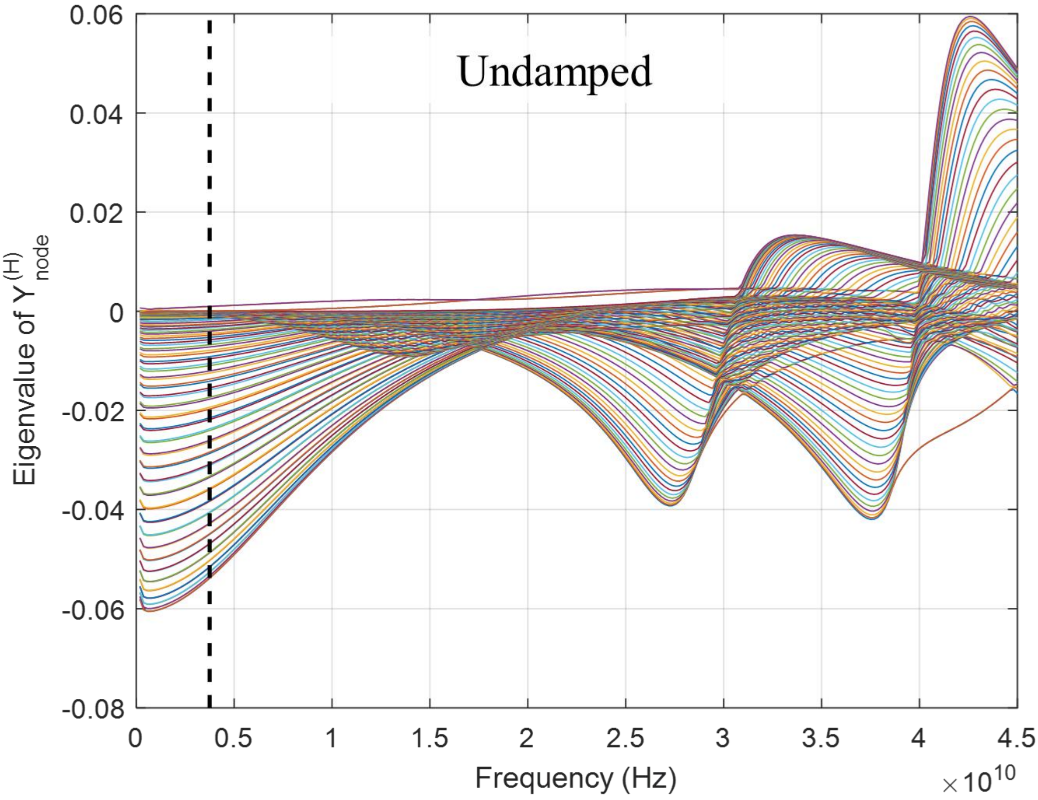

Fig. 4.42. Eigenvalues of the undamped $\mathbf{Y}_{\text{node}}^{(\text{H})}$ of the coplanar strips with $N = 50$.

To establish a port description of the circuit, suppose there is no incident wave, and $2p$ external nodes are selected to define p ports, two nodes for each. We would like to reduce the complete node description to a port description, in closed form.

First we define a *reduction matrix* $\mathbf{A}_{\text{red}} \in \mathbb{R}^{m\times p}$ as $\mathbf{I}_{\text{s}} = \mathbf{A}_{\text{red}}\mathbf{I}_{\text{port}}$, where $\mathbf{I}_{\text{port}} \in \mathbb{C}^{p}$ is the vector of port currents, and

$$\mathbf{A}_{\mathrm{red}_{ij}} = \begin{cases} +1 & \text{if } I_{\mathrm{port}(j)} \text{ enters node } i \\ -1 & \text{if } I_{\mathrm{port}(j)} \text{ leaves node } i \\ 0 & \text{otherwise} \end{cases}$$

Then we find that

$$\mathbf{A}_{\mathrm{red}}^{\mathrm{T}}\mathbf{\Phi} = \begin{pmatrix} \Phi_{1+} - \Phi_{1-} \\ \Phi_{2+} - \Phi_{2-} \\ \vdots \\ \Phi_{p+} - \Phi_{p-} \end{pmatrix} = \mathbf{V}_{\mathrm{port}}$$

where $\mathbf{V}_{\mathrm{port}}$ is the vector of port voltages. Then the relation $\mathbf{Y}_{\mathrm{node}}\mathbf{\Phi} = \mathbf{I}_{\mathrm{s}}$ can be transformed into

$$\mathbf{V}_{\mathrm{port}} = \left(\mathbf{A}_{\mathrm{red}}^{\mathrm{T}}\mathbf{Y}_{\mathrm{node}}^{-1}\mathbf{A}_{\mathrm{red}}\right)\mathbf{I}_{\mathrm{port}} = \mathbf{Z}_{\mathrm{port}}\mathbf{I}_{\mathrm{port}}$$

Explicitly,

$$\mathbf{Z}_{\mathrm{port}} = \mathbf{A}_{\mathrm{red}}^{\mathrm{T}}\mathbf{Y}_{\mathrm{node}}^{-1}\mathbf{A}_{\mathrm{red}} = \mathbf{A}_{\mathrm{red}}^{\mathrm{T}}[(s\overline{\mathbf{P}}^{-1} + \mathbf{Y}) + \mathbf{A}(\mathbf{R} + s\overline{\mathbf{L}})^{-1}\mathbf{A}^{\mathrm{T}}]^{-1}\mathbf{A}_{\mathrm{red}}$$

$$= \mathbf{A}_{\mathrm{red}}^{\mathrm{T}}[(\mathbf{Z}_{\mathrm{P}}^{-1} + \mathbf{Y}) + \mathbf{A}(\mathbf{R} + \mathbf{Z}_{\mathrm{L}})^{-1}\mathbf{A}^{\mathrm{T}}]^{-1}\mathbf{A}_{\mathrm{red}}$$

The matrix $\mathbf{Z}_{\mathrm{port}}$ is exactly the impedance matrix relating the port current $\mathbf{I}_{\mathrm{port}}$ to the port voltage $\mathbf{V}_{\mathrm{port}}$, and may be a suitable candidate to ensure passivity when there is no incident wave excitation.

Consider again the coplanar strips example with $N = 50$. Suppose we identify the two ends of the strips as two ports. Then $\mathbf{Z}_{\mathrm{port}}$ is 2×2, and has only two eigenvalues. The eigenvalues of its Hermitian part for various undamped and damped cases are shown in Fig. 4.43.

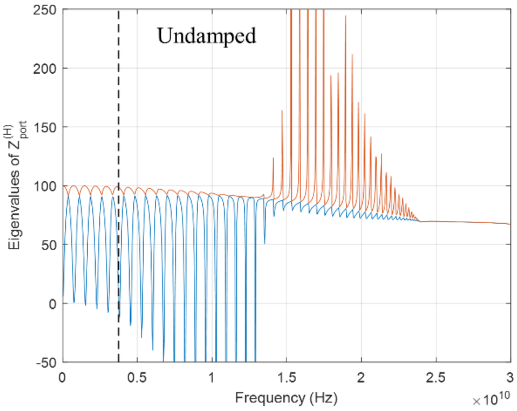

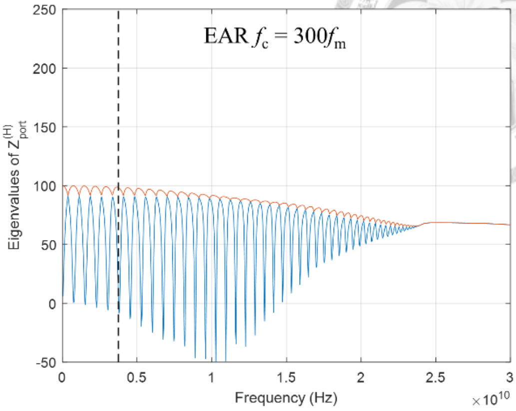

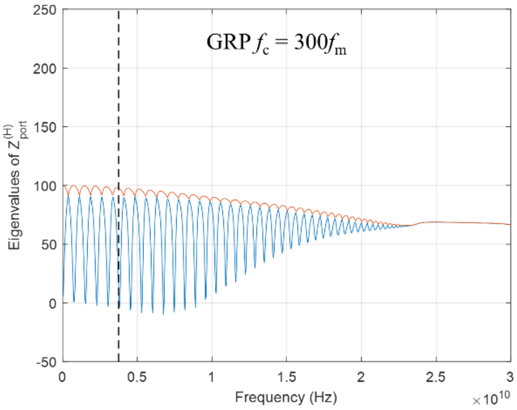

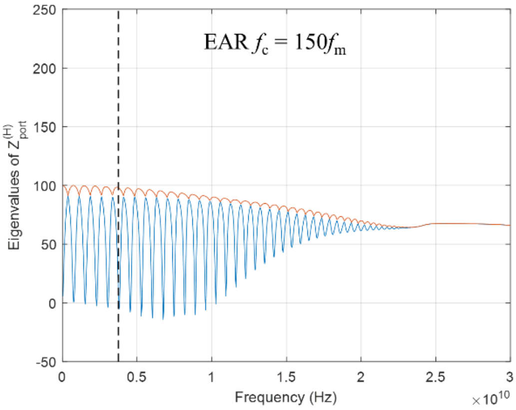

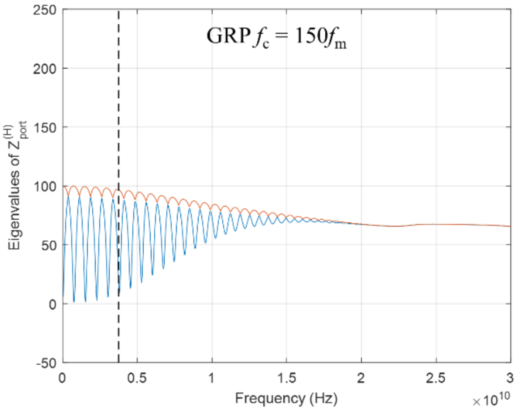

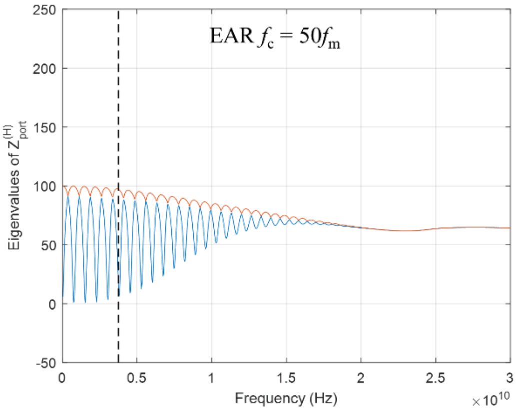

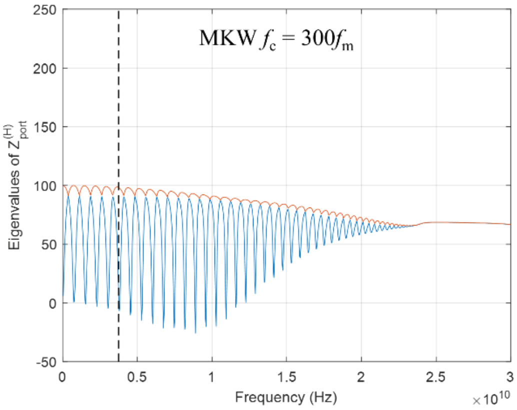

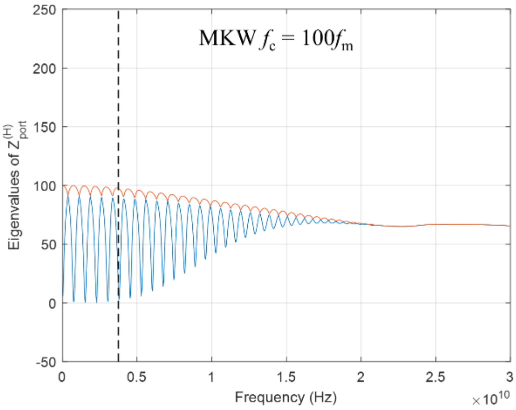

doi: 10.6342/NTU201902629

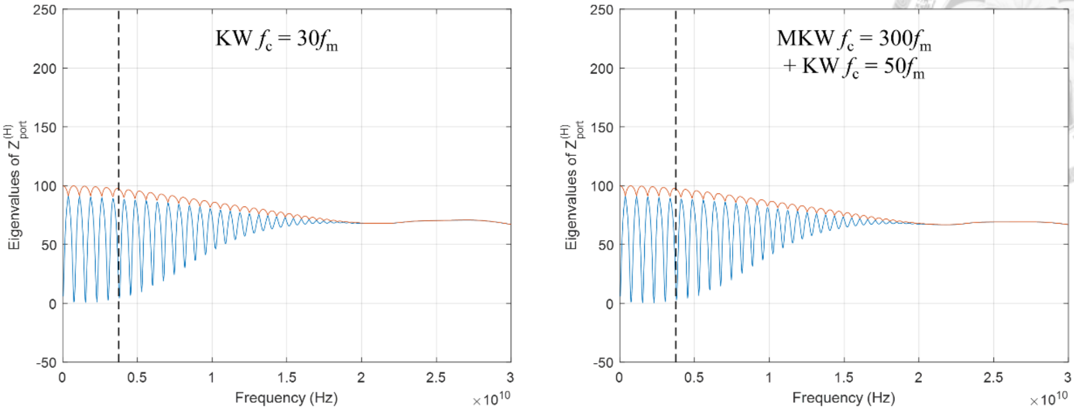

Fig. 4.43. Eigenvalues of $\mathbf{Z}_{\mathrm{port}}^{(\mathrm{H})}$ of the coplanar strips with $N = 50$ for various undamped and damped cases with different cutoff frequencies.

The undamped case has negative eigenvalues at frequencies both below and beyond f_m, which is as expected from our previous studies in section 4.3. The GRP with $f_c = 300f_m$ can help lift many eigenvalues positive, but is not enough to fully passivize $\mathbf{Z}_{\mathrm{port}}$. To completely remove negative eigenvalues, we need GRP with $f_c = 150f_m$. Similarly, for EAR we need $f_c = 50f_m$, for MKW we need $f_c = 100f_m$, and for KW-only we need $f_c = 30f_m$. However, if we combine MKW and KW, then the required cutoff frequencies can be raised to $300f_m$ and $50f_m$, respectively. In this example, all the required cutoff frequencies are larger than $10f_m$, so the impact on low frequency accuracy can be expected to be small.

In obtaining Fig. 4.43, the **Y** matrix was included, which represents the effects of the 100Ω port resistors. If we do not know in advance what kind of circuits will be connected to the port terminals, we can simply ignore **Y** in the expression of $\mathbf{Z}_{\mathrm{port}}$.

Taking the matrix $\mathbf{Z}_{\mathrm{port}}$ as the target for passivity enforcement is not without problems. The first disadvantage, a practical one, is the inability to include incident wave excitation. When $\mathbf{V}_s$ is nonzero, we cannot simply treat $\mathbf{Y}_{\text{node}}$ as an admittance matrix that fully characterizes the system. The subsequent definition of $\mathbf{Z}_{\text{port}}$ is also nullified. The second problem is a theoretical issue. Recall the definition of positive-real matrix in the beginning of section 4.3.2. In addition to having a positive semidefinite Hermitian part, the first requirement is that it is analytic in the RHP. In other words, each element of the $\mathbf{Z}$ matrix cannot have RHP poles. Now, consider the definition of $\mathbf{Z}_{\text{port}}$:

$$\mathbf{Z}_{\text{port}} = \mathbf{A}_{\text{red}}^{\text{T}}\mathbf{Y}_{\text{node}}^{-1}\mathbf{A}_{\text{red}} = \mathbf{A}_{\text{red}}^{\text{T}}[(s\bar{\mathbf{P}}^{-1} + \mathbf{Y}) + \mathbf{A}(\mathbf{R} + s\bar{\mathbf{L}})^{-1}\mathbf{A}^{\text{T}}]^{-1}\mathbf{A}_{\text{red}}$$

If $\mathbf{Y}_{\text{node}}$ is singular at a particular s_0 with Re[s_0] > 0, then $\mathbf{Y}_{\text{node}}^{-1}$ would have a pole at s_0, and $\mathbf{Z}_{\text{port}}$ will also have a pole there. However, due to the twofold matrix inverse, the analyticity of $\mathbf{Z}_{\text{port}}$ is very difficult to ascertain.

As it turns out, we can find a target matrix that simultaneously solves the above two problems. To include the effects of incident wave voltage sources, we treat the two terminals of *each* voltage source as a port. The complete PEEC model then consists of $n+p$ ports, where n is the number of current meshes. Define $\mathbf{A}_{\text{red}} \in \mathbb{R}^{m\times p}$ as before. In addition, we set $\mathbf{Y} = 0$, i.e., in characterizing the passivity of the circuit, we do not add in any external lumped circuit. The reason is that, if we can make the PEEC model itself passive, then arbitrary passive-connection will retain the overall passivity. For this to hold, however, it is important that if we are going to connect lumped circuits to some nodes of the PEEC model, we must include those nodes as ports.

The first half of the MNA equation is

$$s\bar{\mathbf{P}}^{-1}\mathbf{\Phi} + \mathbf{A}\mathbf{I} = \mathbf{I}_{\mathrm{s}}$$

Using $\mathbf{I}_{\mathrm{s}} = \mathbf{A}_{\mathrm{red}}\mathbf{I}_{\mathrm{port}}$, we can rewrite this equation as

$$\mathbf{\Phi} = -\frac{\bar{\mathbf{P}}}{s}\mathbf{A}\mathbf{I} + \frac{\bar{\mathbf{P}}}{s}\mathbf{I}_{\mathrm{s}} = -\mathbf{Z}_{\mathrm{P}}\mathbf{A}\mathbf{I} + \mathbf{Z}_{\mathrm{P}}\mathbf{I}_{\mathrm{s}} = -\mathbf{Z}_{\mathrm{P}}\mathbf{A}\mathbf{I} + \mathbf{Z}_{\mathrm{P}}\mathbf{A}_{\mathrm{red}}\mathbf{I}_{\mathrm{port}}$$

Multiplying both sides with $\mathbf{A}_{\mathrm{red}}^{\mathrm{T}}$, we have

$$\mathbf{A}_{\mathrm{red}}^{\mathrm{T}}\mathbf{\Phi} = \mathbf{V}_{\mathrm{port}} = -\mathbf{A}_{\mathrm{red}}^{\mathrm{T}}\mathbf{Z}_{\mathrm{P}}\mathbf{A}\mathbf{I} + \mathbf{A}_{\mathrm{red}}^{\mathrm{T}}\mathbf{Z}_{\mathrm{P}}\mathbf{A}_{\mathrm{red}}\mathbf{I}_{\mathrm{port}}$$

The second half of the MNA equation is

$$\mathbf{A}^{\mathrm{T}}\mathbf{\Phi} - (\mathbf{R} + s\bar{\mathbf{L}})\mathbf{I} = \mathbf{A}^{\mathrm{T}}\mathbf{\Phi} - (\mathbf{R} + \mathbf{Z}_{\mathrm{L}})\mathbf{I} = -\mathbf{V}_{\mathrm{s}}$$

Substituting the expression for $\mathbf{\Phi}$, we obtain

$$-\mathbf{A}^{\mathrm{T}}\mathbf{Z}_{\mathrm{P}}\mathbf{A}\mathbf{I} + \mathbf{A}^{\mathrm{T}}\mathbf{Z}_{\mathrm{P}}\mathbf{A}_{\mathrm{red}}\mathbf{I}_{\mathrm{port}} - (\mathbf{R} + \mathbf{Z}_{\mathrm{L}})\mathbf{I} = -\mathbf{V}_{\mathrm{s}}$$

Or, equivalently,

$$-\mathbf{A}^{\mathrm{T}}\mathbf{Z}_{\mathrm{P}}\mathbf{A}_{\mathrm{red}}\mathbf{I}_{\mathrm{port}} + [\mathbf{A}^{\mathrm{T}}\mathbf{Z}_{\mathrm{P}}\mathbf{A} + (\mathbf{R} + \mathbf{Z}_{\mathrm{L}})]\mathbf{I} = \mathbf{V}_{\mathrm{s}}$$

Putting the results together, we have the following system of equations:

$$\begin{pmatrix} \mathbf{A}_{\mathrm{red}}^{\mathrm{T}}\mathbf{Z}_{\mathrm{P}}\mathbf{A}_{\mathrm{red}} & -\mathbf{A}_{\mathrm{red}}^{\mathrm{T}}\mathbf{Z}_{\mathrm{P}}\mathbf{A} \\ -\mathbf{A}^{\mathrm{T}}\mathbf{Z}_{\mathrm{P}}\mathbf{A}_{\mathrm{red}} & \mathbf{A}^{\mathrm{T}}\mathbf{Z}_{\mathrm{P}}\mathbf{A} + (\mathbf{R} + \mathbf{Z}_{\mathrm{L}}) \end{pmatrix} \begin{pmatrix} \mathbf{I}_{\mathrm{port}} \\ \mathbf{I} \end{pmatrix} = \begin{pmatrix} \mathbf{V}_{\mathrm{port}} \\ \mathbf{V}_{\mathrm{s}} \end{pmatrix}$$

We immediately recognize that it is an impedance representation for the (p+n)-port network that is excited by mixed current sources and incident waves. The impedance matrix, denoted by $\mathbf{Z}_{\mathrm{mix}}$, is given by

$$\mathbf{Z}_{\mathrm{mix}} = \begin{pmatrix} \mathbf{A}_{\mathrm{red}}^{\mathrm{T}}\mathbf{Z}_{\mathrm{P}}\mathbf{A}_{\mathrm{red}} & -\mathbf{A}_{\mathrm{red}}^{\mathrm{T}}\mathbf{Z}_{\mathrm{P}}\mathbf{A} \\ -\mathbf{A}^{\mathrm{T}}\mathbf{Z}_{\mathrm{P}}\mathbf{A}_{\mathrm{red}} & \mathbf{A}^{\mathrm{T}}\mathbf{Z}_{\mathrm{P}}\mathbf{A} + (\mathbf{R} + \mathbf{Z}_{\mathrm{L}}) \end{pmatrix}$$

Different from $\mathbf{Z}_{\mathrm{port}}$, there is no matrix inverse involved in $\mathbf{Z}_{\mathrm{mix}}$, and we can directly see that all elements of $\mathbf{Z}_{\mathrm{mix}}$ are analytic in the open RHP. Accordingly, it is a perfect target for passivity characterization.

The definition of positive-real matrix as given in section 4.3.2 requires checking the positive definiteness in the entire RHP, which is computationally expensive. In all previous examples, we only consider the behavior of the matrices on the imaginary axis. Rigorously speaking, having a positive definite Hermitian part on the $j\omega$-axis is only a necessary condition for passivity. However, under certain additional constraints, it suffices to check the $j\omega$-axis instead of the entire RHP, according to an important theorem given by Wohlers [56]:

Theorem An $n \times n$ matrix $\mathbf{W}(s)$ all of whose elements are real meromorphic functions is positive-real if and only if

1. $W_{jk}(s)$ has no poles in $\mathrm{Re}[s] > 0$.
2. The poles of $W_{jk}(s)$ on $s = j\omega$ are simple.
3. $\mathbf{W}(j\omega)^{(\mathrm{H})}$ is nonnegative-definite for almost all ω, and

   $$\int_{-\infty}^{\infty} \frac{\mathbf{y}^{\mathrm{H}}\left[\widehat{\mathbf{W}}^{\mathrm{H}}(j\omega) + \widehat{\mathbf{W}}(j\omega)\right]\mathbf{y}}{1+\omega^2}\, d\omega < \infty$$

   for all constant n-vectors $\mathbf{y}$, where $\widehat{\mathbf{W}}(j\omega)$ is the infinitely differentiable part of the boundary value of $\mathbf{W}(s)$ (in the sense of distribution).
4. If $s = j\omega_0$ is a point where $W_{jk}(s)$ has a pole and $\alpha_{jk}(\omega)$ is the residue of this pole, then the matrix formed with these residues, $\boldsymbol{\alpha}(\omega_0)$, must satisfy $\boldsymbol{\alpha}(\omega_0)^{\mathrm{H}} = \boldsymbol{\alpha}(\omega_0)$, it must be

nonnegative-definite, and

$$\sum_i \frac{\mathbf{y}^{\mathrm{H}}\alpha(\omega_i)\mathbf{y}}{1+\omega_i^2} < \infty$$

where the sum extends over all the points $s = j\omega_i$ at which $W_{jk}(s)$ has poles.

5. Asymptotically, $\mathbf{W}(s) \to \mathbf{B}s$ in Re $s > 0$, where $\mathbf{B}$ is a real, constant, symmetric, nonnegative-definite matrix.

The first two conditions are necessary for stability. The first one, especially, is difficult to ascertain for $\mathbf{Z}_{\mathrm{port}}$, but is easily verified for $\mathbf{Z}_{\mathrm{mix}}$. Note that here $\mathbf{W} = \mathbf{Z}$ or $\mathbf{Y}$, which is the transfer function from **I** to **V** or from **V** to **I**. Hence, any double pole on the $j\omega$-axis will imply instability. This, the *transfer function pole*, should be differentiated from the *system pole* described in section 4.1 and numerically computed in section 4.2. The third condition characterizes the behavior of the analytic part of the immittance matrix on the imaginary axis. Since by assumption $\mathbf{W}(s)$ is meromorphic, around any simple pole p the function can be separated into a $\frac{1}{s-p}$ term and an analytic term, the latter representing the “infinitely differentiable part” as stated in the theorem. If on the other hand $\mathbf{W}(s)$ has no poles on the closed RHP, then the infinitely differentiable part is simply $\mathbf{W}(s)$ itself. For the inequality to hold, the Hermitian part of $\mathbf{W}(j\omega)$ must not grow too fast as $\omega \to \infty$. For example, if $|\mathbf{W}^{(\mathrm{H})}(j\omega)|$ is uniformly bounded by a constant, then the inequality holds because $\int_{-\infty}^{\infty} \frac{d\omega}{1+\omega^2} = \tan^{-1}\omega|_{-\infty}^{\infty} = \pi$. The forth condition restricts the behavior at the

doi: 10.6342/NTU201902629

imaginary poles. Recall the theory of NFDE as we surveyed in section 4.1. An NFDE may have a series of poles that asymptotically approach some vertical lines determined by the roots of the ADE. If these “straight-up” poles are exactly on the $j\omega$-axis, then the infinite summation of the fourth condition may diverge. If on the other hand there is only a finite amount of $j\omega$-poles, then the summation inequality always holds, and we only need to check the definiteness of the residue matrices. The final condition characterize the behavior at $|s| \to \infty$ in the RHP. $\mathbf{W}(s)$ cannot grow faster than s, e.g., it cannot have s^2 term. If $\mathbf{W}$ is an impedance matrix, then $\mathbf{W}(s) \to \mathbf{B}s$ represents an inductance matrix $\mathbf{B}$, which must be nonnegative-definite. The statement of this condition follows exactly that of Wohlers. We note that, however, it is possible for a passive $\mathbf{W}(s)$ to be just *bounded* but not in the form of $\mathbf{B}s$. The simplest example would be any resistive network that is made of positive resistors without any reactive elements, giving a constant nonzero impedance matrix $\mathbf{W}$, independent of s. A similar example can be found in pp. 373 of [63], in which the authors said the asymptotic constraint is “not relevant” for the bounded immittance case.

With this theorem, we could now consider the passivity of $\mathbf{Z}_{\text{mix}}$. From the closed-form expression of $\mathbf{Z}_{\text{P}}$ and $\mathbf{Z}_{\text{L}}$, either damped or undamped, we see that they are analytic in the entire RHP. Thus the first condition is met. Next, there is only one simple pole on the $j\omega$-axis: the DC pole of $\mathbf{Z}_{\text{P}}$. Then the second condition is also satisfied. The inequality

doi: 10.6342/NTU201902629

in the third condition can be satisfied if the inductive coupling is damped by either MKW or KW, because the resulting $\mathbf{Z}_{\mathrm{L}}$ has uniformly bounded Hermitian part. The potential coupling $\mathbf{Z}_{\mathrm{P}}$, on the other hand, is always bounded because it is proportional to $1/s$. The GRP structure, however, does not guarantee a bounded $\mathbf{Z}_{\mathrm{L}}^{(\mathrm{H})}$ due to the reason studied in section 4.4.2: if $\mathbf{L}$ is close to singular at some particular frequencies, then at those frequencies the damping $\mathbf{R}_{\mathrm{L}}$ may be ineffective. Since there is only one imaginary pole, the summation inequality of condition 4 holds automatically, regardless any damping structure. The residue matrix of the DC pole is given by

$$\boldsymbol{\alpha}(0) = \lim_{s\to 0} s\mathbf{Z}_{\mathrm{mix}} = \begin{pmatrix} \mathbf{A}_{\mathrm{red}}^{\mathrm{T}}\mathbf{P}\mathbf{A}_{\mathrm{red}} & -\mathbf{A}_{\mathrm{red}}^{\mathrm{T}}\mathbf{P}\mathbf{A} \\ -\mathbf{A}^{\mathrm{T}}\mathbf{P}\mathbf{A}_{\mathrm{red}} & \mathbf{A}^{\mathrm{T}}\mathbf{P}\mathbf{A} \end{pmatrix}$$

where $\mathbf{P}$ is the QS potential matrix. Then, $\boldsymbol{\alpha}(0)$ is positive semidefinite if $\mathbf{P}$ is positive semidefinite. To see this, consider multiplying both sides of $\boldsymbol{\alpha}(0)$ by some arbitrary complex vector $(\mathbf{X}, \mathbf{Y})$ as

$$[\mathbf{X}^{\mathrm{H}}, \mathbf{Y}^{\mathrm{H}}]\boldsymbol{\alpha}(0)\begin{bmatrix}\mathbf{X}\\ \mathbf{Y}\end{bmatrix} = \mathbf{X}^{\mathrm{H}}\mathbf{A}_{\mathrm{red}}^{\mathrm{T}}\mathbf{P}\mathbf{A}_{\mathrm{red}}\mathbf{X} + \mathbf{Y}^{\mathrm{H}}\mathbf{A}^{\mathrm{T}}\mathbf{P}\mathbf{A}\mathbf{Y} - \mathbf{X}^{\mathrm{H}}\mathbf{A}_{\mathrm{red}}^{\mathrm{T}}\mathbf{P}\mathbf{A}\mathbf{Y} - \mathbf{Y}^{\mathrm{H}}\mathbf{A}^{\mathrm{T}}\mathbf{P}\mathbf{A}_{\mathrm{red}}\mathbf{X}$$

$$= [\mathbf{A}_{\mathrm{red}}\mathbf{X} - \mathbf{A}\mathbf{Y}]^{\mathrm{H}}\mathbf{P}[\mathbf{A}_{\mathrm{red}}\mathbf{X} - \mathbf{A}\mathbf{Y}] \geq 0$$

Thus the passivity of the QS PEEC is also important for the passivity of the FW case. If, however, $\mathbf{P}$ is not nonnegative definite, then $\boldsymbol{\alpha}(0)$ may still be positive semidefinite, but we must explicitly check this.

To fulfill the fifth condition, the inductive coupling needs to be damped. The MKW will result in a bounded $\mathbf{Z}_{\mathrm{L}}$. The KW-only will give a positive-definite diagonal inductance matrix, which is also feasible. The GRP, again, has the theoretical uncertainty due to the possible singular $\bar{\mathbf{L}}$ matrix at some frequencies.

In summary, for a given FW PEEC model, if the QS **P** matrix is positive definite, and if we apply either MKW or KW-only, then the passivity of $\mathbf{Z}_{\text{mix}}$ can be determined by the eigenvalues of $\mathbf{Z}_{\text{mix}}^{(\text{H})}$ on the $j\omega$-axis, which in turn represents the passivity of the whole model under the $(p+n)$-port description. If GRP is applied, then theoretically we cannot ensure the passivity just by checking the $j\omega$-axis eigenvalues. A fix to this problem is to combine with KW, which suppresses the off-diagonal terms of $\mathbf{L}_{\text{eq}}$. Nevertheless, practically GRP is as useful as MKW, and is sometimes more effective in achieving a positive definite Hermitian part.

Consider the coplanar strip example with $N = 50$. MATLAB reports that the QS **P** matrix is positive definite. The eigenvalues of $\mathbf{Z}_{\text{mix}}^{(\text{H})}$ on the $j\omega$-axis for various undamped and damped cases are shown in Fig. 4.44. The undamped case has numerous negative eigenvalues, as expected. Since $\mathbf{Z}_{\text{mix}}$ is 102×102, it is far more difficult to make it passive than $\mathbf{Z}_{\text{port}}$. For this structure, we find that neither GRP, MKW, nor EAR, alone, can remove all negative eigenvalues. Instead, we need to combine GRP + EAR + KW, or MKW + EAR + KW, with $f_c = 8f_m$, to fully passivize $\mathbf{Z}_{\text{mix}}$. However, the low frequency eigenvalues are changed greatly.

doi: 10.6342/NTU201902629

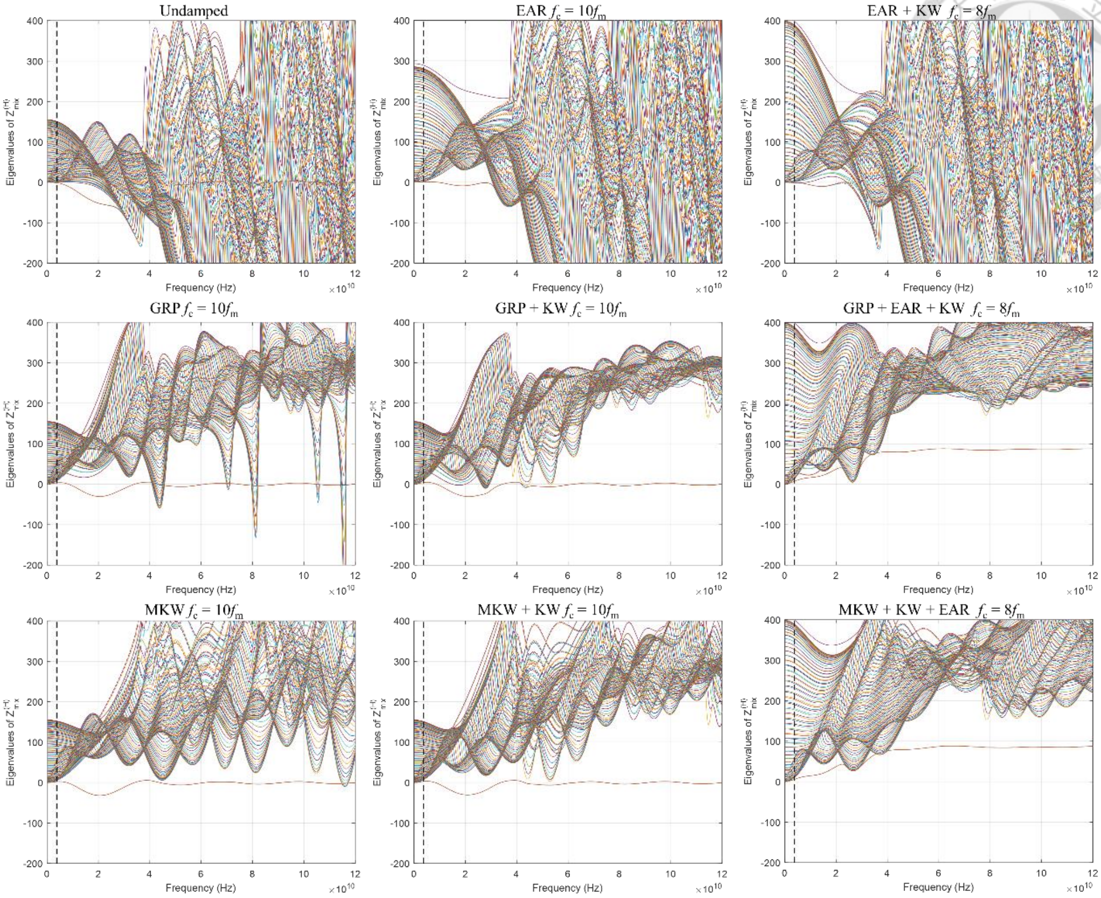

Fig. 4.44. Eigenvalues of $\mathbf{Z}_{\text{mix}}^{(\text{H})}$ of the coplanar strips with N = 50 for various undamped and damped cases.

4.5 Summary

In this chapter, we studied the stability and passivity properties of FW PEEC in detail. Although PEEC is a circuit model, the mathematical form has to be rigorously described in terms of functional differential equations, which is a classical subject in the field of control system analysis. The general FDE theory is difficult, while for a linear system, stability properties can be characterized in terms of its poles, or natural frequencies. The most important difference of linear delayed system from the delay-free counterpart is the presence of infinitely-many poles, which complicates the determination of stability. Classifications of retarded type and neutral type FDEs, and ground poles and sky poles, were presented. FW PEEC, as we found, belongs to NFDE which is rich in complexity.

Various stability tests for PEEC were reviewed in section 4.2, while few of them are applicable to general large-scale problems. The existing stability tests were also classified into sufficient-condition and necessary-condition tests, both kinds having their own special usages. Guided by the results of our survey, we proposed a necessary-condition test which is to numerically locate all the ground poles of the PEEC model by a multivariate Newton's method. Although the sky poles are ignored, in many cases we found that the main cause of instability is the RHP ground poles. Then, under the assumption, or conjecture, that the stability of FW PEEC is determined by the ground poles only, the proposed stability test is both necessary and sufficient.

doi: 10.6342/NTU201902629

In section 4.3, the focus was turned to the passivity of FW PEEC. As we discovered, the standard center-to-center approximation will result in highly power-generating potential and inductive coupling networks, which provide the required energy for an unstable divergent oscillation. The results also show that careless introduction of time delay into a system is very dangerous. An ideal time delay in a complex system, in general, shall not be considered simply as a postponement of certain physical quantities. Instead, high frequency components with period comparable to the delay may experience constructive coupling (interference), which drives the system to instability.

The design of damping was studied in section 4.4, which takes up the largest part of Chapter 4. The existing methodologies were reviewed in detail, and various damping structures, including our own proposed ones, were presented. Although these damping structures are capable of restoring the stability of the system, in the past the design of the required damping level was usually heuristic, lacking a systematic approach. Based on our study of the stability and passivity properties of FW PEEC, we presented two design methods, one targeted at removing RHP ground poles, while the other aimed at fully passivize the model. The stability-based design relied on a modified Newton method which includes the effect of damping structures into its formulation in a concise manner. The passivity-based method, on the other hand, focused on finding the right target to passivize, the target being some impedance or admittance matrices. Various unsuccessful choices were presented including $\mathbf{Z}_{\mathrm{P}}$, $\mathbf{Z}_{\mathrm{branch}}$, and $\mathbf{Y}_{\mathrm{node}}$, which nevertheless gave us a deeper understanding of PEEC, and guided us toward the right targets: $\mathbf{Z}_{\mathrm{port}}$ and $\mathbf{Z}_{\mathrm{mix}}$. The port impedance matrix $\mathbf{Z}_{\mathrm{port}}$, however, still has some theoretical difficulties, and is not applicable for problems with incident waves. The impedance matrix of mixed current source and incident wave, denoted as $\mathbf{Z}_{\mathrm{mix}}$, turns out to be the most suitable target for passivization due to its completeness in describing the system as well as its mathematical simplicity. Examples were provided showing the feasibility of passivizing $\mathbf{Z}_{\mathrm{mix}}$. Comparing the results of both design methods, we clearly saw the difference between stability and passivity: only a small amount of damping would suffice to stabilize the model, while to make the model passive, the required damping is much larger. Although the stability of transient simulation is the final goal, making the model passive is often a useful mean to ensure stability, especially when the external connection of the model is either unknown or nonlinear.

Here we provide a general summary of the design flow of damping. The first step is to determine whether we need a passive model, or simply a stable model. The answer depends on the external connection. If the circuits to be connected at the ports are known, are linear, and can be concisely casted into the MNA equations, then we can choose the stability-based design method. If, on the other hand, the external circuits are either unknown or nonlinear, then we better ensure a passive model. The second step is to choose

doi: 10.6342/NTU201902629

one or more damping structures. For stability-based method, either GRP, MKW, or EAR, alone, may suffice to stabilize the model. For passivity-based method, however, it further depends on the excitation. For problems excited by independent sources connected to the ports of the model only, either damping structure may be sufficient to achieve passivity, but combination of them will make passivization easier. In this case the $\mathbf{Z}_{\text{port}}$ matrix may be chosen as the target for passivization. For problems excited simultaneously by internal sources and incident waves, usually we need a combination of multiple damping structures. In this case, we should check $\mathbf{Z}_{\text{mix}}$ instead of $\mathbf{Z}_{\text{port}}$. The final step is to determine the cutoff frequencies of the damping structures. For stability-based method, any frequency that makes all the RHP poles move back to LHP is a proper cutoff. For passivity-based method, we determine the cutoff frequency by plotting the eigenvalues of the target matrix. Any frequency that makes all the eigenvalues of the target matrix positive can be chosen as the cutoff. Lastly, if the required cutoff frequency is too low, e.g., $f_c < 6f_m$, that degrades the low frequency accuracy, then we may combine more damping structures, or apply higher-order damping structures such as Fig. 4.24 and 4.26, which will help raise the cutoff frequency to an acceptable value. □

doi: 10.6342/NTU201902629

Chapter 5 Conclusion and Future Work

Chapters 2 to 4 of this dissertation dealt with different aspects of FW PEEC. Chapter 2 essentially proved that, at low frequencies, time delay in the model introduces power loss, which corresponds to the physical quantity of total radiated or scattered power, depending on the excitation of the model. Chapter 3 focused on a practical issue: how to conduct time domain simulation of FW PEEC using a standard SPICE? A method utilizing the delayed controlled sources in SPICE was presented, which appears to be the first approach in the literature that can put a FW PEEC into a truly SPICE-compatible form. The significance of this method is that it enables fast, easy, and numerically stable simulation of FW PEEC models using existing SPICEs, while obviating the need for researchers to write their own solvers. With this method, we have conducted several transient simulation of various structures. Instability, as it turns out, seems to be a typical behavior of FW PEEC. This then motivated the study of Chapter 4, the longest chapter of this dissertation. The stability of FW PEEC, the subject we have put our major efforts in, is both rich in theory and practically important. The final goal is to have a stable time domain simulation, while to achieve this objective we have to be able to determine the stability of a given model, we should know the reason for the instability, and we need methods to reestablish the stability. The determination of stability, as we surveyed, is itself a subject deep in theory, heavily studied in various fields especially control system

doi: 10.6342/NTU201902629

analysis. Due to the presence of delay, and particularly the fact that FW PEEC belongs to the neutral type, most of the existing stability tests are only either sufficient or necessary, but not both. Motivated from the past results, we proposed a necessary-condition test for FW PEEC, which is simply to locate all the ground poles of the model, under the QI formulation of MNA, by a multivariate Newton's method. The test is only necessary in that the sky poles are totally neglected. However, examples have invoked the conjecture that the sky poles of PEEC are less relevant to stability than the ground poles, if not totally irrelevant. If this conjecture is true (for PEEC only, not for general delayed system), then the proposed stability test would be both necessary and sufficient, and, as a result of being sufficient, it can be used to design the damping, which is the stability-based method presented in Chapter 4. The passivity of FW PEEC is another issue. Study of passivity was motivated when we tried to find an explanation for the ubiquitous occurrence of unstable responses. The results showed that the center-to-center approximation of standard FW PEEC will result in highly nonpassive inductive and potential coupling networks, and they in turn provide the necessary energy for the unstable resonances. Accordingly, the passivity-based damping design is to make the model passive, thus guaranteed stable. An important observation was that we cannot separately make both inductive coupling and potential coupling passive. Instead, the whole model has to be considered together. Various target matrix candidates were thus studied, and we have

doi: 10.6342/NTU201902629

found a suitable impedance matrix, $\mathbf{Z}_{\mathrm{mix}}$, that treats the whole model together, that includes internal excitation as well as incident wave, and that has a transparent mathematical form, especially without matrix inversion. For $\mathbf{Z}_{\mathrm{mix}}$, the positive-real theorem turns the determination of passivity into testing the eigenvalues of its Hermitian part along the imaginary axis. If $\mathbf{Z}_{\mathrm{mix}}$ is fully passivized, then arbitrary connection with other passive circuits will still be a passive system, and hence guaranteed stable.

An important future work is to apply the methods of this dissertation, including the Newton stability test and the two damping design approaches, to more complicated PEEC models. All the examples given in this dissertation, honestly speaking, is rather simple. In particular, we only consider rectangular meshing. The PEEC model resulting from nonorthogonal discretization [9] will be an interesting test bench. Another direction of research is to verify the correctness of the conjecture by the Lyapunov-based stability tests such as that given by Antonini and Pepe [52]. In particular, it is informative to test if the damped model, damped to the level that passes the Newton necessary-condition test, can also pass the Lyapunov sufficient-condition test. If it does, then it is verified that the ground poles are the only cause of instability, for that specific model. If it does not pass the Lyapunov test, however, we are still unsure about the correctness of the conjecture. The major difficulty of this direction would be to extend the Lyapunov approach of [52] to include the damping resistors and LPFs. □

doi: 10.6342/NTU201902629

THIS PAGE INTENTIONALLY LEFT BLANK.

Appendix A.

The strip dipole subcircuit used in the simulation of Chapter 3.

```
.subckt 20190424_1125_Strip_Dipole_N_20_VCCS     11    12

L1 1 23 0.820866n
R1 23 24 718.390805u
L2 2 25 0.820866n
R2 25 26 718.390805u
L3 3 27 0.820866n
R3 27 28 718.390805u
L4 4 29 0.820866n
R4 29 30 718.390805u
L5 5 31 0.820866n
R5 31 32 718.390805u
L6 6 33 0.820866n
R6 33 34 718.390805u
L7 7 35 0.820866n
R7 35 36 718.390805u
L8 8 37 0.820866n
R8 37 38 718.390805u
L9 9 39 0.820866n
R9 39 40 718.390805u
L10 10 41 0.820866n
R10 41 42 718.390805u
L11 12 43 0.820866n
R11 43 44 718.390805u
L12 13 45 0.820866n
R12 45 46 718.390805u
L13 14 47 0.820866n
R13 47 48 718.390805u
L14 15 49 0.820866n
R14 49 50 718.390805u
L15 16 51 0.820866n
R15 51 52 718.390805u
L16 17 53 0.820866n
R16 53 54 718.390805u
L17 18 55 0.820866n
R17 55 56 718.390805u
L18 19 57 0.820866n
R18 57 58 718.390805u
L19 20 59 0.820866n
R19 59 60 718.390805u
L20 21 61 0.820866n
R20 61 62 718.390805u

GL_1_2 0 63 DELAY 2 25 TD=0.008333n SCALE=0.352706
GL_1_3 0 63 DELAY 3 27 TD=0.016667n SCALE=0.156838
GL_1_4 0 63 DELAY 4 29 TD=0.025000n SCALE=0.102829
GL_1_5 0 63 DELAY 5 31 TD=0.033333n SCALE=0.076686
GL_1_6 0 63 DELAY 6 33 TD=0.041667n SCALE=0.061190
GL_1_7 0 63 DELAY 7 35 TD=0.050000n SCALE=0.050921
GL_1_8 0 63 DELAY 8 37 TD=0.058333n SCALE=0.043610
GL_1_9 0 63 DELAY 9 39 TD=0.066667n SCALE=0.038137
GL_1_10 0 63 DELAY 10 41 TD=0.075000n SCALE=0.033887
GL_1_11 0 63 DELAY 12 43 TD=0.084000n SCALE=0.030249
GL_1_12 0 63 DELAY 13 45 TD=0.092333n SCALE=0.027514
GL_1_13 0 63 DELAY 14 47 TD=0.100667n SCALE=0.025232
GL_1_14 0 63 DELAY 15 49 TD=0.109000n SCALE=0.023300
GL_1_15 0 63 DELAY 16 51 TD=0.117333n SCALE=0.021643
GL_1_16 0 63 DELAY 17 53 TD=0.125667n SCALE=0.020207
GL_1_17 0 63 DELAY 18 55 TD=0.134000n SCALE=0.018949
GL_1_18 0 63 DELAY 19 57 TD=0.142333n SCALE=0.017838
GL_1_19 0 63 DELAY 20 59 TD=0.150667n SCALE=0.016851
GL_1_20 0 63 DELAY 21 61 TD=0.159000n SCALE=0.015967
RLmid_1 63 0 1

EL_1 24 2 VCVS 63 0 1

GL_2_1 0 64 DELAY 1 23 TD=0.008333n SCALE=0.352706
GL_2_3 0 64 DELAY 3 27 TD=0.008333n SCALE=0.352848
GL_2_4 0 64 DELAY 4 29 TD=0.016667n SCALE=0.156838
GL_2_5 0 64 DELAY 5 31 TD=0.025000n SCALE=0.102829
GL_2_6 0 64 DELAY 6 33 TD=0.033333n SCALE=0.076686
GL_2_7 0 64 DELAY 7 35 TD=0.041667n SCALE=0.061191
GL_2_8 0 64 DELAY 8 37 TD=0.050000n SCALE=0.050921
GL_2_9 0 64 DELAY 9 39 TD=0.058333n SCALE=0.043610
GL_2_10 0 64 DELAY 10 41 TD=0.066667n SCALE=0.038137
GL_2_11 0 64 DELAY 12 43 TD=0.075667n SCALE=0.033588
GL_2_12 0 64 DELAY 13 45 TD=0.084000n SCALE=0.030249
GL_2_13 0 64 DELAY 14 47 TD=0.092333n SCALE=0.027514
GL_2_14 0 64 DELAY 15 49 TD=0.100667n SCALE=0.025232
GL_2_15 0 64 DELAY 16 51 TD=0.109000n SCALE=0.023300
GL_2_16 0 64 DELAY 17 53 TD=0.117333n SCALE=0.021643
GL_2_17 0 64 DELAY 18 55 TD=0.125667n SCALE=0.020207
GL_2_18 0 64 DELAY 19 57 TD=0.134000n SCALE=0.018949
GL_2_19 0 64 DELAY 20 59 TD=0.142333n SCALE=0.017838
GL_2_20 0 64 DELAY 21 61 TD=0.150667n SCALE=0.016851
RLmid_2 64 0 1

EL_2 26 3 VCVS 64 0 1

GL_3_1 0 65 DELAY 1 23 TD=0.016667n SCALE=0.156838
GL_3_2 0 65 DELAY 2 25 TD=0.008333n SCALE=0.352848
GL_3_4 0 65 DELAY 4 29 TD=0.008333n SCALE=0.352706
GL_3_5 0 65 DELAY 5 31 TD=0.016667n SCALE=0.156838
GL_3_6 0 65 DELAY 6 33 TD=0.025000n SCALE=0.102829
GL_3_7 0 65 DELAY 7 35 TD=0.033333n SCALE=0.076686
GL_3_8 0 65 DELAY 8 37 TD=0.041667n SCALE=0.061191
GL_3_9 0 65 DELAY 9 39 TD=0.050000n SCALE=0.050921
GL_3_10 0 65 DELAY 10 41 TD=0.058333n SCALE=0.043610
GL_3_11 0 65 DELAY 12 43 TD=0.067333n SCALE=0.037759
GL_3_12 0 65 DELAY 13 45 TD=0.075667n SCALE=0.033588
GL_3_13 0 65 DELAY 14 47 TD=0.084000n SCALE=0.030249
GL_3_14 0 65 DELAY 15 49 TD=0.092333n SCALE=0.027514
GL_3_15 0 65 DELAY 16 51 TD=0.100667n SCALE=0.025232
GL_3_16 0 65 DELAY 17 53 TD=0.109000n SCALE=0.023300
GL_3_17 0 65 DELAY 18 55 TD=0.117333n SCALE=0.021643
GL_3_18 0 65 DELAY 19 57 TD=0.125667n SCALE=0.020207
GL_3_19 0 65 DELAY 20 59 TD=0.134000n SCALE=0.018949
GL_3_20 0 65 DELAY 21 61 TD=0.142333n SCALE=0.017838
RLmid_3 65 0 1

EL_3 28 4 VCVS 65 0 1

GL_4_1 0 66 DELAY 1 23 TD=0.025000n SCALE=0.102829
GL_4_2 0 66 DELAY 2 25 TD=0.016667n SCALE=0.156838
GL_4_3 0 66 DELAY 3 27 TD=0.008333n SCALE=0.352706
GL_4_5 0 66 DELAY 5 31 TD=0.008333n SCALE=0.352848
GL_4_6 0 66 DELAY 6 33 TD=0.016667n SCALE=0.156838
GL_4_7 0 66 DELAY 7 35 TD=0.025000n SCALE=0.102829
GL_4_8 0 66 DELAY 8 37 TD=0.033333n SCALE=0.076686
GL_4_9 0 66 DELAY 9 39 TD=0.041667n SCALE=0.061191
GL_4_10 0 66 DELAY 10 41 TD=0.050000n SCALE=0.050921
GL_4_11 0 66 DELAY 12 43 TD=0.059000n SCALE=0.043115
GL_4_12 0 66 DELAY 13 45 TD=0.067333n SCALE=0.037759
GL_4_13 0 66 DELAY 14 47 TD=0.075667n SCALE=0.033588
```

```
GL_4_14 0 66 DELAY 15 49 TD=0.084000n SCALE=0.030249
GL_4_15 0 66 DELAY 16 51 TD=0.092333n SCALE=0.027514
GL_4_16 0 66 DELAY 17 53 TD=0.100667n SCALE=0.025232
GL_4_17 0 66 DELAY 18 55 TD=0.109000n SCALE=0.023300
GL_4_18 0 66 DELAY 19 57 TD=0.117333n SCALE=0.021643
GL_4_19 0 66 DELAY 20 59 TD=0.125667n SCALE=0.020207
GL_4_20 0 66 DELAY 21 61 TD=0.134000n SCALE=0.018949
RLmid_4 66 0 1

EL_4 30 5 VCVS 66 0 1

GL_5_1 0 67 DELAY 1 23 TD=0.033333n SCALE=0.076686
GL_5_2 0 67 DELAY 2 25 TD=0.025000n SCALE=0.102829
GL_5_3 0 67 DELAY 3 27 TD=0.016667n SCALE=0.156838
GL_5_4 0 67 DELAY 4 29 TD=0.008333n SCALE=0.352848
GL_5_6 0 67 DELAY 6 33 TD=0.008333n SCALE=0.352706
GL_5_7 0 67 DELAY 7 35 TD=0.016667n SCALE=0.156838
GL_5_8 0 67 DELAY 8 37 TD=0.025000n SCALE=0.102829
GL_5_9 0 67 DELAY 9 39 TD=0.033333n SCALE=0.076686
GL_5_10 0 67 DELAY 10 41 TD=0.041667n SCALE=0.061191
GL_5_11 0 67 DELAY 12 43 TD=0.050667n SCALE=0.050247
GL_5_12 0 67 DELAY 13 45 TD=0.059000n SCALE=0.043115
GL_5_13 0 67 DELAY 14 47 TD=0.067333n SCALE=0.037759
GL_5_14 0 67 DELAY 15 49 TD=0.075667n SCALE=0.033588
GL_5_15 0 67 DELAY 16 51 TD=0.084000n SCALE=0.030249
GL_5_16 0 67 DELAY 17 53 TD=0.092333n SCALE=0.027514
GL_5_17 0 67 DELAY 18 55 TD=0.100667n SCALE=0.025232
GL_5_18 0 67 DELAY 19 57 TD=0.109000n SCALE=0.023300
GL_5_19 0 67 DELAY 20 59 TD=0.117333n SCALE=0.021643
GL_5_20 0 67 DELAY 21 61 TD=0.125667n SCALE=0.020207
RLmid_5 67 0 1

EL_5 32 6 VCVS 67 0 1

GL_6_1 0 68 DELAY 1 23 TD=0.041667n SCALE=0.061190
GL_6_2 0 68 DELAY 2 25 TD=0.033333n SCALE=0.076686
GL_6_3 0 68 DELAY 3 27 TD=0.025000n SCALE=0.102829
GL_6_4 0 68 DELAY 4 29 TD=0.016667n SCALE=0.156838
GL_6_5 0 68 DELAY 5 31 TD=0.008333n SCALE=0.352706
GL_6_7 0 68 DELAY 7 35 TD=0.008333n SCALE=0.352848
GL_6_8 0 68 DELAY 8 37 TD=0.016667n SCALE=0.156838
GL_6_9 0 68 DELAY 9 39 TD=0.025000n SCALE=0.102829
GL_6_10 0 68 DELAY 10 41 TD=0.033333n SCALE=0.076686
GL_6_11 0 68 DELAY 12 43 TD=0.042333n SCALE=0.060219
GL_6_12 0 68 DELAY 13 45 TD=0.050667n SCALE=0.050247
GL_6_13 0 68 DELAY 14 47 TD=0.059000n SCALE=0.043115
GL_6_14 0 68 DELAY 15 49 TD=0.067333n SCALE=0.037759
GL_6_15 0 68 DELAY 16 51 TD=0.075667n SCALE=0.033588
GL_6_16 0 68 DELAY 17 53 TD=0.084000n SCALE=0.030249
GL_6_17 0 68 DELAY 18 55 TD=0.092333n SCALE=0.027514
GL_6_18 0 68 DELAY 19 57 TD=0.100667n SCALE=0.025232
GL_6_19 0 68 DELAY 20 59 TD=0.109000n SCALE=0.023300
GL_6_20 0 68 DELAY 21 61 TD=0.117333n SCALE=0.021643
RLmid_6 68 0 1

EL_6 34 7 VCVS 68 0 1

GL_7_1 0 69 DELAY 1 23 TD=0.050000n SCALE=0.050921
GL_7_2 0 69 DELAY 2 25 TD=0.041667n SCALE=0.061191
GL_7_3 0 69 DELAY 3 27 TD=0.033333n SCALE=0.076686
GL_7_4 0 69 DELAY 4 29 TD=0.025000n SCALE=0.102829
GL_7_5 0 69 DELAY 5 31 TD=0.016667n SCALE=0.156838
GL_7_6 0 69 DELAY 6 33 TD=0.008333n SCALE=0.352848
GL_7_8 0 69 DELAY 8 37 TD=0.008333n SCALE=0.352848
GL_7_9 0 69 DELAY 9 39 TD=0.016667n SCALE=0.156838
GL_7_10 0 69 DELAY 10 41 TD=0.025000n SCALE=0.102829
GL_7_11 0 69 DELAY 12 43 TD=0.034000n SCALE=0.075161
GL_7_12 0 69 DELAY 13 45 TD=0.042333n SCALE=0.060219
GL_7_13 0 69 DELAY 14 47 TD=0.050667n SCALE=0.050247
GL_7_14 0 69 DELAY 15 49 TD=0.059000n SCALE=0.043115
GL_7_15 0 69 DELAY 16 51 TD=0.067333n SCALE=0.037759
GL_7_16 0 69 DELAY 17 53 TD=0.075667n SCALE=0.033588
GL_7_17 0 69 DELAY 18 55 TD=0.084000n SCALE=0.030249
GL_7_18 0 69 DELAY 19 57 TD=0.092333n SCALE=0.027514
GL_7_19 0 69 DELAY 20 59 TD=0.100667n SCALE=0.025232
GL_7_20 0 69 DELAY 21 61 TD=0.109000n SCALE=0.023300
RLmid_7 69 0 1

EL_7 36 8 VCVS 69 0 1

GL_8_1 0 70 DELAY 1 23 TD=0.058333n SCALE=0.043610
GL_8_2 0 70 DELAY 2 25 TD=0.050000n SCALE=0.050921
GL_8_3 0 70 DELAY 3 27 TD=0.041667n SCALE=0.061191
GL_8_4 0 70 DELAY 4 29 TD=0.033333n SCALE=0.076686
GL_8_5 0 70 DELAY 5 31 TD=0.025000n SCALE=0.102829
GL_8_6 0 70 DELAY 6 33 TD=0.016667n SCALE=0.156838
GL_8_7 0 70 DELAY 7 35 TD=0.008333n SCALE=0.352848
GL_8_9 0 70 DELAY 9 39 TD=0.008333n SCALE=0.352706
GL_8_10 0 70 DELAY 10 41 TD=0.016667n SCALE=0.156838
GL_8_11 0 70 DELAY 12 43 TD=0.025667n SCALE=0.100091
GL_8_12 0 70 DELAY 13 45 TD=0.034000n SCALE=0.075161
GL_8_13 0 70 DELAY 14 47 TD=0.042333n SCALE=0.060219
GL_8_14 0 70 DELAY 15 49 TD=0.050667n SCALE=0.050247
GL_8_15 0 70 DELAY 16 51 TD=0.059000n SCALE=0.043115
GL_8_16 0 70 DELAY 17 53 TD=0.067333n SCALE=0.037759
GL_8_17 0 70 DELAY 18 55 TD=0.075667n SCALE=0.033588
GL_8_18 0 70 DELAY 19 57 TD=0.084000n SCALE=0.030249
GL_8_19 0 70 DELAY 20 59 TD=0.092333n SCALE=0.027514
GL_8_20 0 70 DELAY 21 61 TD=0.100667n SCALE=0.025232
RLmid_8 70 0 1

EL_8 38 9 VCVS 70 0 1

GL_9_1 0 71 DELAY 1 23 TD=0.066667n SCALE=0.038137
GL_9_2 0 71 DELAY 2 25 TD=0.058333n SCALE=0.043610
GL_9_3 0 71 DELAY 3 27 TD=0.050000n SCALE=0.050921
GL_9_4 0 71 DELAY 4 29 TD=0.041667n SCALE=0.061191
GL_9_5 0 71 DELAY 5 31 TD=0.033333n SCALE=0.076686
GL_9_6 0 71 DELAY 6 33 TD=0.025000n SCALE=0.102829
GL_9_7 0 71 DELAY 7 35 TD=0.016667n SCALE=0.156838
GL_9_8 0 71 DELAY 8 37 TD=0.008333n SCALE=0.352706
GL_9_10 0 71 DELAY 10 41 TD=0.008333n SCALE=0.352848
GL_9_11 0 71 DELAY 12 43 TD=0.017333n SCALE=0.150457
GL_9_12 0 71 DELAY 13 45 TD=0.025667n SCALE=0.100091
GL_9_13 0 71 DELAY 14 47 TD=0.034000n SCALE=0.075161
GL_9_14 0 71 DELAY 15 49 TD=0.042333n SCALE=0.060219
GL_9_15 0 71 DELAY 16 51 TD=0.050667n SCALE=0.050247
GL_9_16 0 71 DELAY 17 53 TD=0.059000n SCALE=0.043115
GL_9_17 0 71 DELAY 18 55 TD=0.067333n SCALE=0.037759
GL_9_18 0 71 DELAY 19 57 TD=0.075667n SCALE=0.033588
GL_9_19 0 71 DELAY 20 59 TD=0.084000n SCALE=0.030249
GL_9_20 0 71 DELAY 21 61 TD=0.092333n SCALE=0.027514
RLmid_9 71 0 1

EL_9 40 10 VCVS 71 0 1

GL_10_1 0 72 DELAY 1 23 TD=0.075000n SCALE=0.033887
GL_10_2 0 72 DELAY 2 25 TD=0.066667n SCALE=0.038137
GL_10_3 0 72 DELAY 3 27 TD=0.058333n SCALE=0.043610
GL_10_4 0 72 DELAY 4 29 TD=0.050000n SCALE=0.050921
GL_10_5 0 72 DELAY 5 31 TD=0.041667n SCALE=0.061191
GL_10_6 0 72 DELAY 6 33 TD=0.033333n SCALE=0.076686
GL_10_7 0 72 DELAY 7 35 TD=0.025000n SCALE=0.102829
GL_10_8 0 72 DELAY 8 37 TD=0.016667n SCALE=0.156838
GL_10_9 0 72 DELAY 9 39 TD=0.008333n SCALE=0.352848
GL_10_11 0 72 DELAY 12 43 TD=0.009000n SCALE=0.317012
GL_10_12 0 72 DELAY 13 45 TD=0.017333n SCALE=0.150457
GL_10_13 0 72 DELAY 14 47 TD=0.025667n SCALE=0.100091
```

```
GL_10_14 0 72 DELAY 15 49 TD=0.034000n SCALE=0.075161
GL_10_15 0 72 DELAY 16 51 TD=0.042333n SCALE=0.060219
GL_10_16 0 72 DELAY 17 53 TD=0.050667n SCALE=0.050247
GL_10_17 0 72 DELAY 18 55 TD=0.059000n SCALE=0.043115
GL_10_18 0 72 DELAY 19 57 TD=0.067333n SCALE=0.037759
GL_10_19 0 72 DELAY 20 59 TD=0.075667n SCALE=0.033588
GL_10_20 0 72 DELAY 21 61 TD=0.084000n SCALE=0.030249
RLmid_10 72 0 1

EL_10 42 11 VCVS 72 0 1

GL_11_1 0 73 DELAY 1 23 TD=0.084000n SCALE=0.030249
GL_11_2 0 73 DELAY 2 25 TD=0.075667n SCALE=0.033588
GL_11_3 0 73 DELAY 3 27 TD=0.067333n SCALE=0.037759
GL_11_4 0 73 DELAY 4 29 TD=0.059000n SCALE=0.043115
GL_11_5 0 73 DELAY 5 31 TD=0.050667n SCALE=0.050247
GL_11_6 0 73 DELAY 6 33 TD=0.042333n SCALE=0.060219
GL_11_7 0 73 DELAY 7 35 TD=0.034000n SCALE=0.075161
GL_11_8 0 73 DELAY 8 37 TD=0.025667n SCALE=0.100091
GL_11_9 0 73 DELAY 9 39 TD=0.017333n SCALE=0.150457
GL_11_10 0 73 DELAY 10 41 TD=0.009000n SCALE=0.317012
GL_11_12 0 73 DELAY 13 45 TD=0.008333n SCALE=0.352848
GL_11_13 0 73 DELAY 14 47 TD=0.016667n SCALE=0.156838
GL_11_14 0 73 DELAY 15 49 TD=0.025000n SCALE=0.102829
GL_11_15 0 73 DELAY 16 51 TD=0.033333n SCALE=0.076686
GL_11_16 0 73 DELAY 17 53 TD=0.041667n SCALE=0.061191
GL_11_17 0 73 DELAY 18 55 TD=0.050000n SCALE=0.050921
GL_11_18 0 73 DELAY 19 57 TD=0.058333n SCALE=0.043610
GL_11_19 0 73 DELAY 20 59 TD=0.066667n SCALE=0.038137
GL_11_20 0 73 DELAY 21 61 TD=0.075000n SCALE=0.033887
RLmid_11 73 0 1

EL_11 44 13 VCVS 73 0 1

GL_12_1 0 74 DELAY 1 23 TD=0.092333n SCALE=0.027514
GL_12_2 0 74 DELAY 2 25 TD=0.084000n SCALE=0.030249
GL_12_3 0 74 DELAY 3 27 TD=0.075667n SCALE=0.033588
GL_12_4 0 74 DELAY 4 29 TD=0.067333n SCALE=0.037759
GL_12_5 0 74 DELAY 5 31 TD=0.059000n SCALE=0.043115
GL_12_6 0 74 DELAY 6 33 TD=0.050667n SCALE=0.050247
GL_12_7 0 74 DELAY 7 35 TD=0.042333n SCALE=0.060219
GL_12_8 0 74 DELAY 8 37 TD=0.034000n SCALE=0.075161
GL_12_9 0 74 DELAY 9 39 TD=0.025667n SCALE=0.100091
GL_12_10 0 74 DELAY 10 41 TD=0.017333n SCALE=0.150457
GL_12_11 0 74 DELAY 12 43 TD=0.008333n SCALE=0.352848
GL_12_13 0 74 DELAY 14 47 TD=0.008333n SCALE=0.352848
GL_12_14 0 74 DELAY 15 49 TD=0.016667n SCALE=0.156838
GL_12_15 0 74 DELAY 16 51 TD=0.025000n SCALE=0.102829
GL_12_16 0 74 DELAY 17 53 TD=0.033333n SCALE=0.076686
GL_12_17 0 74 DELAY 18 55 TD=0.041667n SCALE=0.061191
GL_12_18 0 74 DELAY 19 57 TD=0.050000n SCALE=0.050921
GL_12_19 0 74 DELAY 20 59 TD=0.058333n SCALE=0.043610
GL_12_20 0 74 DELAY 21 61 TD=0.066667n SCALE=0.038137
RLmid_12 74 0 1

EL_12 46 14 VCVS 74 0 1

GL_13_1 0 75 DELAY 1 23 TD=0.100667n SCALE=0.025232
GL_13_2 0 75 DELAY 2 25 TD=0.092333n SCALE=0.027514
GL_13_3 0 75 DELAY 3 27 TD=0.084000n SCALE=0.030249
GL_13_4 0 75 DELAY 4 29 TD=0.075667n SCALE=0.033588
GL_13_5 0 75 DELAY 5 31 TD=0.067333n SCALE=0.037759
GL_13_6 0 75 DELAY 6 33 TD=0.059000n SCALE=0.043115
GL_13_7 0 75 DELAY 7 35 TD=0.050667n SCALE=0.050247
GL_13_8 0 75 DELAY 8 37 TD=0.042333n SCALE=0.060219
GL_13_9 0 75 DELAY 9 39 TD=0.034000n SCALE=0.075161
GL_13_10 0 75 DELAY 10 41 TD=0.025667n SCALE=0.100091
GL_13_11 0 75 DELAY 12 43 TD=0.016667n SCALE=0.156838
GL_13_12 0 75 DELAY 13 45 TD=0.008333n SCALE=0.352848
GL_13_14 0 75 DELAY 15 49 TD=0.008333n SCALE=0.352706
GL_13_15 0 75 DELAY 16 51 TD=0.016667n SCALE=0.156838
GL_13_16 0 75 DELAY 17 53 TD=0.025000n SCALE=0.102829
GL_13_17 0 75 DELAY 18 55 TD=0.033333n SCALE=0.076686
GL_13_18 0 75 DELAY 19 57 TD=0.041667n SCALE=0.061191
GL_13_19 0 75 DELAY 20 59 TD=0.050000n SCALE=0.050921
GL_13_20 0 75 DELAY 21 61 TD=0.058333n SCALE=0.043610
RLmid_13 75 0 1

EL_13 48 15 VCVS 75 0 1

GL_14_1 0 76 DELAY 1 23 TD=0.109000n SCALE=0.023300
GL_14_2 0 76 DELAY 2 25 TD=0.100667n SCALE=0.025232
GL_14_3 0 76 DELAY 3 27 TD=0.092333n SCALE=0.027514
GL_14_4 0 76 DELAY 4 29 TD=0.084000n SCALE=0.030249
GL_14_5 0 76 DELAY 5 31 TD=0.075667n SCALE=0.033588
GL_14_6 0 76 DELAY 6 33 TD=0.067333n SCALE=0.037759
GL_14_7 0 76 DELAY 7 35 TD=0.059000n SCALE=0.043115
GL_14_8 0 76 DELAY 8 37 TD=0.050667n SCALE=0.050247
GL_14_9 0 76 DELAY 9 39 TD=0.042333n SCALE=0.060219
GL_14_10 0 76 DELAY 10 41 TD=0.034000n SCALE=0.075161
GL_14_11 0 76 DELAY 12 43 TD=0.025000n SCALE=0.102829
GL_14_12 0 76 DELAY 13 45 TD=0.016667n SCALE=0.156838
GL_14_13 0 76 DELAY 14 47 TD=0.008333n SCALE=0.352706
GL_14_15 0 76 DELAY 16 51 TD=0.008333n SCALE=0.352848
GL_14_16 0 76 DELAY 17 53 TD=0.016667n SCALE=0.156838
GL_14_17 0 76 DELAY 18 55 TD=0.025000n SCALE=0.102829
GL_14_18 0 76 DELAY 19 57 TD=0.033333n SCALE=0.076686
GL_14_19 0 76 DELAY 20 59 TD=0.041667n SCALE=0.061191
GL_14_20 0 76 DELAY 21 61 TD=0.050000n SCALE=0.050921
RLmid_14 76 0 1

EL_14 50 16 VCVS 76 0 1

GL_15_1 0 77 DELAY 1 23 TD=0.117333n SCALE=0.021643
GL_15_2 0 77 DELAY 2 25 TD=0.109000n SCALE=0.023300
GL_15_3 0 77 DELAY 3 27 TD=0.100667n SCALE=0.025232
GL_15_4 0 77 DELAY 4 29 TD=0.092333n SCALE=0.027514
GL_15_5 0 77 DELAY 5 31 TD=0.084000n SCALE=0.030249
GL_15_6 0 77 DELAY 6 33 TD=0.075667n SCALE=0.033588
GL_15_7 0 77 DELAY 7 35 TD=0.067333n SCALE=0.037759
GL_15_8 0 77 DELAY 8 37 TD=0.059000n SCALE=0.043115
GL_15_9 0 77 DELAY 9 39 TD=0.050667n SCALE=0.050247
GL_15_10 0 77 DELAY 10 41 TD=0.042333n SCALE=0.060219
GL_15_11 0 77 DELAY 12 43 TD=0.033333n SCALE=0.076686
GL_15_12 0 77 DELAY 13 45 TD=0.025000n SCALE=0.102829
GL_15_13 0 77 DELAY 14 47 TD=0.016667n SCALE=0.156838
GL_15_14 0 77 DELAY 15 49 TD=0.008333n SCALE=0.352848
GL_15_16 0 77 DELAY 17 53 TD=0.008333n SCALE=0.352848
GL_15_17 0 77 DELAY 18 55 TD=0.016667n SCALE=0.156838
GL_15_18 0 77 DELAY 19 57 TD=0.025000n SCALE=0.102829
GL_15_19 0 77 DELAY 20 59 TD=0.033333n SCALE=0.076686
GL_15_20 0 77 DELAY 21 61 TD=0.041667n SCALE=0.061191
RLmid_15 77 0 1

EL_15 52 17 VCVS 77 0 1

GL_16_1 0 78 DELAY 1 23 TD=0.125667n SCALE=0.020207
GL_16_2 0 78 DELAY 2 25 TD=0.117333n SCALE=0.021643
GL_16_3 0 78 DELAY 3 27 TD=0.109000n SCALE=0.023300
GL_16_4 0 78 DELAY 4 29 TD=0.100667n SCALE=0.025232
GL_16_5 0 78 DELAY 5 31 TD=0.092333n SCALE=0.027514
GL_16_6 0 78 DELAY 6 33 TD=0.084000n SCALE=0.030249
GL_16_7 0 78 DELAY 7 35 TD=0.075667n SCALE=0.033588
GL_16_8 0 78 DELAY 8 37 TD=0.067333n SCALE=0.037759
GL_16_9 0 78 DELAY 9 39 TD=0.059000n SCALE=0.043115
GL_16_10 0 78 DELAY 10 41 TD=0.050667n SCALE=0.050247
GL_16_11 0 78 DELAY 12 43 TD=0.041667n SCALE=0.061191
GL_16_12 0 78 DELAY 13 45 TD=0.033333n SCALE=0.076686
```

doi: 10.6342/NTU201902629

```
GL_16_13 0 78 DELAY 14 47 TD=0.025000n SCALE=0.102829
GL_16_14 0 78 DELAY 15 49 TD=0.016667n SCALE=0.156838
GL_16_15 0 78 DELAY 16 51 TD=0.008333n SCALE=0.352848
GL_16_17 0 78 DELAY 18 55 TD=0.008333n SCALE=0.352706
GL_16_18 0 78 DELAY 19 57 TD=0.016667n SCALE=0.156838
GL_16_19 0 78 DELAY 20 59 TD=0.025000n SCALE=0.102829
GL_16_20 0 78 DELAY 21 61 TD=0.033333n SCALE=0.076686
RLmid_16 78 0 1

EL_16 54 18 VCVS 78 0 1

GL_17_1 0 79 DELAY 1 23 TD=0.134000n SCALE=0.018949
GL_17_2 0 79 DELAY 2 25 TD=0.125667n SCALE=0.020207
GL_17_3 0 79 DELAY 3 27 TD=0.117333n SCALE=0.021643
GL_17_4 0 79 DELAY 4 29 TD=0.109000n SCALE=0.023300
GL_17_5 0 79 DELAY 5 31 TD=0.100667n SCALE=0.025232
GL_17_6 0 79 DELAY 6 33 TD=0.092333n SCALE=0.027514
GL_17_7 0 79 DELAY 7 35 TD=0.084000n SCALE=0.030249
GL_17_8 0 79 DELAY 8 37 TD=0.075667n SCALE=0.033588
GL_17_9 0 79 DELAY 9 39 TD=0.067333n SCALE=0.037759
GL_17_10 0 79 DELAY 10 41 TD=0.059000n SCALE=0.043115
GL_17_11 0 79 DELAY 12 43 TD=0.050000n SCALE=0.050921
GL_17_12 0 79 DELAY 13 45 TD=0.041667n SCALE=0.061191
GL_17_13 0 79 DELAY 14 47 TD=0.033333n SCALE=0.076686
GL_17_14 0 79 DELAY 15 49 TD=0.025000n SCALE=0.102829
GL_17_15 0 79 DELAY 16 51 TD=0.016667n SCALE=0.156838
GL_17_16 0 79 DELAY 17 53 TD=0.008333n SCALE=0.352706
GL_17_18 0 79 DELAY 19 57 TD=0.008333n SCALE=0.352848
GL_17_19 0 79 DELAY 20 59 TD=0.016667n SCALE=0.156838
GL_17_20 0 79 DELAY 21 61 TD=0.025000n SCALE=0.102829
RLmid_17 79 0 1

EL_17 56 19 VCVS 79 0 1

GL_18_1 0 80 DELAY 1 23 TD=0.142333n SCALE=0.017838
GL_18_2 0 80 DELAY 2 25 TD=0.134000n SCALE=0.018949
GL_18_3 0 80 DELAY 3 27 TD=0.125667n SCALE=0.020207
GL_18_4 0 80 DELAY 4 29 TD=0.117333n SCALE=0.021643
GL_18_5 0 80 DELAY 5 31 TD=0.109000n SCALE=0.023300
GL_18_6 0 80 DELAY 6 33 TD=0.100667n SCALE=0.025232
GL_18_7 0 80 DELAY 7 35 TD=0.092333n SCALE=0.027514
GL_18_8 0 80 DELAY 8 37 TD=0.084000n SCALE=0.030249
GL_18_9 0 80 DELAY 9 39 TD=0.075667n SCALE=0.033588
GL_18_10 0 80 DELAY 10 41 TD=0.067333n SCALE=0.037759
GL_18_11 0 80 DELAY 12 43 TD=0.058333n SCALE=0.043610
GL_18_12 0 80 DELAY 13 45 TD=0.050000n SCALE=0.050921
GL_18_13 0 80 DELAY 14 47 TD=0.041667n SCALE=0.061191
GL_18_14 0 80 DELAY 15 49 TD=0.033333n SCALE=0.076686
GL_18_15 0 80 DELAY 16 51 TD=0.025000n SCALE=0.102829
GL_18_16 0 80 DELAY 17 53 TD=0.016667n SCALE=0.156838
GL_18_17 0 80 DELAY 18 55 TD=0.008333n SCALE=0.352848
GL_18_19 0 80 DELAY 20 59 TD=0.008333n SCALE=0.352848
GL_18_20 0 80 DELAY 21 61 TD=0.016667n SCALE=0.156838
RLmid_18 80 0 1

EL_18 58 20 VCVS 80 0 1

GL_19_1 0 81 DELAY 1 23 TD=0.150667n SCALE=0.016851
GL_19_2 0 81 DELAY 2 25 TD=0.142333n SCALE=0.017838
GL_19_3 0 81 DELAY 3 27 TD=0.134000n SCALE=0.018949
GL_19_4 0 81 DELAY 4 29 TD=0.125667n SCALE=0.020207
GL_19_5 0 81 DELAY 5 31 TD=0.117333n SCALE=0.021643
GL_19_6 0 81 DELAY 6 33 TD=0.109000n SCALE=0.023300
GL_19_7 0 81 DELAY 7 35 TD=0.100667n SCALE=0.025232
GL_19_8 0 81 DELAY 8 37 TD=0.092333n SCALE=0.027514
GL_19_9 0 81 DELAY 9 39 TD=0.084000n SCALE=0.030249
GL_19_10 0 81 DELAY 10 41 TD=0.075667n SCALE=0.033588
GL_19_11 0 81 DELAY 12 43 TD=0.066667n SCALE=0.038137
GL_19_12 0 81 DELAY 13 45 TD=0.058333n SCALE=0.043610
GL_19_13 0 81 DELAY 14 47 TD=0.050000n SCALE=0.050921
GL_19_14 0 81 DELAY 15 49 TD=0.041667n SCALE=0.061191
GL_19_15 0 81 DELAY 16 51 TD=0.033333n SCALE=0.076686
GL_19_16 0 81 DELAY 17 53 TD=0.025000n SCALE=0.102829
GL_19_17 0 81 DELAY 18 55 TD=0.016667n SCALE=0.156838
GL_19_18 0 81 DELAY 19 57 TD=0.008333n SCALE=0.352848
GL_19_20 0 81 DELAY 21 61 TD=0.008333n SCALE=0.352706
RLmid_19 81 0 1

EL_19 60 21 VCVS 81 0 1

GL_20_1 0 82 DELAY 1 23 TD=0.159000n SCALE=0.015967
GL_20_2 0 82 DELAY 2 25 TD=0.150667n SCALE=0.016851
GL_20_3 0 82 DELAY 3 27 TD=0.142333n SCALE=0.017838
GL_20_4 0 82 DELAY 4 29 TD=0.134000n SCALE=0.018949
GL_20_5 0 82 DELAY 5 31 TD=0.125667n SCALE=0.020207
GL_20_6 0 82 DELAY 6 33 TD=0.117333n SCALE=0.021643
GL_20_7 0 82 DELAY 7 35 TD=0.109000n SCALE=0.023300
GL_20_8 0 82 DELAY 8 37 TD=0.100667n SCALE=0.025232
GL_20_9 0 82 DELAY 9 39 TD=0.092333n SCALE=0.027514
GL_20_10 0 82 DELAY 10 41 TD=0.084000n SCALE=0.030249
GL_20_11 0 82 DELAY 12 43 TD=0.075000n SCALE=0.033887
GL_20_12 0 82 DELAY 13 45 TD=0.066667n SCALE=0.038137
GL_20_13 0 82 DELAY 14 47 TD=0.058333n SCALE=0.043610
GL_20_14 0 82 DELAY 15 49 TD=0.050000n SCALE=0.050921
GL_20_15 0 82 DELAY 16 51 TD=0.041667n SCALE=0.061191
GL_20_16 0 82 DELAY 17 53 TD=0.033333n SCALE=0.076686
GL_20_17 0 82 DELAY 18 55 TD=0.025000n SCALE=0.102829
GL_20_18 0 82 DELAY 19 57 TD=0.016667n SCALE=0.156838
GL_20_19 0 82 DELAY 20 59 TD=0.008333n SCALE=0.352706
RLmid_20 82 0 1

EL_20 62 22 VCVS 82 0 1


C1 83 0 0.059965p
C2 84 0 0.083932p
C3 85 0 0.083932p
C4 86 0 0.083932p
C5 87 0 0.083932p
C6 88 0 0.083932p
C7 89 0 0.083932p
C8 90 0 0.083932p
C9 91 0 0.083932p
C10 92 0 0.083932p
C11 93 0 0.059965p
C12 94 0 0.059965p
C13 95 0 0.083932p
C14 96 0 0.083932p
C15 97 0 0.083932p
C16 98 0 0.083932p
C17 99 0 0.083932p
C18 100 0 0.083932p
C19 101 0 0.083932p
C20 102 0 0.083932p
C21 103 0 0.083932p
C22 104 0 0.059965p

GC_1_2 0 105 DELAY 84 0 TD=0.006250n SCALE=0.449506
GC_1_3 0 105 DELAY 85 0 TD=0.014583n SCALE=0.175306
GC_1_4 0 105 DELAY 86 0 TD=0.022917n SCALE=0.110462
GC_1_5 0 105 DELAY 87 0 TD=0.031250n SCALE=0.080755
GC_1_6 0 105 DELAY 88 0 TD=0.039583n SCALE=0.063667
GC_1_7 0 105 DELAY 89 0 TD=0.047917n SCALE=0.052557
GC_1_8 0 105 DELAY 90 0 TD=0.056250n SCALE=0.044752
GC_1_9 0 105 DELAY 91 0 TD=0.064583n SCALE=0.038967
GC_1_10 0 105 DELAY 92 0 TD=0.072917n SCALE=0.034508
GC_1_11 0 105 DELAY 93 0 TD=0.079167n SCALE=0.022690
GC_1_12 0 105 DELAY 94 0 TD=0.084000n SCALE=0.021384
```

doi: 10.6342/NTU201902629

```
GC_1_13 0 105 DELAY 95 0 TD=0.090250n SCALE=0.027874
GC_1_14 0 105 DELAY 96 0 TD=0.098583n SCALE=0.025516
GC_1_15 0 105 DELAY 97 0 TD=0.106917n SCALE=0.023526
GC_1_16 0 105 DELAY 98 0 TD=0.115250n SCALE=0.021824
GC_1_17 0 105 DELAY 99 0 TD=0.123583n SCALE=0.020351
GC_1_18 0 105 DELAY 100 0 TD=0.131917n SCALE=0.019065
GC_1_19 0 105 DELAY 101 0 TD=0.140250n SCALE=0.017932
GC_1_20 0 105 DELAY 102 0 TD=0.148583n SCALE=0.016926
GC_1_21 0 105 DELAY 103 0 TD=0.156917n SCALE=0.016027
GC_1_22 0 105 DELAY 104 0 TD=0.163167n SCALE=0.011010
RCmid_1 105 0 1

EC_1 1 83 VCVS 105 0 1

GC_2_1 0 106 DELAY 83 0 TD=0.006250n SCALE=0.321145
GC_2_3 0 106 DELAY 85 0 TD=0.008333n SCALE=0.349472
GC_2_4 0 106 DELAY 86 0 TD=0.016667n SCALE=0.155382
GC_2_5 0 106 DELAY 87 0 TD=0.025000n SCALE=0.101876
GC_2_6 0 106 DELAY 88 0 TD=0.033333n SCALE=0.075976
GC_2_7 0 106 DELAY 89 0 TD=0.041667n SCALE=0.060624
GC_2_8 0 106 DELAY 90 0 TD=0.050000n SCALE=0.050449
GC_2_9 0 106 DELAY 91 0 TD=0.058333n SCALE=0.043206
GC_2_10 0 106 DELAY 92 0 TD=0.066667n SCALE=0.037784
GC_2_11 0 106 DELAY 93 0 TD=0.072917n SCALE=0.024654
GC_2_12 0 106 DELAY 94 0 TD=0.077750n SCALE=0.023120
GC_2_13 0 106 DELAY 95 0 TD=0.084000n SCALE=0.029969
GC_2_14 0 106 DELAY 96 0 TD=0.092333n SCALE=0.027258
GC_2_15 0 106 DELAY 97 0 TD=0.100667n SCALE=0.024998
GC_2_16 0 106 DELAY 98 0 TD=0.109000n SCALE=0.023084
GC_2_17 0 106 DELAY 99 0 TD=0.117333n SCALE=0.021443
GC_2_18 0 106 DELAY 100 0 TD=0.125667n SCALE=0.020019
GC_2_19 0 106 DELAY 101 0 TD=0.134000n SCALE=0.018773
GC_2_20 0 106 DELAY 102 0 TD=0.142333n SCALE=0.017673
GC_2_21 0 106 DELAY 103 0 TD=0.150667n SCALE=0.016695
GC_2_22 0 106 DELAY 104 0 TD=0.156917n SCALE=0.011450
RCmid_2 106 0 1

EC_2 2 84 VCVS 106 0 1

GC_3_1 0 107 DELAY 83 0 TD=0.014583n SCALE=0.125246
GC_3_2 0 107 DELAY 84 0 TD=0.008333n SCALE=0.349472
GC_3_4 0 107 DELAY 86 0 TD=0.008333n SCALE=0.349473
GC_3_5 0 107 DELAY 87 0 TD=0.016667n SCALE=0.155382
GC_3_6 0 107 DELAY 88 0 TD=0.025000n SCALE=0.101876
GC_3_7 0 107 DELAY 89 0 TD=0.033333n SCALE=0.075976
GC_3_8 0 107 DELAY 90 0 TD=0.041667n SCALE=0.060624
GC_3_9 0 107 DELAY 91 0 TD=0.050000n SCALE=0.050449
GC_3_10 0 107 DELAY 92 0 TD=0.058333n SCALE=0.043206
GC_3_11 0 107 DELAY 93 0 TD=0.064583n SCALE=0.027840
GC_3_12 0 107 DELAY 94 0 TD=0.069417n SCALE=0.025899
GC_3_13 0 107 DELAY 95 0 TD=0.075667n SCALE=0.033278
GC_3_14 0 107 DELAY 96 0 TD=0.084000n SCALE=0.029969
GC_3_15 0 107 DELAY 97 0 TD=0.092333n SCALE=0.027258
GC_3_16 0 107 DELAY 98 0 TD=0.100667n SCALE=0.024998
GC_3_17 0 107 DELAY 99 0 TD=0.109000n SCALE=0.023084
GC_3_18 0 107 DELAY 100 0 TD=0.117333n SCALE=0.021443
GC_3_19 0 107 DELAY 101 0 TD=0.125667n SCALE=0.020019
GC_3_20 0 107 DELAY 102 0 TD=0.134000n SCALE=0.018773
GC_3_21 0 107 DELAY 103 0 TD=0.142333n SCALE=0.017673
GC_3_22 0 107 DELAY 104 0 TD=0.148583n SCALE=0.012093
RCmid_3 107 0 1

EC_3 3 85 VCVS 107 0 1

GC_4_1 0 108 DELAY 83 0 TD=0.022917n SCALE=0.078919
GC_4_2 0 108 DELAY 84 0 TD=0.016667n SCALE=0.155382
GC_4_3 0 108 DELAY 85 0 TD=0.008333n SCALE=0.349473
GC_4_5 0 108 DELAY 87 0 TD=0.008333n SCALE=0.349472
GC_4_6 0 108 DELAY 88 0 TD=0.016667n SCALE=0.155382
GC_4_7 0 108 DELAY 89 0 TD=0.025000n SCALE=0.101876
GC_4_8 0 108 DELAY 90 0 TD=0.033333n SCALE=0.075976
GC_4_9 0 108 DELAY 91 0 TD=0.041667n SCALE=0.060624
GC_4_10 0 108 DELAY 92 0 TD=0.050000n SCALE=0.050449
GC_4_11 0 108 DELAY 93 0 TD=0.056250n SCALE=0.031973
GC_4_12 0 108 DELAY 94 0 TD=0.061083n SCALE=0.029438
GC_4_13 0 108 DELAY 95 0 TD=0.067333n SCALE=0.037410
GC_4_14 0 108 DELAY 96 0 TD=0.075667n SCALE=0.033278
GC_4_15 0 108 DELAY 97 0 TD=0.084000n SCALE=0.029969
GC_4_16 0 108 DELAY 98 0 TD=0.092333n SCALE=0.027258
GC_4_17 0 108 DELAY 99 0 TD=0.100667n SCALE=0.024998
GC_4_18 0 108 DELAY 100 0 TD=0.109000n SCALE=0.023084
GC_4_19 0 108 DELAY 101 0 TD=0.117333n SCALE=0.021443
GC_4_20 0 108 DELAY 102 0 TD=0.125667n SCALE=0.020019
GC_4_21 0 108 DELAY 103 0 TD=0.134000n SCALE=0.018773
GC_4_22 0 108 DELAY 104 0 TD=0.140250n SCALE=0.012811
RCmid_4 108 0 1

EC_4 4 86 VCVS 108 0 1

GC_5_1 0 109 DELAY 83 0 TD=0.031250n SCALE=0.057695
GC_5_2 0 109 DELAY 84 0 TD=0.025000n SCALE=0.101876
GC_5_3 0 109 DELAY 85 0 TD=0.016667n SCALE=0.155382
GC_5_4 0 109 DELAY 86 0 TD=0.008333n SCALE=0.349472
GC_5_6 0 109 DELAY 88 0 TD=0.008333n SCALE=0.349473
GC_5_7 0 109 DELAY 89 0 TD=0.016667n SCALE=0.155382
GC_5_8 0 109 DELAY 90 0 TD=0.025000n SCALE=0.101876
GC_5_9 0 109 DELAY 91 0 TD=0.033333n SCALE=0.075976
GC_5_10 0 109 DELAY 92 0 TD=0.041667n SCALE=0.060624
GC_5_11 0 109 DELAY 93 0 TD=0.047917n SCALE=0.037549
GC_5_12 0 109 DELAY 94 0 TD=0.052750n SCALE=0.034099
GC_5_13 0 109 DELAY 95 0 TD=0.059000n SCALE=0.042715
GC_5_14 0 109 DELAY 96 0 TD=0.067333n SCALE=0.037410
GC_5_15 0 109 DELAY 97 0 TD=0.075667n SCALE=0.033278
GC_5_16 0 109 DELAY 98 0 TD=0.084000n SCALE=0.029969
GC_5_17 0 109 DELAY 99 0 TD=0.092333n SCALE=0.027258
GC_5_18 0 109 DELAY 100 0 TD=0.100667n SCALE=0.024998
GC_5_19 0 109 DELAY 101 0 TD=0.109000n SCALE=0.023084
GC_5_20 0 109 DELAY 102 0 TD=0.117333n SCALE=0.021443
GC_5_21 0 109 DELAY 103 0 TD=0.125667n SCALE=0.020019
GC_5_22 0 109 DELAY 104 0 TD=0.131917n SCALE=0.013621
RCmid_5 109 0 1

EC_5 5 87 VCVS 109 0 1

GC_6_1 0 110 DELAY 83 0 TD=0.039583n SCALE=0.045486
GC_6_2 0 110 DELAY 84 0 TD=0.033333n SCALE=0.075976
GC_6_3 0 110 DELAY 85 0 TD=0.025000n SCALE=0.101876
GC_6_4 0 110 DELAY 86 0 TD=0.016667n SCALE=0.155382
GC_6_5 0 110 DELAY 87 0 TD=0.008333n SCALE=0.349473
GC_6_7 0 110 DELAY 89 0 TD=0.008333n SCALE=0.349472
GC_6_8 0 110 DELAY 90 0 TD=0.016667n SCALE=0.155382
GC_6_9 0 110 DELAY 91 0 TD=0.025000n SCALE=0.101876
GC_6_10 0 110 DELAY 92 0 TD=0.033333n SCALE=0.075976
GC_6_11 0 110 DELAY 93 0 TD=0.039583n SCALE=0.045486
GC_6_12 0 110 DELAY 94 0 TD=0.044417n SCALE=0.040518
GC_6_13 0 110 DELAY 95 0 TD=0.050667n SCALE=0.049781
GC_6_14 0 110 DELAY 96 0 TD=0.059000n SCALE=0.042715
GC_6_15 0 110 DELAY 97 0 TD=0.067333n SCALE=0.037410
GC_6_16 0 110 DELAY 98 0 TD=0.075667n SCALE=0.033278
GC_6_17 0 110 DELAY 99 0 TD=0.084000n SCALE=0.029969
GC_6_18 0 110 DELAY 100 0 TD=0.092333n SCALE=0.027258
GC_6_19 0 110 DELAY 101 0 TD=0.100667n SCALE=0.024998
GC_6_20 0 110 DELAY 102 0 TD=0.109000n SCALE=0.023084
GC_6_21 0 110 DELAY 103 0 TD=0.117333n SCALE=0.021443
GC_6_22 0 110 DELAY 104 0 TD=0.123583n SCALE=0.014540
RCmid_6 110 0 1

EC_6 6 88 VCVS 110 0 1
```

doi: 10.6342/NTU201902629

```
GC_7_1 0 111 DELAY 83 0 TD=0.047917n SCALE=0.037549
GC_7_2 0 111 DELAY 84 0 TD=0.041667n SCALE=0.060624
GC_7_3 0 111 DELAY 85 0 TD=0.033333n SCALE=0.075976
GC_7_4 0 111 DELAY 86 0 TD=0.025000n SCALE=0.101876
GC_7_5 0 111 DELAY 87 0 TD=0.016667n SCALE=0.155382
GC_7_6 0 111 DELAY 88 0 TD=0.008333n SCALE=0.349472
GC_7_8 0 111 DELAY 90 0 TD=0.008333n SCALE=0.349473
GC_7_9 0 111 DELAY 91 0 TD=0.016667n SCALE=0.155382
GC_7_10 0 111 DELAY 92 0 TD=0.025000n SCALE=0.101876
GC_7_11 0 111 DELAY 93 0 TD=0.031250n SCALE=0.057695
GC_7_12 0 111 DELAY 94 0 TD=0.036083n SCALE=0.049921
GC_7_13 0 111 DELAY 95 0 TD=0.042333n SCALE=0.059660
GC_7_14 0 111 DELAY 96 0 TD=0.050667n SCALE=0.049781
GC_7_15 0 111 DELAY 97 0 TD=0.059000n SCALE=0.042715
GC_7_16 0 111 DELAY 98 0 TD=0.067333n SCALE=0.037410
GC_7_17 0 111 DELAY 99 0 TD=0.075667n SCALE=0.033278
GC_7_18 0 111 DELAY 100 0 TD=0.084000n SCALE=0.029969
GC_7_19 0 111 DELAY 101 0 TD=0.092333n SCALE=0.027258
GC_7_20 0 111 DELAY 102 0 TD=0.100667n SCALE=0.024998
GC_7_21 0 111 DELAY 103 0 TD=0.109000n SCALE=0.023084
GC_7_22 0 111 DELAY 104 0 TD=0.115250n SCALE=0.015592
RCmid_7 111 0 1

EC_7 7 89 VCVS 111 0 1

GC_8_1 0 112 DELAY 83 0 TD=0.056250n SCALE=0.031973
GC_8_2 0 112 DELAY 84 0 TD=0.050000n SCALE=0.050449
GC_8_3 0 112 DELAY 85 0 TD=0.041667n SCALE=0.060624
GC_8_4 0 112 DELAY 86 0 TD=0.033333n SCALE=0.075976
GC_8_5 0 112 DELAY 87 0 TD=0.025000n SCALE=0.101876
GC_8_6 0 112 DELAY 88 0 TD=0.016667n SCALE=0.155382
GC_8_7 0 112 DELAY 89 0 TD=0.008333n SCALE=0.349473
GC_8_9 0 112 DELAY 91 0 TD=0.008333n SCALE=0.349473
GC_8_10 0 112 DELAY 92 0 TD=0.016667n SCALE=0.155382
GC_8_11 0 112 DELAY 93 0 TD=0.022917n SCALE=0.078919
GC_8_12 0 112 DELAY 94 0 TD=0.027750n SCALE=0.065034
GC_8_13 0 112 DELAY 95 0 TD=0.034000n SCALE=0.074466
GC_8_14 0 112 DELAY 96 0 TD=0.042333n SCALE=0.059660
GC_8_15 0 112 DELAY 97 0 TD=0.050667n SCALE=0.049781
GC_8_16 0 112 DELAY 98 0 TD=0.059000n SCALE=0.042715
GC_8_17 0 112 DELAY 99 0 TD=0.067333n SCALE=0.037410
GC_8_18 0 112 DELAY 100 0 TD=0.075667n SCALE=0.033278
GC_8_19 0 112 DELAY 101 0 TD=0.084000n SCALE=0.029969
GC_8_20 0 112 DELAY 102 0 TD=0.092333n SCALE=0.027258
GC_8_21 0 112 DELAY 103 0 TD=0.100667n SCALE=0.024998
GC_8_22 0 112 DELAY 104 0 TD=0.106917n SCALE=0.016808
RCmid_8 112 0 1

EC_8 8 90 VCVS 112 0 1

GC_9_1 0 113 DELAY 83 0 TD=0.064583n SCALE=0.027840
GC_9_2 0 113 DELAY 84 0 TD=0.058333n SCALE=0.043206
GC_9_3 0 113 DELAY 85 0 TD=0.050000n SCALE=0.050449
GC_9_4 0 113 DELAY 86 0 TD=0.041667n SCALE=0.060624
GC_9_5 0 113 DELAY 87 0 TD=0.033333n SCALE=0.075976
GC_9_6 0 113 DELAY 88 0 TD=0.025000n SCALE=0.101876
GC_9_7 0 113 DELAY 89 0 TD=0.016667n SCALE=0.155382
GC_9_8 0 113 DELAY 90 0 TD=0.008333n SCALE=0.349473
GC_9_10 0 113 DELAY 92 0 TD=0.008333n SCALE=0.349472
GC_9_11 0 113 DELAY 93 0 TD=0.014583n SCALE=0.125246
GC_9_12 0 113 DELAY 94 0 TD=0.019417n SCALE=0.093390
GC_9_13 0 113 DELAY 95 0 TD=0.025667n SCALE=0.099164
GC_9_14 0 113 DELAY 96 0 TD=0.034000n SCALE=0.074466
GC_9_15 0 113 DELAY 97 0 TD=0.042333n SCALE=0.059660
GC_9_16 0 113 DELAY 98 0 TD=0.050667n SCALE=0.049781
GC_9_17 0 113 DELAY 99 0 TD=0.059000n SCALE=0.042715
GC_9_18 0 113 DELAY 100 0 TD=0.067333n SCALE=0.037410
GC_9_19 0 113 DELAY 101 0 TD=0.075667n SCALE=0.033278
GC_9_20 0 113 DELAY 102 0 TD=0.084000n SCALE=0.029969
GC_9_21 0 113 DELAY 103 0 TD=0.092333n SCALE=0.027258
GC_9_22 0 113 DELAY 104 0 TD=0.098583n SCALE=0.018230
RCmid_9 113 0 1

EC_9 9 91 VCVS 113 0 1

GC_10_1 0 114 DELAY 83 0 TD=0.072917n SCALE=0.024654
GC_10_2 0 114 DELAY 84 0 TD=0.066667n SCALE=0.037784
GC_10_3 0 114 DELAY 85 0 TD=0.058333n SCALE=0.043206
GC_10_4 0 114 DELAY 86 0 TD=0.050000n SCALE=0.050449
GC_10_5 0 114 DELAY 87 0 TD=0.041667n SCALE=0.060624
GC_10_6 0 114 DELAY 88 0 TD=0.033333n SCALE=0.075976
GC_10_7 0 114 DELAY 89 0 TD=0.025000n SCALE=0.101876
GC_10_8 0 114 DELAY 90 0 TD=0.016667n SCALE=0.155382
GC_10_9 0 114 DELAY 91 0 TD=0.008333n SCALE=0.349472
GC_10_11 0 114 DELAY 93 0 TD=0.006250n SCALE=0.321145
GC_10_12 0 114 DELAY 94 0 TD=0.011083n SCALE=0.166835
GC_10_13 0 114 DELAY 95 0 TD=0.017333n SCALE=0.149061
GC_10_14 0 114 DELAY 96 0 TD=0.025667n SCALE=0.099164
GC_10_15 0 114 DELAY 97 0 TD=0.034000n SCALE=0.074466
GC_10_16 0 114 DELAY 98 0 TD=0.042333n SCALE=0.059660
GC_10_17 0 114 DELAY 99 0 TD=0.050667n SCALE=0.049781
GC_10_18 0 114 DELAY 100 0 TD=0.059000n SCALE=0.042715
GC_10_19 0 114 DELAY 101 0 TD=0.067333n SCALE=0.037410
GC_10_20 0 114 DELAY 102 0 TD=0.075667n SCALE=0.033278
GC_10_21 0 114 DELAY 103 0 TD=0.084000n SCALE=0.029969
GC_10_22 0 114 DELAY 104 0 TD=0.090250n SCALE=0.019914
RCmid_10 114 0 1

EC_10 10 92 VCVS 114 0 1

GC_11_1 0 115 DELAY 83 0 TD=0.079167n SCALE=0.022690
GC_11_2 0 115 DELAY 84 0 TD=0.072917n SCALE=0.034508
GC_11_3 0 115 DELAY 85 0 TD=0.064583n SCALE=0.038967
GC_11_4 0 115 DELAY 86 0 TD=0.056250n SCALE=0.044752
GC_11_5 0 115 DELAY 87 0 TD=0.047917n SCALE=0.052557
GC_11_6 0 115 DELAY 88 0 TD=0.039583n SCALE=0.063667
GC_11_7 0 115 DELAY 89 0 TD=0.031250n SCALE=0.080755
GC_11_8 0 115 DELAY 90 0 TD=0.022917n SCALE=0.110462
GC_11_9 0 115 DELAY 91 0 TD=0.014583n SCALE=0.175306
GC_11_10 0 115 DELAY 92 0 TD=0.006250n SCALE=0.449506
GC_11_12 0 115 DELAY 94 0 TD=0.004833n SCALE=0.365943
GC_11_13 0 115 DELAY 95 0 TD=0.011083n SCALE=0.233518
GC_11_14 0 115 DELAY 96 0 TD=0.019417n SCALE=0.130718
GC_11_15 0 115 DELAY 97 0 TD=0.027750n SCALE=0.091028
GC_11_16 0 115 DELAY 98 0 TD=0.036083n SCALE=0.069875
GC_11_17 0 115 DELAY 99 0 TD=0.044417n SCALE=0.056713
GC_11_18 0 115 DELAY 100 0 TD=0.052750n SCALE=0.047729
GC_11_19 0 115 DELAY 101 0 TD=0.061083n SCALE=0.041204
GC_11_20 0 115 DELAY 102 0 TD=0.069417n SCALE=0.036251
GC_11_21 0 115 DELAY 103 0 TD=0.077750n SCALE=0.032360
GC_11_22 0 115 DELAY 104 0 TD=0.084000n SCALE=0.021384
RCmid_11 115 0 1

EC_11 11 93 VCVS 115 0 1

GC_12_1 0 116 DELAY 83 0 TD=0.084000n SCALE=0.021384
GC_12_2 0 116 DELAY 84 0 TD=0.077750n SCALE=0.032360
GC_12_3 0 116 DELAY 85 0 TD=0.069417n SCALE=0.036251
GC_12_4 0 116 DELAY 86 0 TD=0.061083n SCALE=0.041204
GC_12_5 0 116 DELAY 87 0 TD=0.052750n SCALE=0.047729
GC_12_6 0 116 DELAY 88 0 TD=0.044417n SCALE=0.056713
GC_12_7 0 116 DELAY 89 0 TD=0.036083n SCALE=0.069875
GC_12_8 0 116 DELAY 90 0 TD=0.027750n SCALE=0.091028
GC_12_9 0 116 DELAY 91 0 TD=0.019417n SCALE=0.130718
GC_12_10 0 116 DELAY 92 0 TD=0.011083n SCALE=0.233518
GC_12_11 0 116 DELAY 93 0 TD=0.004833n SCALE=0.365943
GC_12_13 0 116 DELAY 95 0 TD=0.006250n SCALE=0.449506
```

```
GC_12_14 0 116 DELAY 96 0 TD=0.014583n SCALE=0.175306
GC_12_15 0 116 DELAY 97 0 TD=0.022917n SCALE=0.110462
GC_12_16 0 116 DELAY 98 0 TD=0.031250n SCALE=0.080755
GC_12_17 0 116 DELAY 99 0 TD=0.039583n SCALE=0.063667
GC_12_18 0 116 DELAY 100 0 TD=0.047917n SCALE=0.052557
GC_12_19 0 116 DELAY 101 0 TD=0.056250n SCALE=0.044752
GC_12_20 0 116 DELAY 102 0 TD=0.064583n SCALE=0.038967
GC_12_21 0 116 DELAY 103 0 TD=0.072917n SCALE=0.034508
GC_12_22 0 116 DELAY 104 0 TD=0.079167n SCALE=0.022690
RCmid_12 116 0 1

EC_12 12 94 VCVS 116 0 1

GC_13_1 0 117 DELAY 83 0 TD=0.090250n SCALE=0.019914
GC_13_2 0 117 DELAY 84 0 TD=0.084000n SCALE=0.029969
GC_13_3 0 117 DELAY 85 0 TD=0.075667n SCALE=0.033278
GC_13_4 0 117 DELAY 86 0 TD=0.067333n SCALE=0.037410
GC_13_5 0 117 DELAY 87 0 TD=0.059000n SCALE=0.042715
GC_13_6 0 117 DELAY 88 0 TD=0.050667n SCALE=0.049781
GC_13_7 0 117 DELAY 89 0 TD=0.042333n SCALE=0.059660
GC_13_8 0 117 DELAY 90 0 TD=0.034000n SCALE=0.074466
GC_13_9 0 117 DELAY 91 0 TD=0.025667n SCALE=0.099164
GC_13_10 0 117 DELAY 92 0 TD=0.017333n SCALE=0.149061
GC_13_11 0 117 DELAY 93 0 TD=0.011083n SCALE=0.166835
GC_13_12 0 117 DELAY 94 0 TD=0.006250n SCALE=0.321145
GC_13_14 0 117 DELAY 96 0 TD=0.008333n SCALE=0.349472
GC_13_15 0 117 DELAY 97 0 TD=0.016667n SCALE=0.155382
GC_13_16 0 117 DELAY 98 0 TD=0.025000n SCALE=0.101876
GC_13_17 0 117 DELAY 99 0 TD=0.033333n SCALE=0.075976
GC_13_18 0 117 DELAY 100 0 TD=0.041667n SCALE=0.060624
GC_13_19 0 117 DELAY 101 0 TD=0.050000n SCALE=0.050449
GC_13_20 0 117 DELAY 102 0 TD=0.058333n SCALE=0.043206
GC_13_21 0 117 DELAY 103 0 TD=0.066667n SCALE=0.037784
GC_13_22 0 117 DELAY 104 0 TD=0.072917n SCALE=0.024654
RCmid_13 117 0 1

EC_13 13 95 VCVS 117 0 1

GC_14_1 0 118 DELAY 83 0 TD=0.098583n SCALE=0.018230
GC_14_2 0 118 DELAY 84 0 TD=0.092333n SCALE=0.027258
GC_14_3 0 118 DELAY 85 0 TD=0.084000n SCALE=0.029969
GC_14_4 0 118 DELAY 86 0 TD=0.075667n SCALE=0.033278
GC_14_5 0 118 DELAY 87 0 TD=0.067333n SCALE=0.037410
GC_14_6 0 118 DELAY 88 0 TD=0.059000n SCALE=0.042715
GC_14_7 0 118 DELAY 89 0 TD=0.050667n SCALE=0.049781
GC_14_8 0 118 DELAY 90 0 TD=0.042333n SCALE=0.059660
GC_14_9 0 118 DELAY 91 0 TD=0.034000n SCALE=0.074466
GC_14_10 0 118 DELAY 92 0 TD=0.025667n SCALE=0.099164
GC_14_11 0 118 DELAY 93 0 TD=0.019417n SCALE=0.093390
GC_14_12 0 118 DELAY 94 0 TD=0.014583n SCALE=0.125246
GC_14_13 0 118 DELAY 95 0 TD=0.008333n SCALE=0.349472
GC_14_15 0 118 DELAY 97 0 TD=0.008333n SCALE=0.349472
GC_14_16 0 118 DELAY 98 0 TD=0.016667n SCALE=0.155382
GC_14_17 0 118 DELAY 99 0 TD=0.025000n SCALE=0.101876
GC_14_18 0 118 DELAY 100 0 TD=0.033333n SCALE=0.075976
GC_14_19 0 118 DELAY 101 0 TD=0.041667n SCALE=0.060624
GC_14_20 0 118 DELAY 102 0 TD=0.050000n SCALE=0.050449
GC_14_21 0 118 DELAY 103 0 TD=0.058333n SCALE=0.043206
GC_14_22 0 118 DELAY 104 0 TD=0.064583n SCALE=0.027840
RCmid_14 118 0 1

EC_14 14 96 VCVS 118 0 1

GC_15_1 0 119 DELAY 83 0 TD=0.106917n SCALE=0.016808
GC_15_2 0 119 DELAY 84 0 TD=0.100667n SCALE=0.024998
GC_15_3 0 119 DELAY 85 0 TD=0.092333n SCALE=0.027258
GC_15_4 0 119 DELAY 86 0 TD=0.084000n SCALE=0.029969
GC_15_5 0 119 DELAY 87 0 TD=0.075667n SCALE=0.033278
GC_15_6 0 119 DELAY 88 0 TD=0.067333n SCALE=0.037410
GC_15_7 0 119 DELAY 89 0 TD=0.059000n SCALE=0.042715
GC_15_8 0 119 DELAY 90 0 TD=0.050667n SCALE=0.049781
GC_15_9 0 119 DELAY 91 0 TD=0.042333n SCALE=0.059660
GC_15_10 0 119 DELAY 92 0 TD=0.034000n SCALE=0.074466
GC_15_11 0 119 DELAY 93 0 TD=0.027750n SCALE=0.065034
GC_15_12 0 119 DELAY 94 0 TD=0.022917n SCALE=0.078919
GC_15_13 0 119 DELAY 95 0 TD=0.016667n SCALE=0.155382
GC_15_14 0 119 DELAY 96 0 TD=0.008333n SCALE=0.349472
GC_15_16 0 119 DELAY 98 0 TD=0.008333n SCALE=0.349473
GC_15_17 0 119 DELAY 99 0 TD=0.016667n SCALE=0.155382
GC_15_18 0 119 DELAY 100 0 TD=0.025000n SCALE=0.101876
GC_15_19 0 119 DELAY 101 0 TD=0.033333n SCALE=0.075976
GC_15_20 0 119 DELAY 102 0 TD=0.041667n SCALE=0.060624
GC_15_21 0 119 DELAY 103 0 TD=0.050000n SCALE=0.050449
GC_15_22 0 119 DELAY 104 0 TD=0.056250n SCALE=0.031973
RCmid_15 119 0 1

EC_15 15 97 VCVS 119 0 1

GC_16_1 0 120 DELAY 83 0 TD=0.115250n SCALE=0.015592
GC_16_2 0 120 DELAY 84 0 TD=0.109000n SCALE=0.023084
GC_16_3 0 120 DELAY 85 0 TD=0.100667n SCALE=0.024998
GC_16_4 0 120 DELAY 86 0 TD=0.092333n SCALE=0.027258
GC_16_5 0 120 DELAY 87 0 TD=0.084000n SCALE=0.029969
GC_16_6 0 120 DELAY 88 0 TD=0.075667n SCALE=0.033278
GC_16_7 0 120 DELAY 89 0 TD=0.067333n SCALE=0.037410
GC_16_8 0 120 DELAY 90 0 TD=0.059000n SCALE=0.042715
GC_16_9 0 120 DELAY 91 0 TD=0.050667n SCALE=0.049781
GC_16_10 0 120 DELAY 92 0 TD=0.042333n SCALE=0.059660
GC_16_11 0 120 DELAY 93 0 TD=0.036083n SCALE=0.049921
GC_16_12 0 120 DELAY 94 0 TD=0.031250n SCALE=0.057695
GC_16_13 0 120 DELAY 95 0 TD=0.025000n SCALE=0.101876
GC_16_14 0 120 DELAY 96 0 TD=0.016667n SCALE=0.155382
GC_16_15 0 120 DELAY 97 0 TD=0.008333n SCALE=0.349473
GC_16_17 0 120 DELAY 99 0 TD=0.008333n SCALE=0.349473
GC_16_18 0 120 DELAY 100 0 TD=0.016667n SCALE=0.155382
GC_16_19 0 120 DELAY 101 0 TD=0.025000n SCALE=0.101876
GC_16_20 0 120 DELAY 102 0 TD=0.033333n SCALE=0.075976
GC_16_21 0 120 DELAY 103 0 TD=0.041667n SCALE=0.060624
GC_16_22 0 120 DELAY 104 0 TD=0.047917n SCALE=0.037549
RCmid_16 120 0 1

EC_16 16 98 VCVS 120 0 1

GC_17_1 0 121 DELAY 83 0 TD=0.123583n SCALE=0.014540
GC_17_2 0 121 DELAY 84 0 TD=0.117333n SCALE=0.021443
GC_17_3 0 121 DELAY 85 0 TD=0.109000n SCALE=0.023084
GC_17_4 0 121 DELAY 86 0 TD=0.100667n SCALE=0.024998
GC_17_5 0 121 DELAY 87 0 TD=0.092333n SCALE=0.027258
GC_17_6 0 121 DELAY 88 0 TD=0.084000n SCALE=0.029969
GC_17_7 0 121 DELAY 89 0 TD=0.075667n SCALE=0.033278
GC_17_8 0 121 DELAY 90 0 TD=0.067333n SCALE=0.037410
GC_17_9 0 121 DELAY 91 0 TD=0.059000n SCALE=0.042715
GC_17_10 0 121 DELAY 92 0 TD=0.050667n SCALE=0.049781
GC_17_11 0 121 DELAY 93 0 TD=0.044417n SCALE=0.040518
GC_17_12 0 121 DELAY 94 0 TD=0.039583n SCALE=0.045486
GC_17_13 0 121 DELAY 95 0 TD=0.033333n SCALE=0.075976
GC_17_14 0 121 DELAY 96 0 TD=0.025000n SCALE=0.101876
GC_17_15 0 121 DELAY 97 0 TD=0.016667n SCALE=0.155382
GC_17_16 0 121 DELAY 98 0 TD=0.008333n SCALE=0.349473
GC_17_18 0 121 DELAY 100 0 TD=0.008333n SCALE=0.349472
GC_17_19 0 121 DELAY 101 0 TD=0.016667n SCALE=0.155382
GC_17_20 0 121 DELAY 102 0 TD=0.025000n SCALE=0.101876
GC_17_21 0 121 DELAY 103 0 TD=0.033333n SCALE=0.075976
GC_17_22 0 121 DELAY 104 0 TD=0.039583n SCALE=0.045486
RCmid_17 121 0 1

EC_17 17 99 VCVS 121 0 1
```

```
GC_18_1 0 122 DELAY 83 0 TD=0.131917n SCALE=0.013621
GC_18_2 0 122 DELAY 84 0 TD=0.125667n SCALE=0.020019
GC_18_3 0 122 DELAY 85 0 TD=0.117333n SCALE=0.021443
GC_18_4 0 122 DELAY 86 0 TD=0.109000n SCALE=0.023084
GC_18_5 0 122 DELAY 87 0 TD=0.100667n SCALE=0.024998
GC_18_6 0 122 DELAY 88 0 TD=0.092333n SCALE=0.027258
GC_18_7 0 122 DELAY 89 0 TD=0.084000n SCALE=0.029969
GC_18_8 0 122 DELAY 90 0 TD=0.075667n SCALE=0.033278
GC_18_9 0 122 DELAY 91 0 TD=0.067333n SCALE=0.037410
GC_18_10 0 122 DELAY 92 0 TD=0.059000n SCALE=0.042715
GC_18_11 0 122 DELAY 93 0 TD=0.052750n SCALE=0.034099
GC_18_12 0 122 DELAY 94 0 TD=0.047917n SCALE=0.037549
GC_18_13 0 122 DELAY 95 0 TD=0.041667n SCALE=0.060624
GC_18_14 0 122 DELAY 96 0 TD=0.033333n SCALE=0.075976
GC_18_15 0 122 DELAY 97 0 TD=0.025000n SCALE=0.101876
GC_18_16 0 122 DELAY 98 0 TD=0.016667n SCALE=0.155382
GC_18_17 0 122 DELAY 99 0 TD=0.008333n SCALE=0.349472
GC_18_19 0 122 DELAY 101 0 TD=0.008333n SCALE=0.349473
GC_18_20 0 122 DELAY 102 0 TD=0.016667n SCALE=0.155382
GC_18_21 0 122 DELAY 103 0 TD=0.025000n SCALE=0.101876
GC_18_22 0 122 DELAY 104 0 TD=0.031250n SCALE=0.057695
RCmid_18 122 0 1

EC_18 18 100 VCVS 122 0 1

GC_19_1 0 123 DELAY 83 0 TD=0.140250n SCALE=0.012811
GC_19_2 0 123 DELAY 84 0 TD=0.134000n SCALE=0.018773
GC_19_3 0 123 DELAY 85 0 TD=0.125667n SCALE=0.020019
GC_19_4 0 123 DELAY 86 0 TD=0.117333n SCALE=0.021443
GC_19_5 0 123 DELAY 87 0 TD=0.109000n SCALE=0.023084
GC_19_6 0 123 DELAY 88 0 TD=0.100667n SCALE=0.024998
GC_19_7 0 123 DELAY 89 0 TD=0.092333n SCALE=0.027258
GC_19_8 0 123 DELAY 90 0 TD=0.084000n SCALE=0.029969
GC_19_9 0 123 DELAY 91 0 TD=0.075667n SCALE=0.033278
GC_19_10 0 123 DELAY 92 0 TD=0.067333n SCALE=0.037410
GC_19_11 0 123 DELAY 93 0 TD=0.061083n SCALE=0.029438
GC_19_12 0 123 DELAY 94 0 TD=0.056250n SCALE=0.031973
GC_19_13 0 123 DELAY 95 0 TD=0.050000n SCALE=0.050449
GC_19_14 0 123 DELAY 96 0 TD=0.041667n SCALE=0.060624
GC_19_15 0 123 DELAY 97 0 TD=0.033333n SCALE=0.075976
GC_19_16 0 123 DELAY 98 0 TD=0.025000n SCALE=0.101876
GC_19_17 0 123 DELAY 99 0 TD=0.016667n SCALE=0.155382
GC_19_18 0 123 DELAY 100 0 TD=0.008333n SCALE=0.349473
GC_19_20 0 123 DELAY 102 0 TD=0.008333n SCALE=0.349473
GC_19_21 0 123 DELAY 103 0 TD=0.016667n SCALE=0.155382
GC_19_22 0 123 DELAY 104 0 TD=0.022917n SCALE=0.078919
RCmid_19 123 0 1

EC_19 19 101 VCVS 123 0 1

GC_20_1 0 124 DELAY 83 0 TD=0.148583n SCALE=0.012093
GC_20_2 0 124 DELAY 84 0 TD=0.142333n SCALE=0.017673
GC_20_3 0 124 DELAY 85 0 TD=0.134000n SCALE=0.018773
GC_20_4 0 124 DELAY 86 0 TD=0.125667n SCALE=0.020019
GC_20_5 0 124 DELAY 87 0 TD=0.117333n SCALE=0.021443
GC_20_6 0 124 DELAY 88 0 TD=0.109000n SCALE=0.023084
GC_20_7 0 124 DELAY 89 0 TD=0.100667n SCALE=0.024998
GC_20_8 0 124 DELAY 90 0 TD=0.092333n SCALE=0.027258
GC_20_9 0 124 DELAY 91 0 TD=0.084000n SCALE=0.029969
GC_20_10 0 124 DELAY 92 0 TD=0.075667n SCALE=0.033278
GC_20_11 0 124 DELAY 93 0 TD=0.069417n SCALE=0.025899
GC_20_12 0 124 DELAY 94 0 TD=0.064583n SCALE=0.027840
GC_20_13 0 124 DELAY 95 0 TD=0.058333n SCALE=0.043206
GC_20_14 0 124 DELAY 96 0 TD=0.050000n SCALE=0.050449
GC_20_15 0 124 DELAY 97 0 TD=0.041667n SCALE=0.060624
GC_20_16 0 124 DELAY 98 0 TD=0.033333n SCALE=0.075976
GC_20_17 0 124 DELAY 99 0 TD=0.025000n SCALE=0.101876
GC_20_18 0 124 DELAY 100 0 TD=0.016667n SCALE=0.155382
GC_20_19 0 124 DELAY 101 0 TD=0.008333n SCALE=0.349473
GC_20_21 0 124 DELAY 103 0 TD=0.008333n SCALE=0.349472
GC_20_22 0 124 DELAY 104 0 TD=0.014583n SCALE=0.125246
RCmid_20 124 0 1

EC_20 20 102 VCVS 124 0 1

GC_21_1 0 125 DELAY 83 0 TD=0.156917n SCALE=0.011450
GC_21_2 0 125 DELAY 84 0 TD=0.150667n SCALE=0.016695
GC_21_3 0 125 DELAY 85 0 TD=0.142333n SCALE=0.017673
GC_21_4 0 125 DELAY 86 0 TD=0.134000n SCALE=0.018773
GC_21_5 0 125 DELAY 87 0 TD=0.125667n SCALE=0.020019
GC_21_6 0 125 DELAY 88 0 TD=0.117333n SCALE=0.021443
GC_21_7 0 125 DELAY 89 0 TD=0.109000n SCALE=0.023084
GC_21_8 0 125 DELAY 90 0 TD=0.100667n SCALE=0.024998
GC_21_9 0 125 DELAY 91 0 TD=0.092333n SCALE=0.027258
GC_21_10 0 125 DELAY 92 0 TD=0.084000n SCALE=0.029969
GC_21_11 0 125 DELAY 93 0 TD=0.077750n SCALE=0.023120
GC_21_12 0 125 DELAY 94 0 TD=0.072917n SCALE=0.024654
GC_21_13 0 125 DELAY 95 0 TD=0.066667n SCALE=0.037784
GC_21_14 0 125 DELAY 96 0 TD=0.058333n SCALE=0.043206
GC_21_15 0 125 DELAY 97 0 TD=0.050000n SCALE=0.050449
GC_21_16 0 125 DELAY 98 0 TD=0.041667n SCALE=0.060624
GC_21_17 0 125 DELAY 99 0 TD=0.033333n SCALE=0.075976
GC_21_18 0 125 DELAY 100 0 TD=0.025000n SCALE=0.101876
GC_21_19 0 125 DELAY 101 0 TD=0.016667n SCALE=0.155382
GC_21_20 0 125 DELAY 102 0 TD=0.008333n SCALE=0.349472
GC_21_22 0 125 DELAY 104 0 TD=0.006250n SCALE=0.321145
RCmid_21 125 0 1

EC_21 21 103 VCVS 125 0 1

GC_22_1 0 126 DELAY 83 0 TD=0.163167n SCALE=0.011010
GC_22_2 0 126 DELAY 84 0 TD=0.156917n SCALE=0.016027
GC_22_3 0 126 DELAY 85 0 TD=0.148583n SCALE=0.016926
GC_22_4 0 126 DELAY 86 0 TD=0.140250n SCALE=0.017932
GC_22_5 0 126 DELAY 87 0 TD=0.131917n SCALE=0.019065
GC_22_6 0 126 DELAY 88 0 TD=0.123583n SCALE=0.020351
GC_22_7 0 126 DELAY 89 0 TD=0.115250n SCALE=0.021824
GC_22_8 0 126 DELAY 90 0 TD=0.106917n SCALE=0.023526
GC_22_9 0 126 DELAY 91 0 TD=0.098583n SCALE=0.025516
GC_22_10 0 126 DELAY 92 0 TD=0.090250n SCALE=0.027874
GC_22_11 0 126 DELAY 93 0 TD=0.084000n SCALE=0.021384
GC_22_12 0 126 DELAY 94 0 TD=0.079167n SCALE=0.022690
GC_22_13 0 126 DELAY 95 0 TD=0.072917n SCALE=0.034508
GC_22_14 0 126 DELAY 96 0 TD=0.064583n SCALE=0.038967
GC_22_15 0 126 DELAY 97 0 TD=0.056250n SCALE=0.044752
GC_22_16 0 126 DELAY 98 0 TD=0.047917n SCALE=0.052557
GC_22_17 0 126 DELAY 99 0 TD=0.039583n SCALE=0.063667
GC_22_18 0 126 DELAY 100 0 TD=0.031250n SCALE=0.080755
GC_22_19 0 126 DELAY 101 0 TD=0.022917n SCALE=0.110462
GC_22_20 0 126 DELAY 102 0 TD=0.014583n SCALE=0.175306
GC_22_21 0 126 DELAY 103 0 TD=0.006250n SCALE=0.449506
RCmid_22 126 0 1

EC_22 22 104 VCVS 126 0 1

.ends 20190424_1125_Strip_Dipole_N_20_VCCS
```

REFERENCE

[1] A. E. Ruehli, “Equivalent circuit models for three-dimensional multiconductor systems,” *IEEE Trans. Microw. Theory Techn.*, vol. 22, no. 3, pp. 216-221, Mar. 1974.

[2] J. M. Jin, *The Finite Element Method in Electromagnetics*, 3rd ed., Hoboken, NJ: Wiley, 2014.

[3] R. F. Harrington, *Field Computation by Moment Methods*, 1st ed., NY: Macmillan, 1968.

[4] A. Taflove and S. C. Hagness, *Computational Electrodynamics: The Finite-Difference Time-Domain Method*, 3rd ed., Norwood, MA: Artech House, 2005.

[5] A. E. Ruehli, “Inductance calculations in a complex integrated circuit environment,” *IBM J. Res. Develop.*, vol. 16, no. 5, pp. 470–481, Sept. 1972.

[6] C.-W. Ho, A. E. Ruehli, and P. A. Brennan, “The modified nodal approach to network analysis,” *IEEE Trans. Circuits and Systems*, vol. cas-22, no. 6, pp. 504–509, June 1975.

[7] L. O. Chua, C. A. Desoer, and E. S. Kuh, *Linear and Nonlinear Circuits*, NY: McGraw-Hill, 1987.

[8] A. E. Ruehli and H. Heeb, “Circuit models for three-dimensional geometries including dielectric,” *IEEE Trans. Microw. Theory Techn.*, vol. 40, no. 7, pp. 1507–1516, July 1992.

doi: 10.6342/NTU201902629

[9] A. Ruehli, G. Antonini, J. Esch, J. Ekman, A. Mayo, and A. Orlandi, “Nonorthogonal PEEC formulation for time- and frequency-domain EM and circuit modeling,” *IEEE Trans. Electromagn. Compat.*, vol. 45, no. 2, pp. 167-176, 2003.

[10] A. E. Ruehli, G. Antonini, and L. Jiang. “Skin-effect loss models for time- and frequency-domain PEEC solver,” *Proc. IEEE*, vol. 101, no. 2, pp. 451-472, Feb. 2013.

[11] J. D. Jackson, *Classical Electrodynamics*, 3rd ed., NY: Wiley, 1999.

[12] R. F. Harrington, *Time Harmonic Electromagnetic Fields*, NY: Wiley-IEEE Press, 2001.

[13] D. J. Griffiths, *Introduction to Electrodynamics*, 3rd ed., NJ: Prentice-Hall, 1999.

[14] Y. Wang, V. Jandhyala, and C.-J. Shi, “Coupled electromagnetic-circuit simulation of arbitrarily-shaped conducting structures,” in *Proc. IEEE Elect. Perf. Electron. Packag. Conf.*, Cambridge, MA, Oct. 2001, pp. 233–236.

[15] A. E. Ruehli, G. Antonini, and L. Jiang. *Circuit Oriented Electromagnetic Modeling Using the PEEC Techniques*. Hoboken NJ: Wiley-IEEE Press 2017.

[16] C. Wollenberg and A. Gurisch, “Analysis of 3-D interconnect structures with PEEC using SPICE,” *IEEE Trans. Electromagn. Compat.*, vol. 41, no. 4, pp. 412-417, Nov. 1999.

doi: 10.6342/NTU201902629

[17] H. Heeb and A. E. Ruehli, “Three-dimensional interconnect analysis using partial element equivalent circuits,” *IEEE Trans. Circuits Syst. I, Fundam. Theory Appl.*, vol. 39, no. 11, pp. 974-982, Nov 1992.

[18] J. Nitsch, F. Gronnwald, and G. Wollenberg. *Radiating Nonuniform Transmission-Line Systems and the Partial Element Equivalent Circuit Method*. Hoboken NJ: Wiley, 2009.

[19] Kochetov, S. V. “Time- and frequency-domain modeling of passive interconnection structures in field and circuit analysis.” Habilitation Dissertation, Otto-von-Guericke-University Magdeburg, Germany, 2008.

[20] P. J. Restle, A. E. Ruehli, S. G. Walker and G. Papadopoulos, “Full-wave PEEC time-domain method for the modeling of on-chip interconnects,” *IEEE Trans. Comput.-Aided Design Integr. Circuits Syst.*, vol. 20, no. 7, pp. 877-886, Jul 2001.

[21] A. E. Ruehli and A. C. Cangellaris, “Progress in the methodologies for the electrical modeling of interconnects and electronic packages,” *Proc. IEEE*, vol. 89, no. 5, pp. 740–771, May. 2001.

[22] Y. Dou and K.-L. Wu, “A passive PEEC-based micromodeling circuit for high speed interconnection problems,” *IEEE Trans. Microw. Theory Techn.*, vol. 66, no. 3, pp. 1201-1214, Mar. 2018.

[23] B. P. Nayak, S. R. Vedicherla and D. Gope, “Nonorthogonal 2.5-D PEEC for Power Integrity Analysis of Package-Board Geometries,” *IEEE Trans. Microw. Theory Techn.*, vol. 65, no. 4, pp. 1203-1214, April 2017.

[24] H. Chen, Y. Du and M. Chen, “Lightning Transient Analysis of Radio Base Stations,” *IEEE Trans. Power Del*., vol. 33, no. 5, pp. 2187-2197, Oct., 2018.

[25] J. Park, J. Lee, B. Seol and J. Kim, “Fast and Accurate Calculation of System-Level ESD Noise Coupling to a Signal Trace by PEEC Model Decomposition,” *IEEE Trans. Microw. Theory Techn.*, vol. 65, no. 1, pp. 50-61, Jan. 2017.

[26] S. Thamm, S. V. Kochetov, G. Wollenberg and M. Leone, “Alternative PEEC Modeling with Partial Reluctances and Capacitances for Power Electronics Applications,” *2007 7th International Symposium on Electromagnetic Compatibility and Electromagnetic Ecology*, Saint-Petersburg, 2007, pp. 56-59.

[27] L. K. Yeung and K.-L. Wu, “PEEC modeling of radiation problems for microstrip structures,” *IEEE Trans. Antennas Propag.*, vol. 61, no. 7, pp. 3648–3655, July. 2013.

[28] N. Xia, M. Tian, Y. Fu, Q. Zhou and J. Guo, “A Hybrid Meshing Technique for Ferromagnetic Structure Based on PEEC Method,” *IEEE Trans. Magn.*, vol. 51, no. 11, pp. 1-4, Nov. 2015.

doi: 10.6342/NTU201902629

[29] C.-C. Chou, W.-C. Lee, and T.-L. Wu, "A rigorous proof on the radiation resistance in generalized PEEC model," *IEEE Trans. Microw. Theory Techn.*, vol. 64, no. 12, pp. 4091-4097, Dec. 2016.

[30] C.-C. Chou and T.-L. Wu, "Direct Simulation of the Full-Wave Partial Element Equivalent Circuit Using Standard SPICE [Application Notes]," *IEEE Microwave Magazine*, vol. 20, no. 6, pp. 22-34, June 2019.

[31] G. Wollenberg and S. V. Kochetov, "Fast computation of radiated power distribution in coupled wire systems by the PEEC method," *2003 IEEE Int. Symp. on Electromagn. Compat., 2003. EMC '03.*, Istanbul, 2003, pp. 1152-1155 Vol. 2.

[32] Y. S. Cao, L. J. Jiang, and A. E. Ruehli, "Distributive radiation and transfer characterization based on the PEEC method," *IEEE Trans. Electromagn. Compat.*, vol. 57, no. 4, pp. 734–742, Aug. 2015.

[33] L. K. Yeung and K.-L. Wu, "Generalized partial element equivalent circuit (PEEC) modeling with radiation effect," *IEEE Trans. Microw. Theory Techn.*, vol. 59, no. 10, pp. 2377–2384, Oct. 2011.

[34] R. S. Elliott, *Antenna Theory and Design*, 2nd ed., Wiley-IEEE Press, 2003, pp. 64.

[35] A. Ishimaru, *Electromagnetic Wave Propagation, Radiation, and Scattering*, NJ: Prentice Hall, 1991, pp. 279–281.

[36] S. A. Schelkunoff, “Theory of antennas of arbitrary size and shape,” *Proceedings of the IRE*, vol. 29, no. 9, pp. 493-521, Sept, 1941.

[37] G. Antonini, “SPICE equivalent circuits of frequency-domain responses,” *IEEE Trans. Electromagn. Compat.*, vol. 45, no. 3, pp. 502-512, Aug. 2003.

[38] A. Bellen, N. Guglielmi and A. E. Ruehli, “Methods for linear systems of circuit delay differential equations of neutral type,” *IEEE Trans. Circuits Syst. I, Fundam. Theory Appl.*, vol. 46, no. 1, pp. 212-215, Jan 1999.

[39] S. V. Kochetov and G. Wollenberg, “Stability of full-wave PEEC models: reason for instabilities and approach for correction,” *IEEE Trans. Electromagn. Compat.*, vol. 47, no. 4, pp. 738-748, Nov. 2005.

[40] S. V. Kochetov and G. Wollenberg, “Stable and Effective Full-Wave PEEC Models by Full-Spectrum Convolution Macromodeling,” *IEEE Trans. Electromagn. Compat.*, vol. 49, no. 1, pp. 25-34, Feb. 2007.

[41] Synopsis, “HSPICE User Guide: Simulation and Analysis,” Version E-2010.12, Dec. 2010.

[42] H. K. Khalil, *Nonlinear Systems*, 3rd ed., Upper Saddle River, NJ: Prentice-Hall, 2000.

[43] G. F. Franklin, J. D. Powell, and A. Emami-Naeini, *Feedback Control of Dynamic Systems*, 2nd ed., MA: Addison-Wesley, 1993.

doi: 10.6342/NTU201902629

[44] K. Gu, V. L. Kharitonov, and J. Chen, *Stability of Time-Delay Systems*, Birkhauser, 2003.

[45] S. H. Friedberg, A. J. Insel, and L. E. Spence, *Linear Algebra*, 4th ed., NJ: Pearson Education, 2003.

[46] D. Henry, “Linear autonomous neutral functional differential equations,” *J. Differential Equations*, vol. 15, pp. 106-128, 1974.

[47] K. Gu, “A review of some subtleties of practical relevance for time-delay systems of neutral type,” *ISRN Applied Mathematics*, vol. 2012, article ID 725783, 2012.

[48] R. Datko, “A procedure for determination of the exponential stability of certain differential-difference equations,” *Quarterly of Applied Mathematics*, vol. 36, pp. 279-292, Oct. 1978.

[49] A. E. Ruehli, U. Miekkala and H. Heeb, “Stability of discretized partial element equivalent EFIE circuit models,” *IEEE Trans. Antennas Propag.*, vol. 43, no. 6, pp. 553-559, June 1995.

[50] J. E. Garrett, A. E. Ruehli and C. R. Paul, “Accuracy and stability improvements of integral equation models using the partial element equivalent circuit (PEEC) approach,” *IEEE Trans. Antennas Propag.*, vol. 46, no. 12, pp. 1824-1832, Dec 1998.

doi: 10.6342/NTU201902629

[51] D. Yue and Q.-L. Han, “A delay-dependent stability criterion of neutral systems and its application to a partial element equivalent circuit model,” *IEEE Trans. Circuits Systems II: Express Briefs*, vol. 51, no. 12, pp. 685-689, Dec. 2004.

[52] G. Antonini and P. Pepe, “Input-to-State Stability Analysis of Partial-Element Equivalent-Circuit Models,” *IEEE Trans. Circuits Systems I: Regular Papers*, vol. 56, no. 3, pp. 673-684, March 2009.

[53] X.-M. Zhang and Q.-L. Han, “A New Stability Criterion for a Partial Element Equivalent Circuit Model of Neutral Type,” *IEEE Trans. Circuits Systems II: Express Briefs*, vol. 56, no. 10, pp. 798-802, Oct. 2009.

[54] L. W. Johnson and R. D. Riess, *Numerical Analysis*, Addison-Wesley, 1977.

[55] J. P. Montgomery, “On the Complete Eigenvalue Solution of Ridged Waveguide,” *IEEE Trans. Microw. Theory Techn.*, vol. 19, no. 6, pp. 547-555, Jun. 1971.

[56] M. R. Wohlers, *Lumped and Distributed Passive Networks*. NY: Academic Press, 1969.

[57] J. Ekman, G. Antonini, A. Orlandi and A. E. Ruehli, “Impact of partial element accuracy on PEEC model stability,” *IEEE Trans. Electromagn. Compat.*, vol. 48, no. 1, pp. 19-32, Feb. 2006.

doi: 10.6342/NTU201902629

[58] J. Ekman, G. Antonini and A. E. Ruehli, “Toward improved time domain stability and passivity for full-wave PEEC models,” *2006 IEEE Int. Symp. Electromagn. Compat.*, Portland, OR, USA, 2006, pp. 544-549.

[59] K. M. Coperich, A. E. Ruehli and A. Cangellaris, “Enhanced skin effect for partial-element equivalent-circuit (PEEC) models,” *IEEE Trans. Microw. Theory Techn.*, vol. 48, no. 9, pp. 1435-1442, Sept. 2000.

[60] A. E. Ruehli, G. Antonini and L. Ljiang, “Passivization of EM PEEC solutions in the frequency and time domain,” *2013 International Conference on Electromagnetics in Advanced Applications (ICEAA)*, Torino, 2013, pp. 1273-1276.

[61] G. Antonini, D. Deschrijver and T. Dhaene, “Broadband Macromodels for Retarded Partial Element Equivalent Circuit (rPEEC) Method,” *IEEE Trans. Electromagn. Compat.*, vol. 49, no. 1, pp. 35-48, Feb. 2007.

[62] M. Swaminathan and A. E. Engin, *Power Integrity Modeling and Design for Semiconductors and Systems*, MA: Pearson Education, 2008.

[63] S. Grivet-Talocia and B. Gustavsen, *Passive Macromodeling: Theory and Applications*, Hoboken, NJ, USA: Wiley, 2016.

doi: 10.6342/NTU201902629

PUBLICATION LIST

I. Journal paper, magazine article, and book chapter

[1] **C.-C. Chou**, S.-S. Weng, Y.-C. Lu and T.-L. Wu, “EMI-Reduction Coding Based on 8b/10b,” *IEEE Trans. Electromagn. Compat.* (Accepted to be published.)

[2] **C.-C. Chou** and T.-L. Wu, “Direct Simulation of the Full-Wave Partial Element Equivalent Circuit Using Standard SPICE [Application Notes],” *IEEE Microwave Magazine*, vol. 20, no. 6, pp. 22-34, June 2019.

[3] T.-L. Wu and **C.-C. Chou**, “Chp.16: Differential-Mode Equalizers with Common-Mode Filtering, in Ferran Martin, Lei Zhu, Jiasheng Hong, Francisco Medina, Editor, Balanced Microwave Filters,” Wiley-IEEE Press, Mar. 2018.

[4] **C.-C. Chou** and T.-L. Wu, “Analysis of Peak and Statistical Spectrum of Random Nonreturn-to-Zero Digital Signals,” *IEEE Trans. Electromagn. Compat.*, vol. 59, no. 6, pp. 2002-2013, Dec. 2017.

[5] **C.-C. Chou**, W.-C. Lee, and T.-L. Wu, “A rigorous proof on the radiation resistance in generalized PEEC model,” *IEEE Trans. Microw. Theory Techn.*, vol. 64, no. 12, pp. 4091-4097, Dec. 2016.

[6] **C.-C. Chou**, S.-Y. Hsu, and T.-L. Wu, “Estimation Method for Statistical Eye Diagram in a Nonlinear Digital Channel,” *IEEE Trans. Electromagn. Compat.*, vol. 57, no. 6, pp. 1655-1664, Dec. 2015.

[7] H.-H. Chuang, **C.-C. Chou**, Y.-J. Chang, and T.-L. Wu, “A Branched Reflector Technique to Reduce Crosstalk Between Slot-Crossing Signal Lines,” *IEEE Microw. Wireless Compon. Letters*, vol. 22, no. 7, pp. 342-344, July 2012.

II. Conference paper

[1] **C.-C. Chou** and T.-L. Wu, “EMI-reduction coding based on 8b/10b,” *IEEE Int. Symp. EMCSI*, Washington, DC, 2017, pp. 373-376.

[2] Y.-A. Hsu, **C.-C. Chou**, C.-H. Cheng, and T.-L. Wu, “A radiation prediction method based on partial element equivalent circuit,” *APEMC*, Shenzhen, 2016, pp. 706-708.

[3] **C.-C. Chou** and T.-L. Wu, “Statistical eye diagram prediction for a 8b10b-coded channel using pulse response,” *IEEE 23rd EPEPS*, Portland, OR, 2014, pp. 43-46.

[4] S.-Y. Hsu, **C.-C. Chou** and T.-L. Wu, "Signal integrity: Influence of non-linear driver, different bit rates, and estimation by different algorithms," *APEMC*, 2014.

[5] **C.-C. Chou**, H.-H. Chuang, T.-L. Wu, S.-H. Weng, and C.-K. Cheng, “Eye prediction of digital driver with power distribution network noise,” *IEEE 21st EPEPS*, Tempe, AZ, 2012, pp. 131-134.

[6] Y.-J. Chang, **C.-C. Chou**, H.-H. Chuang, C.-N. Chiu, and T.-L. Wu, "A new solution and its estimation method for slot-crossing signals to reduce ISI-increased crosstalk," *2012 APEMC*, Singapore, 2012, pp. 41-44.

doi: 10.6342/NTU201902629